J. Astrophys. Astr. (2004) **25,** 1–55

Optical Variability Properties of High Luminosity AGN Classes

C. S. Stalin[1,2,3], Gopal-Krishna[2], Ram Sagar[1] & Paul J. Wiita[4]
[1]*Aryabhatta Research Institute of Observational Sciences (ARIES), Manora Peak Nainital 263 129, India.*
[2]*National Centre for Radio Astrophysics, TIFR, Pune University Campus, Pune 411 007, India.*
[3]*Laboratoire de Physique Corpusculaire et Cosmolgie, College de France, 11 pl. Marcelin Berthelot, F-75231, Paris Cedex 5, France.*
[4]*Department of Physics & Astronomy, MSC 8R0314, Georgia State University, Atlanta, Georgia 30303-3088, USA.*

Received 2003 June 24; accepted 2004 June 22

Abstract. We present the results of a comparative study of the intra-night optical variability (INOV) characteristics of radio-loud and radio-quiet quasars, which involves a systematic intra-night optical monitoring of seven sets of high luminosity AGNs covering the redshift range $z \simeq 0.2$ to $z \simeq 2.2$. The sample, matched in the optical luminosity – redshift ($M_B - z$) plane, consists of seven radio-quiet quasars (RQQs), eight radio lobe-dominated quasars (LDQs), five radio core-dominated quasars (CDQs) and six BL Lac objects (BLs). Systematic CCD observations, aided by a careful data analysis procedure, have allowed us to detect INOV with amplitudes as low as about 1%. Present observations cover a total of 113 nights (720 hours) with only a single quasar monitored as continuously as possible on a given night. Considering the cases of only unambiguous detections of INOV we have estimated duty cycles (DCs) of 17%, 12%, 20% and 61% for RQQs, LDQs, CDQs, and BLs, respectively. The much lower amplitude and DC of INOV shown by RQQs compared to BLs may be understood in terms of their having optical synchrotron jets which are modestly misdirected from us. From our fairly extensive dataset, no general trend of a correlation between the INOV amplitude and the apparent optical brightness of the quasar is noticed. This suggests that the physical mechanisms of INOV and long term optical variability (LTOV) do not have a one-to-one relationship and different factors are involved. Also, the absence of a clear negative correlation between the INOV and LTOV characteristics of blazars of our sample points toward an inconspicuous contribution of accretion disk fluctuations to the observed INOV. The INOV duty cycle of the AGNs observed in this program suggests that INOV is associated predominantly with the highly polarized optical emission components. We also report new VLA imaging of two RQQs ($1029+329$ & $1252+020$) in our sample which has yielded a 5 GHz detection in one of them ($1252+020$; $S_{5\,\mathrm{GHz}} \simeq 1$ mJy).

Key words. Galaxies: active—galaxies: jets—galaxies: photometry—quasars: general.

1. Introduction

The question of why only a small fraction of quasars are radio-loud has been debated for almost forty years. Various arguments have been put forward to explain this apparent radio-loud/radio-quiet dichotomy. Although the existence of the dichotomy has even been questioned (e.g., Goldschmidt *et al.* 1999; White *et al.* 2000), a recent careful analysis of the tricky selection effects indicates that it may be real (Ivezic *et al.* 2002). It has been argued recently that the radio emission correlates with the mass of the nuclear black hole (e.g., Dunlop *et al.* 2003 and references therein); however, this assertion has been questioned (Ho 2002; Woo & Urry 2002). McLure & Dunlop (2001) stress the possible importance of accretion rate and changes in accretion mode to this dichotomy.

On the theoretical side, two main approaches have been put forward to explain this dichotomy. In one scenario, the jets in RQQs are absent or inherently weak. Some possible mechanisms identify this differentiating factor with the spin of the black hole (Wilson & Colbert 1995; Blandford 2000), or magnetic configurations (Meier 2002). Wills (1996) suggested that all quasars launch jets but those aimed into a galactic disk are destroyed by interactions with the dense gas and thus appear radio-quiet. An extreme variant of this possibility is the hypothesis that the relativistic jets in RQQs are largely snuffed out before escaping the nuclear region itself due to heavy inverse Compton losses (Kundt 2002). As a consequence, jets on radio emitting physical scales are quenched, even though they might emit substantial amounts of non-thermal optical synchrotron emission on micro-arcsecond scales. Unfortunately, such μ arcsec scales are beyond the reach of any existing imaging telescopes and the only way to probe their conditions is through flux variability observations.

Although intra-night optical variability (INOV) or "microvariability" was convincingly established for blazars over a decade ago (e.g., Miller, Carini & Goodrich 1989; Carini, Noble & Miller 1998), the question of whether RQQs also show INOV has remained controversial (Gopal-Krishna *et al.* 1995, 2000; Jang & Miller 1995, 1997; Rabbette *et al.* 1998; de Diego *et al.* 1998; Romero *et al.* 1999; Carini *et al.* 1999). Likewise, the cause of INOV is still a much debated issue. However, for blazars (CDQs and BL Lacs) which are believed to be dominated by non-thermal Doppler boosted emission from jets (e.g., Blandford & Rees 1978), the occurrence of rapid intensity variations in both the radio and optical bands is believed to be due to shocks propagating down their relativistic jets (e.g., Marscher & Gear 1985). Intra-night variability in blazars may well arise from instabilities or turbulent fluctuations in the flow of such jets (e.g., Hughes, Aller & Aller 1992; Marscher, Gear & Travis 1992). Alternate models, which invoke accretion disk instabilities or perturbations (e.g., Mangalam & Wiita 1993; for a review see Wiita 1996) may also explain INOV, particularly in RQQs, where any contribution from the jets, if they are at all present, is weak.

While conclusive evidence for the presence of jets in RQQs is far from clear, deep VLA observations hint at the presence of weak jets even in RQQs (Kellermann *et al.* 1989; Miller, Rawlings & Saunders 1993; Kellermann *et al.* 1994; Papadopoulos *et al.* 1995; Kukula *et al.* 1998; Blundell & Beasley 1998; Blundell & Rawlings 2001). The existence of incipient nuclear jets in RQQs have also been inferred from radio spectral index measurements of optically selected quasar samples (Falcke, Patnaik & Sherwood 1996). If indeed optical synchrotron jets exist even in RQQs, then a fairly

robust signature of such un-imageable (because at the micro-arcsecond scale) jets can come from detection of INOV at the level exhibited by their radio loud counterparts, namely the LDQs. To persue these issues, a project to search for INOV in the four major classes of powerful AGNs was initiated in 1998 as a collaborative effort between the Aryabhatta Research Institute of Observational Sciences (ARIES), Nainital and the National Centre for Radio Astrophysics (NCRA), Pune. The present paper presents the detailed results of this project, part of which has been published elsewhere (Gopal-Krishna *et al.* 2003, hereafter GSSW03; Stalin *et al.* 2004, SGSW04; Sagar *et al.* 2004, SSGW04).

2. Selection of the sample

AGNs in general, have very different observational characteristics including a huge range in luminosity, redshift and power across the electromagnetic spectrum. Also, the co-moving number density of quasars detected at a given absolute magnitude is found to undergo a rapid evolution with redshift (Schmidt & Green 1983; Boyle *et al.* 2000; Wisotzki 2000). Therefore, sample selection is crucial for studying INOV of quasars. To avoid selection biases introduced by differences in luminosity and redshift, the objects were selected such that all objects in a given set have similar optical magnitudes, in addition to having very similar redshifts; they are thus well matched in the optical luminosity–redshift plane. Our sample, selected from the catalog of Véron-Cetty & Véron (1998), consists of seven sets of AGNs covering a total redshift range from $z = 0.17$ to $z = 2.2$. Each set was designed to consist of a radio-quiet quasar (RQQ), a radio lobe-dominated quasar (LDQ), a radio core-dominated quasar (CDQ) and/or a BL Lac object (BL). These seven sets cover seven narrow redshift intervals centered at $z = 0.21$, 0.26, 0.35, 0.43, 0.51, 0.95 and 1.92. However, it was not possible to find seven complete sets that satisfied our other observationally dictated criteria (sufficiently bright to allow dense temporal sampling and having several suitable nearby comparison stars), so our entire sample actually consists of 26, not 28, QSOs with the distribution of 7 RQQs, 8 LDQs, 5 CDQs and 6 BLs. The slight unevenness in number is because the two QSOs $1308 + 326$ and $1512 + 370$ were initially selected as CDQs, but better radio data classified $1512 + 370$ as an LDQ (see SGSW04), while the blazar $1308 + 326$ was found to be a BL Lac (see SSGW04). Due to the paucity of BL Lacs at low z, one object ($1215 + 303$) serves as a member of both Sets 1 and 2, and none was available in the highest redshift bin. The general properties of the objects monitored in this program are given in Table 1.

The magnitude range for the QSOs in our sample is $-30.0 < M_B < -24.3$ (assuming $H_0 = 50\,\mathrm{km\ s^{-1}\,Mpc^{-1}}$, $q_0 = 0$). This implies that we are dealing with luminous AGNs, which are legitimately classified as QSOs, and in all cases the underlying galaxy contamination to the luminosity of the AGN is $< 10\%$. Moreover, since the AGN of the four different types are similarly distributed in the $z - M_B$ plane, this selection criterion minimises selection biases such as K-corrections, evolutionary effects and any other differences linked to redshift and luminosity. Conservatively, we have included in our sample only those RQQs for which the K-corrected ratio of 5 GHz to 2500 Å flux densities is less than 1 i.e., $R^* < 1$ (see Table 1) even though the usual criterion used to call a QSO an RQQ is $R < 10 (R = f(5\,\mathrm{GHz})/f(B)$; Kellermann *et al.* 1989).

Table 1. General information on radio-quiet, lobe-dominated, core-dominated and BL Lac objects monitored in the present programme.

Set no.	Object	Other name	Type	RA(2000)	Dec(2000)	B (mag)	M_B (mag)	z	%Pol† (opt)	log $R^{*\ddagger}$
1.	0945+438	US 995	RQQ	09 48 59.4	+43 35 18	16.45	−24.3	0.226	—	< -0.07
	2349−014	PKS 2349−01	LDQ	23 51 56.1	−01 09 13	15.45	−24.7	0.174	0.91	2.47
	1309+355	PG 1309+355	CDQ	13 12 17.7	+35 15 23	15.60	−24.7	0.184	0.31*	1.36
	1215+303	B2 1215+30	BL	12 17 52.0	+30 07 01	16.07	−24.8	0.237	8.0	2.63
2.	0514−005	1E 0514−0030	RQQ	05 16 33.5	−00 27 14	16.26	−25.1	0.291	—	< 0.06
	1004+130	PG 1004+130	LDQ	10 07 26.2	+12 48 56	15.28	−25.6	0.240	0.78	2.29
	1128+315	B2 1128+31	CDQ	11 31 09.4	+31 14 07	16.00	−25.3	0.289	0.62	2.43
3.	1252+020	Q 1252+0200	RQQ	12 55 19.7	+01 44 13	15.48	−26.2	0.345	—	−0.28
	0134+329	3C 48.0	LDQ	01 37 41.3	+33 09 35	16.62	−25.2	0.367	1.41	3.93
	1512+370	B2 1512+37	LDQ	15 14 43.0	+36 50 50	16.25	−25.6	0.370	1.17	3.57
	0851+202	OJ 287	BL	08 54 48.8	+20 06 30	15.91	−25.5	0.306	12.50	3.32
4.	1101+319	TON 52	RQQ	11 04 07.0	+31 41 11	16.00	−26.2	0.440	—	< -0.41
	1103−006	PKS 1103−006	LDQ	11 06 31.8	−00 52 53	16.39	−25.7	0.426	0.37	2.80
	1216−010	PKS 1216−010	CDQ	12 18 35.0	−01 19 54	16.17	−25.9	0.415	6.90**	2.34
	0735+178	PKS 0735+17	BL	07 38 07.4	+17 42 19	16.76	−25.4	>0.424	14.10	3.55
5.	1029+329	CSO 50	RQQ	10 32 06.0	+32 40 21	16.00	−26.7	0.560	—	< -0.64
	0709+370	B2 0709+37	LDQ	07 13 09.4	+36 56 07	15.66	−26.8	0.487	—	2.08
	0955+326	3C 232	CDQ	09 58 20.9	+32 24 02	15.88	−26.7	0.530	0.53	2.74
	0219+428	3C 66A	BL	02 22 39.6	+43 02 08	15.71	−26.5	0.444	11.70	2.83
6.	0748+294	QJ 0751+2919	RQQ	07 51 12.3	+29 19 38	15.00	−29.0	0.910	—	−0.68
	0350−073	3C 94	LDQ	03 52 30.6	−07 11 02	16.93	−27.2	0.962	1.42	3.07
	1308+326	B2 1308+32	BL	13 10 28.7	+32 20 44	15.61	−28.6	0.997	10.20	2.71
	0235+164	AO 0235+164	BL	02 38 38.9	+16 37 00	16.46	−27.6	0.940	14.90	3.29
7.	1017+279	TON 34	RQQ	10 19 56.6	+27 44 02	16.06	−29.8	1.918	—	< -0.49
	0012+305	B2 0012+30	LDQ	00 15 35.9	+30 52 30	16.30	−29.1	1.619	—	1.76
	1225+317	B2 1225+31	CDQ	12 28 24.8	+31 28 38	16.15	−30.0	2.219	0.16	2.26

‡R* is the ratio of the 5 GHz to 2500 Å flux densities calculated following Stocke *et al.* (1992).

†Optical polarization are from Wills *et al.* (1992) except those marked with * (Berriman *et al.* 1990) and ** (Hutsemekers & Lamy 2001).

3. Radio observations and reductions

Since radio flux data were not available for two of our QSOs ($1252+020$ and $1029+329$), in order to ascertain their radio classification, we took VLA[1] snapshots at 5 GHz in the BnC configuration, in a dual intermediate frequency mode with a total on-source integration time of 10 minutes. The resulting images, made using the CLEAN algorithm within the AIPS software, are shown in Fig. 1 (rms noise $\sim 50\mu$Jy). While the QSO $1252+020$ was found be associated with an extended weak radio source of 1 ± 0.1 mJy, the other QSO, $1029+329$, has no radio counterpart down to a 3-sigma limit of 0.15 mJy. Therefore both are properly classified as RQQs, with $R = 0.52$ and $R < 0.23$, respectively.

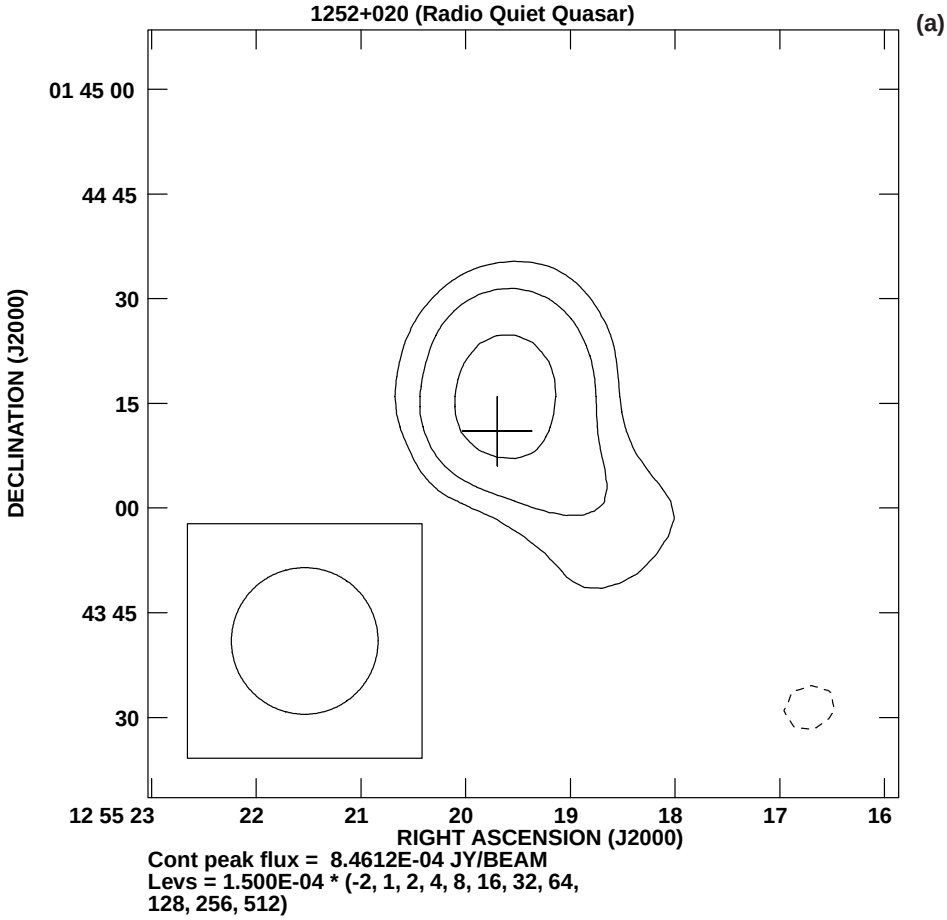

Figure 1. (*Continued*)

[1]The Very Large Array (VLA) of the National Radio Astronomy Observatory is operated by Associated Universities, Inc. under a cooperative agreement with the National Science Foundation.

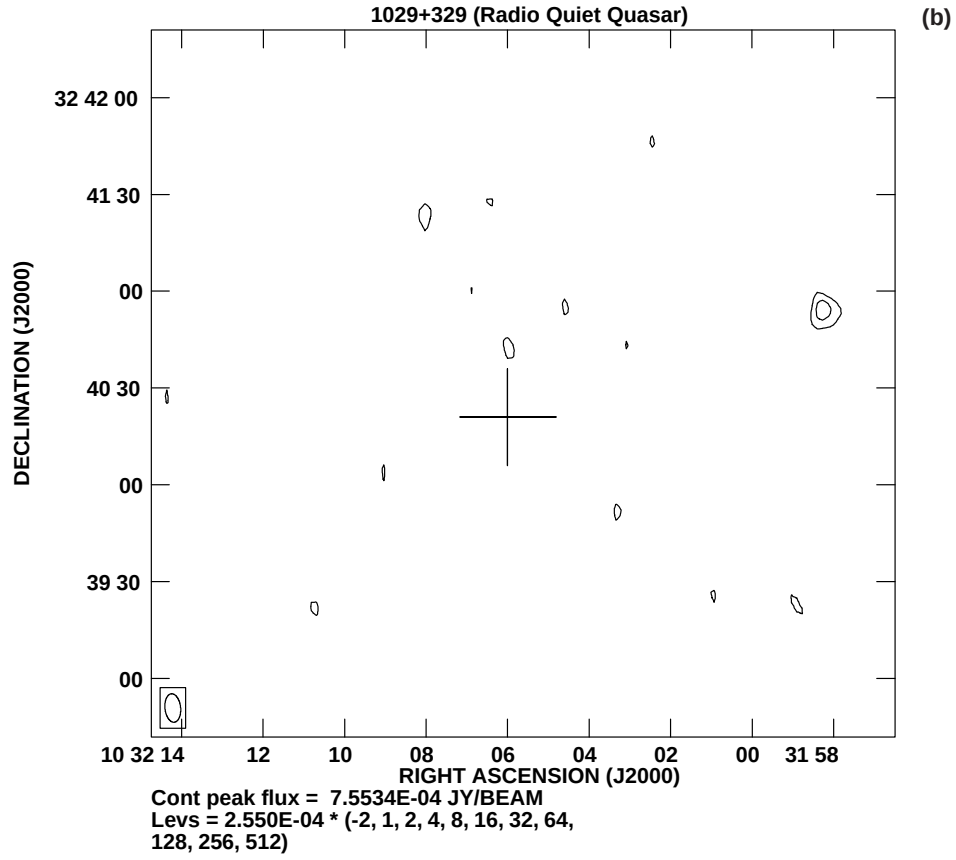

Figure 1(a–b). VLA 5 GHz total intensity images of the quasars 1252+020 (left) and 1029+329 (right). The synthesised beams are shown in the inset boxes.

4. Optical observations and data reductions

4.1 *The instrument*

The optical observations of the selected quasars were carried out using the 104 cm Sampurnanand telescope of the ARIES, Nainital. This is an RC system with a f/13 beam (Sagar 1999). The detector used for the observations was a cryogenically cooled $2048 \times 2048\,\mathrm{pixel}^2$ CCD, except prior to October 1999, when a smaller CCD of size $1024 \times 1024\,\mathrm{pixel}^2$ was used. In each CCD, a pixel corresponds to a square of 0.38 arcsec size, covering a total sky area of about $12' \times 12'$ in the case of larger CCD and about $6' \times 6'$ in the case of smaller CCD. To increase the S/N ratio, observations were carried out in 2×2 binned mode. Practically all the observations were carried out using R filter, except on two nights, where quasi-simultaneous R and I filter observations were done. The choice of the R filter in this observational program is because of its being at the maximum response of the CCD systems; thus the time resolution achievable for each object is maximised.

4.2 *Observing strategy*

The main goal of this program was to obtain lengthy temporally dense data trains for each object on each night it was observed, in order to be able to detect low level intra-night variations at high S/N. The optical monitoring of blazars has shown that the probability of observing INOV in a given night is greatly enhanced by continuous monitoring for at least 3 to 4 hours (Carini 1990). Accordingly, we attempted to monitor each object for a minimum of 5 hours per night, with a time resolution of the order of 10 minutes. However, on occasions when the object was in a faint state, the sampling time could be up to 30 minutes.

Another important strategy was to center the field of view so as to cover as many suitable comparison stars as possible within the CCD frame. For each of our quasars we could get at least two, but often more, comparison stars within 1 magnitude of the quasar's brightness in the frame. Several putative sources were eliminated from our sample if they had no suitable comparison stars in their vicinities. The availability of multiple comparison stars allowed us to identify and discount any comparison star which itself varied during a given night, thus allowing reliable differential photometry of the QSO. The positions and apparent B and R magnitudes of all the comparison stars used in our differential photometry are given in SGSW04 and SSGW04 and so will not be repeated here. The entire programme consists of observations on 113 nights from October 1998 through May 2002, adding up to 720 hours of useful observations (i.e., 6.4 hours/night on average). A log of the observations along with the basic results are given in Table 2.

4.3 *Data reduction*

Preliminary processing of the images as well as the photometry was done using the IRAF[2] software. The bias level of the CCD is determined from several bias frames (generally more than seven) taken intermittently during our observations over the night. A mean bias frame was formed using the task *zerocombine* in IRAF which was then subtracted from all the image frames of the night. Care was also taken in forming the mean bias frame such that they are not affected by cosmic-ray (CR) hits. The routine step of dark frame subtraction was not performed as the CCDs used in the observations were cryogenically cooled to -120° C at which temperature the amount of thermal charge is negligible for the exposure times of the present observations. Flat fielding was done by taking several twilight sky frames which were then median combined to generate the flat field template which was then used to derive the final frames; any errors in the flat field template were well within 0.1%. Finally CR hits seen in the flat fielded target frames were removed using the facilities available in MIDAS[3].

[2]IRAF is distributed by the National Optical Astronomy Observatories, which is operated by the Association of Universities for Research in Astronomy, Inc. under co-operative agreement with the National Science Foundation.

[3]MIDAS stands for Munich Image and Data Analysis System and has been designed and developed by the European Southern Observatory (ESO) in Munich, Germany.

Table 2. A log of observations and basic results of INOV of the QSOs.

Set no.	Object (type)	Date	N (obs)	T (hr)	INOV status*	$C_{\rm eff}^{\dagger}$	$\psi^{\dagger}$ %	$\tau^{\ddagger}$ (hr)	$P^{\ddagger}$ (hr)	$\eta_{\rm obs}^{\S}$	$\delta_{\rm obs}^{\S}$	Ref. to DLCs
1.	0945+438	15.01.99	44	8.0	NV							Present work
	(RQQ)	26.02.00	31	6.3	NV							Present work
		23.01.01	24	6.6	NV							Present work
	2349−01	13.10.01	34	6.8	V	3.6	2.2			0.02		SGSW04
	(LDQ)	17.10.01	39	7.6	V	3.1	1.5			0.02		SGSW04
		18.10.01	40	7.7	V	3.2	1.6	5.0		0.02		SGSW04
	1309+355	25.03.99	39	6.7	NV							Present work
	(CDQ)	01.04.01	32	4.6	NV							Present work
		02.04.01	41	5.2	NV							Present work
	1215+303	20.03.99	21	7.0	V	5.5	3.5	4.2		0.74	1.8	SSGW04
	(BL)	25.02.00	28	5.9	NV							Present work
		31.03.00	27	5.0	NV							Present work
		19.04.02	23	6.8	V	4.9	1.8	>6.8		0.05	1.0	SSGW04
2.	0514−005	09.12.01	25	5.3	NV							Present work
	(RQQ)	10.12.01	23	5.8	NV							Present work
		19.12.01	35	7.5	NV							Present work
	1004+130	27.02.99	30	4.3	NV							Present work
	(LDQ)	16.02.99	36	6.5	NV							Present work
		29.03.00	21	3.8	NV							Present work
		30.03.00	26	4.6	NV							Present work
		18.02.01	42	5.5	NV							Present work
		24.03.01	50	6.4	NV							SGSW04
	1128+315	18.01.01	31	5.7	NV							Present work
	(CDQ)	09.03.02	27	8.2	NV							SGSW04
		10.03.02	28	8.3	NV							Present work
3.	1252+020	22.03.99	36	6.4	V	3.3	2.3					SGSW04
	(RQQ)	09.03.00	29	6.1	NV							Present work
		03.04.00	19	4.3	V	3.6	0.9	>4.3		0.04		SGSW04
		26.04.01	20	4.6	NV							Present work
		18.03.02	19	7.3	NV							Present work

Table 2. (*Continued*)

Set no.	Object (type)	Date	N (obs)	T (hr)	INOV status*	$C_{\rm eff}^{\dagger}$	$\psi^{\dagger}$ %	$\tau^{\ddagger}$ (hr)	$P^{\ddagger}$ (hr)	$\eta_{\rm obs}^{\S}$	$\delta_{\rm obs}^{\S}$	Ref. to DLCs
3.	0134+329	07.11.01	33	6.5	NV							Present work
	(LDQ)	08.11.01	32	6.7	NV							Present work
		13.11.01	46	8.6	NV							Present work
	1512+370	23.03.02	24	7.0	NV							Present work
	(LDQ)	27.03.02	28	7.0	NV							Present work
		21.04.02	11	4.3	V	2.8	2.6	0.4		0.53	1.60	Present work
		23.04.02	15	5.3	NV							Present work
		01.05.02	19	6.6	V	3.0	3.9	0.4	1.8,3.4,5.6	0.18	1.29	Present work
	0851+202	29.12.98	19	6.8	V	2.8	2.3	>6.8		0.12	1.20	SSGW04
	(BL)	31.12.99	29	5.6	V	6.5	3.8	3.0		0.07	1.07	SSGW04
		28.03.00	22	4.2	V	5.8	5.0	1.2		0.88	1.77	SSGW04
		17.02.01	48	6.9	V	2.7	2.8	2.0	3.8	0.36	1.48	SSGW04
4.	1101+319	12.03.99	39	8.5	NV							Present work
	(RQQ)	04.04.00	22	5.6	NV							Present work
		21.04.01	21	6.1	V	2.6	1.2	0.8		0.11	1.17	SGSW04
		22.04.01	21	5.8	NV							Present work
	1103−006	17.03.99	23	3.8	NV							Present work
	(LDQ)	18.03.99	40	7.5	V	3.1	2.4	0.6		0.55	1.62	SGSW04
		06.04.00	13	3.9	PV	2.1	1.2					SGSW04
		25.03.01	28	7.2	NV							SGSW04
		14.04.01	19	4.5	NV							Present work
		22.03.02	15	5.8	PV	2.2	0.7					SGSW04
	1216−010	11.03.02	22	8.0	V	3.2	7.3	1.8	3.2	0.29	1.42	SSGW04
	(CDQ)	13.03.02	24	8.5	V	2.6	3.8	1.2	2.2	0.16	1.26	SSGW04
		15.03.02	11	3.9	V	3.9	5.5	1.0	2.2	0.77	1.73	SSGW04
		16.03.02	22	8.2	V	6.6	14.1	>8.2				SSGW04
	0735+178	26.12.98	49	7.8	NV							SGSW04
	(BL)	30.12.99	65	7.4	NV							Present work
		25.12.00	43	6.0	NV							Present work
		24.12.01	43	7.3	V	2.8	1.0	>8.1		0.05	1.00	SSGW04

Table 2. (*Continued*)

Set no.	Object (type)	Date	N (obs)	T (hr)	INOV status*	$C_{\rm eff}^{\dagger}$	$\psi^{\dagger}$ %	$\tau^{\ddagger}$ (hr)	$P^{\ddagger}$ (hr)	$\eta_{\rm obs}^{\S}$	$\delta_{\rm obs}^{\S}$	Ref. to DLCs
5.	1029+329	13.03.99	45	8.4	—	—	—	—	—	—	—	—
	(RQQ)	02.03.00	19	5.0	NV							Present work
		05.04.00	19	5.3	V	4.3	1.3	>6.2		0.13	1.21	SGSW04
		23.03.01	20	5.8	NV							Present work
		06.03.02	31	8.5	NV							SGSW04
		08.03.02	17	6.1	V	2.8	1.1					SGSW04
	0709+370	20.01.01	29	6.5	NV							Present work
	(LDQ)	21.01.01	29	6.2	NV							Present work
		25.01.01	31	7.1	NV							Present work
		20.12.01	49	7.9	V	3.1	1.4	4.4	7.0	0.007		SGSW04
		21.12.01	48	7.5	NV							Present work
	0955+326	19.02.99	36	6.5	NV							Present work
	(CDQ)	03.03.00	37	6.3	NV							Present work
		05.03.00	34	6.9	PV	2.2	0.7					SSGW04
	0219+428	14.11.98	118	6.5	V	6.0	5.4	>6.5		1.04	1.83	SSGW04
	(BL)	13.11.99	123	5.7	V	>6.6	5.5	>5.9		4.91	2.50	SSGW04
		24.10.00	73	9.1	V	5.8	4.3	>9.1		1.39	1.94	SSGW04
		26.10.00	82	10.1	V	3.5	3.2	4.9		1.14	1.87	SSGW04
		01.11.00	103	9.0	V	2.9	2.2	3.9		0.26	1.39	SSGW04
		24.11.00	71	5.1	NV							Present work
		01.12.00	59	5.1	V	>6.6	8.0	>5.1		2.14	2.12	SSGW04
6.	0748+294	14.12.98	22	7.6	NV							Present work
	(RQQ)	13.01.99	56	8.3	NV							Present work
		09.12.99	26	5.1	NV							Present work
		24.11.00	28	5.4	NV							Present work
		01.12.00	32	6.0	NV							SGSW04
		25.12.01	30	5.4	NV							SGSW04
	0350−073	14.11.01	31	6.6	NV							Present work
	(LDQ)	15.11.01	26	5.5	NV							Present work
		18.11.01	25	5.7	NV							Present work

Table 2. (*Continued*)

Set no.	Object (type)	Date	N (obs)	T (hr)	INOV status*	$C_{\rm eff}^{\dagger}$	$\psi^{\dagger}$ %	$\tau^{\ddagger}$ (hr)	$P^{\ddagger}$ (hr)	$\eta_{\rm obs}^{\S}$	$\delta_{\rm obs}^{\S}$	Ref. to DLCs
6.	1308+326	23.03.99	17	6.0	—	—	—	—	—	—	—	—
	(BL)	26.04.00	16	5.6	NV							Present work
		03.05.00	19	6.7	—	—	—	—	—	—	—	—
		17.03.02	19	7.7	V	3.1	3.4	1.2,4.4		5.39	2.55	SSGW04
		20.04.02	14	5.8	NV							Present work
		02.05.02	15	5.1	NV							Present work
	0235+164	13.11.98	36	4.4	—	—	—	—	—	—	—	—
	(BL)	12.11.99	39	6.6	V	>6.6	12.8	3.6		2.48	2.18	SSGW04
		14.11.99	34	6.2	V	3.2	10.3	3.4		1.23	1.90	SSGW04
		22.10.00	39	7.9	V	2.6	7.6			1.71	2.03	SSGW04
		28.10.00	29	6.8	—	—	—	—	—	—	—	—
7.	1017+279	14.03.99	43	7.3	NV							Present work
	(RQQ)	14.01.00	33	7.1	NV							Present work
		27.02.00	33	8.1	NV							Present work
	0012+305	18.01.01	17	3.6	NV							Present work
	(LDQ)	20.01.01	14	3.2	NV							Present work
		24.01.01	14	2.9	NV							Present work
		14.10.01	20	5.7	NV							Present work
		21.10.01	22	5.7	NV							SGSW04
		22.10.01	24	6.2	NV							Present work
	1225+317	07.03.99	49	6.6	NV							Present work
	(CDQ)	07.04.00	23	6.0	NV							Present work
		20.04.01	34	7.4	NV							Present work

*V (for variables); PV (for probable variables); NV (for non-variables); — (for poor data).
$^{\dagger}C_{\rm eff}$ and ψ indicate the statistical significance and amplitude of variability.
‡Variability timescales, τ, and "periods", P from structure functions.
§Efficiency, $\eta_{\rm obs}$, and Doppler factor, $\delta_{\rm obs}$, in the framework of relativistic beaming models.

4.4 *Photometry*

Aperture photometry on both the AGN and the comparison stars present on the flat-fielded CCD frames were carried out using the task *phot* in IRAF. A critical input to be specified to *phot* was the radius of the aperture used to perform the photometry. The selection of this aperture determines the S/N for each object in the frame. In an investigation by Howell (1989) the issue of an optimum aperture to maximize the S/N was discussed; this nominally optimum aperture is found to lie close to the FWHM of the PSF of the stars on the frame. By choosing an aperture that is relatively close to the FWHM of a source, clearly some of the total flux from the source will be left out of the aperture. However, in this work only magnitude differences, and not the absolute fluxes, are important. Hence, this procedure of selecting an optimum aperture was promising for enhancing the photometric precision of the observations, since the S/N was maximised. The procedure we followed for finding an optimum aperture was identical to that used in Noble (1995). We specified several aperture radii (starting from the median FWHM of the night and then incrementing by 0.2 pixels) and then identified the aperture that yielded magnitudes of stars such that the scatter or variance of the resulting steadiest pair of Star – Star differential light curves (DLCs) was minimised. This process of finding the optimum aperture is illustrated in Fig. 2, which shows five DLCs for the same pair of comparison stars in the field of the quasar $1017 + 279$ observed on 27th February 2000. The larger variance at small apertures is due to the inclusion of fewer source pixels, whereas the larger variance at large apertures is due to too many noise pixels compared to source pixels.

The local sky background (instead of a mean over the entire CCD chip) estimated around the QSO and each of the comparison stars is subtracted from the counts over the optimum aperture to get the instrumental magnitudes for generating the DLCs. This sky subtraction (with fluctuations across the CCD chip within 0.1%) is not a major issue in this technique of differential photometry. The overall errors due to flat fielding, background subtraction and any effects in the instrument during our observations are well below 0.3%, which is also the typical standard deviation attained in the DLCs involving comparison stars.

5. Potential sources of spurious intensity variations

5.1 *Variable seeing*

One potential source of spurious variability in aperture photometry is the contamination arising from the host galaxy of the AGN recorded on the CCD frame. This is because the surface brightness profile of any underlying galaxy will not respond to atmospheric seeing fluctuations in a manner similar to the central AGN. Thus, intra-night fluctuations in the seeing could result in the variable contribution from the host galaxy within the aperture, producing spurious changes in the brightness that could be mistaken for AGN variability. Recently the effect of spurious variations introduced in the DLCs by atmospheric seeing fluctuations has been quantitatively addressed by Cellone, Romero & Combi (2000) through extensive simulations. These authors conclude that spurious differential magnitude variations due to seeing fluctuation can be substantial for AGN with relatively brighter hosts (such as Seyfert galaxies) when too small photometric apertures are used.

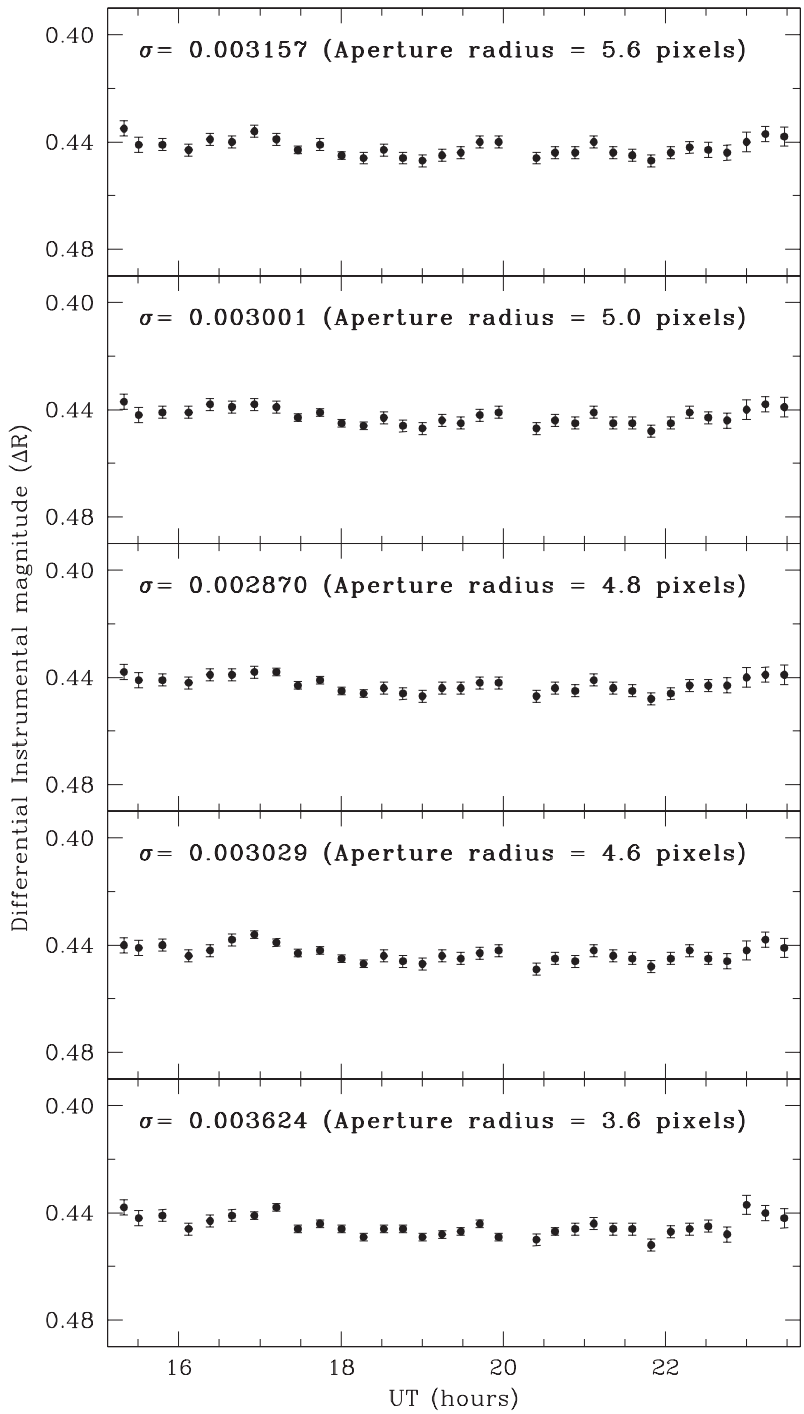

Figure 2. DLCs involving stars S2 and S3 in the field of the RQQ 1017 + 279 observed on 27th February 2000, for five different aperture radii showing the selection of optimum aperture. The minimum scatter occurs at an aperture radius of 4.8 pixels.

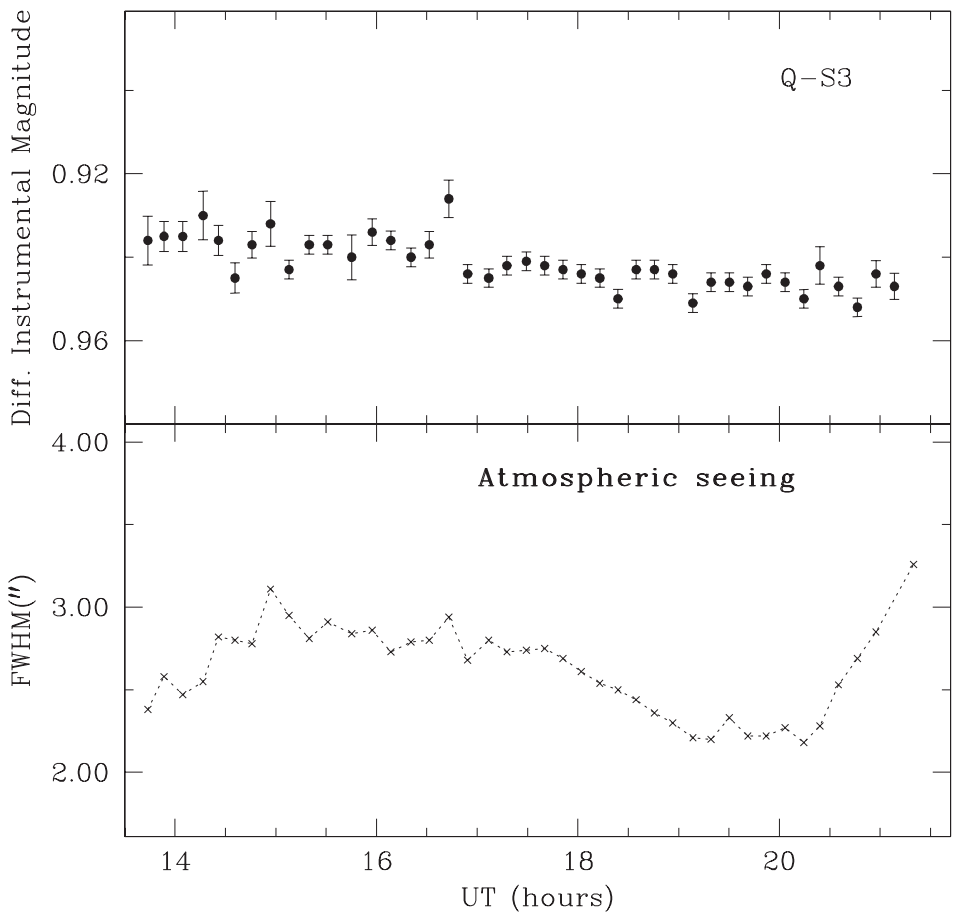

Figure 3. DLC of the LDQ 2349 − 014 observed on 17th October 2001 (top) and the variation of seeing during that night (bottom panel). The aperture radius used for the photometry is 5″.

Our data are very unlikely to be affected by this problem in any measurable sense, since all the AGNs in our sample are luminous ($M_B < -24.3$ mag); even though the host galaxies of powerful quasars are also typically fairly luminous galaxies, the nucleus is usually highly dominant *vis-à-vis* the host galaxy. In fact, the underlying host galaxy is not seen in any CCD images of our quasars except one, (LDQ 2349 − 014) which belongs to the lowest-redshift bin of our sample. We therefore conclude that except in the case of LDQ 2349 − 014, the host galaxies are fainter than $R \sim 19$ mag, while the quasars are brighter than $R \sim 17$ mag. Hence, applying the results of Cellone *et al.* (2000) for our quasar and host galaxy magnitudes and our adopted photometric apertures ranging from 3 to 7 arcsec, which are always rather large compared to the seeing FWHM lying between 1.4 and 4.4 arcsec, leads us to conclude that any such putative spurious variations should be well under 0.01 mag.

To explicitly consider the worst case scenario, Fig. 3 shows the DLC (with respect to Star 3) of the dimmest quasar relative to its host in our sample, LDQ 2349 − 014; also in this figure is the variation of atmospheric seeing during the observing night. If seeing variations were to play a role, one would expect to see the quasar plus host

galaxy appear to relatively brighten (dim) when the seeing is better (worse), as more (less) of the galaxy's light will be included in the aperture. As Fig. 3 shows, while the seeing worsened over the first hour or so of the observations the quasar remained essentially constant in luminosity; as the seeing improved between 17 and 20 UT the quasar dimmed slightly; and as the seeing dramatically worsened over the last hour of observations, the data became a little noisier but the mean quasar brightness didn't change. Either no (or a negative to the expected) correlation is found between the seeing variations and the DLC, thereby eliminating the possibility that the steady, slow decline seen in the quasar DLC is an artefact arising from the rather substantial seeing fluctuations.

5.2 *Effects of colours of the comparison stars*

Even on the clearest nights, objects are dimmed due to extinction by the Earth's atmosphere. The amount of dimming depends on the airmass, the wavelength of observation and the prevailing atmospheric conditions. The observed magnitude (m_λ) is related to the magnitude above the Earth atmosphere (m_{λ_o}) as (Henden & Kaitchuck 1982)

$$m_\lambda = m_{\lambda_o} + (K'_\lambda + K''_\lambda c)X, \tag{1}$$

where K'_λ and K''_λ are respectively the principal and second-order extinction coefficients, c is the colour index of the observed object and X is the airmass in the direction of the object. An advantage of performing differential photometry between the target and comparison stars located on the same CCD frame is that first-order extinction effects on the differential magnitude cancels out, as both the comparison stars and the target are seen through nearly identical atmospheric layers making the same X. However, K''_λ, which is applied to the colour of the object, can affect the differential magnitude. From equation (1) the differential magnitude between two objects of colour indices $c1$ and $c2$ is given by

$$\Delta m_\lambda = \Delta m_{\lambda_o} + K''_\lambda X \Delta c, \tag{2}$$

where $\Delta c = c1 - c2$, is the difference between the observed colour indices of the two objects. The relation between the standard and observed colour differences between the two objects can be written as

$$\Delta C = \mu \Delta c, \tag{3}$$

where $\Delta C = C1 - C2$, is the difference between the standard colour indices of the two objects. As μ is close to unity for the CCD systems used in the present observations, the observed colour index difference is not too different from the standard colour index difference. The values of $\Delta(B - R)$ between any quasar and comparison stars in our sample range between 0.4 and -2.5 mag. In order to investigate the effects of these colour differences on the DLCs of the quasars under study, the following analyses have been carried out.

From linear least square fitting of equation (2) for Δm_λ against Δc for the comparison stars using the standard colour index $C \equiv (B - R)$ taken from the United States Naval Observatory (USNO) catalog[4] to the observations we found that the effect of

[4]http://archive.eso.org/skycat/servers/usnoa.

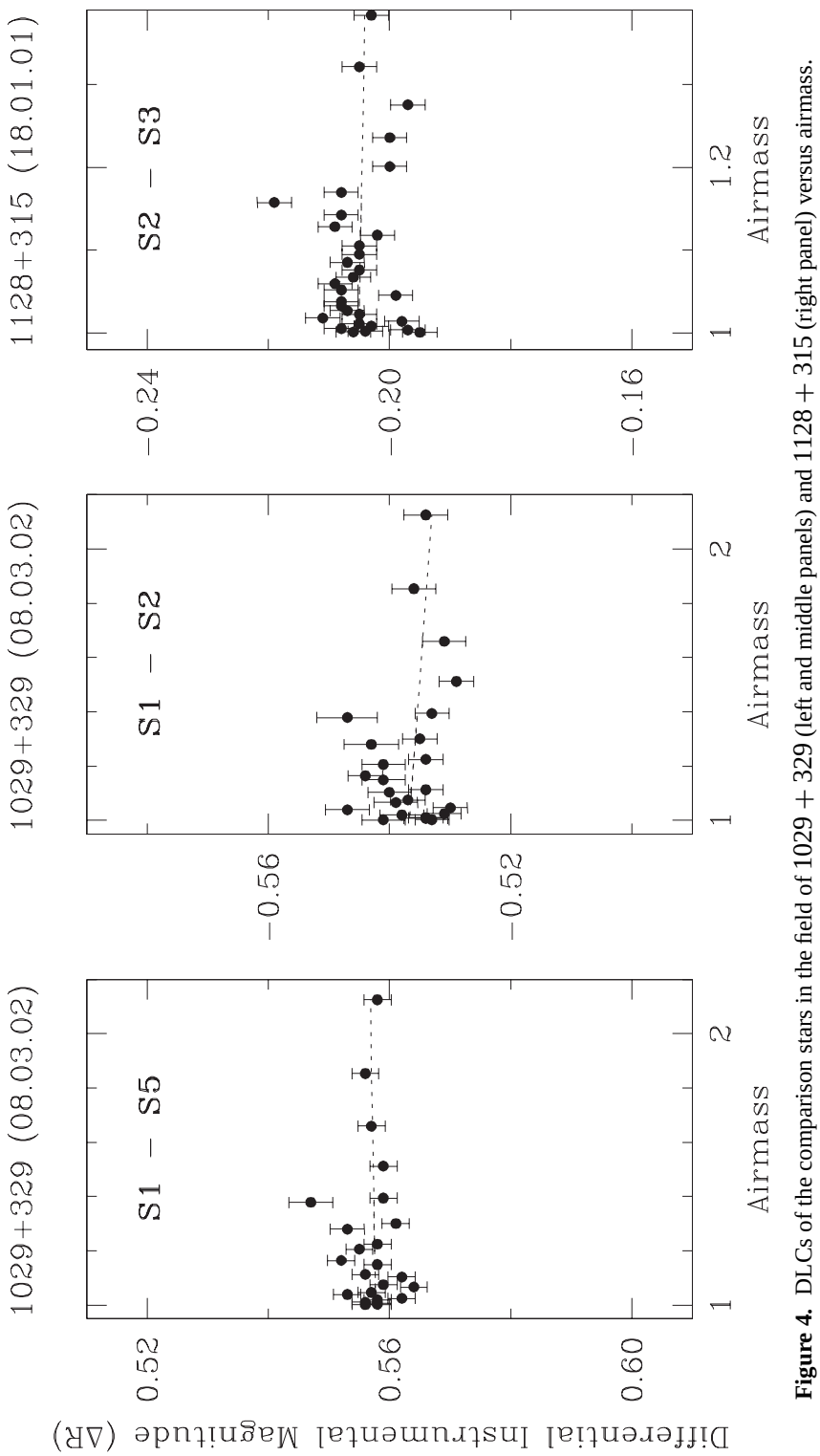

Figure 4. DLCs of the comparison stars in the field of 1029 + 329 (left and middle panels) and 1128 + 315 (right panel) versus airmass.

second-order extinction is virtually negligible, although we note that USNO magnitudes have errors of up to 0.3 mag. Therefore, to further carefully investigate the effect of colour differences between the objects on their observed DLCs, we have shown in Fig. 4 (left panel) the observed instrumental magnitude difference (Δm_λ in equation 2) between the stars S1 and S5 plotted against the airmass, whereas the middle panel shows the magnitude difference between S1 and S2 plotted against the airmass. Both of these DLCs are for the observations of the source $1029 + 329$ carried out on the night of 8th March 2002 up to a maximum hour angle of 5 hours corresponding to $X \simeq 2.2$. Observations on the other objects in our sample were rarely carried out at airmasses greater than this value. The colour difference $\Delta(\mathrm{B}-\mathrm{R})$ between S1 and S2 is 1.9 while between S1 and S5 it is 0.9. From Fig. 4 (left and middle panels) it is seen that despite a rather large range in airmass and a fairly large colour difference between the three stars, no artificial variations are introduced. Least square fits to the data sets shown in the left and middle panels of Fig. 4 yield slopes ($K''_\lambda \Delta c$ in equation 2) of -0.0008 ± 0.0023 and 0.0033 ± 0.0037, which are essentially zero. Also shown in Fig. 4 (right panel) is the observed instrumental magnitude difference between stars S2 and S3, having a large difference in colour index of -1.4, in the field of the QSO $1128 + 315$, as observed on 18th January 2001. Linear regression analysis yields a slope of 0.0026 ± 0.0089, which is again indistinguishable from zero. Any such effect is thus less than the photometric error of individual data points on the DLCs, and so we conclude that the colour differences between our sets of quasars and the comparison stars used in the differential photometry will not have any significant effects on the DLCs (see also GSSW03) even if account is taken of the errors in the magnitudes of the USNO catalog used for knowing the colours of the QSOs and stars. Similar conclusions were also drawn by Carini *et al.* (1992) in their study of rapid variability of blazars.

5.3 *Error estimation of the data points in the DLCs*

Determination of the basic variability parameters, such as peak-to-peak variability amplitudes, requires a realistic estimate of the photometric errors of individual data points of a given DLC. It has been argued recently in the literature that the photometric errors given by the reduction routines in IRAF and DAOPHOT underestimate the true errors. Considering the differences between the magnitudes of the added and recovered stars using the *addstar* routine of DAOPHOT, Gopal-Krishna *et al.* (1995) found that the formal errors returned by DAOPHOT are too small by a factor of about 1.75. Similarly, Garcia *et al.* (1999) found that the error given by the *phot* task in IRAF is underestimated by a median factor of 1.73. In this work we have made an independent estimate of this systematic error factor. To do this we have considered those 108 nights of observations (out of the total 113 nights) which we have found useful for INOV studies. Out of these, we have identified 74 DLCs pertaining to 'well behaved' (i.e., stable) comparison stars. Only the best available star—star DLC for each of these nights were considered. The unweighted mean of a DLC consisting of N data points having amplitude X_i, is given by

$$\langle X \rangle = \frac{1}{N} \sum_{i=1}^{N} X_i, \tag{4}$$

and the variance of the DLC is

$$S^2 = \frac{1}{N-1}\sum_{i=1}^{N}(X_i - \langle X\rangle)^2. \quad (5)$$

Both intrinsic source variability and measurement uncertainty contribute to this observed variance. Under the assumptions that both components are normally distributed and combine in quadrature the observed variance can be written as (see Edelson *et al.* 2002)

$$S^2 = \langle X\rangle^2\sigma_{XS}^2 + \langle\sigma_{err}^2\rangle. \quad (6)$$

The first term on the right represents the intrinsic scatter induced by source variability, and the second term is the contribution of measurement noise as returned by the *phot* task in IRAF. Assuming that the scatter of the data points is predominantly due to statistical uncertainty in the measurements, we have

$$\langle\sigma_{err}^2\rangle = \frac{1}{N}\sum_{i=1}^{N}\sigma_{err,i}^2. \quad (7)$$

As we have considered here only star–star DLCs, the contribution of source variability to the observed variance S^2 may be taken to be zero and therefore S^2 becomes equal to the average of the squares of the measurement errors $\langle\sigma_{err}^2\rangle$.

For each DLC we computed the quantity

$$Q = S^2 - \eta^2\langle\sigma_{err}^2\rangle, \quad (8)$$

where η^2 is the factor by which the average of the squares of the measurement errors should be incremented. For various assumed values of η we calculated the average of Q for the entire set of the 74 DLCs, as well as the numbers of DLCs for which Q was found to be positive and negative, respectively. The condition of the mean value of Q being equal to zero (i.e. $\langle Q\rangle = 0$), is satisfied for $\eta = 1.55$. On the other hand, the median value of Q is zero for $\eta = 1.40$. Thus, we adopt a value of $\eta = 1.50$ in further analysis. Note that this value is somewhat lower than 1.75 estimated in Gopal-Krishna *et al.* (1995) and the 1.73 reported by Garcia *et al.* (1999).

6. Optical variability

In all, 113 nights of observations were carried out; however, the data on 5 of these nights were found to be too noisy for the purpose of searching for INOV, and hence were used only for long term optical variability (LTOV) measurements (section 6.2). The basic statistics on the detection of INOV for the different AGN classes are summarized in Table 3. The DLCs for a total of 42 nights of observations (8 for RQQs, 10 for LDQs, 6 for CCQs, and 18 for BL Lacs) have already been reported in SGSW04 and SSGW04. Here we present, in Fig. 5, the DLCs for the remaining 66 nights of observations, covering 7 RQQs (21 nights), 7 LDQs (27 nights), 4 CDQs (10 nights) and 4 BL Lacs (8 nights).

Table 3. Statistics on the detection of INOV for different AGN classes. The number of sources (N_s) monitored on N_o nights during N_d hours showed INOV in N_i sources during N_{ni} nights for N_{di} hours. The corresponding numbers are given in 2nd, 4th, 5th, 3rd, 6th and 7th columns respectively.

Type	N_s	N_i	N_o	N_d	N_{ni}	N_{di}	DC* (%)	$\langle\delta_{\rm obs}\rangle^\dagger$
RQQ	7	3	29	185	5	28	17	1.19
LDQ	8	4	37	218	7	48	12	1.62
CDQ	5	1	16	107	4	29	20	1.47
BL	6	6	26	172	17	119	61	1.96
Total	26	14	108	682	33	224		

*Duty cycle.
†Mean of the Doppler factors for that group.

6.1 *Intra-night optical variability*

This observing programme has led to the first clear detection of INOV in RQQs (see GSSW03), with additional data supporting this important result presented in SGSW04 and in Tables 2 and 3. A clear distinction between the INOV nature of the two classes of presumably relativistically beamed radio-loud AGNs (CDQs and BL Lacs) is found for the first time, in the sense that BL Lacs are certainly more frequently variable than are CDQs (SSGW04); this is also clear from Table 3.

To make a claim of INOV in a given night, we have employed a statistical criterion based on the parameter C, similar to that followed by Jang & Miller (1997), with the added advantage that for each AGN we have DLCs relative to multiple comparison stars. This allows us to discard any variability candidates for which the multiple DLCs do not show clearly correlated trends, both in amplitude and time. We define C for a given DLC as the ratio of its standard deviation, σ_T, and the mean σ of its individual data points, $\eta\sigma_{\rm err}$. This value of C_i for the ith DLC of the AGN has the corresponding probability, p_i, that the DLC is steady (non-variable), assuming a normal distribution. For a given AGN on a given night we then compute the joint probability, P, by multiplying the values of p_i's for the individual DLCs available for the AGN. We consider a quasar to be variable if $C_{\rm eff} > 2.57$, which corresponds to a confidence level of variability in excess of 99%. A quasar is occasionally classified as a probable variable (PV) if $2.57 \geq C_{\rm eff} > 2.00$, giving rise to a confidence level between 90% and 99%. The values of $C_{\rm eff}$ for variable and probable variable quasars along with the nightly variability status of each of the quasars monitored in this program are given in Table 2.

To quantify the variability amplitude of a DLC we adopt the commonly used definition (e.g., Heidt & Wagner 1996; Romero *et al.* 1999)

$$\psi = \sqrt{(D_{\rm max} - D_{\rm min})^2 - 2\sigma^2}, \tag{9}$$

where $D_{\rm max}$, $D_{\rm min}$ are the maximum and minimum in the quasar differential lightcurve relative to a stable star and $\sigma^2 = \eta^2\langle\sigma_{\rm err}^2\rangle$. By subtracting off (in quadrature) the corrected errors from the total variability, this expression for ψ gives a fairer estimate of the true amplitude of variability. We have found the correction factor $\eta \simeq 1.50$ (see section 5.3). The values of ψ for quasars showing INOV are given in Table 2. A key result is that all 4 types of luminous AGN do sometimes exhibit INOV when observed

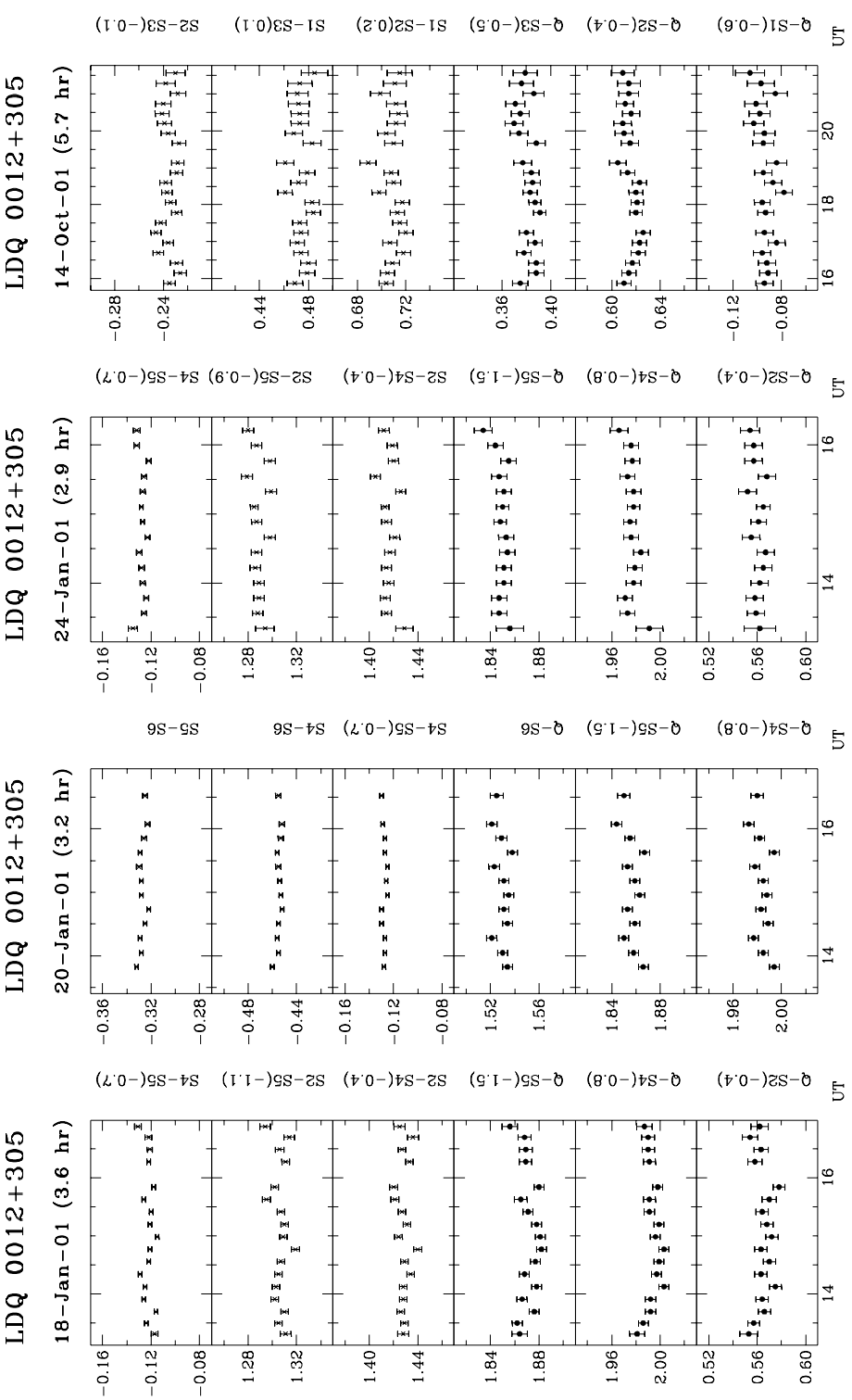

Figure 5. (*Continued*)

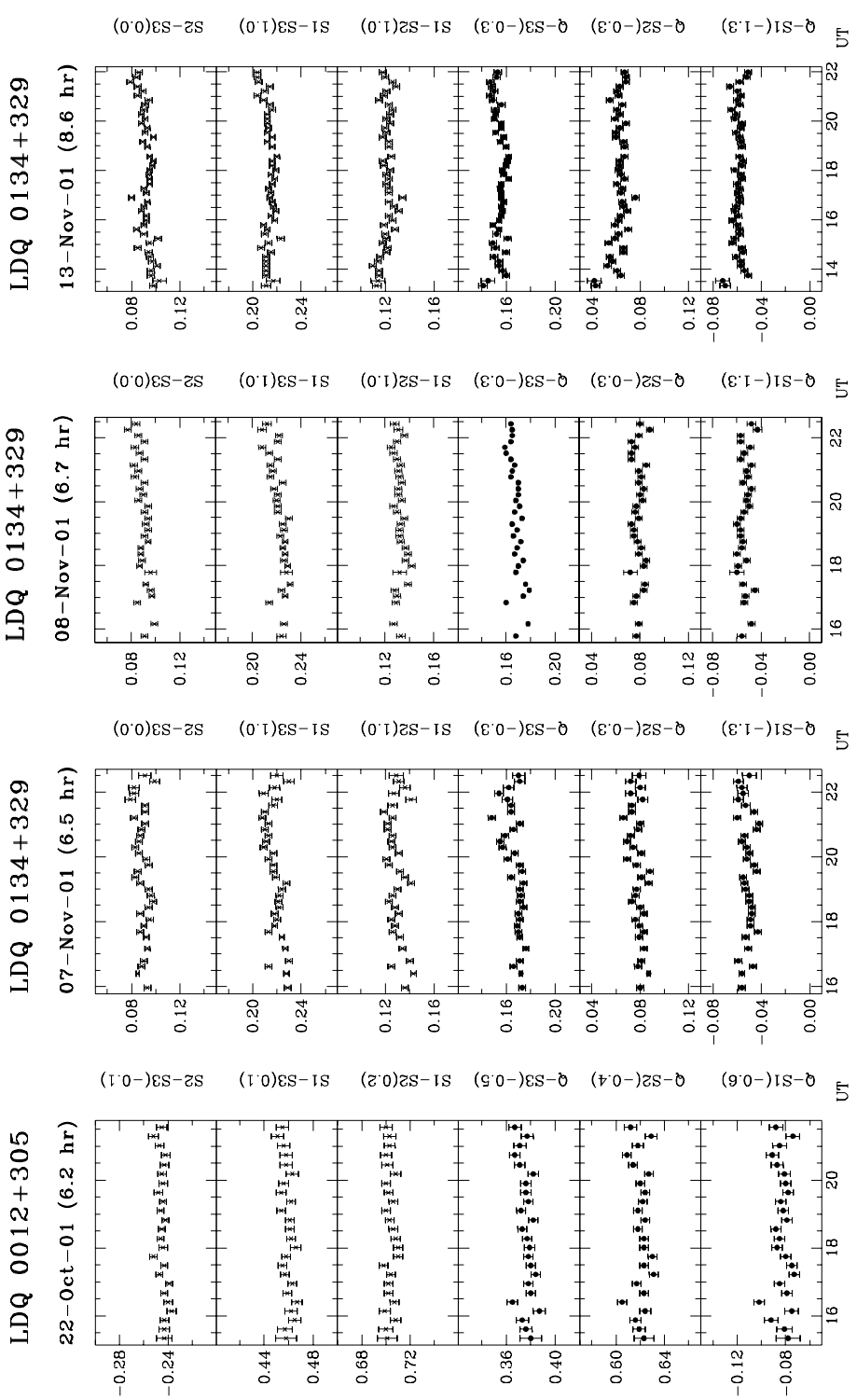

Figure 5. (*Continued*)

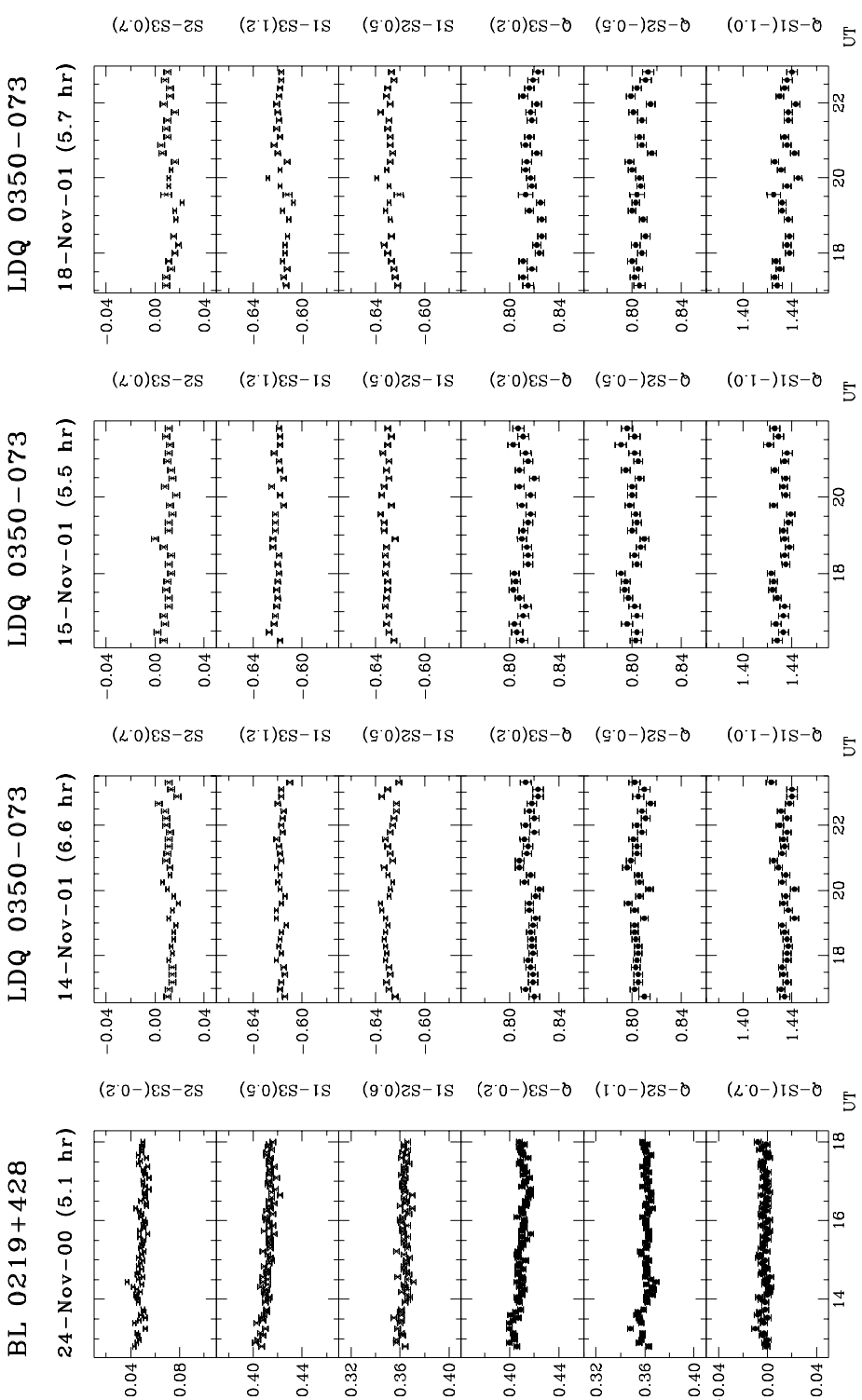

Figure 5. (*Continued*)

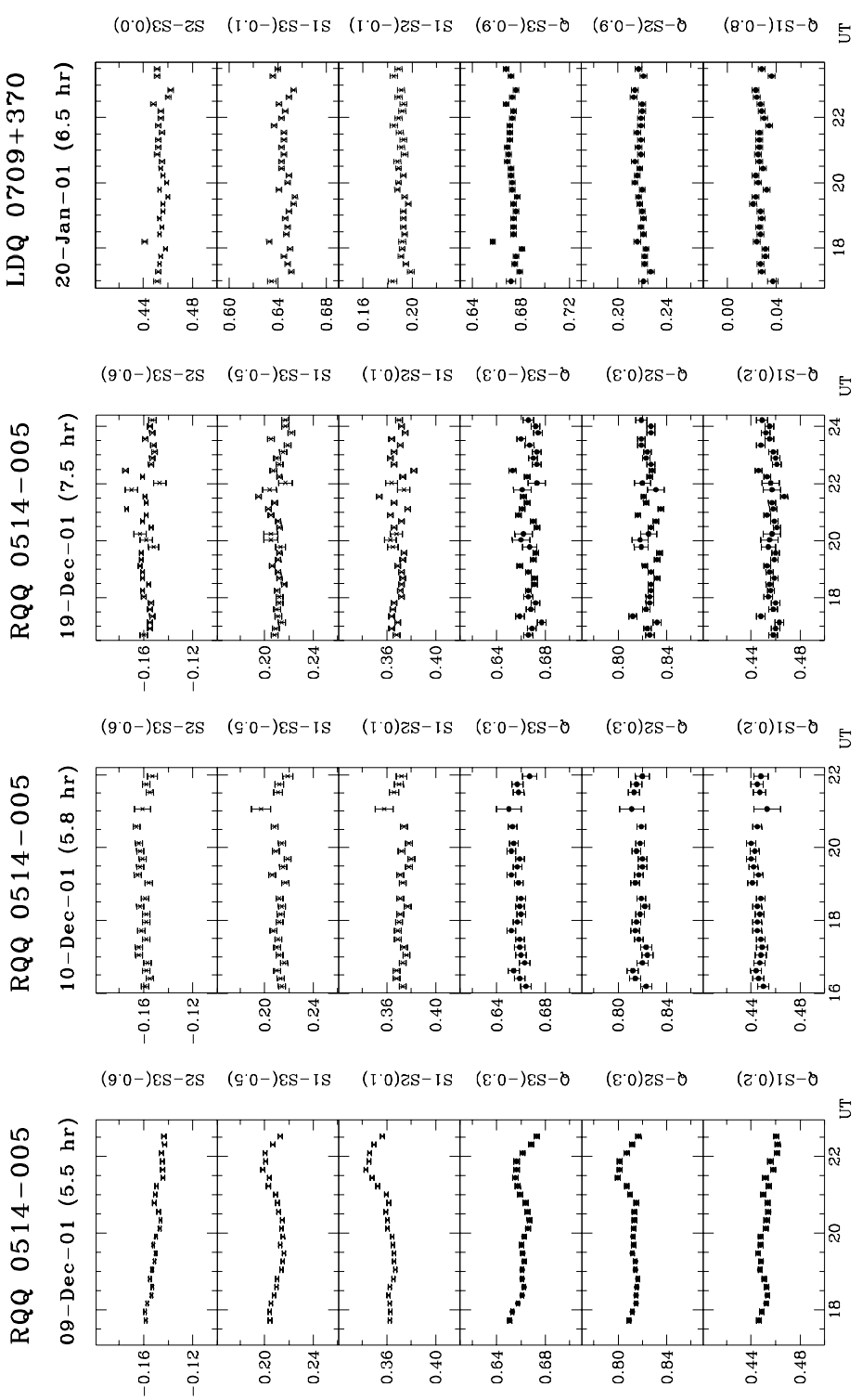

Figure 5. (*Continued*)

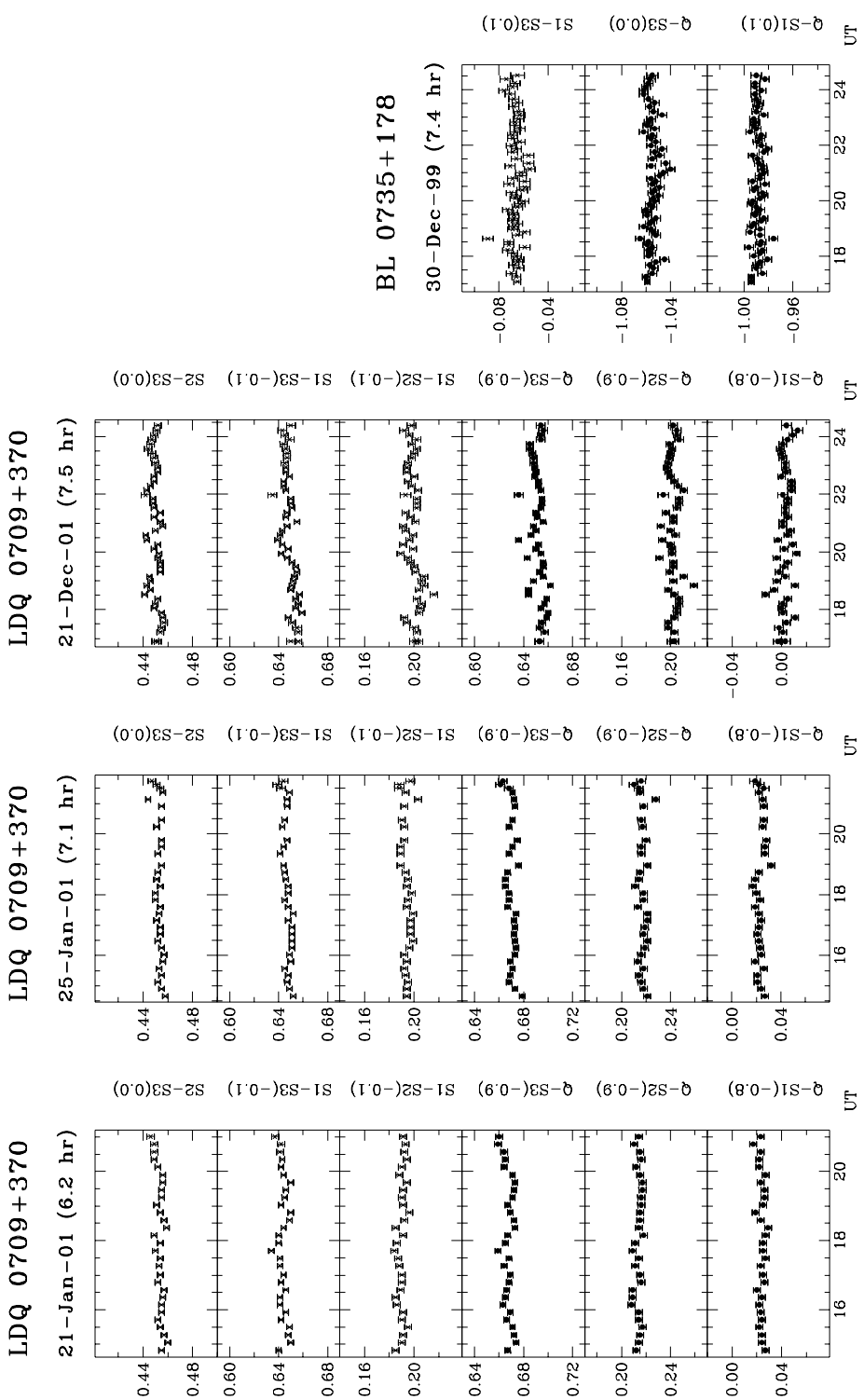

Figure 5. (*Continued*)

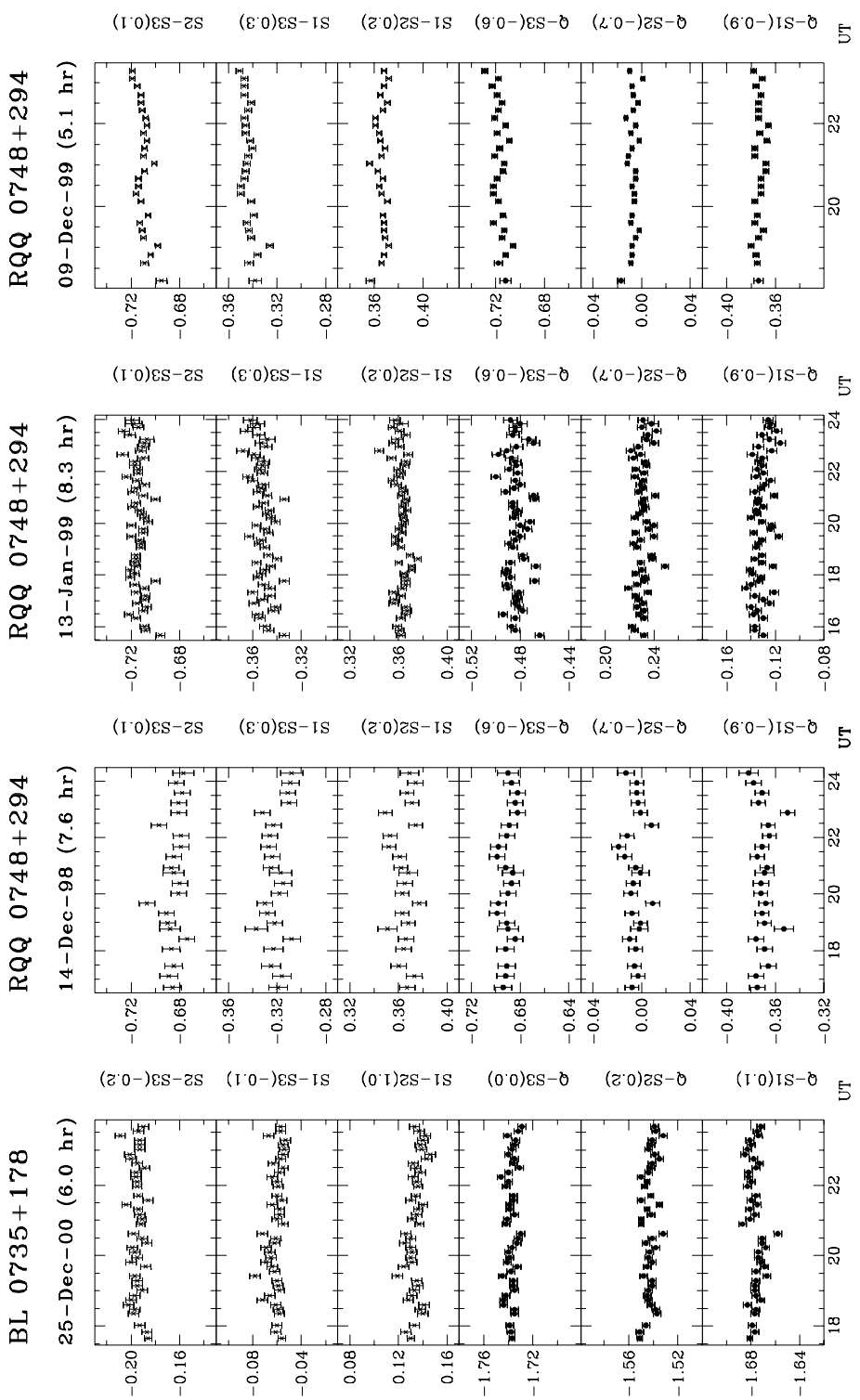

Figure 5. (*Continued*)

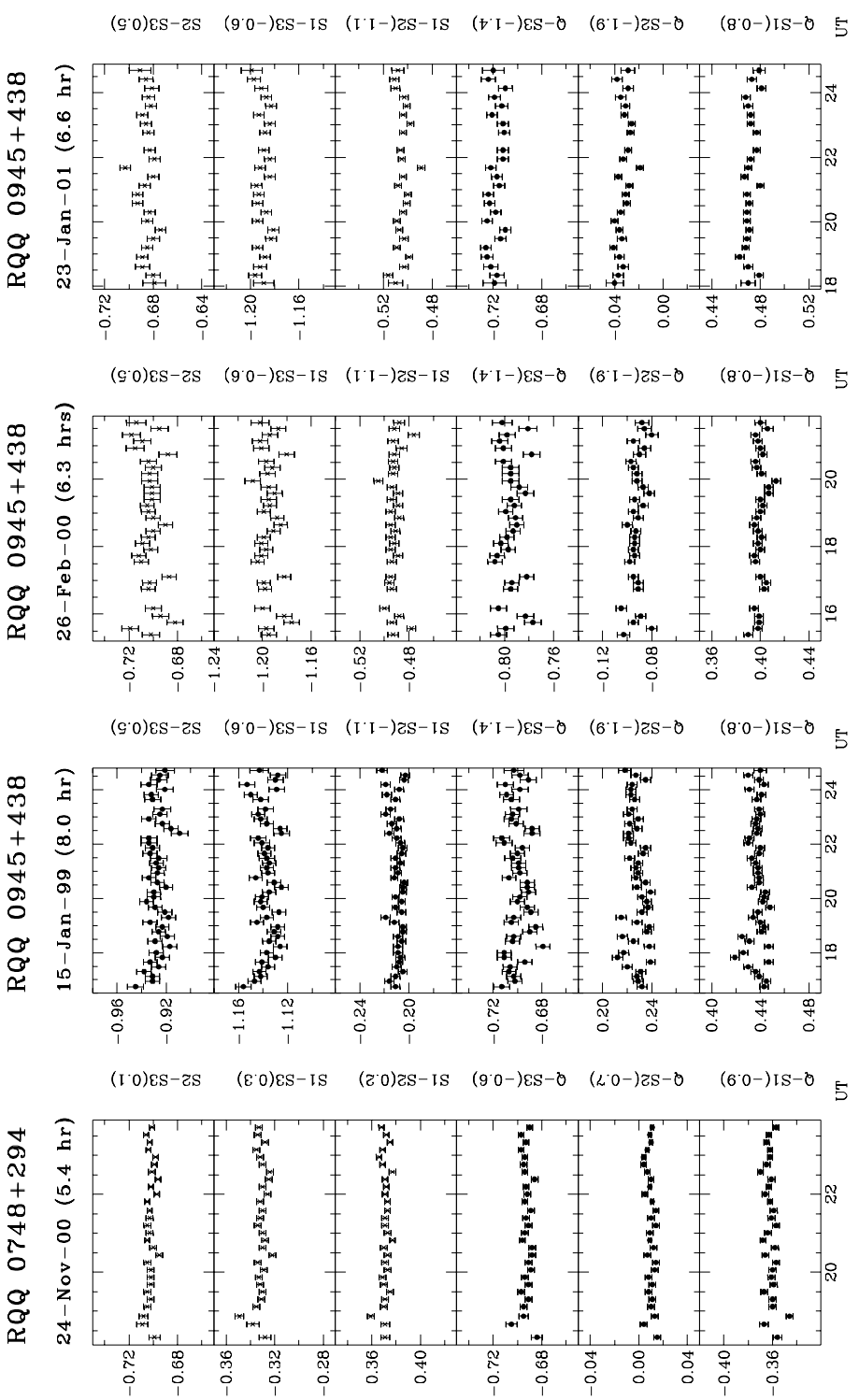

Figure 5. (*Continued*)

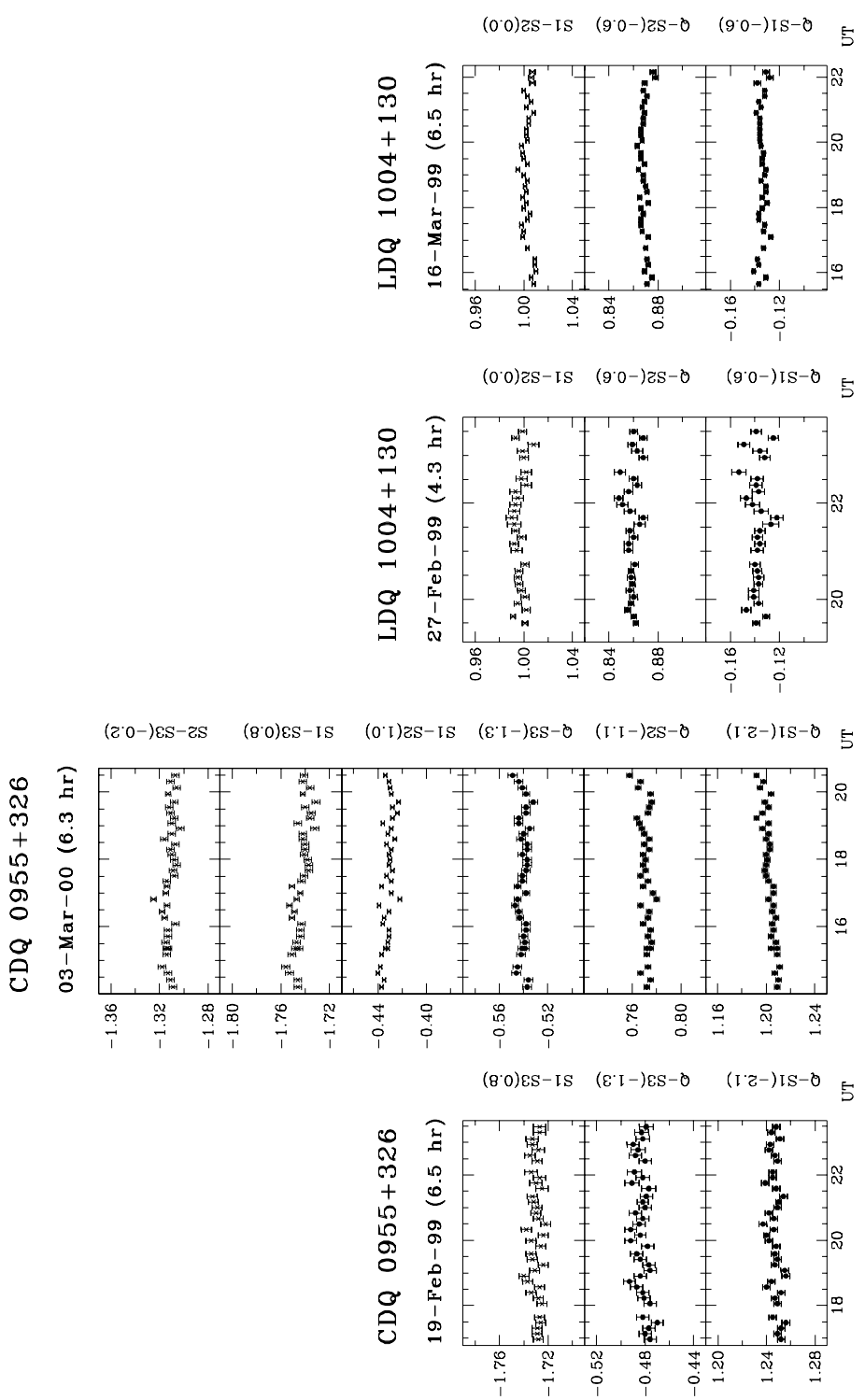

Figure 5. (*Continued*)

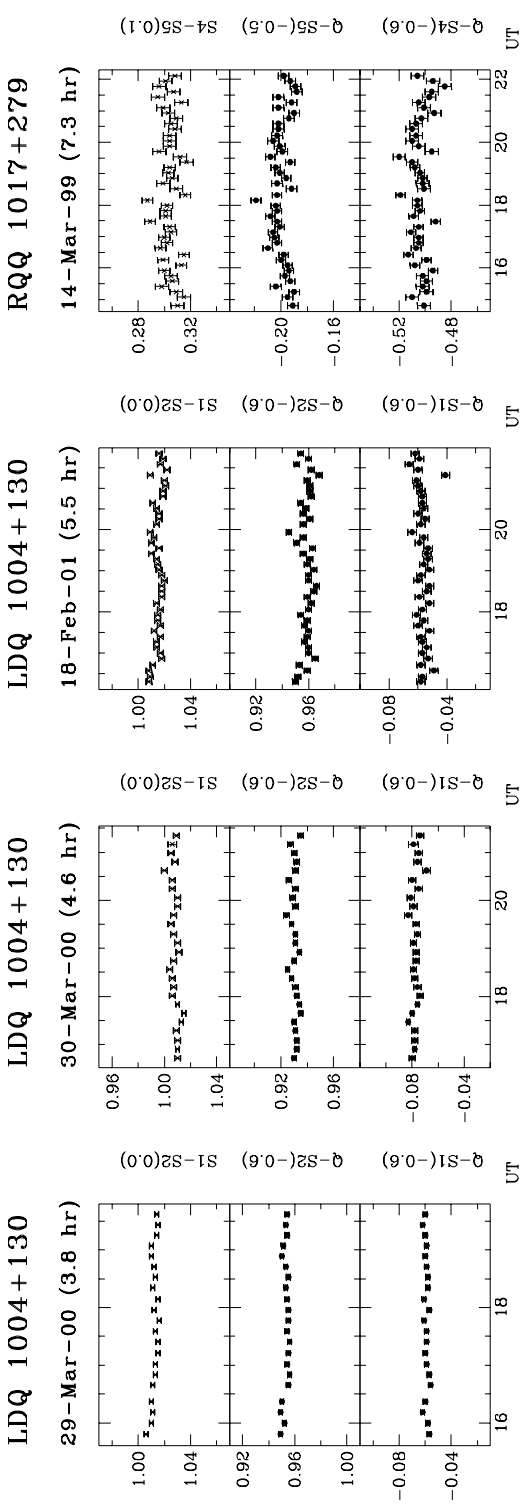

Figure 5. (*Continued*)

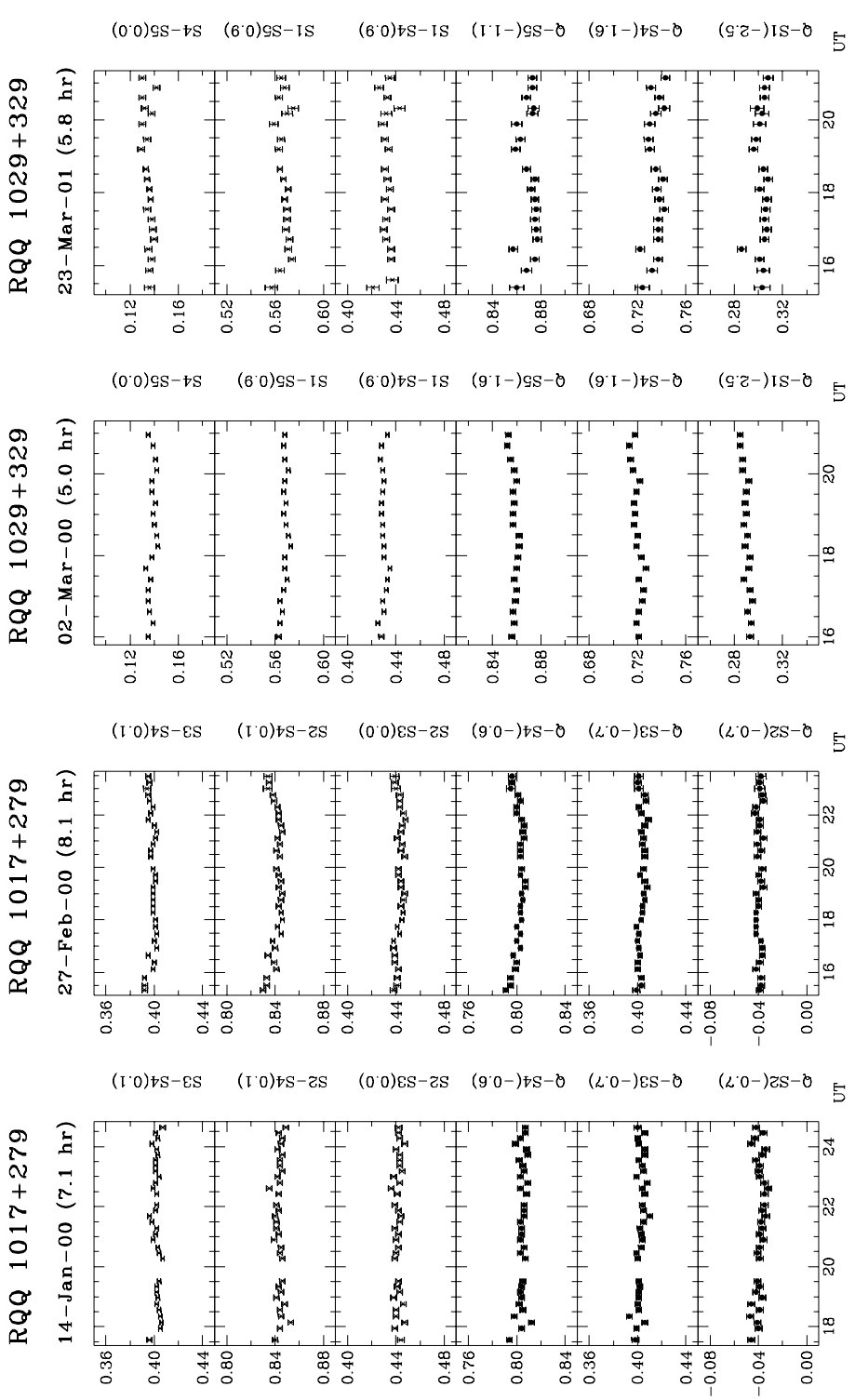

Figure 5. (*Continued*)

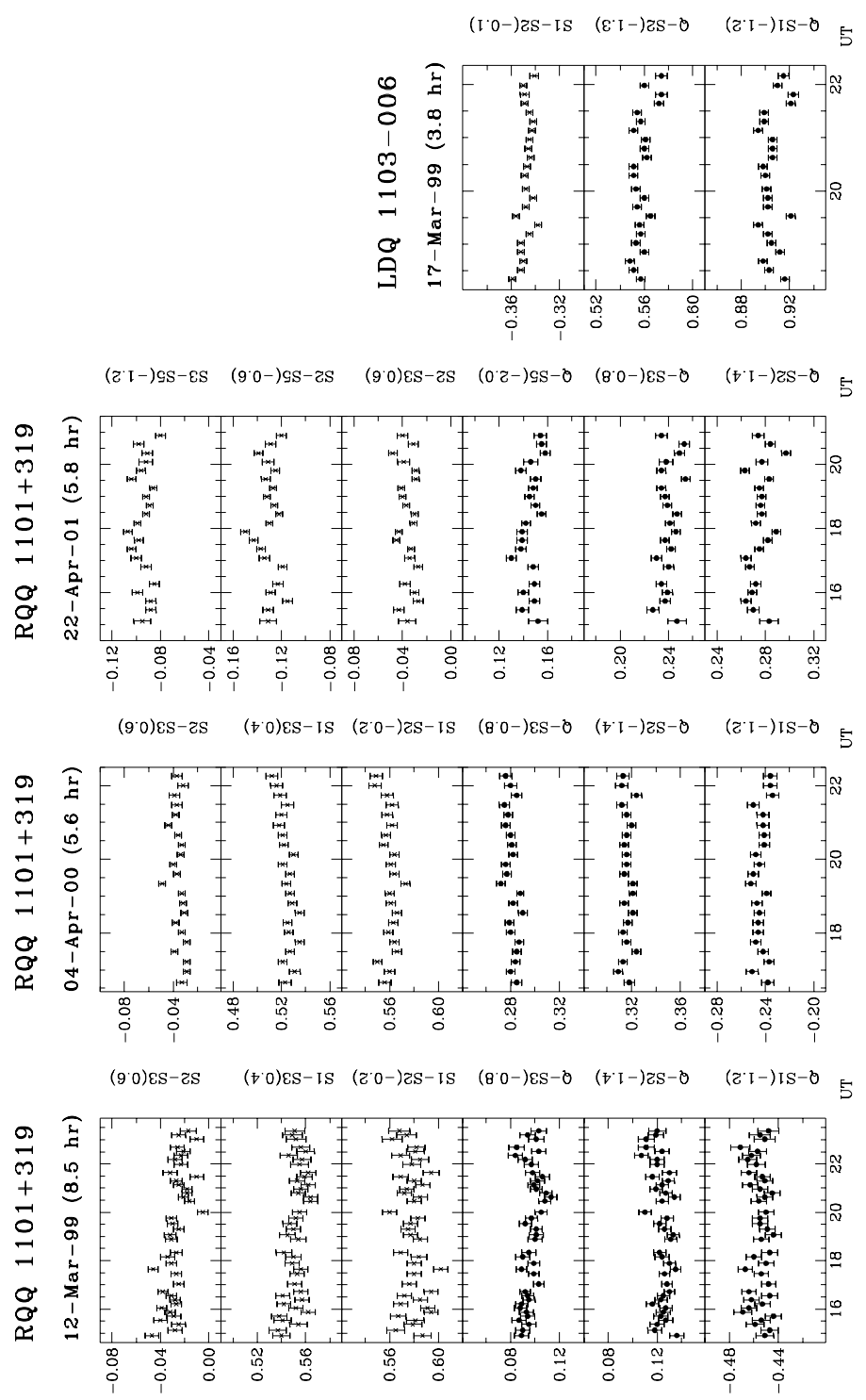

Figure 5. (*Continued*)

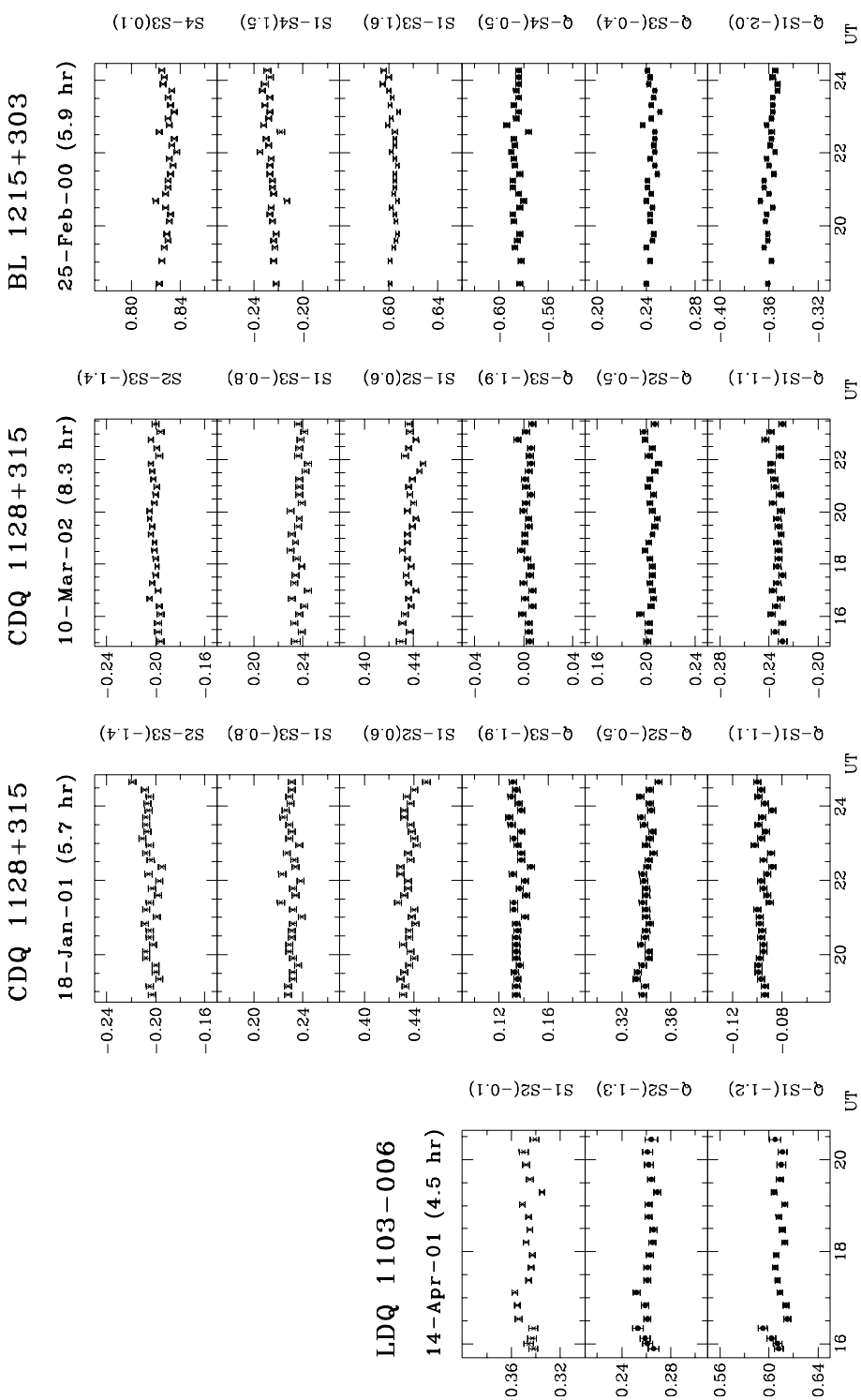

Figure 5. (*Continued*)

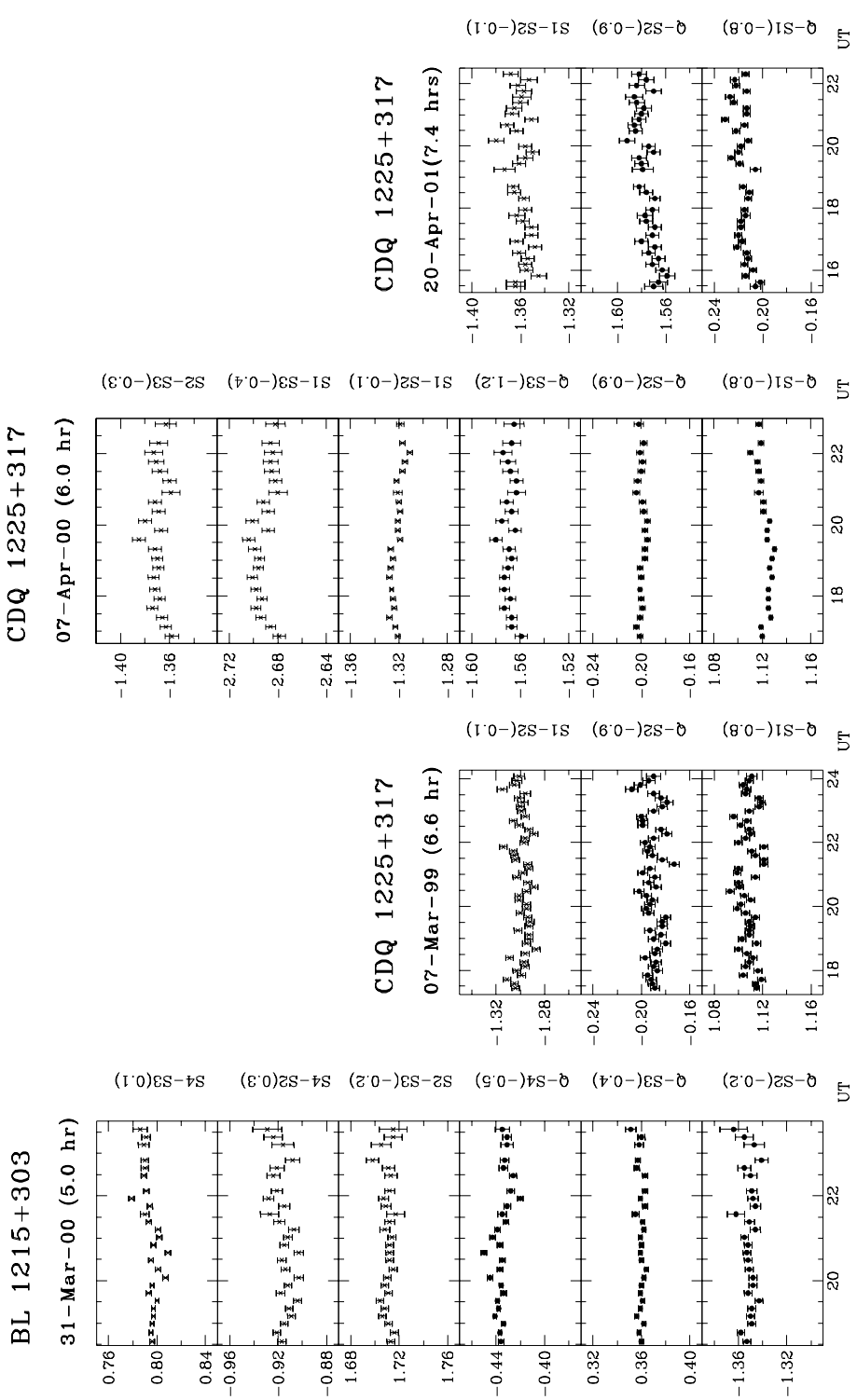

Figure 5. (*Continued*)

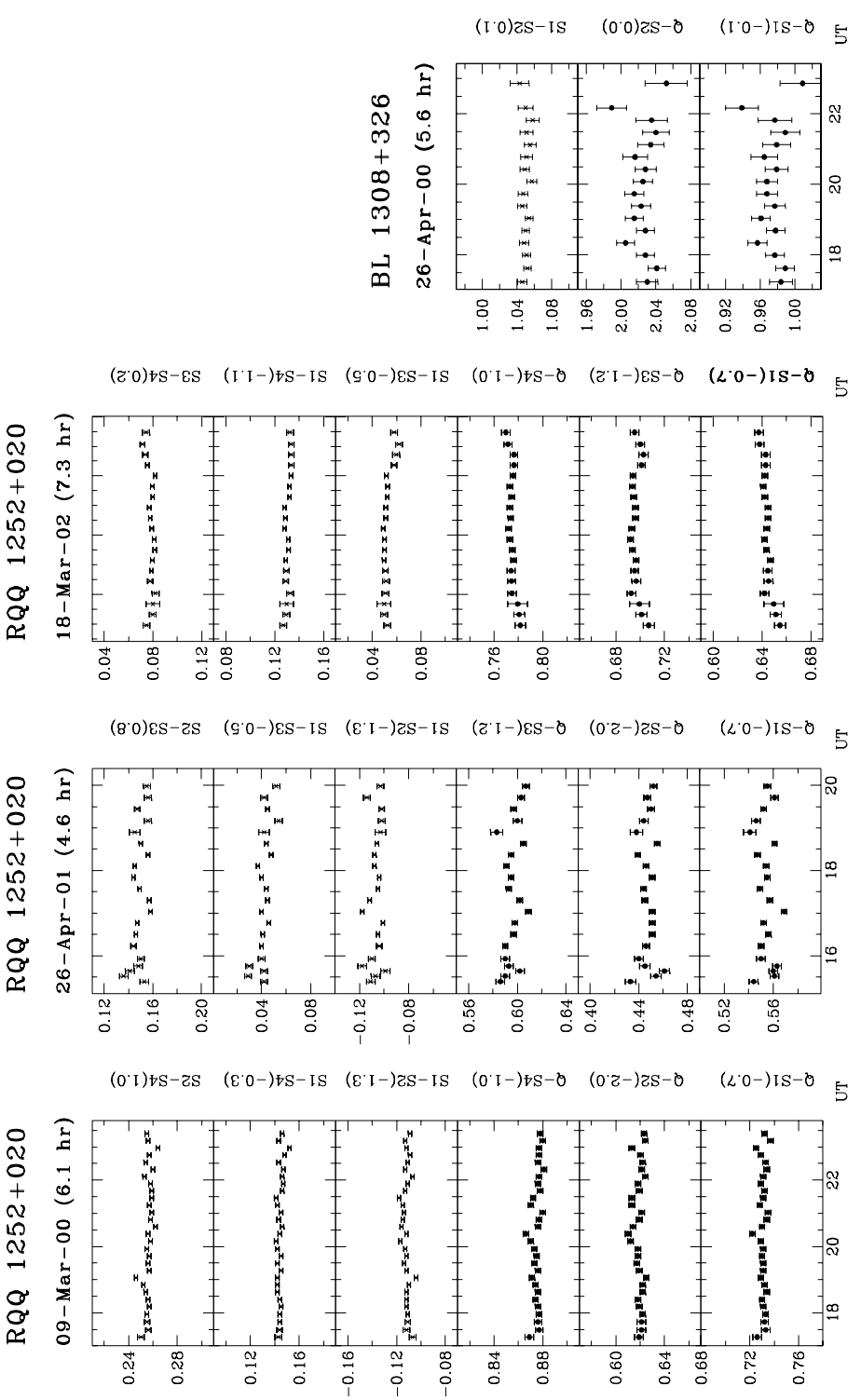

Figure 5. (*Continued*)

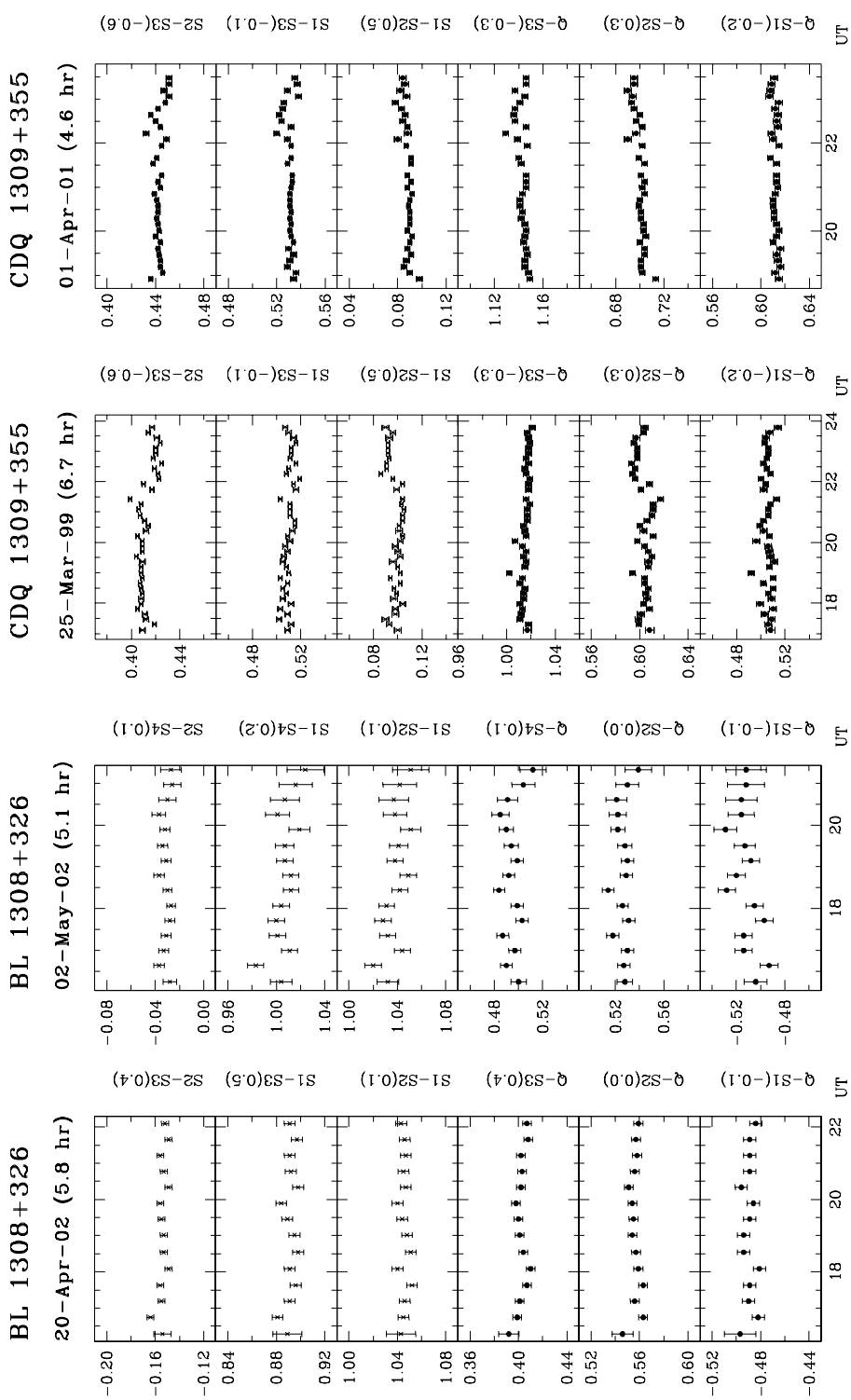

Figure 5. (*Continued*)

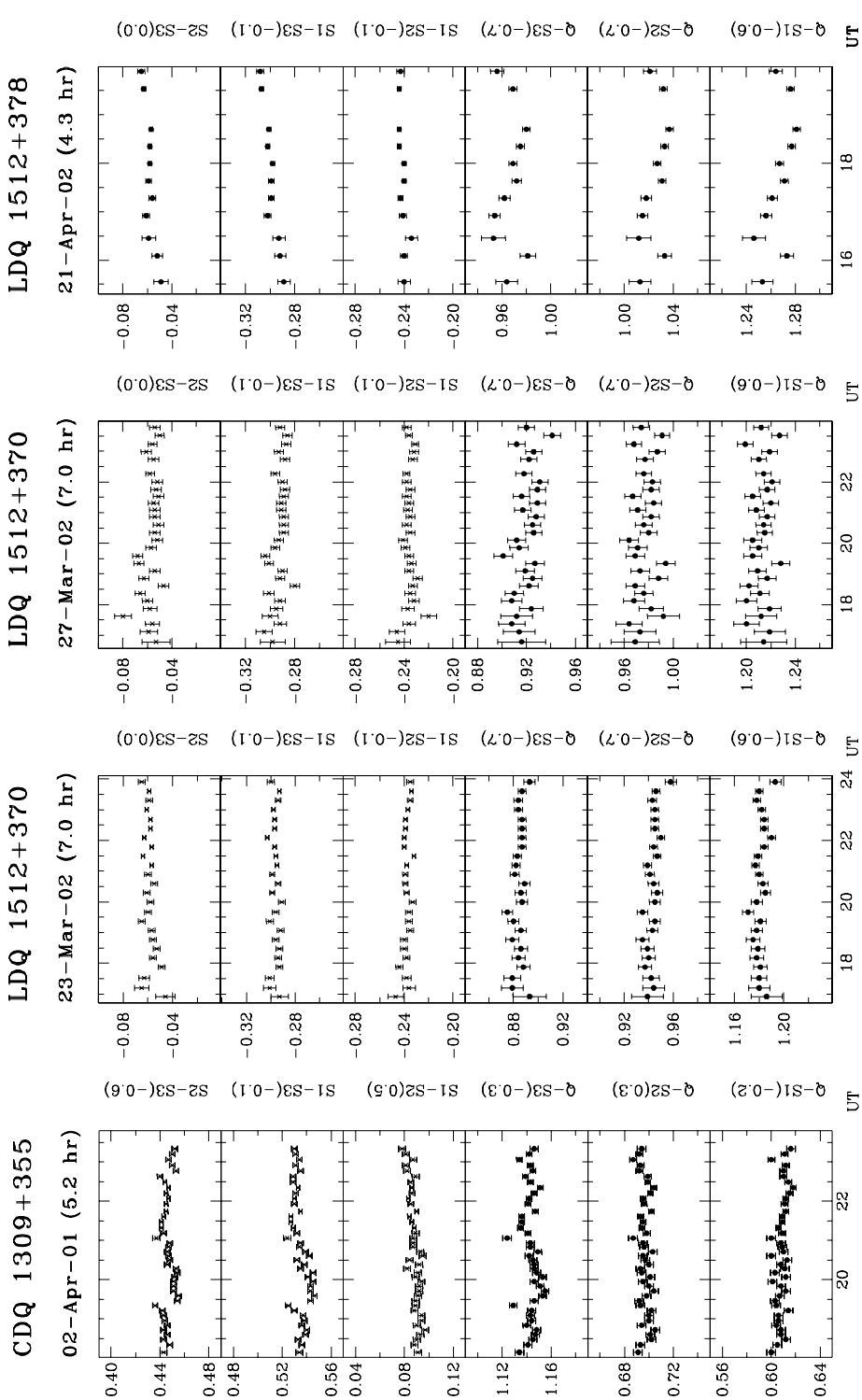

Figure 5. (*Continued*)

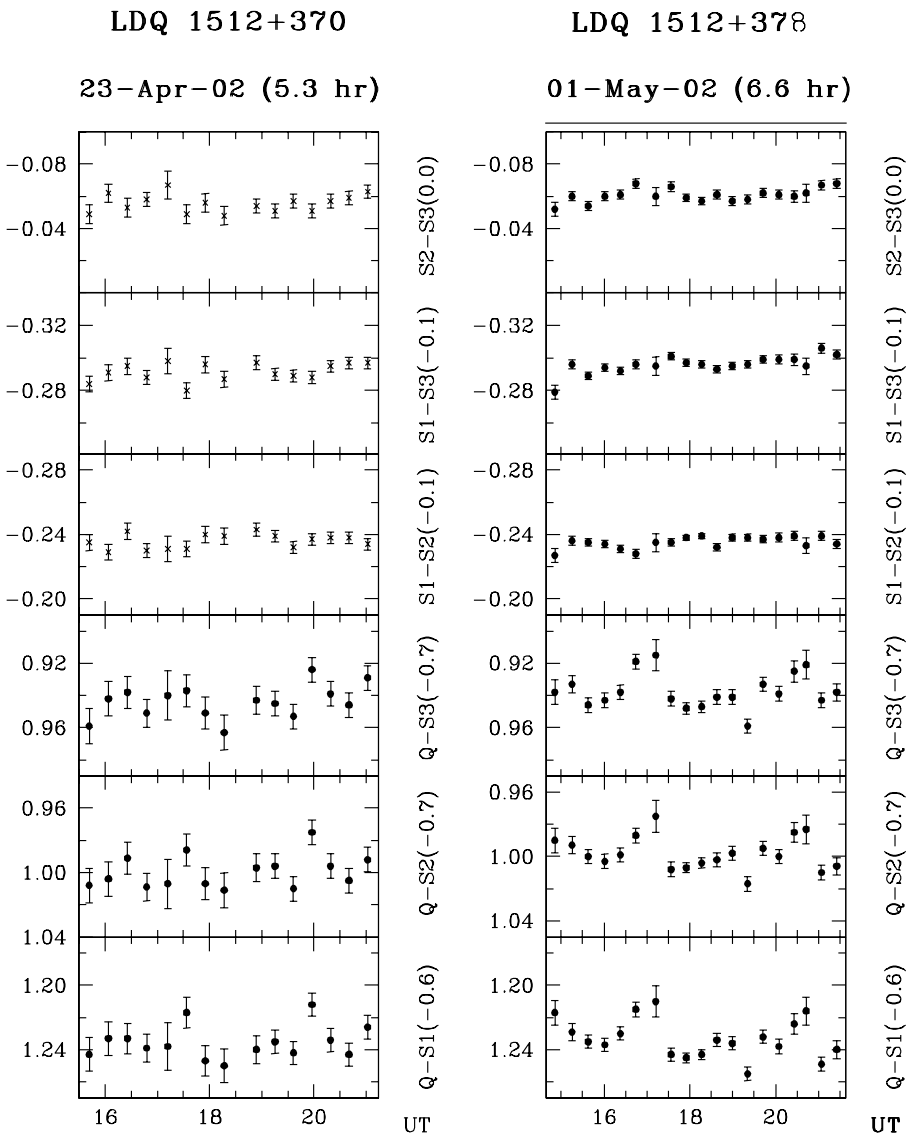

Figure 5. Differential R-band lightcurves of the different types of quasars. The name of the object, the date and duration of observations in hours are given on the top of each panel. The objects being compared and their colour differences (in parentheses) label the right side of each sub-panel.

carefully, but that BL Lacs show far large values of ψ much more frequently (see SSGW04).

6.1.1 *Structure function analysis*

Structure function (SF) analysis is a useful pointer to the variability characteristics of the lightcurves, such as the time-scales and possible periodicities. The general

definition of SF and associated properties are described, e.g., by Simonetti *et al.* (1985), and Hughes, Aller & Aller (1992), Heidt & Wagner (1996). Following Simonetti *et al.* (1985) we have defined the first-order SF as

$$D_X^1(\tau) = \frac{1}{N(\tau)} \sum_{i=1}^{N} [X(i+\tau) - X(i)]^2, \tag{10}$$

where τ = time lag, $N(\tau) = \sum w(i)w(i+\tau)$, and the weighting factor $w(i) = 1$ if a measurement exists for the ith interval, and 0 otherwise. The error in each point in the computed SF is

$$\sigma^2(\tau) = \frac{8\sigma_{\delta X}^2}{N(\tau)} D_X^1(\tau), \tag{11}$$

where $\sigma_{\delta X}^2$ is the measured noise variance.

Since the sampling of our DLCs is quasi-uniform, we have determined the SFs using an interpolation algorithm. For any time lag τ, the value of $X(i+\tau)$ was calculated by linear interpolation between the two adjacent data points. A typical time scale in the light curve (i.e., time between a maximum and a minimum, or vice versa) is indicated by a local maximum in the SF. In the case of a monotonically increasing SF, the source possesses no typical time-scale smaller than the total duration of observations. A minimum in the SF is an indication of periodicity. The SF plots for 1 CDQ and 6 BL Lacs which showed definite INOV during 21 nights of observation are given in SSGW04. Here in Fig. 6, we present SF plots for 3 RQQs and 3 LDQs which showed confirmed INOV during 10 nights of observations. The inferred variability timescale(s) and "period"(s) are given in Table 2. Because none of our light curves were long enough to show more than two maxima or minima, it should be stressed that we are not claiming that we detect actual periodic component of the INOV in any of our sources. Because the SFs for individual sources are usually different from night to night, the chance that any nominal "periods" detected in the SFs are of physical origin is further reduced.

6.1.2 *Duty cycles of intra-night optical variability*

The high precision of our data permit the estimation of INOV duty cycle (DC) not only for different AGN classes, but also for different levels of INOV amplitudes. The DC of INOV of a given class of objects is given by (Romero *et al.* 1999)

$$DC = 100 \frac{\sum_{i=1}^{n} N_i (1/\Delta t_i)}{\sum_{i=1}^{N} (1/\Delta t_i)} \ \%, \tag{12}$$

where $\Delta t_i = \Delta t_{i,\mathrm{obs}}(1+z)^{-1}$ is the duration (corrected for cosmological redshift) of the ith monitoring session of the source in the selected class. N_i equals 0 or 1, depending on whether the object was respectively, non-variable, or variable during Δt_i.

A DC of 17% was found for RQQs considering only sessions for which INOV was unambiguously detected. This value is roughly midway between the lower values published by Jang & Miller (1997) and Romero *et al.* (1999) and the higher estimate of de Diego *et al.* (1998). For LDQs, a DC of only $\sim$ 12% is found for clear detection

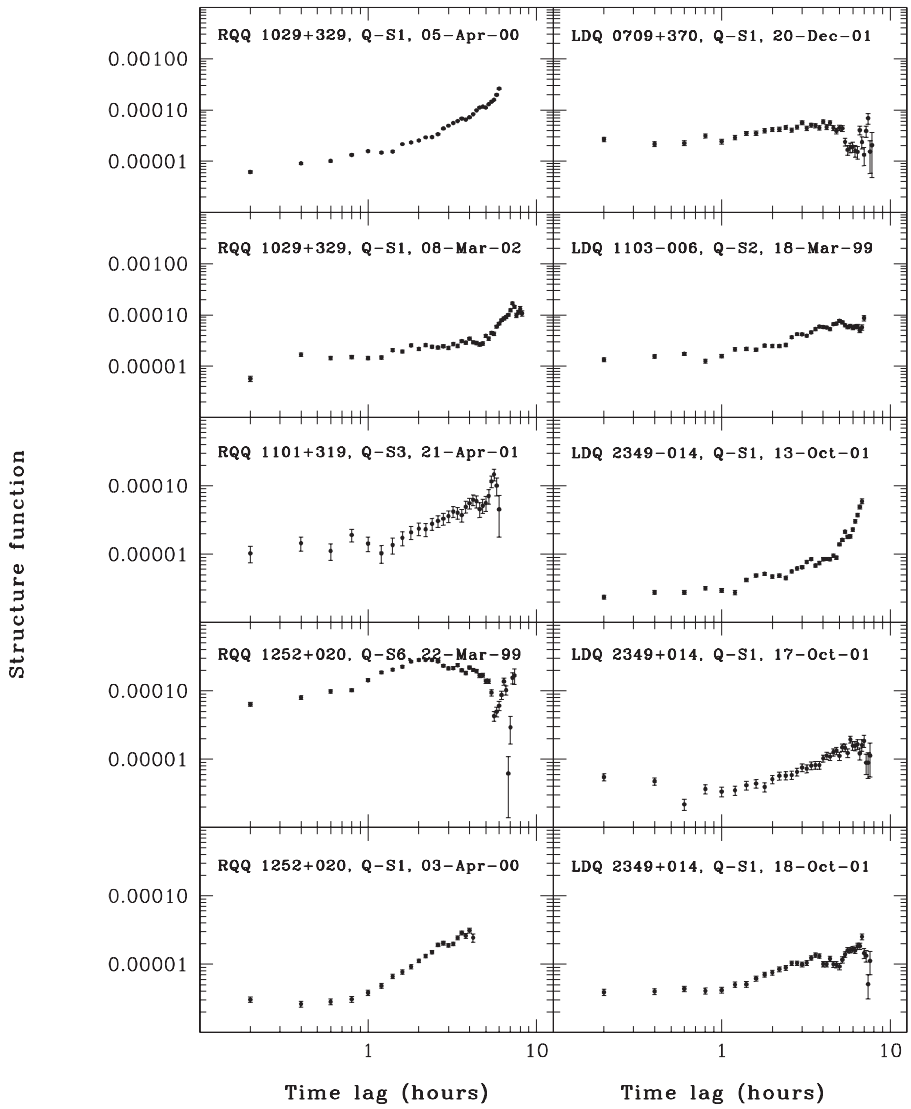

Figure 6. First order structure function of RQQs (left panels) and LDQs (right panels) which have shown INOV, given in increasing order of right ascension.

of INOV; however, this rises to about 18% if the two cases of probable detection are included. Also, a distinction is found in DCs between the two presumably relativistically beamed AGN classes, namely BL Lacs and CDQs. BL Lacs are found to show a high DC, $\sim$ 61%, whereas CDQs show a DC of only $\sim$ 20%. These results are summarised in Table 3. However, separating the CDQs into high polarization (CDQ-HP) and low polarization (CDQ-LP) subsets may be relevant, although we stress that there is only one CDQ-HP in the sample ($1216-010$) and only 4 CDQ-LPs; CDQ-LPs show very low DC ($< 10\%$), whereas a much higher value of DC is found for the single CDQ-HP source (100%). It thus appears that INOV may be more closely connected

to high optical polarization than to Doppler boosting *per se*. Such polarized emission is commonly attributed to shocks in relativistic jets (see SSGW04 for additional discussion).

6.1.3 *Relativistic beaming, Doppler factors, and accretion efficiency*

We have estimated the observed Doppler factor ($\delta_{\rm obs}$) and accretion efficiency ($\eta_{\rm obs}$) for our dataset within the framework of the relativistic beaming models (e.g., Marscher & Scott 1980). The apparent R magnitudes of the quasars (m_R) were obtained from their observed DLCs using the apparent R magnitudes of the comparison stars given in USNO catalog. These were converted to observed monochromatic fluxes (S_R) following Bessel (1979) as

$$S_R = 3.08 \times 10^{-23} 10^{-0.4 m_R} \quad \text{W m}^{-2}\text{Hz}^{-1}. \tag{13}$$

The rest-frame observed monochromatic luminosity of the source at frequency ν_o (which we take as the frequency corresponding to the V-band)

$$L_{\nu_o} = 4\pi \left(\frac{cz}{H_o}\right)^2 \left(1 + \frac{z}{2}\right)^2 S_{\nu_o} \qquad \text{for} \quad q_o = 0, \tag{14}$$

where

$$S_{\nu_o} = S_{\nu_{\rm obs}} \left[\frac{\nu_o}{\nu_{\rm obs}(1+z)}\right]^{\alpha} (1+z)^{-1}, \tag{15}$$

and where $\nu_{\rm obs}$ = frequency corresponding to R-band, $S_{\nu_{\rm obs}}$ = flux observed in R-band, and $\alpha = d(\ln S)/d(\ln \nu)$; we take $\alpha = -1$ which is typical for the spectra of quasars in the visible band.

The observed bolometric luminosity is then calculated from this monochromatic luminosity, using the scaling factor given by Elvis *et al.* (1994) for V-band as

$$L_{Bol}/L_V = 13.2, \tag{16}$$

where $L_V = \nu L_\nu$ at V-band ($\nu = 5.456 \times 10^{14}$ Hz) (Elvis *et al.* 1994).

We have defined $\Delta t_{\rm min}$ as the minimum variability time-scale observed for a clearly detected fluctuation on a given night, corrected to the intrinsic value in the source frame, by dividing the observed $\Delta t_{\rm obs}$ by $(1+z)$. Luminous outbursts of energy ΔL (ergs s^{-1}), cannot occur on time-scales, $\Delta t_{\rm min}$, much shorter than the light crossing time of the emitting region. In this case, the inferred efficiency ($\eta_{\rm obs}$) for the conversion of accreted matter into energy for the case of spherical, homogeneous, non-relativistically beamed co-moving emitter is given as (Fabian & Rees 1979)

$$\eta_{\rm obs} \geq 5 \times 10^{-43} \Delta L / \Delta t_{\rm min}. \tag{17}$$

Assuming that the bolometric luminosity also changes in the same manner as does the flux during the outburst (e.g., Zhang, Fan & Cheng 2002), we have estimated $\eta_{\rm obs}$, taking ΔL to be the variable fraction of the bolometric luminosity during $\Delta t_{\rm min}$.

It is commonly accepted that the immense energy production in AGN is due to accretion onto black holes (BHs). The efficiency of conversion of mass to energy

through that accretion via thin disks is typically taken as 0.057 for non-rotating BHs but can range up to 0.32 for rapidly rotating black holes (e.g., Paczyński & Wiita 1980; Frank, King & Raine 1986). However, if the accretion is essentially spherical (a Bondi flow) or radiatively inefficient then the efficiency factor can be considerably lower (e.g., Quataert & Narayan 1999). We have calculated the lower limit of $\eta_{\rm obs}$ for all the quasars in our sample which show definite variability and the results are given in Table 2. If $\eta_{\rm obs}$ is found to be greater than 0.1, relativistic beaming is usually invoked to explain the observations.

Once $\eta_{\rm obs}$ has been estimated, one can calculate self-consistent (though clearly somewhat arbitrary, thanks to the several assumptions made in this subsection) limits on $\delta_{\rm obs}$. We have $\Delta L({\rm obs}) = \delta_{\rm obs}^{3+\alpha} \Delta L(int)$ and $\Delta t_{\rm min}({\rm obs}) = \delta_{\rm obs}^{-1} \Delta t_{\rm min}(int)$, where (int) refers to intrinsic quantities (Worrall 1986; Frank, King & Raine 1986). If we employ Equation (17) as an equality so as to provide a lower bound, $\eta_{\rm obs} = 5 \times 10^{-43} \Delta L({\rm obs})/\Delta t_{\rm min}({\rm obs})$, we then find $\eta_{int} = 5 \times 10^{-43} \Delta L(int)/\Delta t_{\rm min}(int)$, and thus

$$\delta_{\rm obs} \geq (\eta_{\rm obs}/\eta_{int})^{1/(4-\alpha)}. \tag{18}$$

If η_{int} is assumed to be known, a lower bound to $\delta_{\rm obs}$ can now be calculated. We assume a conservative value of $\eta_{int} = 0.05$, which is almost equal to the value of 0.057 derived from non-rotating BH thin accretion disk theory (e.g., Paczyński & Wiita 1980) in estimating δ. The derived $\delta_{\rm obs}$ lower bounds for all the variable objects with $\eta_{\rm obs} \geq 0.1$ in our sample are given in Table 2. The average and median values of $\eta_{\rm obs}$ are 0.89 and 0.33 respectively, while $\delta_{\rm obs}$ range between 1 and 2.55 with both a mean and a median of 1.6.

Only 2 RQQs ever showed $\eta_{\rm obs} > 0.1$ and both just barely did so. Only 1 LDQ had such high variability (on just one occasion); similarly, only 1 CDQ showed high variability, but did so on three nights. In contrast, 5 of 6 BL Lacs evinced $\eta_{\rm obs} > 0.1$, most on more than one occasion. The mean values of these lower bounds to $\delta_{\rm obs}$ for the different classes of AGN are tabulated in the last column of Table 3. As would be expected for the unification scheme, the values for BL Lacs are highest and those for RQQs are lowest. We stress that this computation produces only lower bounds to δ and most estimates of δ for blazars as obtained from Very Long Baseline Interferometry are somewhat higher (e.g., Kellermann *et al.* 2004).

6.2 *Long term optical variability*

Long term optical variability (LTOV) is seen in 20 out of 26 objects in our sample during the period of our observations. The number of epochs covered range between three and seven and the total time span covered range between about a week to three years. Table 4 presents the LTOV results for our sample. This was quantified by identifying at least one stable ('well behaved') comparison star common to all the epochs and then calculating the mean optical magnitude of the quasar relative to that star for each epoch. The night for which the quasar had the minimum optical brightness is taken as the base level for LTOV and the resulting offset values of the quasars magnitudes are given in Table 4, in the sequence of increasing brightness. Thus, these data provide a decent quantitative description of the LTOV of the quasars. It may, however, be noted that due to the scheduling constraints, the total time span covered is highly variable from quasar to quasar, as can be seen from our log of observations in Table 2. The

Table 4. Results for Long Term Optical Variability of the QSOs.

Object	Type	Date	Q-S1 (mag)	Q-S2 (mag)	Q-S3 (mag)	S1-S2 (mag)	S1-S3 (mag)	S2-S3 (mag)
2349−014	LDQ	17.10.01	0.000	0.000	0.000	0.000	0.000	0.000
		13.10.01	0.030	0.035	0.047	0.005	0.016	0.011
		18.10.01	0.046	0.048	0.049	0.002	0.002	−0.001
1309+355	LDQ	01.04.01	0.000	0.000	0.000	0.000	0.000	0.000
		02.04.01	0.004	0.003	0.000	0.000	−0.004	−0.004
		25.03.99	0.107	0.097	0.128	−0.010	0.021	0.031
1215+303	BL	25.04.01	0.000		0.000			0.000
		19.04.01	0.108		0.098			−0.010
		31.03.00	0.201		0.206			0.006
		25.02.00	0.344		0.322			−0.022
		20.03.99	0.522		0.468			−0.054
0514−005	RQ	19.12.01	0.000	0.000	0.000	0.000	0.000	0.000
		09.12.01	0.004	0.014	0.006	0.010	0.002	−0.008
		10.12.01	0.011	0.007	0.009	−0.004	−0.002	0.002
1004+130	LDQ	18.02.01	0.000	0.000		0.000		
		24.03.01	−0.003	0.001		0.004		
		29.03.00	0.002	0.005		0.003		
		30.03.00	0.021	0.028		0.007		
		16.03.99	0.077	0.089		0.012		
		27.02.99	0.081	0.099		0.018		
1128+310	CDQ	18.01.01	0.000	0.000	0.000	0.000	0.000	0.000
		09.03.02	0.135	0.136	0.130	0.001	−0.005	−0.006
		10.03.02	0.037	0.136	0.132	−0.001	−0.006	−0.004
1252+020	RQQ	09.03.00	0.000	0.000		0.000		
		03.04.00	0.006	0.002		−0.003		
		18.03.02	0.087	0.082		−0.005		
		26.04.01	0.177	0.183		0.006		
0134+329	LDQ	07.11.01	0.000	0.000	0.000	0.000	0.000	0.000
		08.11.01	0.002	−0.001	−0.001	−0.003	−0.004	0.000
		13.11.01	0.008	0.016	0.013	0.008	0.005	−0.003
1512+370	LDQ	21.04.02	0.000	0.000	0.000	0.000	0.000	0.000
		23.04.02	0.031	0.025	0.023	−0.005	−0.008	−0.002
		01.05.02	0.033	0.027	0.030	−0.006	−0.003	0.003
		27.03.02	0.054	0.048	0.047	−0.005	−0.007	−0.002
		23.03.02	0.085	0.082	0.082	−0.003	−0.003	0.001
0851+202	BL	31.12.99	0.000	0.000	0.000	0.000	0.000	0.000
		29.12.98		0.601	0.695			0.094
		28.03.00	0.936	0.928	0.906	−0.009	−0.031	−0.020
		17.02.01	1.631	1.628	1.624	−0.004	−0.007	−0.003
1101+319	RQQ	04.04.00		0.000	0.000			0.000
		22.04.01		0.041	0.042			0.000
		21.04.01		0.052	0.050			−0.003
		12.03.99		0.193	0.184			−0.009
1103−006	LDQ	06.04.00	0.000	0.000	0.000			
		17.03.99	0.018	0.018	−0.004			
		18.03.99	0.021	0.021	−0.001			
		14.04.01	0.316	0.314	−0.003			
		25.03.01	0.318	0.314	−0.005			
		22.03.02	0.329	0.324	−0.006			

Table 4. (*Continued*)

Object	Type	Date	Q-S1 (mag)	Q-S2 (mag)	Q-S3 (mag)	S1-S2 (mag)	S1-S3 (mag)	S2-S3 (mag)
1216−010	CDQ	15.03.02	0.000	0.000		0.000		
		11.03.02	0.087	0.085		−0.001		
		13.03.02	0.106	0.102		−0.003		
		16.03.02	0.140	0.135		−0.004		
0735+178	BL	26.12.98	0.000		0.000		0.000	
		30.12.99	0.457		0.465		0.008	
		24.12.01	0.720		0.715		−0.005	
		25.12.00	1.145		1.147		0.002	
0709+370	LDQ	20.01.01	0.000	0.000	0.000	0.000	0.000	0.000
		25.01.01	0.005	0.002	0.003	−0.003	−0.002	0.001
		21.01.01	0.004	0.005	0.006	0.001	0.002	0.000
		21.12.01	0.025	0.017	0.021	−0.008	−0.004	0.004
		20.12.01	0.040	0.029	0.033	−0.011	−0.008	0.004
0955+326	CDQ	19.02.99	0.000		0.000		0.000	
		03.03.00	0.044		0.057		0.013	
		05.03.00	0.047		0.060		0.013	
0219+428	BL	24.10.00	0.000		0.000		0.000	
		26.10.00	0.255		0.256		0.001	
		24.11.00	0.277		0.281		0.003	
		01.11.00	0.331		0.330		−0.001	
		13.11.99	0.449		0.449		0.000	
		01.12.00	0.622		0.631		0.010	
		14.11.98	0.691		0.684		−0.007	
0748+294	BL	13.01.99	0.000	0.000	0.000	0.000	0.000	0.000
		25.12.01	0.231	0.221	0.214	−0.010	−0.017	−0.007
		24.11.00	0.231	0.221	0.210	−0.009	−0.021	−0.012
		01.12.00	0.237	0.226	0.209	−0.010	−0.028	−0.017
		14.12.98	0.239	0.236	0.207	−0.002	−0.031	−0.029
		09.12.99	0.242	0.238	0.234	−0.004	−0.008	−0.004
0350−073	LDQ	14.11.01	0.000	0.000	0.000	0.000	0.000	0.000
		18.11.01	0.000	−0.001	−0.001	0.000	0.000	0.000
		15.11.01	0.000	0.005	0.006	0.002	0.003	0.002
1308+326	BL	26.04.00	0.000	0.000		0.000		
		03.05.00	0.016	0.009		−0.006		
		23.03.99	0.204	0.203		0.000		

LTOV nature of 11 quasars (6 CDQs and 5 BLs) are discussed by SSGW04, while the light curves for another 3 quasars (2 LDQs and 1 RQQ) are presented by SGSW04. Here we present the LTOV light curves of the remaining 12 objects (Figs. 7 and 8) of our sample and comment on those individual sources in increasing order of redshift.

LDQ 2349−014, $z = 0.174$: This QSO was monitored for three epochs which covered a time baseline of only five days. Over this time span the QSO was found to vary significantly. It faded by about 0.03 mag over four days between 13th October 2001 and 17th October 2001 and within the next 24 hours it brightened by about 0.05 mag (Fig. 8).

RQQ 0945+438, $z = 0.226$. This object was observed on three epochs and the time baseline extends over nearly three years. As neither of the comparison stars remained stable between our first epoch and the subsequent two epochs, we have considered

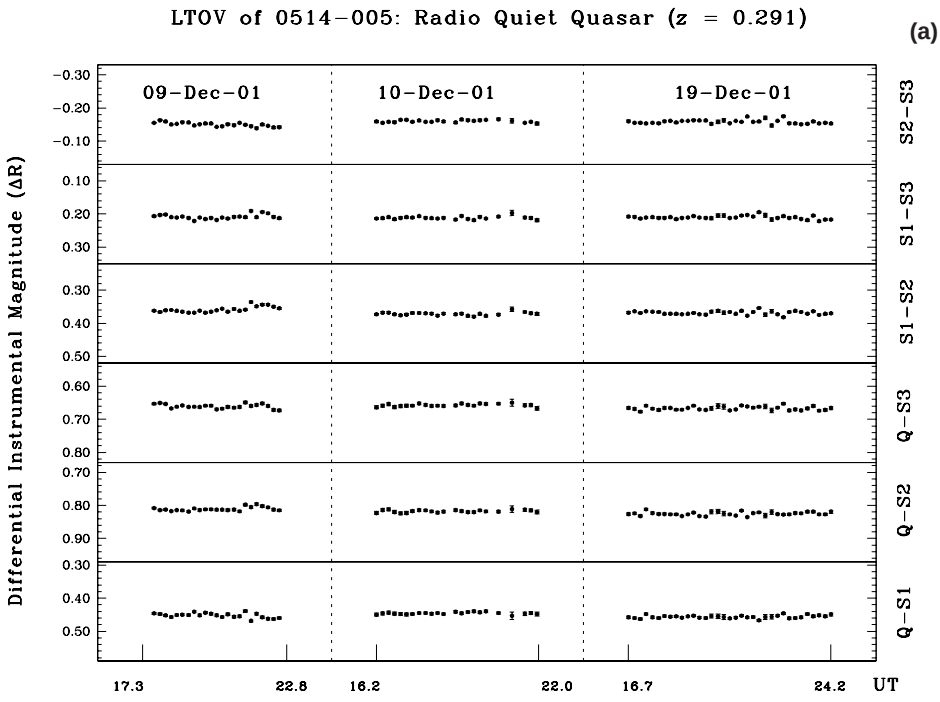

Figure 7. (*Continued*)

only the latter two epochs 26th February 2000 and 23rd January 2001 to examine the LTOV. The quasar dimmed by 0.07 mag within about a year between the two epochs (Fig. 7).

RQQ 0514−005, $z = 0.291$. Our three epochs of observations of this quasar covered a time baseline of only 11 days. The QSO did not show any change in brightness in about 24 hours between the first two epochs, but it faded by about 0.01 mag between 10th December 2001 and 19th December 2001 (Fig. 7).

RQQ 1252+020, $z = 0.345$: This QSO was monitored for five epochs; however, for LTOV only four epochs could be considered as the first epoch (22nd March 1999) lacks common comparison stars with the later four epochs. The total time baseline covered was about 2 years. The quasar remained at the same brightness level during the first two epochs of observations (9th March 2000 and 3rd April 2000). It brightened by about 0.18 mag when observed a year later on 26th April 2001. Observations on 18th March 2002 showed the object to have dimmed by about 0.10 mag compared to 26th April 2001 (Fig. 7).

LDQ 0134+329, $z = 0.367$: Three nights of observations were taken for this object, but they cover a time baseline of just six days. The object remained at the same brightness level during the first two days (7th and 8th November 2001), but dimmed by about 0.02 mag when observed again on 13th November 2001 (Fig. 8).

LDQ 1512+370, $z = 0.370$: This quasar was monitored on five epochs covering a time baseline of about 40 days. The object showed a gradual fading by about 0.09 mag between the first (23rd March 2002) and the third epochs (21st April 2002). It bright-

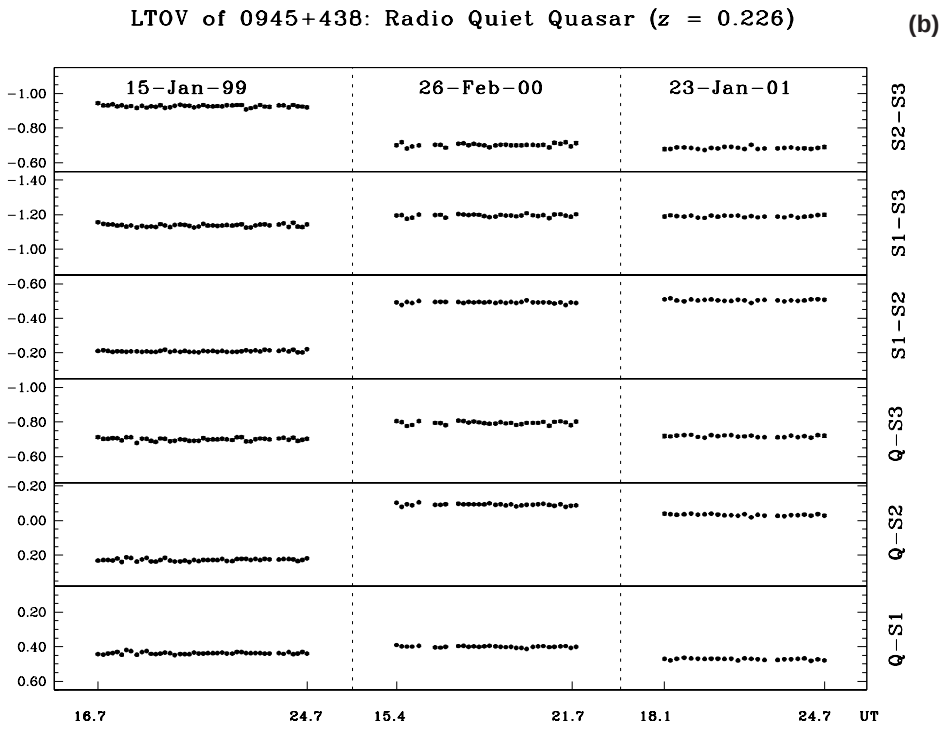

Figure 7. (*Continued*)

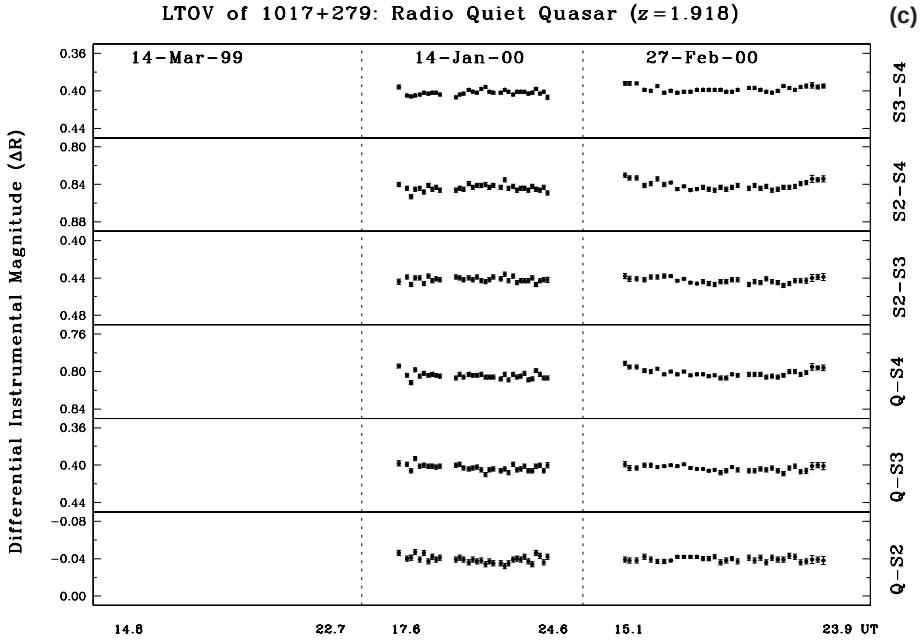

Figure 7. (*Continued*)

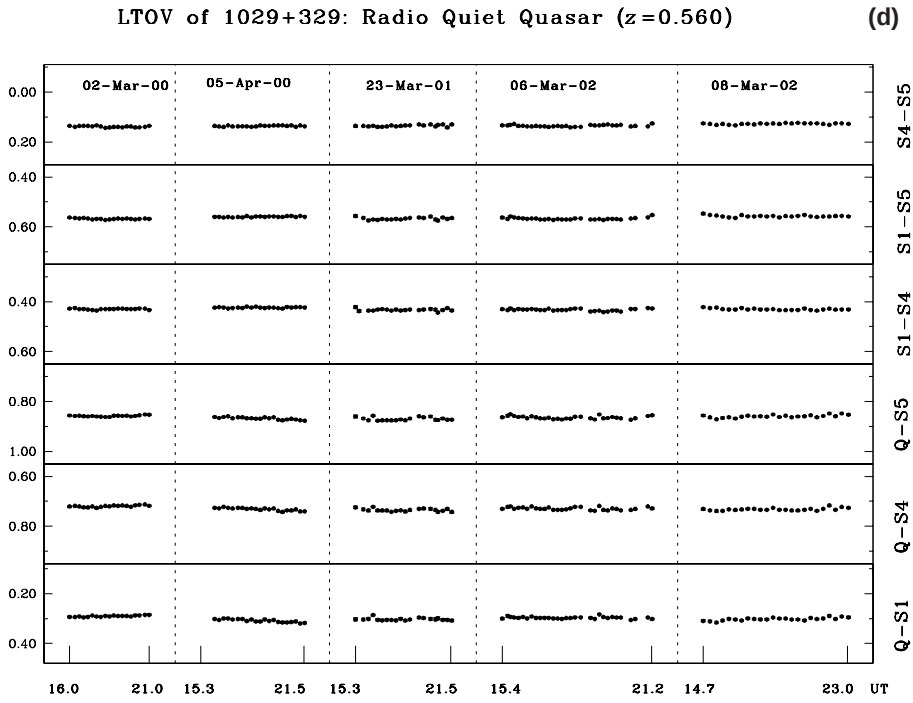

Figure 7. (*Continued*)

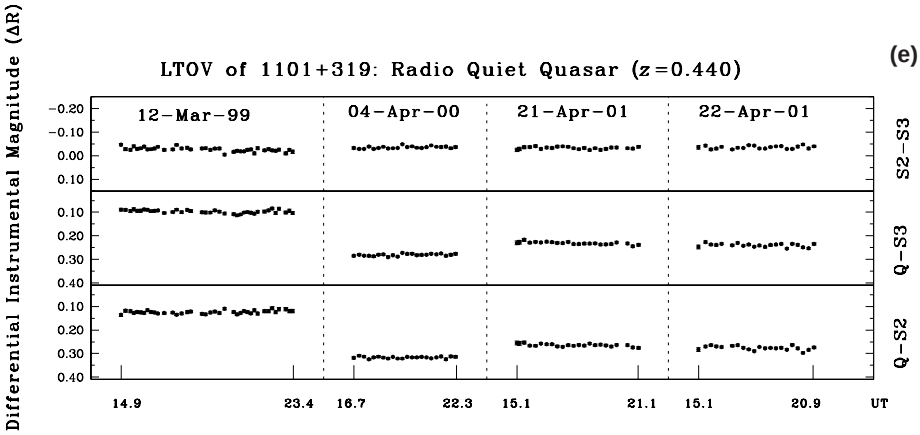

Figure 7. (*Continued*)

ened by about 0.03 mag when observed two days later on 23rd April 2002 and remained at the same brightness level during the last epoch of our observations (1st May 2002) (Fig. 8).

RQQ 1101+319, $z = 0.440$: Both brightening and fading were clearly present in our four epochs of observations which cover a time baseline of about two years. A fading

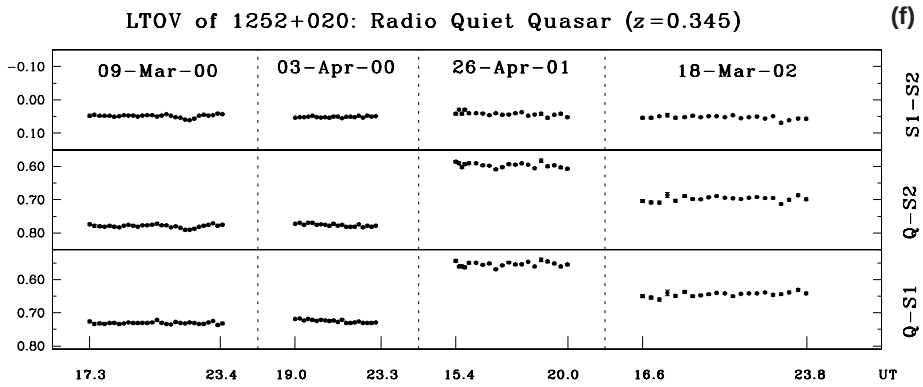

Figure 7(a–f). Long term variability of 6 radio-quiet quasars observed in this programme.

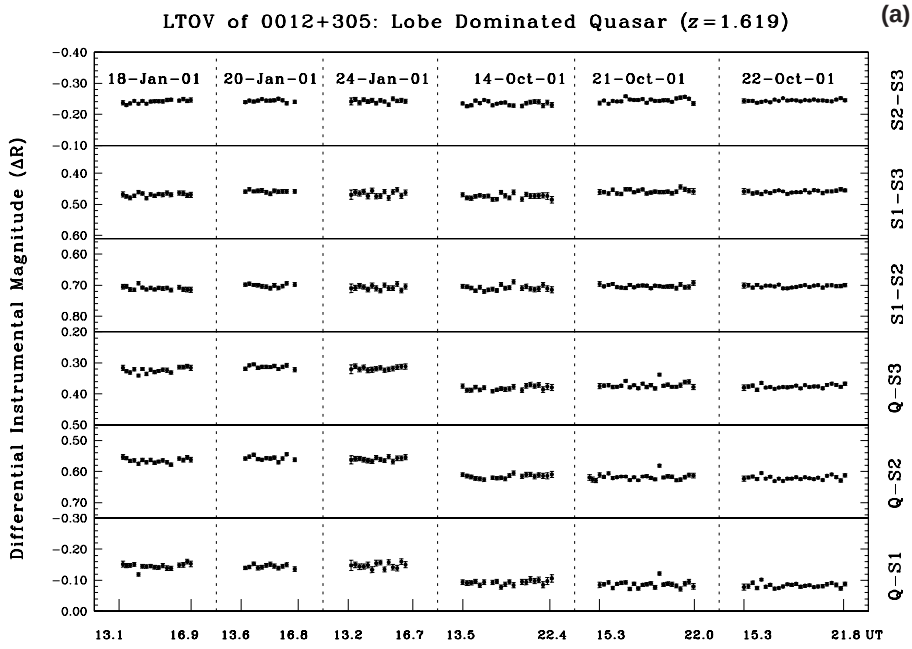

Figure 8. (*Continued*)

of about 0.19 mag was noticed in a year between the first two epochs of observations (12th March 1999 and 4th April 2000). When observed a year later (21st April 2001) a reversal in this trend was noticed whereby the quasar brightened by about 0.06 mag and thereafter remained fairly steady during the next 24 hours (Fig. 7).

LDQ 0709+37, $z = 0.487$: The LTOV of this QSO can be gleaned from the five epochs of observations done in the year 2001. It remained at the same brightness level during the first three epochs of observations during January 2001. However, it

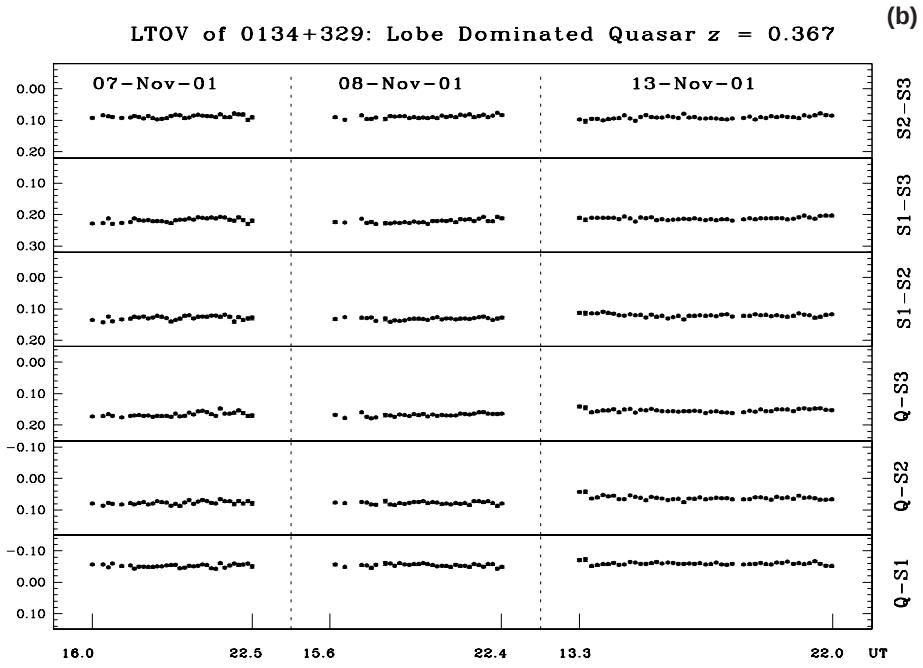

Figure 8. (*Continued*)

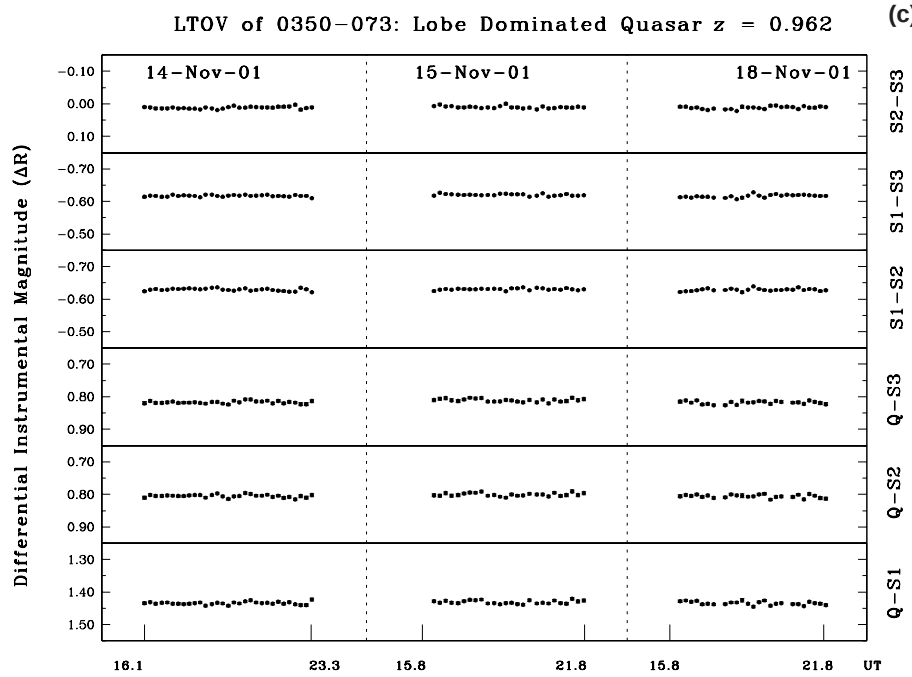

Figure 8. (*Continued*)

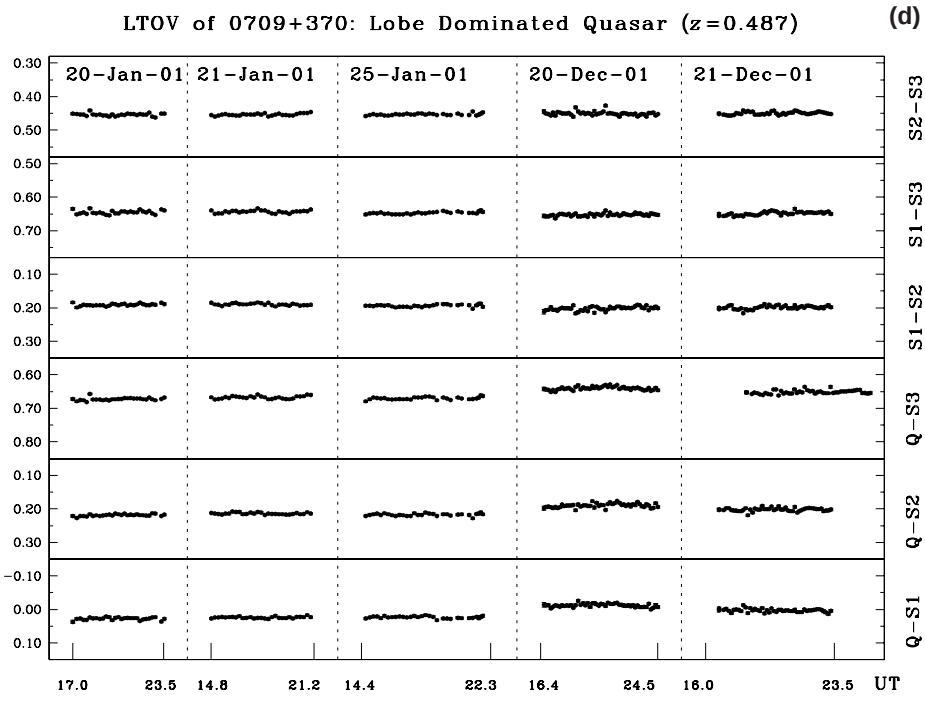

Figure 8. (*Continued*)

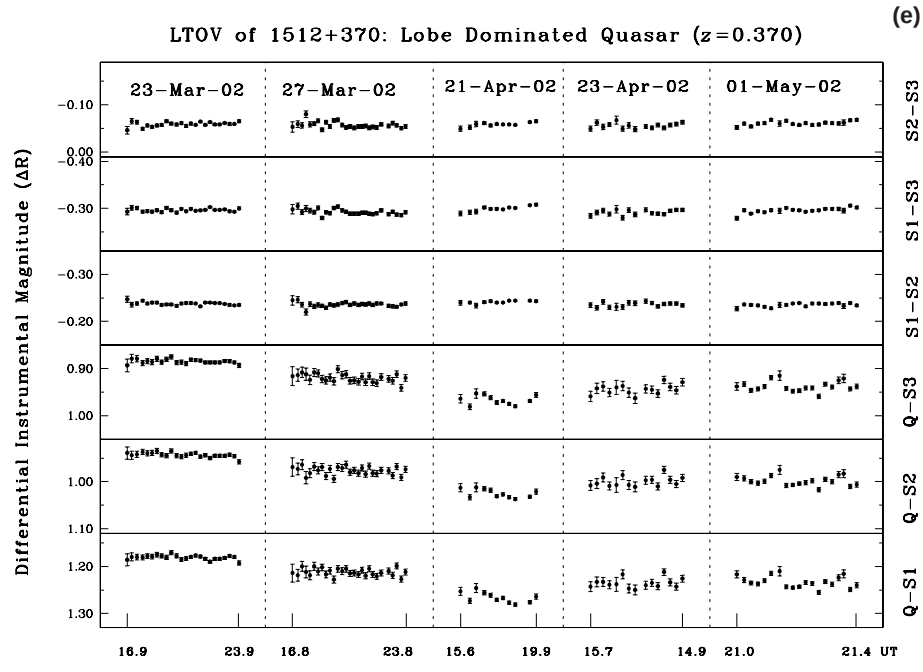

Figure 8. (*Continued*)

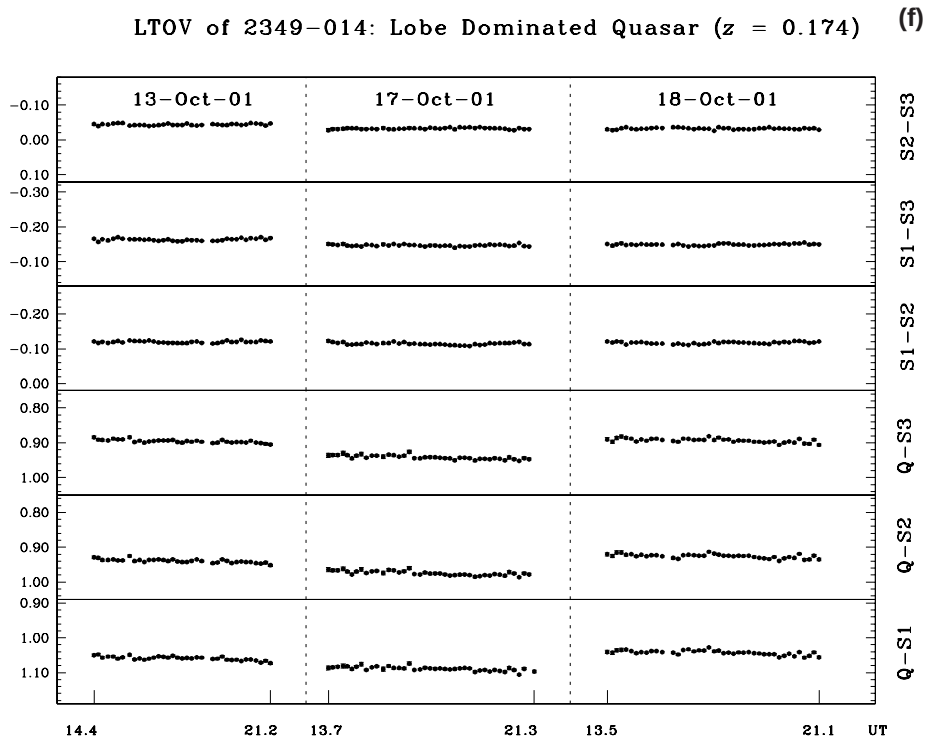

Figure 8(a–f). Long term variability of 6 lobe-dominated quasars observed in this programme.

brightened by about 0.03 mag when observed on 20th December 2001 and then faded by about 0.09 mag within the next 24 hours (between 20th and 21st December 2001; see Fig. 8).

RQQ 1029+329, $z = 0.560$: This QSO was monitored on six nights; however, for characterizing the LTOV only the later five epochs were considered due to the lack of common comparison stars in the first epoch of observation. The QSO remained at the same brightness level during our last five epochs of observations (between 2nd March 2000 and 8th March 2002) covering a two year baseline (Fig. 7).

LDQ 0350−073, $z = 0.962$: The quasar was found not to show any variability during our three epochs of observations within a week (during 14th to 18th November 2001) (Fig. 8).

LDQ 0012+305, $z = 1.619$. The quasar was found to be variable from our six epochs of observations encompassing about 10 months during 2001. It remained at the same brightness level during the first three epochs of observations and then faded by about 0.06 mag when observed nine months later on 14th October 2001. It then remained at the same brightness level for the next week during which it was monitored on three nights (Fig. 8).

RQQ 1017+279, $z = 1.918$. This quasar was monitored on three epochs. However, its LTOV could only be probed from the later two epochs, due to the lack of common comparison stars between them and the first epoch. The quasar remained at the same

flux level between the last two epochs (i.e., 14th January 2000 and 27th February 2000) separated by seven weeks (Fig. 7).

7. Do INOV and LTOV of blazars have a common origin?

A perception has gradually evolved that the most common cause of rapid optical variability of blazars is associated with disturbance occurring within their relativistic jets. For instance, Romero *et al.* (1999) have argued that while the LTOV arises due to large-scale relativistic shocks propagating through the jet, the INOV occurs due to the interception of these shocks by small scale magnetic irregularities in the jet. Similarly, Marscher *et al.* (1992) suggested that turbulence interacting with the shock could neatly explain the fast variations. To support or falsify these ideas, one needs to have a very large database of INOV monitoring observations at multiple epochs. Although such a compendium does not yet exist, our fairly extensive monitoring allows us to perform a check by searching for a correlation between the INOV amplitude and the level of optical brightness of the quasar.

If indeed both INOV and LTOV are phenomena related to relativistic jets then the best objects to look for the (presumably positive) correlation between them are blazars, for which at least the association of LTOV with the jet is rather secure (e.g., Hughes *et al.* 1992). To do this we have considered only the AGN for which we have LTOV data extending over at least two year baselines and for which INOV was clearly detected on at least two nights. For these 4 BL Lacs the values of INOV and LTOV for different nights are taken from Tables 2 and 4 respectively, and are plotted in Fig. 9. In no object, a clear correlation is seen between the INOV and LTOV amplitudes for these luminous AGNs whose optical emission is believed to be dominated by relativistic jets. In addition to the 4 objects plotted in Fig. 9, two additional BL Lacs, two RQQs and 1 CDQ also showed INOV on two or more occasions, but with total time spans less than two years; for these objects too, no correlations were found between INOV and LTOV. Thus, from an observational point of view, there is as yet no strong case for common origin of LTOV and INOV in the optical output of blazars.

7.1 *Do accretion disks contribute to INOV?*

The relation of INOV to the long term variability nature of quasars can be used to ascertain the contribution of any possible disk emission fluctuations to INOV (e.g., Mangalam & Wiita 1993; Wiita 1996; Xiong *et al.* 2000). Several Optically Violent Variables (OVV) including 3C 345 (Bregman *et al.* 1986; Smith *et al.* 1986), PKS $0420-014$, B2 $1156+295$ and 3C 454.3 (Smith *et al.* 1988) supply photometric and polarimetric evidence for substantial accretion disk contributions to their emission. But the general absence of a Big Blue Bump in BL Lac amounts to a lack of an accretion disk component that exists in most quasars (Sun & Malkan 1989). Still it has been claimed that in one of the best studied BL Lacs, $2155-304$, an accretion disk does seem to contribute to the spectrum (Wandel & Urry 1991), although, optical polarimetry implies that any disk contribution, if present, is fairly small (Smith & Sitko 1991).

If INOV is found to be inversely correlated to the brightness state of the object this may provide evidence for an accretion disk contribution to the observed INOV. This is because the disk component will be relatively more prominent when the object is in a quiescent state and jets are weaker. We again refer to Fig. 9 for a comparison of

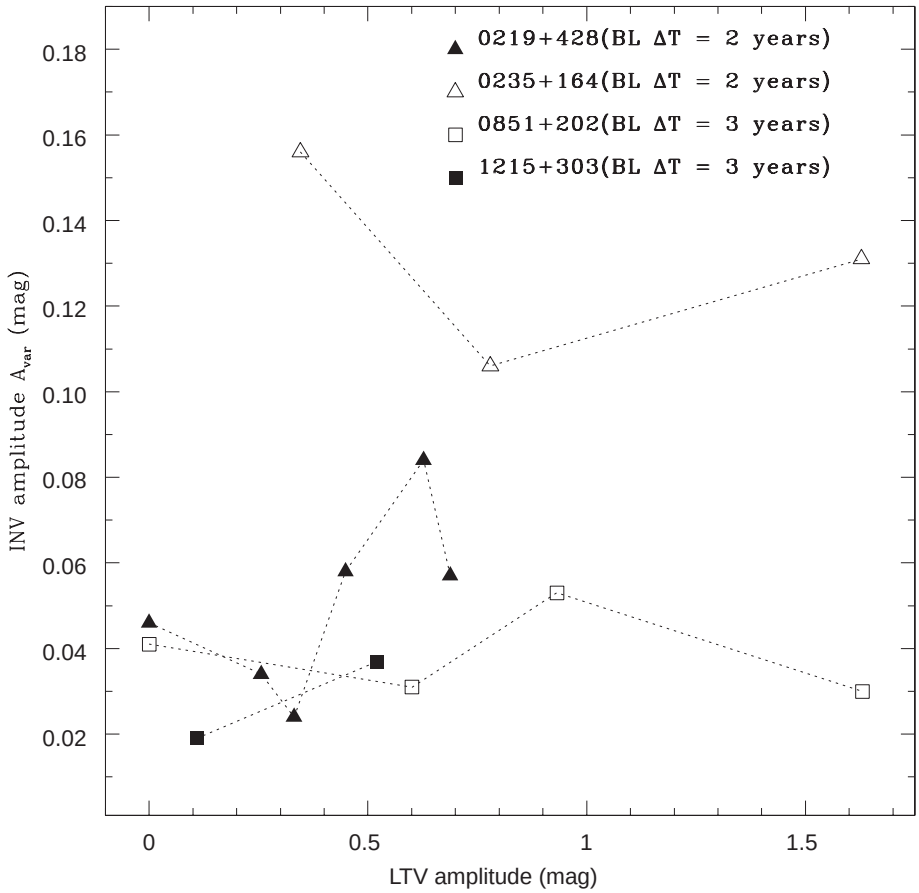

Figure 9. Comparison of INOV against LTOV.

INOV against LTOV for all the BL Lacs in our sample with significant LTOV time spans. No inverse correlation between INOV and LTOV is noticed, suggesting little contribution of an accretion disk to the observed INOV in any of these sources. Of course this dataset is so small that no firm conclusions in this regard can be drawn, and much larger studies are required. Some additional data in the literature (e.g., Carini *et al.* 1998) is also in accord with these results.

7.2 *INOV in the context of the starburst models of AGN*

In the starburst model (Terlevich *et al.* 1992; Terlevich & Melnik 1985) of AGNs, variability results from random superposition of events such as supernova explosions generating rapidly evolving compact supernova remnants (cSNRs) due to the interaction of their ejecta with the putative high density circumstellar environment. This model is supported by the striking similarity between the optical spectra of some AGNs and of cSNRs (Filippenko *et al.* 1989). The characteristics of an event (i.e., light curve, amplitude and time-scale) results from the combination of complicated processes (Terlevich

et al. 1992). Still, the lightcurves of AGNs of various absolute luminosities and redshifts can be predicted from the model and are found to be reasonably consistent with the observed dependence of the structure functions on luminosity and redshift (Fernandes, Aretxaga & Terlevich 1996; Cristiani *et al.* 1996). The lightcurves of cSNRs are still poorly known. While they seem to be consistent with the optical lightcurves of the low luminosity AGNs, NGC 4151 and NGC 5548 (Aretxaga & Terlevich 1994), as argued by Fernandes, Aretxaga & Terlevich (1997) and references therein, starburst models may be useful in explaining variability of modest amplitude in very weak AGN ($M_B \sim -20$ is the peak of a cSNR). As the energies involved in the intra-night fluctuations we have detected are at least an order of magnitude above the maxima expected from these SN models, it appears that they are not applicable to the variability events associated even with the non-blazar type luminous AGNs (Tables 2 and 4).

8. Conclusions

In this extensive optical monitoring programme, an effort has been made to understand the INOV characteristics of the four major classes of luminous AGNs, namely radio-quiet quasars, radio-lobe dominated quasars, radio-core dominated quasars and BL Lac objects. While the sample size, particularly for RQQs, is larger than previous studies, and our level of precision in obtaining INOV results is better than in most previous efforts, the sample size is still too small to provide absolutely firm conclusions. Bearing in mind that caveat, the major finding of this present study, which subsumes and refines those given in GSSW03, SGSW04, and SSGW04 are:

1. The first clear evidence of INOV in RQQs has been found from this observational programme (GSSW03). We have verified the radio-quiet nature of two members of this sample from VLA observations.
2. BL Lac objects are found to show a high DC of INOV (61%). In contrast, LDQs, CDQs and RQQs show smaller, comparable, INOV duty cycles ($\sim$ 20%). Our estimate of the DC of RQQs is much higher than 3% found by Romero *et al.* (1999); we attribute this to our better sensitivity, allowing us to claim detections that earlier observers could not see. Still, we find there is a marked difference between the INOV properties of blazars and radio-quiet quasars, in contrast to the conclusions reached by de Diego *et al.* (1998), namely that INOV occurs as frequently in RQQs as it does in all RLQs. This different conclusion of ours is probably due to both our higher sensitivity, and temporally much denser monitoring achieved in our program compared to that of de Diego *et al.* (1998).
3. The high DCs and amplitudes of variations shown by BL Lacs strongly suggests that relativistic beaming plays an important role in their observed INOV. Nonetheless, the much lower DC and amplitude of INOV, shown by LDQs and RQQs may still be understood within the framework of unified models, as the jets of these objects are believed to be modestly misaligned from our direction (see GSSW03; SSGW04). In those papers, we argued that LDQs and even RQQs could possess relativistic, optical synchrotron nuclear jets on micro-arcsecond scales. Their intrinsic optical variability might thus be similar to BL Lacs, as we showed that their observed milder INOV could be attributed to their (micro) jets being modestly misaligned from our direction (and so having lower Doppler factors, δ).

Thus, the observed difference in the micro-variability nature of LDQs and RQQs compared to BL Lacs could be accounted for in terms of their optically emitting nuclear jets undergoing different degrees of Doppler boosting in our direction. Observers located in suitably different directions may well find these same LDQs and RQQs to be large-amplitude rapid variables (GSSW03).

4. For blazars, no positive correlation is noticed between the INOV amplitude and the apparent optical brightness (Fig. 9). This suggests that the physical mechanisms for intra-night and long-term optical variability do not have a one-to-one relationship, and other factors are involved. Likewise, the absence of a clear negative correlation between the INOV and LTOV characteristics of the blazars in our sample points toward an inconspicuous contribution of the accretion disk to the observed INOV, though we stress that our sample size is very small and no firm conclusions can yet be drawn.
5. An apparent distinction is found for the first time between the INOV properties of the two classes of relativistically beamed radio-loud AGNs (RLQs), namely, BL Lacs and CDQs. The latter are found to exhibit a rather low INOV duty cycle, roughly that exhibited by RQQs and LDQs. Moreover BL Lacs show higher amplitude and DC of INOV. But in considering only the single CDQ which has high optical polarization $1216-010$, we found that it resembles BL Lacs, both in amplitude and DC of INOV. It thus appears that the mere presence of a prominent (and hence presumably Doppler boosted) radio core does not guarantee INOV; instead, it may well be that the more crucial factor is the optical polarization of the core emission. Such polarized emission is normally associated with shocks in a relativistic jet. This may suggest that the INOV is associated predominantly with highly polarized quasars (see SSGW04); however, it must be stressed that our sample of CDQs is too small to assign a strong level of confidence to this fascinating result.
6. Even though the percentage luminosity variations implied by the INOV for these luminous AGNs is small, the total power involved is still so enormous so as to render a starburst/supernova explanation untenable for these rapid events.

Additional monitoring of a variety of AGN types are necessary to verify the results we have presented here. While data on BL Lacs is reasonably good at this point (e.g. Carini *et al.* 1998 and references therein), more detailed studies of additional RQQs and both high- and low-polarized CDQs are absolutely necessary.

Acknowledgements

The help rendered by the technical staff at the 104 cm telescope of ARIES, Nainital is thankfully acknowledged. This research has made use of the NASA/IPAC Extragalactic Database (NED), which is operated by the Jet Propulsion Laboratory, California Institute of Technology, under contract with the National Aeronautics and Space Administration. The anonymous referee is thanked for comments which helped in improving the paper. CSS thanks NCRA for hospitality and use of its facilities and is also grateful for hospitality at GSU, where some revisions to this paper were carried out. PJW's efforts were partially supported by Research Program Enhancement funds to PEGA at GSU, and he is grateful for the continuing hospitality at Princeton University Observatory.

References

Angel J. R. P., Stockman H. S. 1980, *ARA&A*, **18**, 321.
Aretxaga I., Terlevich R. 1994, *MNRAS*, **269**, 462.
Bessel M. S. 1979, *PASP*, **91**, 589.
Berriman G., Schmidt G. D., West S. C., Stockman H. S. 1990, *ApJS*, **74**, 869.
Blandford R. J. 2000, *Trans. Roy. Soc. A*, **358**, 811.
Blandford R. J., Rees M. J. 1978, in Pittsburgh Conference on BL Lac Objects, (ed.) A. Wolfe (U. Pittsburgh) p. 328.
Blundell K. M., Beasley A. J. 1998, *MNRAS*, **299**, 165.
Blundell K. M., Rawlings S. 2001, *ApJL*, **562**, L5.
Boyle B. J., Shanks T., Croom S. M., Smith R. J., Miller L., *et al.* 2000, *MNRAS*, **317**, 1014.
Bregman J. N., Glassgold A.E., Huggins P. J., Kinney A. L. 1986, **301**, 708.
Carini M. T. 1990, Ph.D. thesis, Georgia State University, Atlanta, USA.
Carini M. T., Miller H. R., Noble J. C., Goodrich B. D. 1992, *AJ*, **104**, 15.
Carini M. T., Noble J. C., Miller H. R. 1998, *AJ*, **116**, 2667.
Carini, M., Noble, J., Amadi, O., Fendley, C., Simmons, De., Williams, S. 1999, *BAAS*, **31**, 1397.
Cellone S. A., Romero G. E., Combi J. A. 2000, *AJ*, **119**, 1534.
Cirasuolo M., Magliocchetti A., Celloti A., Danese L. 2003 (astro-ph/0301526).
Cristiani S., Trentini S., La Franca F., Aretxaga I., Andreani P., Vio R., Gemmo A. 1996, *A&A*, **306**, 395.
de Diego J. A., Dultzin-Hacyan D., Ramirez A., Benitez E. 1998, *ApJ*, **501**, 69.
Dunlop J. S., McLure R. J., Kukula M. J., Baum S. A., O'Dea C. P., Hughes D. H. 2003, *MNRAS*, **340**, 1095.
Edelson R. A., Turner T. J., Pounds K., Vaughan S., *et al.* 2002, *ApJ*, **568**, 610.
Elvis M., Wilkes B. J., McDowell J. C., Green R. F., Bechtold J., Willner S. P., Oey M. S., Polomski E., Curti R. 1994, *ApJS*, **95**, 1.
Fabian A. C., Rees M. J. 1979, in X-ray Astronomy (eds) W. A. Barty and L. E. Peterson (Oxford: Pergamon Press) p. 381.
Falcke H., Patnaik A. R., Sherwood W. 1996, *ApJ*, **473**, L13.
Fernandes C. R., Terlevich R., Aretxaga I. 1997, *MNRAS*, **289**, 318.
Fernandes C. R., Aretxaga I, Terlevich R. 1996, *MNRAS*, **282**, 1191.
Filippenko A. V. 1989, *AJ*, 97, 726.
Frank J., King A. R., Raine D. J. 1986, Accretion Power in Astrophysics (Cambridge: Cambridge University Press).
Garcia A., Sodre L., Jablonski F. J., Terlevich R. J. 1999, *MNRAS*, **309**, 803.
Goldschmidt, P., Kukula, M. J., Miller, L., Dunlop, J. S. 1999, *ApJ*, **511**, 612.
Gopal-Krishna, Sagar R., Wiita P. J. 1995, *MNRAS*, **274**, 701.
Gopal-Krishna, Gupta A. C., Sagar R., Wiita P. J., Chaubey U. S., Stalin C. S. 2000, *MNRAS*, **314**, 888.
Gopal-Krishna, Stalin C. S., Sagar R., Wiita P. J. 2003, *ApJ*, **586**, L25 (GSSW03).
Ho L. C. 2002, *ApJ*, **564**, 120.
Heidt J., Wagner S. J. 1996, *A&A*, **305**, 42.
Henden A. A., Kaitchuck R. H. 1982, Astronomical Photometry, p. 52 (Van Nostrand Reinhold, New York).
Howell S. B. 1989, *PASP*, **101**, 616.
Hughes P. A., Aller A. D., Aller M. F. 1992, *ApJ*, **396**, 469.
Hutsemekers D., Lamy H. 2001, *A&A*, **367**, 381.
Ivezic Z., *et al.* 2002, *AJ*, **124**, 2364.
Jang M., Miller H. R. 1995, *ApJ*, **452**, 582.
Jang M., Miller H. R. 1997, *AJ*, **114**, 565.
Kellermann K. I., Sramek R., Schmidt M., Shaffer D. B., Green R. 1989, *AJ*, **98**, 1195.
Kellermann K. I., Sramek R. A., Schmidt M., Green R. F., Shaffer D. B. 1994, *AJ*, **108**, 1163.
Kellermann K. I., *et al.* 2004, *ApJ*, in press (astro-ph/0403320).
Kukula M. J., Dunlop J. S., Hughes D. H., Rawlings S. 1998, *MNRAS*, **297**, 366.
Kundt W. 2002, *New Astronomy Reviews*, **46**, 257.
Mangalam A. V., Wiita P. J. 1993, *ApJ*, **406**, 420.
Marscher A. P., Gear W. K. 1985, *ApJ*, **298**, 114.

Marscher A. P., Gear W. K., Travis J. P. 1992, in *Variability of Blazars*, (eds.) E. Valtaoja, M. Valtonen (Cambridge: Cambridge Univ. Press) p. 85.
Marscher A., Scott J. S. 1980, *PASP*, **92**, 127.
McLure R. J., Dunlop J. 2001 in *QSO hosts and their environments*, (eds.) I. Marquez, *et al.* (Dordrecht: Kluwer) p. 27.
Meier D. L. 2002, *New Astronomy Reviews*, **46**, 247.
Miller P., Rawlings S., Saunders R. 1993, *MNRAS*, **263**, 425.
Miller H. R., Carini M. T., Goodrich B. D. 1989, *Nature*, **337**, 627.
Monet, D. G., *et al.* 2003, *AJ*, **125**, 984.
Noble J. C. 1995, *Ph.D. thesis, Georgia State University, Atlanta*, USA.
Paczyński B., Wiita P. J. 1980, *A&A*, **88**, 23.
Papadopoulos P. P., Seaquist E. R., Wrobel J. M., Binette L. 1995, *ApJ*, **446**, 150.
Quataert, E., Narayan, R. 1999, *ApJ*, **516**, 399.
Rabbette M., McBreen B., Smith N., Steel S. 1998, *A&AS*, **129**, 445.
Romero C. E., Cellone S. A., Combi J. A. 1999, *A&AS*, **135**, 477.
Sagar R., 1999, *Current Science*, **77**, 643.
Sagar R., Stalin, C. S., Gopal-Krishna, Wiita P. J. 2004, *MNRAS*, **348**, 176 (SSGW04).
Schmidt M., Green R. F. 1983, *ApJ*, **269**, 352.
Simonetti J. H., Cordes J. M., Heeschen D. S. 1985, *ApJ*, **296**, 46.
Smith P. S., Sikto M. L. 1991, *ApJ*, **383**, 580.
Smith P. S., Balonek T. J., Heckert P. A., Elston R. 1986, *ApJ*, **305**, 484.
Smith A. G., Leacock R. J., Webb J. R. 1988, in *Variability in Active Galactic Nuclei*, (eds.) H.R. Miller, P.J. Wiita (Berlin: Springer) p. 158.
Stalin C. S., Gopal-Krishna, Sagar R., Wiita P. J. 2004, *MNRAS*, **350**, 175 (SGSW04).
Stocke T. J., Morris S. L., Weymann R. J., Foltz C. B. 1992, *ApJ*, **396**, 487.
Sun W. H., Malkan M. A. 1989, *ApJ*, **346**, 68.
Terlevich R., Melnick J. 1985, *MNRAS*, **213**, 84.
Terlevich R., Tenorio-Tagle G., Franco J., Melnick J. 1992, *MNRAS*, **255**, 713.
Veron-Cetty M. P., Veron P. 1998, *ESO Scientific Report* No. 18.
Wandel A., Urry C. M. 1991, *ApJ*, **367**, 78.
White, R. L., *et al.* 2000, *ApJS*, **126**, 133.
Wiita P. J. 1996, in *Blazar Continuum Variability*, (eds.) H.R. Miller, J.R. Webb, J.C. Noble, *Astr. Soc. Pacific Conf. Ser.* 110, (ASP, San Francisco) p. 42.
Wills B. J. 1996, in *Jets from Stars and Galactic Nuclei, Lecture Notes in Physics*, Vol. **471**, (ed) W. Kundt, (Berlin: Springer) p. 213.
Wills B. J., Wills D., Breger M., Antonucci R. R. J., Barvainis R. 1992, *ApJ*, **398**, 454.
Wilson A. S., Colbert E. J. M. 1995, *ApJ*, **438**, 62.
Wisotzki L. 2000, *A&A*, **353**, 853.
Woo J. M., Urry C. M. 2002, *ApJ*, **581**, L5.
Worrall D. M. 1986, *ApJ*, **303**, 589.
Xiong, Y., Wiita, P. J., Bao, G. 2000, *PASJ*, **52**, 1097.
Zhang L. Z., Fan J. H., Cheng K. S. 2002, *PASJ*, **54**, 159.

J. Astrophys. Astr. (2004) **25,** 57–65

Associated HI Absorption in the $z = 3.4$ Radio Galaxy B2 0902 + 343 Observed with the GMRT

Poonam Chandra[1,2], Govind Swarup[3], Vasant K. Kulkarni[3], & Nimisha G. Kantharia[3]
[1]*Tata Institute of Fundamental Research, Mumbai 400 005, India.*
[2]*Joint Astronomy Programme, IISc, Bangalore 560 012, India.*
e-mail: poonam@tifr.res.in,
[3]*National Centre for Radio Astrophysics, TIFR, Pune 411 007, India.*
e-mail: swarup@ncra.tifr.res.in, e-mail: vasant@ncra.tifr.res.in
e-mail: ngk@ncra.tifr.res.in

Received 2004 January 28; accepted 2004 June 14

Abstract. We have made observations of the associated HI absorption of a high redshift radio galaxy 0902+34 at $z = 3.395$ with the Giant Meterwave Radio Telescope in the 323 ± 1 MHz band. We find a narrow absorption line with a flux density of 11.5 mJy at a redshift of 3.397 consistent with that observed by Uson *et al.* (1991), Briggs *et al.* (1993) and de Bruyn (1996). A weak broad absorption feature reported by de Bruyn (1996) has not been detected in our observations. We also place an upper limit of 4 mJy (2σ) on emission line strength at the position where Uson *et al.* (1991) claimed to have found a narrow emission line.

Key words. Galaxies: active; absorption lines—radio lines; galaxies—radio galaxies; individual (0902 + 343).

1. Introduction

It is believed that the epoch of galaxy formation lies beyond $z \geq 5$ but there is considerable uncertainty in their subsequent evolution. Radio galaxies and quasars at high redshifts are useful in studying the early stage of formation of galaxies. Many high redshifted radio galaxies and quasars have been looked at for associated absorption of continuum radiation by neutral hydrogen (HI). Associated absorption provides invaluable information about the environment surrounding astronomical objects. This can be studied either by redshifted 21-cm absorption of HI against the radio continuum or by narrow absorption in the spectra of Ly-α emission or absorption. Till date there is only one object beyond redshift $z \geq 3$ in which associated 21-cm absorption has been found. This is the radio galaxy B2 0902 + 343 at a redshift of $z = 3.395$ in which associated absorption was found by Uson *et al.* (1991) and later confirmed by Briggs *et al.* (1993) and de Bruyn (1996).

The radio galaxy B2 0902 + 343 was first identified with an optical object by Lilly (1988) under "1 Jansky empty field survey". Its very flat optical broad spectral energy distribution indicates that it may be a 'protogalaxy', undergoing its first major burst

of star formation (Einsenhardt & Dickinson 1992). The spatial extension of this radio source is 7" × 4". The galaxy shows a bizarre radio structure in high resolution radio images (Carilli 1995). The radio source has two outer lobes and a prominent nuclear core source with a flat spectral index. The flux density of the core at 1.665 GHz is $\sim$ 10 mJy, being about 2.4 % of the strength of the entire source at that frequency. At the northern end of a sharp knotty jet emerging from the core, with a sharp 90° bend towards its outer end, is located a prominent hot spot and also a long 'plume' of emission with an ultra steep spectral index of -3.3. The southern lobe consists of two components having perpendicular orientation with respect to the direction of the core. The source seems to be oriented at an angle of about 45° to 60° with respect to the sky plane (Carilli 1995). Moreover this is one of the unique high redshifted sources which does not follow radio-optical alignment effect. HST observations by Pentericci *et al.* (1999) show that the optical galaxy consists of two regions of approximately the same flux density with a void or valley in between. Astrometry measurements show that the radio core is situated in the valley (Pentericci *et al.* 1999) but do not rule out the possibility that the radio core could be coincident with any of the two components. The presence of narrow Ly-α emission distinguishes it from a high redshifted quasar. Also, recent Chandra observations by Fabian *et al.* (2002) has found X-ray emission from the source. The centroid of the X-ray emission (J2000 09 05 30.17, +34 07 56) is coincident with the flat spectrum nuclear core source (J2000 09 05 30.13, +34 07 56.1), which suggests it to be an AGN.

This peculiar galaxy and its surroundings have been searched for absorption and emission features by several workers using various radio telescopes. Uson *et al.* (1991) detected a narrow absorption line of 11 mJy associated with B2 0902+343. In addition, they claimed to have found an emission line of 11 mJy located about 33' away from the galaxy, which was ascribed to emission by a massive HI condensate as expected for a Zeldov'ich 'pancake'. Subsequent observations by Briggs *et al.* (1993) using the Arecibo Radio Telescope and by de Bruyn (1996) using Westerbork Radio Telescope (WSRT) confirmed the presence of the narrow associated line but did not detect the emission line. The possible presence of a broad absorption feature extending to several hundred km s^{-1} on the blue-ward side of the narrow absorption feature has been reported by de Bruyn (1996). Cody *et al.* (2003) looked for the presence of OH gas in the galaxy to get an insight in the molecular content of the galaxy but did not detect redshifted 1665/1667 MHz OH lines. They put a 1.5σ upper limit of 3.6 mJy, which gives an upper limit on the OH column density of $N(OH) \leq 10^{15}$ cm^{-2}.

We have observed the radio galaxy B2 0902+343 with the Giant Meterwave Radio Telescope (GMRT) in the band 323 ± 1 MHz for studying the associated absorption features. We have detected the narrow absorption line component. However, the broad absorption feature claimed by de Bruyn (1996) is absent in our results. We also place a 2σ upper limit of 4 mJy at the position of the emission line claimed by Uson *et al.* (1991). We present observations and data analysis in section 2. Results are given in section 3 and discussions and conclusions in section 4.

2. Observations and data analysis

Observations of the radio galaxy B2 0902 + 343 were made with the GMRT in March 1999 and on May 15th, 2000 near 323 MHz. GMRT is an aperture synthesis radio telescope situated about 80 km north of Pune in India. It consists of 30 fully steerable

parabolic dishes of 45 meter diameter each, spread over an extent of about 25 km (Swarup *et al.* 1991). Fourteen out of the 30 antennas are located within a compact array of about 1 square km in size and the remaining 16 antennas are located along a Y-shaped array, with each arm of about 14 km length.

In March 1999, observations of the radio galaxy B2 0902 + 343 were made for ~ 8 hours with 12 to 15 antennas. Although observations were made with 128 channels over a bandwidth of 2 MHz centered at 323 MHz, the data were good for only the central part of 1 MHz. 3C286 was used as flux calibrator and 3C216 and 0834 + 555 were used as phase calibrators. RMS noise of the continuum map after collapsing 40 channels was 4 mJy. RMS noise on the line images, after subtracting the continuum was 1.4 mJy.

On May 15th 2000, observations were made for 6 hours on the source, when only 15 good antennas were available. The observations were made with 128 channels over a bandwidth of 2 MHz. Therefore, the width of each channel was 15.6 kHz. 3C48 and 3C286 were used as flux calibrators. 3C216 was used as a phase calibrator. 3C48, 3C286 and 3C216 were also used as bandpass calibrators. The phase calibrator was observed for 8 minutes after every 40 minutes.

The data were analyzed using Astronomical Image Processing System (AIPS) of NRAO. The gains of the antennas were determined using the flux and phase calibrators after flagging any bad data. The flux densities of 3C48 and 3C286 were calculated to be 43.64 Jy and 26.03 Jy respectively, on the scales of Baars *et al.* (1977) using the AIPS task SETJY. The flux density of 3C216 was found to be 16.65 ± 0.21 Jy. After bandpass calibration using the flux and phase calibrators, AIPS task SPFLG was run on the source 0902 + 34 to flag any data showing RFI. In total, the amount of good data that could be used finally was 76%. We then averaged several line free channels and made a continuum map of the source using AIPS task IMAGR. We also did self calibration in order to get rid of residual phase errors and to improve the quality of the map. The resolution of the map was 39" $\times$ 30". The continuum flux density of the source was found to be 1.357 ± 0.008 Jy. The dynamic range obtained in continuum map was ~ 450. The source is not resolved in our map. The continuum map was then subtracted from the line data using UVSUB. AIPS task UVLIN was then run and the line free channels were used for the baseline fitting. The UVLIN output was used for making a spectral cube of the data. The narrow absorption feature towards B2 0902+343 was clearly detected but no other absorption or emission feature was seen in the spectral cube covering the field of view of the 45-m antennas of the GMRT.

3. Results

3.1 *HI absorption narrow line*

Figure 1 shows the HI absorption profile obtained from the observations made on 15th May 2000. The dashed dot line shows a one-component Gaussian fit to the observed absorption line. We find that there is a continuum offset of about 1 mJy. We have made one-component Gaussian fit after removing this "continuum" of 1 mJy offset and the results are summarized in Table 1. A possible weak absorption feature reported by Briggs *et al.* (1993) near 322.5 MHz is not seen in our observations.

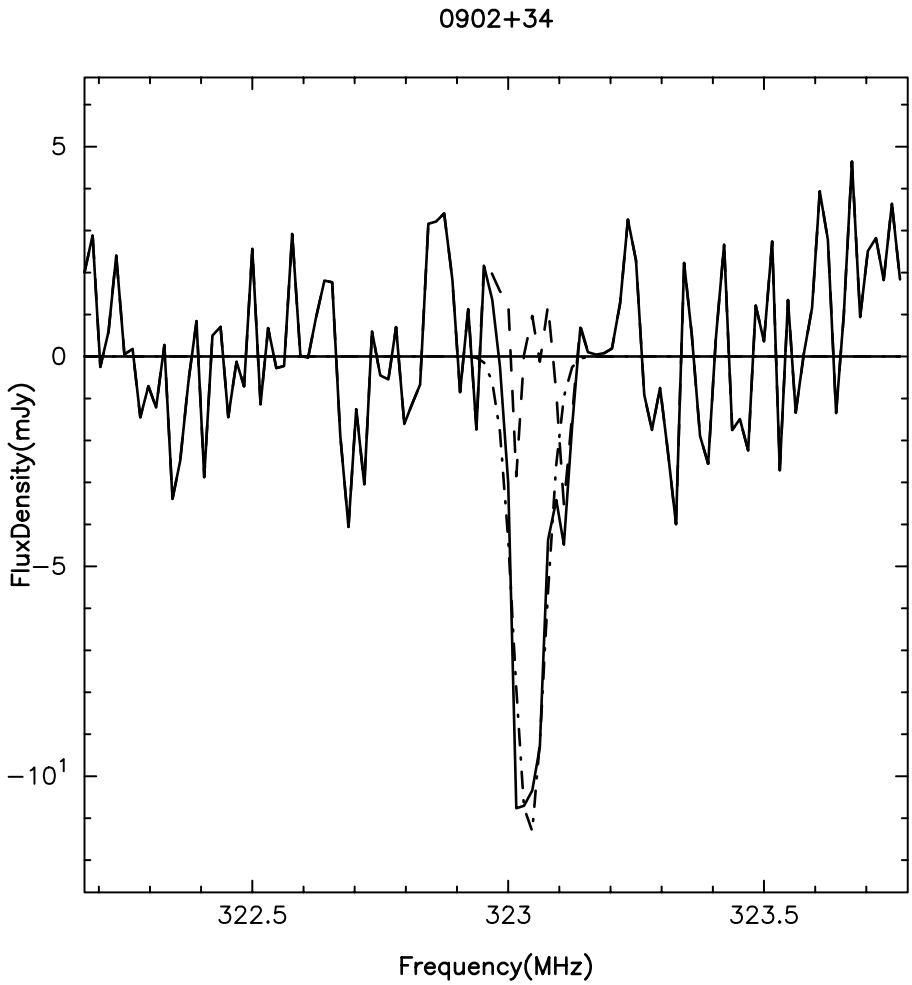

Figure 1. One-component Gaussian fit to the absorption line observed on 15th May, 2000. Dot-dashed line shows Gaussian fit to the observed absorption feature. Dashed line shows residual to the Gaussian fit.

Table 1. Best fit Gaussian parameters for the March, 1999 and May, 2000 data.

Date of observn	Gaussian fit	Line depth mJy	Position of line MHz	Redshift z	FWHM kms^{-1}	rms mJy/beam
2000 May	1-comp.	11.5	323.062 ± 0.005	3.397	76 ± 6	1.8
1999 Mar	1-comp.	11.1	323.058 ± 0.005	3.397	72 ± 6	1.4

The absorption profile for the March 1999 observations is shown in Fig. 2. This spectrum shows the presence of a small asymmetric profile towards the higher frequency. Hence, we have made both one-component and two-component Gaussian fit to this data. In Table 1, we summarize the results of only 1-component Gaussian fit, since we find from the two-component Gaussian fit that the asymmetry towards higher frequency end of the abosrption line is not significant.

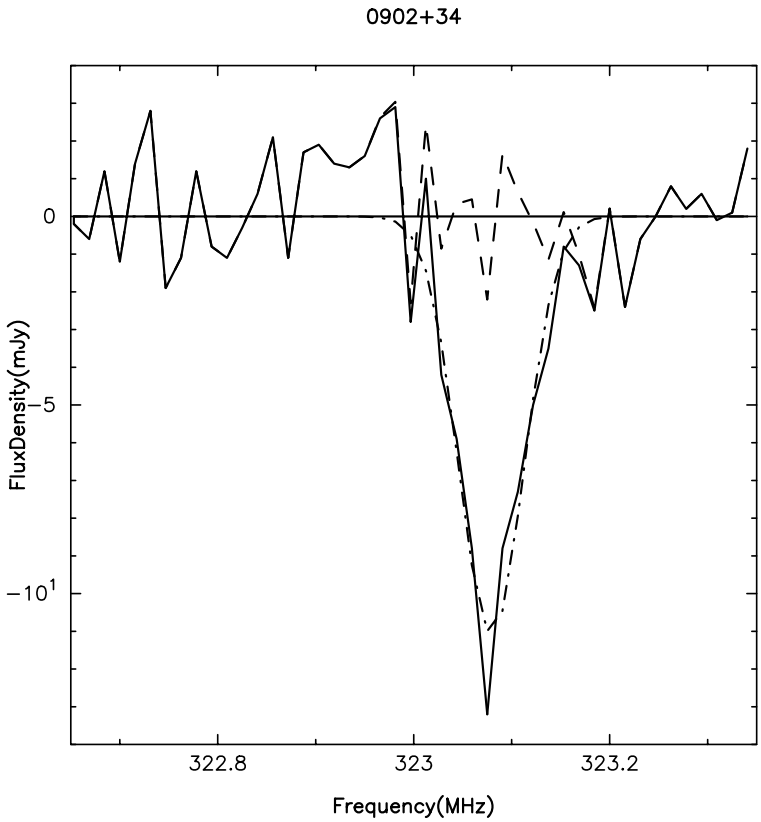

Figure 2. One-component Gaussian fit to the absorption line observed on March, 1999. Dot-dashed line shows a fit to the observed absorption feature and dashed line shows residual to the Gaussian fit.

3.2 *Broad HI absorption line*

de Bruyn (1996) reported the possible presence of a weak broad absorption feature extending several hundred km s^{-1} blue-ward (at a higher frequency) of the prominent narrow absorption line. In order to search for its presence in the GMRT observations, we have removed the Gaussian fit shown in Figs. 1 and 2 and then convolved the residuals with a Gaussian profile of FWHM of 100 km s^{-1}. The smoothed residual spectra of GMRT observations on May 15, 2000 are shown in Fig. 3. No broad absorption feature is visible in either spectra. Since a digital file of the spectrum observed with WSRT by de Bruyn was not saved by him (private communication), we have carefully digitized the data from the spectrum published by him as Figure 1 (de Bruyn 1996). We have fitted a Gaussian to the narrow feature of his spectrum and found that the narrow absorption line has a FWHM of 80 ± 8 km s^{-1}. We have also convolved the residuals of his data with 100 km s^{-1} FWHM as shown in the last panel of Fig. 3. Figure 3 shows the possible presence of a broad absorption feature at 3σ level in the WSRT observations. However, we place an upper limit of 3 mJy at 3σ level from the GMRT data of 15th May 2000.

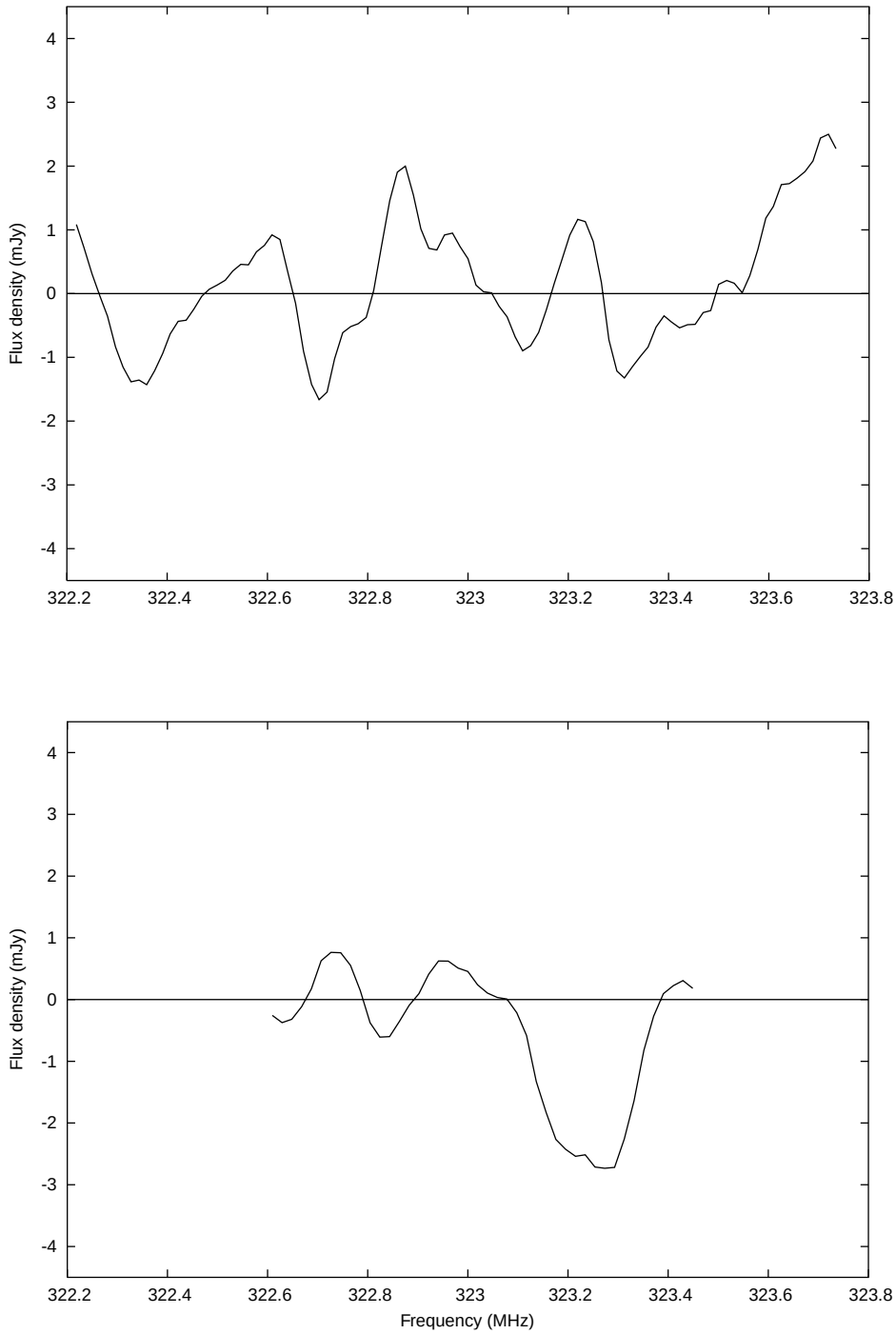

Figure 3. Upper panel shows the residuals of one-component Gaussian fit to absorption line observed in May, 2000. Lower panel shows the same for de Bruyn's dataset.

3.3 *Non-detection of HI emission*

Uson *et al.* (1991) had claimed the detection of an HI emission feature of 11 mJy at a frequency of 323.041 MHz, towards the direction of $\alpha = 09^h03.8^m$, $\delta = 33^\circ52'$ (B 1950), which is 33' away from the position of the source B2 0923 + 343. We made the spectral cube with 200" resolution (same resolution as used by Uson *et al.* (1991)) and corrected it for primary beam pattern. We do not see any emission feature at the given position. We place a 2σ upper limit of 4 mJy at the position of the above emission feature. The GMRT spectrum towards this direction is shown in Fig. 4.

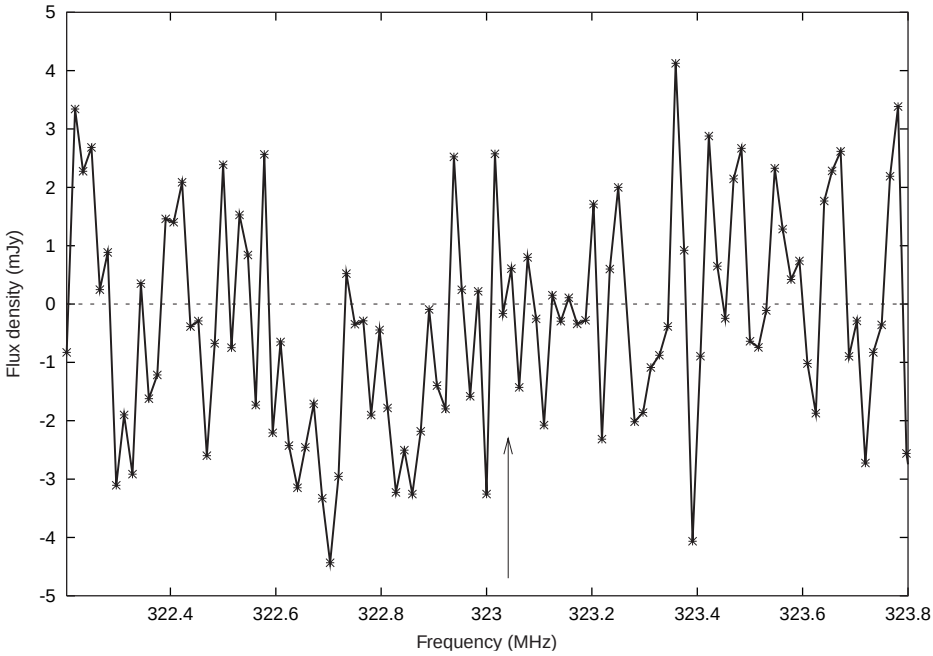

Figure 4. Spectrum at the position of emission claimed by Uson *et al.* (1991) at $09^h03.8^m$, 33° 52' (B 1950) and frequency of about 323.0 MHz. Arrow points towards the frequency at which Uson *et al.* found the emission.

3.4 *Search for HI absorption towards background sources*

Although the probability of a strong radio source being located in a cluster near B2 0902 + 343 is small, we have searched for any absorption features towards three radio sources in the field of view of the primary beam of the 45 m dishes of the GMRT (see Table 2). No absorption lines were detected.

4. Discussions and conclusions

Our observations show that the depth of the HI absorption at a redshift (doppler shift corrected) of 3.3967 ± 0.0002 is 11.5 mJy with a FWHM of 74 ± 6 km s^{-1} (see Tables 1 and 3). In our GMRT observations with only 15 antennas, we could not get sufficient

Table 2. The sources in the FoV, looked for any possible absorption feature.

Source	Position J2000	Flux density Jy
1	09 07 17.6, +33 44 10	0.675 ± 0.008
2	09 06 19.4, +34 17 32	0.289 ± 0.008
3	09 04 32.7, +34 32 12	0.183 ± 0.008

Table 3. Details of all observations of $0902 + 34$ by various workers.

Obs. Date	Telescope	Time hours	Line depth mJy	FWHM . kms^{-1}	rms mJy/beam	References
Apr, 91	VLA	14	11.4	270 ± 50	1.8	Uson *et al.* 1991
1992	Arecibo		14	90	1.9	Briggs *et al.* 1993
1995	WSRT	144*	12	100**	1	de Bruyn 1996
May, 00	WSRT	12	15.9	120 ± 50	2.4	Cody *et al.* 2003
Mar, 99	GMRT	8	11.1	72 ± 6	1.4	This paper
May, 00	GMRT	6	11.5	76 ± 6	1.8	This paper

* As mentioned in Rottgering *et al.* (1999).
** Our estimate to the data of de Bruyn data gives line depth of 9.93 ± 1.45 mJy, FWHM of 80 ± 8 km s^{-1}.

resolution to locate the position of the line. The possible scenarios for its position could be either the northern hot spot or a tori/jet surrounding the nuclear source. The observed depth of the narrow absorption line of 11.5 mJy is close to the observed flux density of the radio nucleus (flux density of 9.5 mJy at 1.65 GHz), implying 100% absorption (optical depth of 1) by cold HI gas which could be present in a disk or tori. Associated HI absorption has been found in many compact steep spectrum sources (Vermeulen *et al.* 2003). However, only absorptions up to about 10–40 % have been seen in these sources. Assuming that the surrounding disk has a scale size such that it covers a possible steep spectrum core and part of the base of the jet, Rottgering *et al.* (1999) have suggested that the observed absorption may be associated with a steep spectrum core. In that case the required optical depth could be much less, say 20%.

Although associated HI absorption is generally not seen in extended powerful radio galaxies, there are some radio galaxies in which HI absorption is seen against the hot spots (Morganti 2002 and references therein). de Bruyn (1996) has suggested that the absorption is likely to be against the northern hot spot. The hot spot has an angular size of 0.2" and contains about 75% of the total flux density. Its extrapolated flux density at 323 MHz is $\sim$ 1 Jy. In this case optical depth of only 1.2% is required, which is pretty reasonable. The implied column density, N(HI) $\sim 1.6 \times 10^{21}$ cm^{-2}, assuming optical depth of 0.012 and a mean spin temperature of 1000 K. The HI gas could be surrounding the hot spot which is not an unlikely scenario considering that the optical observations of B2 $0902 + 343$ indicates it to be a protogalaxy. The source may be associated with a merging galaxy located near the hot spot or dwarf galaxy along the line of sight, as a possible scenario suggested by Rottgering *et al.* (1999).

Considering the above discussion, it seems to us that the HI absorption could be associated with the hot spot. However, sub arcsec high-resolution observations at low frequencies are required in order to determine the location of the absorber.

We conclude with the following results:

- We have detected a narrow absorption line with the GMRT in B2 0902+343 with flux density of 11.5 mJy which has a half-power velocity width of 74 ± 6 km s^{-1}. The line depth is consistent with previous observations.
- The broad absorption feature indicated by de Bruyn (1996) is not seen in our observations. We also do not detect the emission line (33' away) as claimed by Uson *et al.* (1991) which is consistent with the results by Briggs *et al.* (1993) using the Arecibo Radio telescope and de Bruyn (1996) using the WSRT.

Acknowledgements

We thank the staff of the GMRT who made these observations possible. GMRT is run by the National Centre for Radio Astrophysics of the Tata Institute of Fundamental Research. We acknowledge valuable comments by Prof. Rajaram Nityananda. N. G. Kantharia is thankful to the late Prof. K. R. Anantharamaiah for suggesting in 1999, the observation of this source. We thank the anonymous referee for useful comments.

References

Baars, J. W. M., Genzel, R., Pauliny-Toth, I. I. K., & Witzel, A. 1977 *Astron. Astrophys.*, **61**, 99.
Briggs, F. H., Sorar, E., Taramopoulos, A. 1993, *Astrophys. J.*, **415**, L99.
Carilli, C. L. 1995, *Astron. Astrophys.*, **298**, 77.
Cody, A. M., Braun, R. 2003, *Astron. Astrophys.*, **400**, 871.
de Bruyn, A. G. 1996, *Cold Gas at High Redshift, Proc. of workshop on 25th anniversary of WSRT*, in Hoogeven, The Netherlands, August 28–30, 1995, (eds.) M.N. Bremer & N. Malcolm. Astroph. and Space Sci. Lib., 206, 171.
Eisenhardt, R., Dickinson, M. 1992, *Astrophys. J.*, **47**, L399.
Fabian, A. C., Crawford, C. S., Iwasawa, K. 2002, *Mon. Not. R. Acad. Soc.*, **331**, L57.
Lilly, S. J. 1988, *Astrophys. J.*, **333**, 161.
Morganti, R. 2002, *ASP Conference Proceedings*, **258**, (eds.) R. Maiolino, A. Marconi & N. Nagar, (San Francisco, ASP) page 63.
Pentericci, L., Rottgering, H., Miley, G. K. *et al.* 1999, *Astron. Astrophys.*, **341**, 329.
Rottgering, H., de Bruyn, G., Pentericci, L., & Miley, G. 1999, *Proc. of the coll. at Amsterdam in Oct 97.* (eds.) H. J. A. Rottgering, R. N. Best and Lehnert.
Swarup, G., Ananthkrishnan, S., Kapahi, V. K., Rao, A. P., Subrahmanya, C. R., Kulkarni, V. K. 1991, *Current Science*, **60**, 95.
Uson, J. M., Bagri, D. S. Cornwell, T. J. 1991, *Phys. Rev. Lett.*, **67**, 3328.
Vermeulen, R. C., Pihlstrom, Y. M., Tschager, W., de Vries, W. H. *et al.* 2003, *Astron. Astrophys.*, **404**, 861.

J. Astrophys. Astr. (2004) **25,** 67–80

HI Fluctuations at Large Redshifts: III – Simulating the Signal Expected at GMRT

Somnath Bharadwaj* & Pennathur Sridharan Srikant†
*Department of Physics and Meteorology and Center for Theoretical Studies, I.I.T. Kharagpur, 721 302, India.
e-mail: somnath@phy.iitkgp.ernet.in
†Department of Physics and Meteorology, I.I.T. Kharagpur, 721 302, India.
†Present address: Department of Physics, University of Utah, USA.

Received 2003 August 25; accepted 2004 April 7

Abstract. We simulate the distribution of neutral hydrogen (HI) at the redshifts $z = 1.3$ and 3.4 using a cosmological N-body simulation along with a prescription for assigning HI masses to the particles. The HI is distributed in clouds whose properties are consistent with those of the damped Lyman-α absorption systems (DLAs) seen in quasar spectra. The clustering properties of these clouds are identical to those of the dark matter. We use this to simulate the redshifted HI emission expected at 610 MHz and 325 MHz, two of the observing bands at the GMRT. These are used to predict the correlations expected between the complex visibilities measured at different baselines and frequencies in radio-interferometric observations with the GMRT. The visibility correlations directly probe the power spectrum of HI fluctuations at the epoch when the HI emission originated, and this holds the possibility of using HI observations to study large-scale structures at high z.

Key words. Cosmology: theory, observations, large scale structures—radiation.

1. Introduction

Observations of Lyman-α absorption lines seen in quasar spectra are an important probe of the distribution of neutral hydrogen (HI) at high redshifts. These observations show that the bulk of the neutral gas in the redshift range $1 \leq z \leq 3.5$ is in HI clouds with column densities greater than 2×10^{20} atoms/cm^2 (Lanzetta *et al.* 1995; Storrie-Lombardi *et al.* 1996; Péroux *et al.* 2001). The damped Lyman-α absorption lines produced by these clouds indicate $\Omega_{\rm gas}(z)$, the comoving density of neutral gas expressed as a fraction of the present critical density, to be nearly constant at a value $\Omega_{\rm gas}(z) \sim 10^{-3}$ (Péroux *et al.* 2001).

In this paper we simulate the HI emission expected from these clouds. The aim of the exercise is to investigate the possibility of detecting the redshifted HI emission using the Giant Meterwave Radio Telescope (GMRT; Swarup *et al.* 1991). We focus on two of the GMRT frequency bands centered at 610 MHz and 325 MHz corresponding to HI

emission from redshifts $z = 1.3$ and 3.4. The HI flux from individual clouds ($< 10\mu$Jy) is too weak to be detected by GMRT unless the image of the cloud is significantly magnified by an intervening cluster gravitational lens (Saini *et al.* 2001). Although we may not be able to detect individual clouds, the redshifted HI emission from the distribution of clouds will appear as a background radiation in low frequency radio observations. In three earlier papers (Bharadwaj *et al.* 2001; Bharadwaj & Sethi 2001 and Bharadwaj & Pandey 2003; hereafter referred to as Paper a, b and c respectively), and in the present paper we investigate issues related to calculating the expected signal and detecting it.

We propose (Papers b and c) that the optimal observational strategy for detecting this signal is to deal directly with the complex visibilities measured in radio interferometric observations. Briefly introducing the terms involved, we remind the reader that the quantity measured in radio interferometric observations with an array of antennas is the complex visibility $V(\mathbf{U}, \nu)$. This is measured for every pair of antennas at every frequency channel in the observation band. For every pair of antennas it is convenient to express the visibility as a function of $\mathbf{U} = \mathbf{d}/\lambda$ i.e., the separation between the two antennas $\mathbf{d}$ expressed in units of the wavelength λ. We refer to the different possible values of $\mathbf{U}$ as baselines. One of the big advantages of dealing directly with the visibilities is that the system noise contribution to the visibilities is uncorrelated. The visibilities respond only to the fluctuations in the redshifted HI emission. In Paper b we showed that the correlation expected between the visibilities $V(\mathbf{U}, \nu)$ and $V(\mathbf{U}, \nu+\Delta\nu)$ measured at the same baseline at two slightly different frequencies is

$$\langle V(\mathbf{U}, \nu) V^*(\mathbf{U}, \nu + \Delta\nu)\rangle = \frac{[\bar{I} b D \theta_0]^2}{2r^2} \int_0^\infty dk_\parallel P(k) \left[1 + \beta \frac{k_\parallel^2}{k^2}\right]^2 \cos(k_\parallel r' \Delta\nu), \quad (1)$$

where $k = \sqrt{(2\pi U/r)^2 + k_\parallel^2}$, $\bar{I}_0$ is the specific intensity expected from the HI emission if the HI were uniformly distributed, $\theta_0 = 0.6 \times \theta_{\rm FWHM}$, $\theta_{\rm FWHM}$ being the angular width of the primary beam of the individual antennas, r is the comoving distance to the HI from which the radiation originated, and $b^2 D^2 P(k) \left[1 + \beta \frac{k_\parallel^2}{k^2}\right]^2$ is the power spectrum of the fluctuations in the HI distribution in redshift space at the epoch when the HI emission originated.

To summarize, the visibility-visibility cross-correlation (hereafter refereed to as the visibility correlation) directly probes the power spectrum of HI fluctuations at the epoch where the HI emission originated. This holds the possibility of allowing us to study the large scale structures at high redshifts. A point to note is that the visibility correlations at a baseline U receives contribution from the power spectrum only for Fourier mode $k > k_{\rm min} = (2\pi/r)U$, and for the CDM-like power spectrum most of the contribution comes from Fourier modes around $k_{\rm min}$. So, it may be said that the correlations at a baseline U probes the power spectrum at the Fourier mode $(2\pi/r)U$.

In the earlier work we treated the HI as being continuously distributed whereas in reality the HI resides in discrete gas clouds. In addition, it was assumed that the HI distribution is an unbiased representation of the underlying dark matter distribution, and we used the linear theory of density perturbations to follow the evolution of fluctuations in the dark matter distribution. It is these assumptions which allow us to express the power spectrum of fluctuations in the HI distribution in redshift space at the epoch when the HI emission originated (in equation 1) in terms of b the linear

bias parameter (taken to be 1), D the growing mode of linear density perturbations (Peebles 1980) at the epoch when the HI emission originated, $P(k)$ the present power spectrum of dark matter density fluctuations calculated using linear theory and the factor $\left[1+\beta\frac{k_\parallel^2}{k^2}\right]^2$ which takes the power spectrum from real space to redshift space in the linear theory of redshift distortions (Kaiser 1987) . Here we report progress on two counts. First, we have used a PM N-body code to evolve the fluctuations in the dark matter distribution, thereby incorporating possible non-linear effects. Second, we have assigned HI masses to the dark matter particles in the N-body code and this was used to simulate the redshifted HI emission. So we have also been able to incorporate the fact that the HI gas is contained in discrete clouds. The predictions for the HI signal expected at GMRT presented in this paper incorporate both these effects. We still retain the assumption that the HI is an unbiased tracer of the dark matter.

We next present a brief outline of this paper. In section 2 we discuss the method that was used to simulate the HI signal, and in section 3. we present the results of our investigations. In section 4 we discuss the results and present conclusions.

Finally, it should be pointed out that there have been alternative lines of approach investigating the possibility of using HI observations to study large scale structures at $z \sim 3$ (Sunyaev & Zeldovich 1975; Subramanian & Padmanabhan 1993; Kumar *et al.* 1995; Weinberg *et al.* 1996; Bagla *et al.* 1997; Bagla & White 2002). The reader is referred to Papers a and b for a detailed comparison of these approaches with that adopted here.

2. Methodology

We have simulated the visibility correlations expected at two of the GMRT observing frequency bands centered at $\nu_c = 610\,\mathrm{MHz}$ and $325\,\mathrm{MHz}$. The simulations were carried out in three steps:

- Using a PM N-body code to simulate the dark matter distribution at the redshift where the HI emission originated
- Assigning HI masses to the particles used in the N-body code and calculating the flux expected from each HI cloud
- Calculating the complex visibilities arising from the distribution of HI clouds and computing the visibility correlations.

We next discuss the salient features of each of these steps. The values $h = 0.7$, $\Omega_{m0} = 0.3$ and $\Omega_{\Lambda 0} = 0.7$ were used throughout.

2.1 *The N-body simulations*

We have used a Particle-Mesh (PM) N-body code to simulate the dark matter distribution at the redshift z where the HI emission originated. The simulation volume was a cubic box of comoving volume L^3. The size L was chosen so that it is approximately twice the comoving distance subtended by θ_{FWHM} of the GMRT primary beam.

The values of r the comoving distance to the region from where the HI emission originated, the grid spacing of the mesh ΔL, and the number of dark matter particles used in each simulation N_{DM} are all shown in table 1.

Table 1.

ν_c (MHz)	z	$\theta_{\rm FWHM}$	r (Mpc)	L (Mpc)	ΔL (Mpc)	$N_{\rm DM}$	$N_{\rm SIM}$	z_{in}
610	1.33	0.9°	4030	128	0.5	128^3	4	19
325	3.37	1.8°	6686	512	1	256^3	4	9

The initial power spectrum of dark matter density fluctuations at $z_{\rm in}$ (shown in table 1) is normalized to COBE (Bunn & White 1996), and its shape is determined using the analytic fitting form for the CDM power spectrum given by Efstathiou *et al.* (1992). The value of the shape parameter turns out to be $\Gamma = 0.2$ for the set of cosmological parameters used here. We have run the N-body code for $N_{\rm SIM}$ (table 1) independent realisations of the initial conditions and the final results for the visibility correlations were averaged over all the realisations.

The N-body code gives the final positions and peculiar velocities of the $N_{\rm DM}$ dark matter particles in the simulation. The power spectrum of the density fluctuations in the dark matter distribution at $z = 1.33$ and $z = 3.37$ is shown in Figs. 1 and 2 respectively. In both the figures we have shown the power spectrum for the range of Fourier modes which will make a significant contribution to the visibility correlation at the baselines where the signal is expected to be strongest. We find that at $z = 1.33$ (610 MHz) the power spectrum obtained from the N-body simulation shows

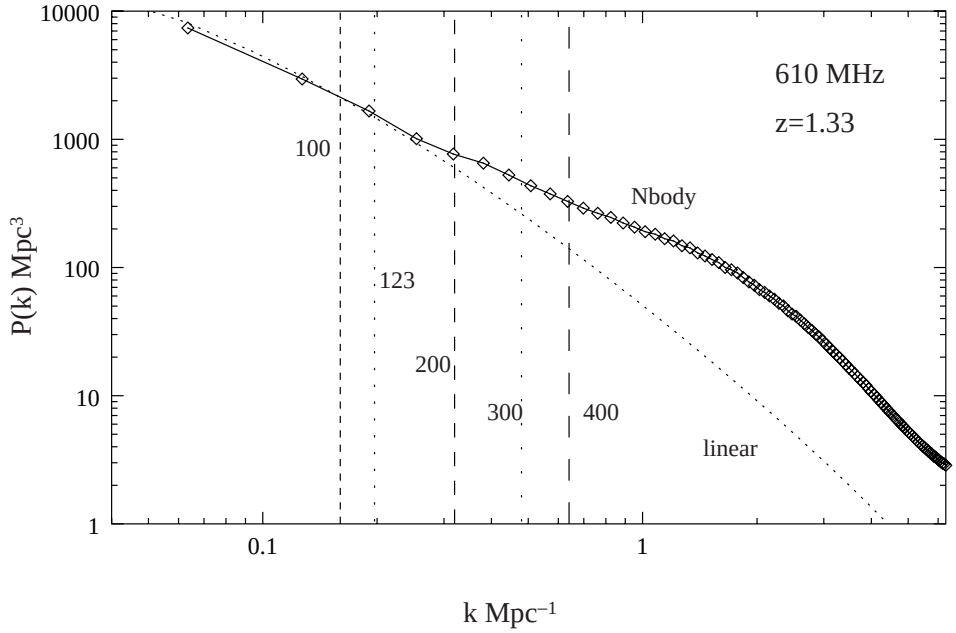

Figure 1. This shows the power spectrum of density fluctuations in the dark matter distribution at $z = 1.33$. The vertical lines show the smallest Fourier mode $k_{\rm min} = (2\pi/r)U$ which contributes to the visibility correlations at a baseline U. This is shown for the different values of U indicated in the figure.

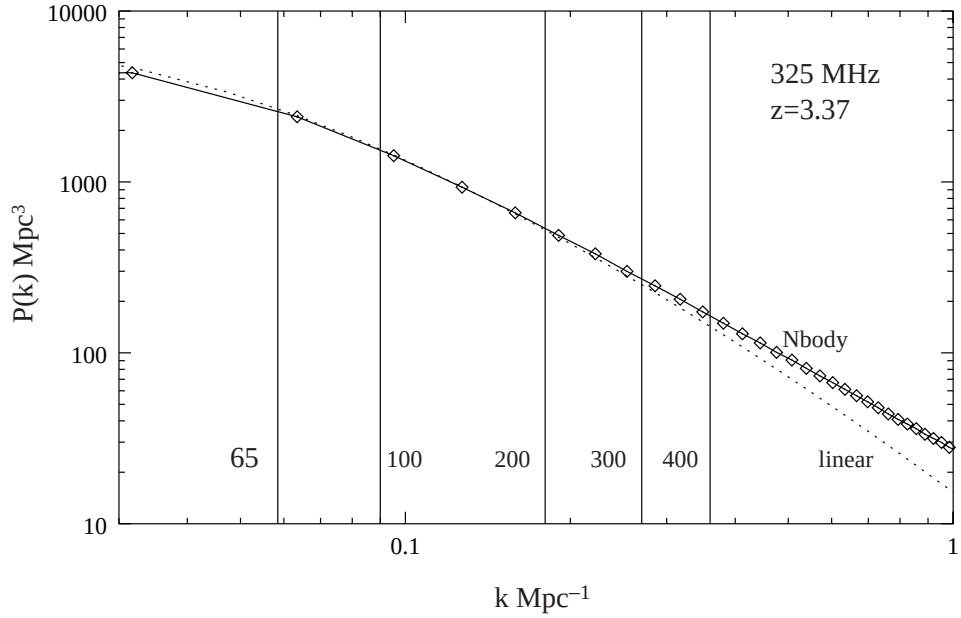

Figure 2. This is the same as Fig. 1 except that it is at $z = 3.37$ which corresponds to 325 MHz.

substantial differences from the power spectrum calculated using linear theory at Fourier modes $k \geq 0.3\,\mathrm{Mpc}^{-1}$. Converting to baselines, we expect non-linear effects to be important for $U \geq 200$. At $z = 3.37$ (325 MHz) there are differences between the N-body and linear power spectrum at $k \geq 0.3\,\mathrm{Mpc}^{-1}$, but the non-linear effects are not as pronounced as at 610 MHz. Converting to baselines, non-linear effects will influence the signal at baselines $U \geq 400$.

2.2 *Assigning HI masses*

We model the HI clouds as randomly oriented rotating disks of radius R, column density N_{HI} and rotation velocity V. The values of R and V are held fixed in each simulation, and we have run simulations with different sets of values for these parameters. It is assumed that the column densities have a power law distribution in the range $2 \times 10^{20} \leq N_{\mathrm{HI}}/(\mathrm{atoms/cm}^2) \leq 1 \times 10^{22}$ and the comoving number density of HI clouds with column densities in the interval dN_{HI} is $BN_{\mathrm{HI}}^{-\alpha}\,dN_{\mathrm{HI}}$. The total comoving number density of HI clouds at redshift z is

$$n_{\mathrm{HI}}^{c}(z) = B \int_{N_{\mathrm{HI}}[\mathrm{min}]}^{N_{\mathrm{HI}}[\mathrm{max}]} N_{\mathrm{HI}}^{-\alpha}\,dN_{\mathrm{HI}} \tag{2}$$

and the comoving mass density is

$$\rho_{\mathrm{HI}}^{c}(z) = B \int_{N_{\mathrm{HI}}[\mathrm{min}]}^{N_{\mathrm{HI}}[\mathrm{max}]} (\pi R^2 N_{\mathrm{HI}} m_{\mathrm{HI}}) N_{\mathrm{HI}}^{-\alpha}\,dN_{\mathrm{HI}}, \tag{3}$$

where $m_{\rm HI}$ is the mass of the hydrogen atom. The normalisation coefficient B is determined by using equation (3) to calculate $\Omega_{\rm gas}(z)$

$$\Omega_{\rm gas}(z) = \frac{4}{3}\Omega_{\rm HI}(z) = \frac{4}{3}\frac{8\pi G}{3H_0^2}\rho^c_{\rm HI}(z). \tag{4}$$

We use $\Omega_{\rm gas} = 10^{-3}$ in all the simulations.

This model fixes the total number of HI clouds in the simulation volume $N_{\rm clouds} = L^3 n^c_{\rm HI}(z)$. The total number of clouds scale as

$$N_{\rm clouds} \propto \frac{1-\alpha}{2-\alpha}R^{-2}, \tag{5}$$

as we vary α the slope of the column density distribution or the radius of the clouds R. For large values of R the HI is distributed in a few clouds with large masses, whereas there are many clouds with low HI masses when R is small. Our model has three free parameters, namely α, R and V. We have run simulations varying α and R (table 2) for $V = 100\,{\rm km/s}$ and $200\,{\rm km/s}$.

We randomly select $N_{\rm clouds}$ particles from the output of the N-body simulation and these are identified as HI clouds. The HI mass of each cloud is $M_{\rm HI} = \pi R^2 N_{\rm HI} m_{\rm HI}$, where the column density is drawn randomly from the power-law distribution discussed earlier. The center of the simulation volume is aligned with the center of the GMRT primary beam and it is located at a comoving distance corresponding to the redshift z. The comoving distance to each cloud is used to calculate its angular position and redshift. The redshift is used to determine the luminosity distance which is used to calculate the flux from the individual clouds. The effect of the peculiar velocity is incorporated when calculating ν_o the frequency at which the HI emission from each

Table 2.

ν_c (MHz)	α	R Kpc	$n^c_{\rm HI}(z)$ Mpc^{-3}	$N_{\rm clouds}$
610	1.2	10	2.0×10^{-2}	42467
610	1.2	8	3.2×10^{-2}	66354
610	1.2	5	8.1×10^{-2}	169865
610	1.2	2	5.1×10^{-1}	1061651
610	1.7	10	3.7×10^{-2}	76764
610	1.7	8	5.7×10^{-2}	119943
610	1.7	5	1.5×10^{-1}	307055
610	1.7	2	9.2×10^{-1}	1919088
325	0.8	10	1.3×10^{-2}	1799234
325	1.2	10	2.0×10^{-2}	2717825
325	1.2	8	3.2×10^{-2}	4246602
325	1.2	5	8.1×10^{-2}	10871300

cloud is received. The line width $\Delta\nu$ of the HI emission line from each cloud is calculated using $\Delta\nu = \mid \sin\theta \mid 2\nu_o V/c$, where $2\nu_o V/c$ is the line width if the disk of the galaxy were viewed edge on and θ is the angle between the normal to the disk and the line of sight.

To summarize, at the end of this stage of the simulation we have $N_{\rm clouds}$ HI clouds. For each cloud we have its angular position $\vec{\theta}^a$,and the flux density F^a, frequency ν_o^a and line-width $\Delta\nu^a$ of the redshifted HI emission. Here the index a ($1 \leq a \leq N_{\rm clouds}$) refers to the different clouds in the simulation.

2.3 *Calculating visibility correlations*

We first describe how we have calculated the complex visibilities that would be measured in GMRT radio observations of the HI distribution generated in the simulation. The observations are carried out at NC frequency channels $\{\nu_1, \nu_2, \nu_3, \ldots, \nu_{NC}\}$ covering a frequency band B centered at the frequency ν_c. We have used $B = 8$ MHz and $NC = 64$ at $\nu_c = 610$ MHz, and $B = 8$ MHz and $NC = 128$ at $\nu_c = 325$ MHz.

For the purpose of this paper we assume that the antennas are distributed on a plane, and that they all point vertically upwards. The beam pattern $A(\vec{\theta})$ quantifies how the individual antenna, pointing upwards, responds to signals from different directions in the sky. This is assumed to be a Gaussian $A(\vec{\theta}) = e^{-\theta^2/\theta_0^2}$ where $\theta_0 = 0.6 \times \theta_{\rm FWHM}$ (table 1).

The position of each antenna can be denoted by a two dimensional vector $\mathbf{d}_i$. The quantity measured in interferometric observations is the visibility $V(\mathbf{U}, \nu)$ which is recorded for every independent pair of antennas (baseline) at every frequency channel in the band. For any pair of antennas, the visibility depends on the vector $\mathbf{d} = \mathbf{d}_i - \mathbf{d}_j$ joining the position of the two antennas. It is convenient to express the visibility as a function of the variable $\mathbf{U}$ which is $\mathbf{d}$ expressed in units of the wavelength i.e., $\mathbf{U} = \mathbf{d}/\lambda$. The signal arising from the clustering pattern of the HI clouds will be strongest at the small baselines, and our calculations have been limited to this. We have considered a square grid of baselines extending from $-U_{\rm max}$ to $U_{\rm max}$ with resolution δU. We have used $U_{\rm max} = 400$ and $\delta U = 10$. The complex visibility has been calculated for each baseline $\mathbf{U}$ on the grid using

$$V(\mathbf{U}, \nu) = \sum_{a=1}^{N_{\rm clouds}} A(\vec{\theta}^a)\, F^a e^{-i2\pi \mathbf{U}\cdot\vec{\theta}^a}\, O\left(\frac{\mid \nu - \nu_o^a \mid}{\Delta\nu^a}\right), \tag{6}$$

where the function $O(x)$ is defined such that $O(x) = 1$ for $x \leq 1$, else $O(x) = 0$. It is to be noted that in an actual GMRT observation the baselines will have a complicated distribution depending on which part of the sky is observed and the duration of the observation. Given the fact that the signal we are interested in is statistical in nature, and that we are interested in making generic predictions about the signal expected in a typical GMRT observation, a square grid of baselines is adequate.

The final step in the simulation is to calculate the visibility correlation $\langle V(\mathbf{U}, \nu) V^*(\mathbf{U}, \nu + \Delta\nu)\rangle$. The angular brackets $\langle\rangle$ indicate the ensemble average, and we have averaged over the $N_{\rm SIM}$ different realisation of the N-body simulation. In addition, the correlation depends only on the separation in frequency $\mid \Delta\nu \mid$, and the magnitude $U = \mid \mathbf{U} \mid$. So, for a fixed value of $\Delta\nu$ and U we have averaged over all possible pairs of frequencies and baselines which match these values.

The analytic calculations (Papers b and c) where the HI is assumed to have a continuous distribution, predict the imaginary part of the visibility correlation function to be zero, and the clustering signal is manifest in only the real part. In the simulations we get a very small, but non-zero imaginary component. This is not discussed in the rest of the paper where we present results for the real component only.

3. Results

In this section we present results for the visibility correlation as obtained from our simulations. We compare these with the analytic predictions of Papers b and c and investigate the effect of two factors:

(1) the non-linear evolution of the density fluctuations, and
(2) the discrete nature of the HI distribution.

To get a better understanding of the second effect, we present results varying the parameters of the HI distribution.

3.1 *610 MHz*

Figure 3 shows the visibility correlations for $U = 100$, the results at smaller baselines show a similar behaviour. The visibility correlation at the baseline $U = 100$ receives

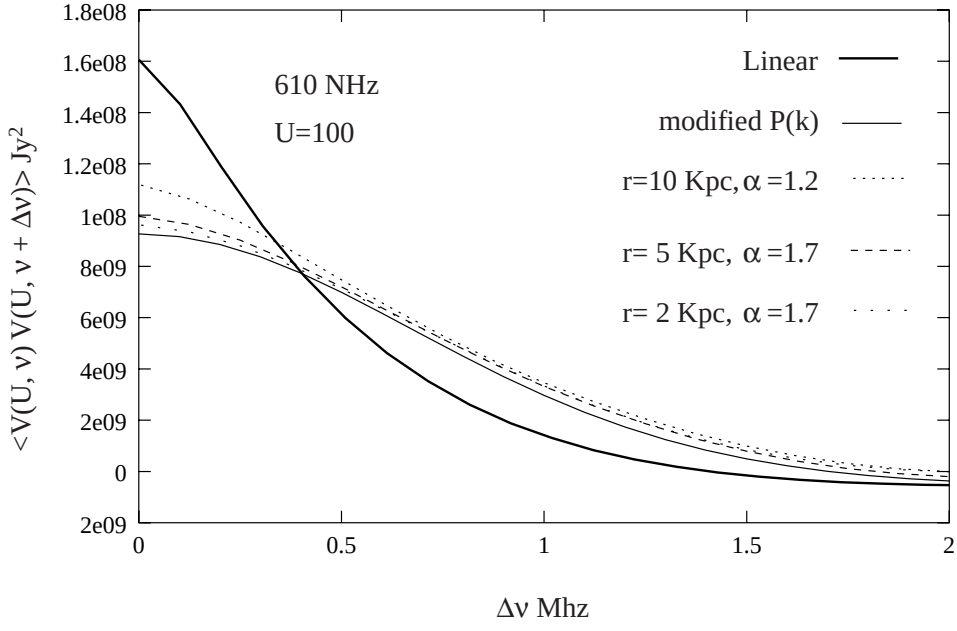

Figure 3. This shows the correlation expected between the visibilities $V(\mathbf{U}, \nu)$ and $V(\mathbf{U}, \nu + \Delta\nu)$ at the same baselines at two different frequencies. The rotational velocity of the HI disk is assumed to be $V = 200\,\mathrm{km/s}$. The other parameters of the HI distribution take on values shown in the figure. These results are for the 610 MHz band.

contributions mainly from Fourier modes around $k \sim 0.2\,\mathrm{Mpc}^{-1}$ which is in the linear regime (Fig. 1), and we expect a good agreement with the analytic, linear predictions. We find that for $\Delta\nu < 0.5$MHz the analytic predictions are larger than the correlations obtained in the simulations, and this is reversed for $\Delta\nu > 0.5$ MHz. This discrepancy can be explained if we take into account the fact that visibility correlation actually responds to the clustering in redshift space. It is known (e.g., Suto & Suginohara 1991; Graman *et al.* 1993; Fisher *et al.* 1994; Brainerd *et al.* 1996; Bromley *et al.* 1997) that non-linear effects can be important in redshift space even on scales where the clustering in real space is well described by linear perturbation theory. It has been shown that this can be modeled by taking into account the effect of the random motions along the line of sight (e.g., Fisher *et al.* 1994; Peacock & Dodds 1994; Ballinger *et al.* 1996). We incorporate this by multiplying the power spectrum with $\exp[-k_\parallel^2\sigma^2]$ in our analytic formulas for the visibility correlation. This gives the modified formula

$$\langle V(\mathbf{U},\nu)V^*(\mathbf{U},\nu+\Delta\nu)\rangle = \frac{[\bar{I}bD\theta_0]^2}{2r^2}\int_0^\infty dk_\parallel P(k)\left[1+\beta\frac{k_\parallel^2}{k^2}\right]^2 \times \exp[-k_\parallel^2\sigma^2]\cos(k_\parallel r'\,\Delta\nu) \tag{7}$$

for the visibility correlation. We find that for $\sigma = 200\,\mathrm{km/s}/H_0$ this gives a good fit to the results of the simulations, and this is also shown in the figure. We next shift our attention to how the results depend on the parameters of the HI distribution. We find that for $r = 10$ Kpc where the bulk of the HI is distributed in a few clouds with large HI masses the results show a 20% increment at small values of $\Delta\nu$ compared to the models with smaller values of r. This excess correlation at small $\Delta\nu$ arises from the fact that the HI emission from an individual cloud will be spread across a width $\delta\nu$ in frequency. The correlation between the HI emission from the same HI cloud at two different frequencies will contribute to the visibility correlations when $\Delta\nu \leq \delta\nu$. The contribution from this signal is significant in comparison to that arising from the clustering of the HI clouds when the total HI is distributed in a few clouds with large HI masses each. The contribution to the visibility correlation from within individual HI clouds goes down as r is reduced and the HI is distributed among many clouds each with small HI masses. There is very little difference between the results for $r = 5$ Kpc and 2 Kpc and we may treat this as the result if the HI were continuously distributed.

The results in Fig. 3 are for the rotational velocity $V = 200$ km/s. We have also done simulations using $V = 100$ km/s. We find that there are differences ($< 20\%$) only at small values of $\Delta\nu$. The effect of decreasing V is to decrease the frequency width of the HI emission line from individual clouds which results in a higher value of the HI flux density. This does not effect the clustering signal but enhances the contribution to the visibility correlation arising from the emission of a single HI cloud. As changing V does not affect the results very much, in this subsection we show the results for $V = 200$ km/s only.

Figure 4 shows the results for $U = 300$. We find that the discrepancy between the linear, analytic predictions and the results of our simulations increases at larger values of U. Except at very small values of $\Delta\nu$, the simulated values are larger than the linear predictions. This is because the larger baselines probe smaller length scales

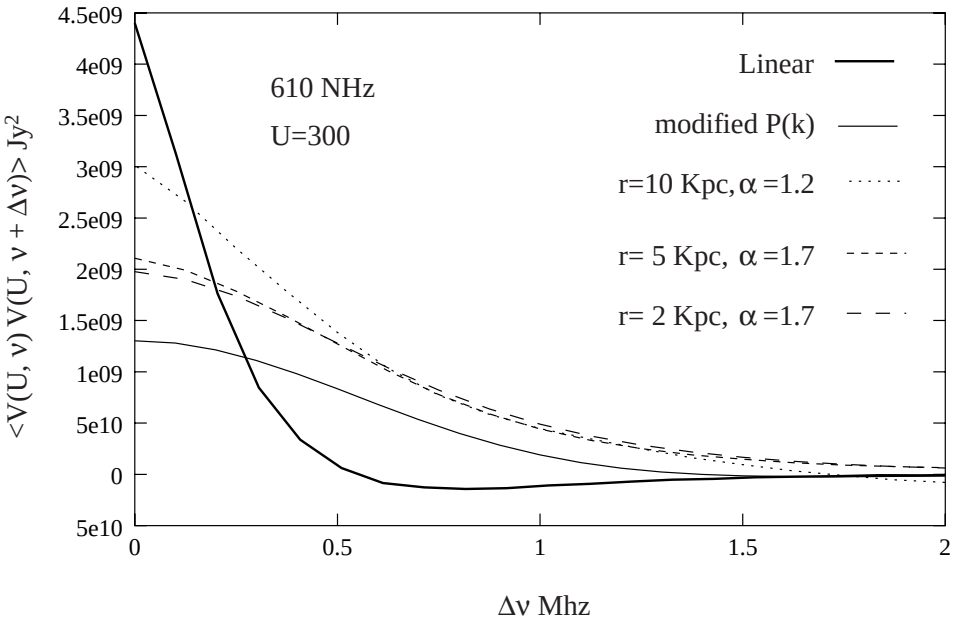

Figure 4. This is the same as Fig. 3 except that it shows results for $U = 300$.

which are significantly nonlinear (figure 1) and the amplitude of the fluctuations is larger than predicted by linear theory. At smaller scales the fluctuations are non-linear even in real space, and the modified formula (equation 7) based on only redshift space considerations grossly underestimates the visibility correlations. An important point is that at larger values of U the visibility correlations calculated in the simulations do not fall as sharply with increasing $\Delta\nu$ as predicted in the linear calculations. In Paper c we found that the visibility correlations decay as $\propto \exp[-\Delta\nu/K]$, where the decay constant varies as $K \propto U^{-0.8}$ i.e., the decay is faster at larger baselines. Our simulations show that the decay with increasing $\Delta\nu$ is slower than predicted using linear theory. This is a consequence of the fact that the density fluctuations are non-linear on the length-scales being probed at these baselines. Another point to note is that the dependence on the parameters R and α, becomes relatively more pronounced at large values of U.

3.2 *325 MHz*

A point which should be mentioned right at the start is that at 325 MHz we are restricted in the values of R for which we are able to carry out simulations. At 325 MHz the simulation volume is pretty large (table 1) and for $R = 2$ Kpc the total number of HI clouds in the simulation volume becomes too large for our computational resources. Also, in this subsection we use $V = 100$ km/s in our simulations. Figure 5 shows the results for the visibility correlations at $U = 100$. The behaviour at smaller baselines is not very different. We find that for $\Delta\nu < 1$ MHz the predictions of the analytic, linear calculations (Paper c) are very close to the values obtained in the simulation

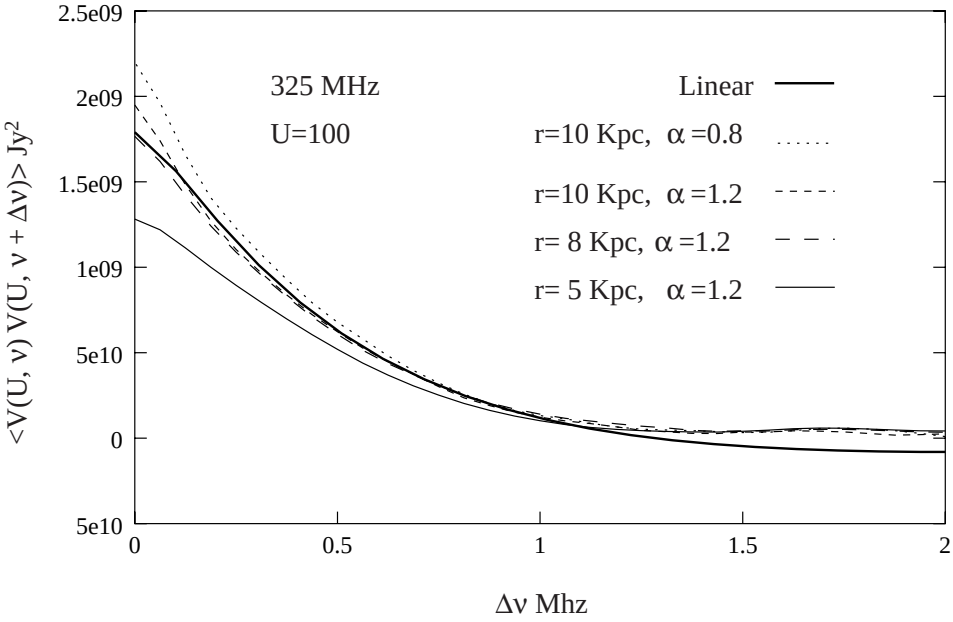

Figure 5. This shows the expected correlation between the visibilities $V(\mathbf{U}, \nu)$ and $V(\mathbf{U}, \nu + \Delta\nu)$ at the same baselines at two different frequencies. The rotational velocity of the HI disk is assumed to be $V = 100\,\mathrm{km/s}$. The other parameters of the HI distribution take on values shown in the figure. These results are for the 325 MHz band.

for $r = 8$ Kpc and $\alpha = 1.2$. The results of the simulation are slightly larger than the analytic predictions when $r = 10$ Kpc, and they are somewhat smaller than the analytic predictions at $r = 5$ Kpc. For $\Delta\nu > 1$ MHz the results of the simulation are the same for all the parameters, and the value is slightly more than the analytic prediction. The power spectrum (Fig. 2) is in the linear regime at the Fourier modes which contribute to the visibility correlations at $U = 100$. The discrepancy between the analytic predictions and the results of our simulations can be attributed to a combination of the two factors discussed earlier:

(1) the effect of random motions on the redshift space clustering and
(2) correlations between the HI emission from the same cloud at different frequency channels.

Figure 6 shows the visibility correlations at $U = 400$. We find that the behaviour of the visibility correlations does not change very much for baselines in the range $100 < U \leq 400$. The power spectrum (Fig. 2) starts getting non-linear at Fourier modes corresponding to $U = 400$, but the effect is not very significant.

4. Discussion and conclusions

We take up for discussion two issues pertaining to the way we have modeled the distribution of HI clouds. First is our assumption that the HI clouds responsible for damped Lyman-α absorption lines are rotating disks, all with the same radius and

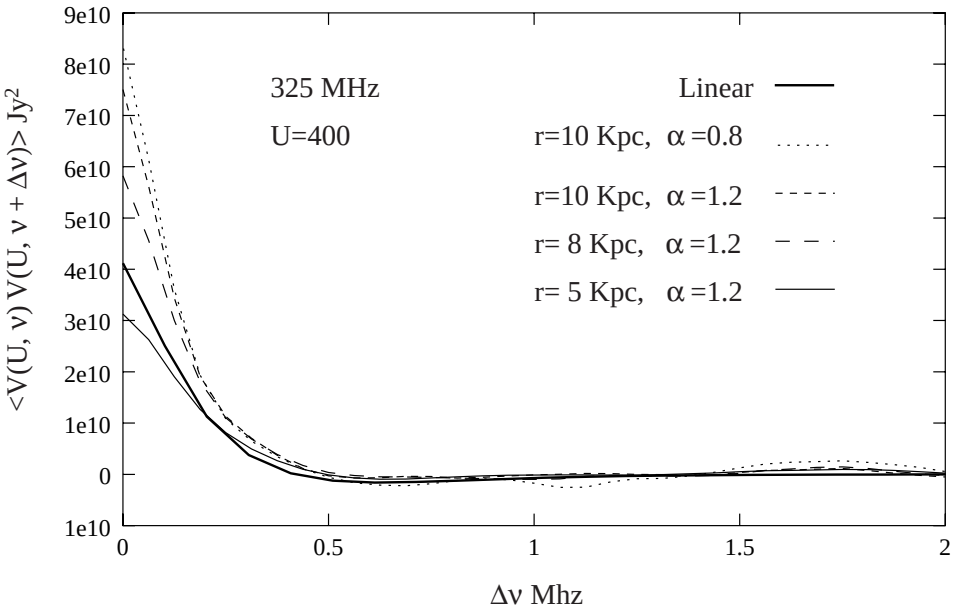

Figure 6. This is the same as Fig. 5 except that it shows results for $U = 400$.

rotational velocity. Prochaska and Wolfe (1998) have proposed that these HI clouds are the gaseous progenitors of present day galaxies. They have attempted to explain the observed kinematic of the damped Lyman-α absorption lines using a thick, rotating disk model for the HI clouds. Another model (Haehnelt *et al.* 1998) proposes that the observations could be better explained by modeling the absorption systems as protogalactic gas clumps undergoing merger. The second issue is our assumption that the HI column densities have a power law distribution and our choice of the value of the index α. Lanzetta *et al.*(1991) show that the column density distribution at $z \simeq 2.5$ can be described by a power law with $\alpha \simeq 1.7$. In a later paper Lanzetta *et al.* (1995) show that the column density distribution evolves quite strongly with redshift, there being a tendency toward more high column density clouds at higher redshifts. In our work we have run simulations for two values of the index i.e., $\alpha = 1.2$ and 1.7. Having very briefly reviewed some of the prevalent views and having compared our assumptions with them, we note that our simulations seem to indicate that the visibility correlation signal does not depend very critically on the details of the properties of the HI clouds. We find that the visibility correlation signal has contribution from mainly two effects:

(1) correlations caused by the emission from the same cloud to different frequency channels, and
(2) the clustering of the clouds in redshift space.

The first effect is seen in the correlation at small values of $\Delta\nu$, where $\Delta\nu$ is smaller than the width of the HI line from an individual cloud. This effect manifests itself as a rise in the visibility correlations at small values of $\Delta\nu$ (< 0.5MHz). This effect is enhanced if the HI is distributed in a few clouds with large HI masses as compared to

the situation where the HI is in many small clouds with low HI masses. This seems to be the only effect of the fact that the HI is distributed in discrete HI clouds and is not continuously distributed. This is also the only place where the details of the HI distribution affects the visibility correlation.

We next turn our attention to the contribution to the visibility correlation signal from the clustering of the HI clouds. We may take the results for the visibility correlations at the values of the parameters R and α where $N_{\rm clouds}$ is maximum as representing the results when the discrete nature of the HI distribution can be neglected (continuum limit). This assumption is justified at 610 MHz where there is very little difference in the results between $R = 5$ Kpc and $R = 2$ Kpc. We have not carried out simulations for $R < 5$ Kpc at 325 MHz, and simulations with smaller values of R are needed at this frequency before we can be sure that the results for $R = 5$ Kpc really represent the continuum limit. Let us first discuss the results at the baselines for which the visibility correlation probes the power spectrum at length-scales which are in the linear regime. This is true for baselines with $U \leq 100$ at 610 MHz (Fig. 1). At 325 MHz most of the baselines which we have studied probe the power spectrum in the linear regime (Fig. 2). For all these baselines we find that the simulated values are less than the predictions of linear theory at small $\Delta\nu$ and the simulated values are larger than the linear predictions at large $\Delta\nu$. The transition occurs in the range $\Delta\nu \sim 0.5 - 1$ MHz. We propose that this discrepancy is a consequence of the fact that the fluctuations in the HI distribution in redshift space may be non-linear even on length-scales where linear theory holds in real space. This can be modeled by incorporating the effect of random peculiar velocities on the redshift space HI distribution. We show that including this effect gives a good fit to the simulated results at $U = 100$ for 610 MHz. At larger baselines the visibility correlation probes the power spectrum on length-scales where it is non-linear. Non-linear effects start influencing the visibility correlation at baselines $U \geq 200$ for 610 MHz, and these effects are very significant by $U = 400$. As a consequence of these effects the simulated visibility correlations do not fall off with increasing $\Delta\nu$ as quickly as predicted by linear theory. Also, the simulated values are larger than the linear predictions everywhere except at very small values of $\Delta\nu$. The range of $\Delta\nu$ where the simulated values are less than the linear predictions decreases with increasing U.

In conclusion we note that the HI signal predicted by our simulations are not drastically different from the analytic predictions presented earlier. In this paper we have been able to address the effects of the discrete nature of the HI distribution and the non-linear nature of the HI fluctuations in redshift space. We now have the tools necessary to simulate the HI signal expected at the GMRT. A full simulation of a GMRT observation requires us to also include the system noise as well as various galactic and extragalactic radio sources. Only then will we be able to make definite predictions as to whether it will be possible to detect the HI signal or not. Work is currently underway on this. The preliminary results indicate that it will be possible to have a 5σ detection at 610 MHz with one thousand hours of observation.

Acknowledgement

S. B. would like to thank Jasjeet S Bagla, Jayaram N Chengalur and Shiv K Sethi for useful discussions. S. B. would also like to acknowledge BRNS, DAE, Govt. of India, for financial support through sanction No. 2002/37/25/BRNS.

References

Bagla, J. S., Nath, B., Padmanabhan, T. 1997, *MNRAS*, **289**, 671.
Bagla, J. S., White, M. 2002, astro-ph/0212228.
Ballinger, W. E., Peacock, J. A., Heavens, A. F. 1996, *MNRAS*, **282**, 877.
Bharadwaj, S., Nath, B., Sethi, S. K. 2001, *JAA*, **22**, 21.
Bharadwaj, S., Sethi, S. K. 2001, *JAA*, **22**, 293.
Bharadwaj, S., Pandey, S. K. 2003, *JAA*, **24**, 23.
Brainerd, T. G., Bromley, B. C., Warren, M. S., Zurek, W. H. 1996, *Ap. J.*, **464**, L103.
Bromley, B. C., Warren, M. S., Zurek, W. H. 1997, *Ap. J.*, **475**, 414.
Bunn, E. F., White, M. 1996, *Ap. J.*, **460**, 1071.
Efstathiou, G., Bond, J. R., White, S. D. M. 1992, *MNRAS*, **250**, 1p.
Fisher, K. B., Davis, M., Strauss, M. A., Yahil, A., Huchra, J. P. 1994, *MNRAS*, **267**, 927.
Haehnelt, M. G., Steinmetz, M., Rauch, M. 1998, *Ap. J.*, **495**, 647.
Kaiser, N. 1987, *MNRAS*, **227**, 1.
Kumar, A., Padmanabhan, T., Subramanian, K. 1995, *MNRAS*, **272**, 544.
Lanzetta, K. M., Wolfe, A. M., Turnshek, D. A., Lu, L. 1991, *Ap. JS.*, **77**, 1.
Lanzetta, K. M., Wolfe, A. M., Turnshek, D. A. 1995, *Ap. J.*, **430**, 435.
Peacock, J. A., Dodds, S. J. 1994, *MNRAS*, **267**, 1020.
Peebles, P. J. E. 1980, *The Large-Scale Structure of the Universe*, (Princeton: Princeton University Press)
Péroux, C., McMahon, R. G., Storrie-Lombardi, L. J., Irwin, M. J. 2001, *MNRAS*, **346**, 1103.
Prochask, J. X., Wolfe, A. M. 1998, *Ap. J.*, **507**, 113.
Saini, T., Bharadwaj, S., Sethi, K. S. 2001, *Ap. J.*, **557**, 421.
Storrie–Lombardi, L. J., McMahon, R. G., Irwin, M. J. 1996, *MNRAS*, **283**, L79.
Subramanian, K., Padmanabhan, T. 1993, *MNRAS*, **265**, 101.
Sunyaev, R. A., Zeldovich, Ya. B. 1975, *MNRAS*, **171**, 375.
Suto, Y., Suginohara, T. 1991, *ApJL*, **370**, L15.
Swarup, G., Ananthakrishan, S., Kapahi, V. K., Rao, A. P., Subrahmanya, C. R., Kulkarni, V. K. 1991, *Curr. Sci.*, **60**, 95.
Weinberg, D. H., Hernquist, L., Katz, N. S., Miralda-Escude, J. 1996, *Cold Gas at High Redshift* (eds.) M Bremer, H Rottgering, C Carilli and P van de Werf, (Dordrecht: Kluwer)

J. Astrophys. Astr. (2004) **25,** 81–91

Angular Momentum Transport in Quasi-Keplerian Accretion Disks

Prasad Subramanian,[1] B. S. Pujari[2] & Peter A. Becker[3]
[1]*Inter-University Center for Astronomy and Astrophysics, P.O Bag 4, Ganeshkhind, Pune 411 007, India.*
e-mail: psubrama@iucaa.ernet.in
[2]*Dept. of Physics, University of Pune, Pune 411 007, India.*
e-mail: bspujari@rediffmail.com
[3]*School of Computational Sciences, George Mason University, Fairfax, VA 22030, USA.*
e-mail: pbecker@gmu.edu

Received 2003 May 9; accepted 2004 March 16

Abstract. We reexamine arguments advanced by Hayashi & Matsuda (2001), who claim that several simple, physically motivated derivations based on mean free path theory for calculating the viscous torque in a quasi-Keplerian accretion disk yield results that are inconsistent with the generally accepted model. If correct, the ideas proposed by Hayashi & Matsuda would radically alter our understanding of the nature of the angular momentum transport in the disk, which is a central feature of accretion disk theory. However, in this paper we point out several fallacies in their arguments and show that there indeed exists a simple derivation based on mean free path theory that yields an expression for the viscous torque that is proportional to the radial derivative of the angular velocity in the accretion disk, as expected. The derivation is based on the analysis of the epicyclic motion of gas parcels in adjacent eddies in the disk.

Key words. Accretion—viscosity, disks, angular momentum.

1. Introduction

Accretion disks around a central compact object are ubiquitous in astrophysics. In such systems, the plasma accreting onto the central object typically takes the form of a swirling disk. The disk-like nature of accretion is due to the angular momentum originally carried by the accreting material, and also to the spin of the central object, which provides a preferred axis of rotation. At a given radius in a quasi-Keplerian accretion disk, the average motion of the gas parcels is an approximately circular Keplerian orbit, combined with a radial sinking motion as the parcel gradually moves deeper into the potential well of the central mass. The radial velocity is far smaller than the Keplerian (azimuthal) velocity. A detailed description of quasi-Keplerian accretion disks can be found in Pringle (1981), among several other references.

The specific angular momentum (angular momentum per unit mass) carried by a parcel of gas in a quasi-Keplerian accretion disk is very close to the Keplerian value $\sqrt{GMR}$, where R is the radius measured from the central object with mass M. It

follows that a parcel of plasma has to lose angular momentum in order to sink from a larger orbit into a smaller one and eventually cross the event horizon. In the absence of strong winds or jets, the angular momentum must therefore flow *outwards* in such an accretion disk in order to enable accretion to proceed. In disks of turbulent fluid, the flow of angular momentum is due to the exchange of plasma parcels in neighboring annuli with different angular velocities. This fluid picture may describe certain astrophysical cases such as the rings of Saturn, but in many other cases of astrophysical interest, the coupling between adjacent annuli is provided not by "parcel interchange," but rather by the magnetic field. In either the fluid or magnetohydrodynamical (MHD) scenarios, the angular momentum flow is expressed as a torque between neighboring annuli. Our focus here is on the fluid picture, and on the validity of the various attempts to analyze quantitatively the angular momentum transport associated with the interchange of parcels.

There are several previous papers in which derivations of the viscous torque in fluid dynamical situations are developed based on simple, physically motivated arguments (e.g., Frank et al. 1985, 1992, 2002; Hartmann 1998). However, some of these do not yield an expression for the viscous torque that is proportional to the radial derivative of the angular velocity. This is a problem because the viscosity is fundamentally due to the "rubbing" of matter in adjacent radial annuli in the disk, and consequently the viscosity should *vanish* in the case of solid body rotation with $\Omega(R) =$ constant, where $\Omega(R)$ is the angular velocity in the disk at radius R. Hayashi & Matsuda (2001; hereafter HM) recognized this point, and attempted to clear up some of the confusion by carefully examining the previously published derivations of the viscosity that were based on the mean free path approach. They concluded that the mean free path approach inevitably leads to an inward rather than outward flow of angular momentum in the disk, which is unphysical. However, we argue that the reasoning of HM was flawed because they did not consider the epicyclic nature of the parcel trajectories. We present a simple derivation based on mean free path theory, combined with the actual epicyclic motion of the gas parcels, that in fact yields a physically reasonable expression for the viscous torque between neighboring annuli in a quasi-Keplerian accretion disk.

We discuss the standard fluid dynamical formulation of viscous torques in an accretion disk in section 2. We then discuss the problems with the various previous derivations that attempted to utilize a mean free path approach to compute the viscous torque in section 3. In section 4 we present a simple physical derivation based on analysis of the epicyclic (ballistic) motion of gas parcels in adjacent eddies, and we demonstrate that this approach yields the expected form for the torque in terms of the gradient of the angular velocity. We present our final conclusions in Section 5.

2. Standard fluid dynamics treatment of viscous torque

The equation of motion for a viscous, incompressible fluid can be written as (Landau & Lifshitz 1987)

$$\frac{\partial \vec{v}}{\partial t} + (\vec{v} \cdot \vec{\nabla})\, \vec{v} = \frac{\vec{F}}{\rho}, \tag{1}$$

where the force density $\vec{F}$ is defined via the viscous stress tensor σ_{ik} as follows:

$$F_i = \frac{\partial\, \sigma_{ik}}{\partial\, x_k},$$
$$\sigma_{ik} = -p\,\delta_{ik} + \eta\left(\frac{\partial\, v_i}{\partial\, x_k} + \frac{\partial\, v_k}{\partial\, x_i}\right). \tag{2}$$

The fluid velocity is denoted by $\vec{v}$ and its density and pressure by ρ and p, respectively. The coefficient of dynamic viscosity (g cm^{-1}s^{-1} in cgs units) is denoted by η and we have used the Einstein summation convention in equation (2). For the special case of a thin, azimuthally symmetric accretion disk, the only non-negligible component of the viscous stress tensor in cylindrical coordinates (R, ϕ, z) is

$$\sigma_{R\,\phi} = -\eta\, R\, \frac{\partial\, \Omega}{\partial R}. \tag{3}$$

The viscous stress (force per unit area) is thus directly proportional to the radial derivative of the angular velocity. This is by far the cleanest and most rigorous way to derive the azimuthal equation of motion for a quasi-Keplerian accretion disk (see, for example, chapter 1 of Subramanian 1997). It is implicitly assumed that the dynamic viscosity η arises out of local effects, i.e., due to momentum exchange between neighboring annuli of the accretion disk, as with molecular viscosity. It is well known (Shakura & Sunyaev 1973; Pringle 1981) that molecular viscosity is far too small to account for angular momentum transport in accretion disks around active galactic nuclei. Identifying suitable candidates for the microphysical viscosity mechanism operative in such disks is a subject of intensive research.

3. Simplified treatments of viscous torque in accretion disks

Pringle (1981) derived the azimuthal component of the equation of motion in accretion disks starting from first principles in a simple, physically motivated manner. The equation reads as follows:

$$\frac{\partial\, (\Sigma\, R^3\, \Omega)}{\partial\, t} + \frac{\partial\, (\Sigma\, v_{_R}\, R^3\, \Omega)}{\partial\, R} = -\frac{1}{2\pi}\frac{\partial \mathcal{G}}{\partial R}, \tag{4}$$

where Σ is the surface density of plasma in the disk, $v_{_R} < 0$ is the radial accretion velocity, and $\mathcal{G} > 0$ is the torque exerted by the material inside radius R on the material outside that radius. Throughout the remainder of the paper, we shall assume that the disk has a steady-state (time-independent) stucture, although this is not essential for our results. In the standard approach introduced by Shakura & Sunyaev (1973) and adopted by Pringle (1981), the torque $\mathcal{G}$ is related to Ω via

$$\mathcal{G} = 4\pi\, R^2 H \sigma_{R\,\phi} = -2\pi\, R^3 \Sigma\, \nu \frac{\mathrm{d}\Omega}{\mathrm{d}R}, \tag{5}$$

where $H(R)$ is the half-thickness of the disk at radius R and $\nu = \eta/\rho$ is the kinematic viscosity coefficient. The stress and torque are therefore proportional to $\mathrm{d}\Omega/\mathrm{d}R$, in

agreement with equation (3). This prescription has been applied in many disk stucture calculations. In particular, it has been shown recently (Becker & Le 2003) that fully relativistic and self-consistent models for hot, advection-dominated accretion disks can be constructed by applying the Shakura-Sunyaev viscosity prescription throughout the entire disk, including the region close to the event horizon.

A number of authors have attempted to confirm the general form of equation (5) by using simple physical arguments. However, several of these derivations have errors in them, and they do not always result in an expression for $\mathcal{G}$ that is proportional to $\mathrm{d}\Omega/\mathrm{d}R$, as pointed out by HM. We briefly review the relevant derivations below, and we also point out errors in the approach adopted by HM. We then present a new, heuristic derivation of equation (5) that is based on a careful analysis of the ballistic motion of two parcels as they exchange radii. This derivation leads to the expected conclusion that $\mathcal{G} \propto \mathrm{d}\Omega/\mathrm{d}R$.

Although the argument given by HM is rather indirect, their main point can be understood through a simple examination of the angular momentum transport resulting from the interchange of fluid elements in a disk that is rotating as a solid body, i.e., with $\Omega(R) = \Omega_0 =$ constant. In this case, the angular momentum per unit mass, denoted by $J \equiv R^2\,\Omega(R)$, is given by $J = R^2\,\Omega_0$, and this quantity increases rather strongly as a function of the radius R. Hence if two parcels of fluid on opposite sides of radius R were exchanged due to some turbulent or convective process, then clearly angular momentum would be transported in the *inward* direction, since the blob that was originally outside the annulus will have more angular momentum than the interior blob. However, this result is unphysical, because in the case of solid body rotation, there is no "rubbing" between adjacent fluid annuli, and therefore there should be no torque and no angular momentum transport. Any successful microphysical model for the angular momentum transport in the disk based on mean free path theory must somehow resolve this apparent paradox. In the following sections, we provide a detailed consideration of the reasoning employed in the previous published derivations, including that of HM, and we conclude that when properly carried out, the mean free path approach can yield a result for the viscous torque that correctly vanishes in the case of solid body rotation.

3.1 *Derivation of $\mathcal{G}$ by Hartmann (1998)*

The specific angular momentum $J_{\rm in}$ carried by material originating at a radius $R-\lambda/2$ in a quasi-Keplerian accretion disk is given by Hartmann (1998) as $J_{\rm in} = (R - \lambda/2)\,\Omega(R-\lambda/2)$, where λ is the mean free path over which parcels of plasma exchange angular momentum. As pointed out by HM, this expression is incorrect, and the correct expression should read as follows:

$$J_{\rm in} = \left(R - \frac{\lambda}{2}\right)^2\,\Omega\left(R - \frac{\lambda}{2}\right). \tag{6}$$

One can write an analogous expression for $J_{\rm out}$, the specific angular momentum carried by material originating at a radius $R + \lambda/2$, by reversing the sign of λ. As shown by HM, if one expands $\Omega(R - \lambda/2)$ to first order in λ as $\Omega(R - \lambda/2) \sim \Omega(R) - (\lambda/2)(\mathrm{d}\Omega/\mathrm{d}R)$, the result obtained for the difference between the specific angular momenta is

$$J_{\rm in} - J_{\rm out} = -\lambda \frac{\rm d}{{\rm d}R} (R^2 \Omega). \tag{7}$$

The characteristic time for the interchange of the matter between the two radii is $\Delta t = \lambda/w$, where w is the turbulent velocity of the fluid parcels. The total mass of fluid involved in the interchange is $\Delta M = 2\pi R \lambda \Sigma$, and it follows that the net rate of flow of angular momentum from the inner ring at $R - \lambda/2$ towards the outer ring at $R + \lambda/2$ (or equivalently, the viscous torque exerted by the ring at $R - \lambda/2$ on the ring at $R + \lambda/2$) is

$$\mathcal{G} = \frac{\Delta M}{\Delta t} (J_{\rm in} - J_{\rm out}) = 2\pi R \, \Sigma \, w \, (J_{\rm in} - J_{\rm out}), \tag{8}$$

or

$$\mathcal{G} = -2\pi R \, \Sigma \, \beta \, \nu \frac{\rm d}{{\rm d}R} (R^2 \Omega), \tag{9}$$

where we have set $\nu = w\lambda/\beta$, with β denoting a constant of order unity. The viscous torque in a quasi-Keplerian accretion disk should tend to smooth out gradients in the angular velocity so as to attain solid body rotation (${\rm d}\Omega/{\rm d}R = 0$). However, the expression for the viscous torque in equation (9) is such that it tends to attain a flow with *constant angular momentum*, i.e., the "equilibrium" condition is ${\rm d}(R^2 \Omega)/{\rm d}R = 0$. As HM point out, this expression is therefore unphysical.

3.2 *Derivation of $\mathcal{G}$ by Frank et al. (1992)*

We next turn our attention to another derivation of the viscous torque given by Frank *et al.* (1992). At the heart of their derivation is the claim that the linear velocity of material at radius $R - \lambda/2$ as seen by an observer situated at radius R is given by

$$v_{\rm rel}\left(R - \frac{\lambda}{2}\right) = \left(R - \frac{\lambda}{2}\right) \Omega \left(R - \frac{\lambda}{2}\right) + \Omega(R) \frac{\lambda}{2}. \tag{10}$$

Based on this, one can write an expression for $L_{\rm in}$, the rate at which angular momentum crosses an annulus at radius R in the direction of increasing R, as

$$\begin{aligned} L_{\rm in} &= 2\pi R \, \Sigma \, w \left(R - \frac{\lambda}{2}\right) v_{\rm rel}\left(R - \frac{\lambda}{2}\right) \\ &= 2\pi R \, \Sigma \, w \left(R - \frac{\lambda}{2}\right) \left[\left(R - \frac{\lambda}{2}\right) \Omega \left(R - \frac{\lambda}{2}\right) + \Omega(R) \frac{\lambda}{2}\right] \\ &\simeq 2\pi R \, \Sigma \, w \left(R - \frac{\lambda}{2}\right) \left[R \, \Omega(R) - R \frac{\lambda}{2} \frac{{\rm d}\Omega}{{\rm d}R}\right], \end{aligned} \tag{11}$$

where we have expanded $\Omega(R-\lambda/2)$ to first order in λ to arrive at the final expression. We can write an analogous expression for $L_{\rm out}$, the rate at which angular momentum crosses radius R in the inward direction, by reversing the sign of λ. To first order in λ, the torque exerted on the plasma outside radius R by the plasma inside that radius is then

$$\mathcal{G} = L_{\rm in} - L_{\rm out} = -2\pi R^2 \beta \nu \Sigma \frac{\rm d}{{\rm d}R}(R\,\Omega). \tag{12}$$

Since the right-hand side is proportional to ${\rm d}(R\,\Omega)/{\rm d}R$, in this case the torque will lead to a uniform *linear velocity*, and not to a uniform *angular velocity* as we require on physical grounds. As HM point out, this expression for $\mathcal{G}$ is therefore also incorrect.

3.3 *Correction proposed by HM*

HM claim that this is because Frank et al. (1992) have used an incorrect expression for $v_{\rm rel}$ (i.e., equation (10)). They assert that the linear velocity of the plasma at $(R-\lambda/2)$ as viewed by an observer at radius R should instead be given by

$$v_{\rm rel}\left(R-\frac{\lambda}{2}\right) = \left(R-\frac{\lambda}{2}\right)\Omega\left(R-\frac{\lambda}{2}\right) - R\,\Omega(R) + \Omega(R)\,\frac{\lambda}{2}. \tag{13}$$

By employing this expression for $v_{\rm rel}$ and following the same procedure used to obtain equation (12), they find that to first order in λ,

$$\mathcal{G} = L_{\rm in} - L_{\rm out} = -2\pi R^3 \beta \nu \Sigma \frac{{\rm d}\Omega}{{\rm d}R}. \tag{14}$$

This expression for $\mathcal{G}$ does indeed have the correct dependence on ${\rm d}\Omega/{\rm d}R$, but nonetheless we claim that equation (13) for the relative velocity used by HM is incorrect. The correct expressions for the relative velocities are in fact (see, e.g., Mihalas & Binney 1981)

$$\begin{aligned} v_{\rm rel}\left(R-\frac{\lambda}{2}\right) &= \left(R-\frac{\lambda}{2}\right)\Omega\left(R-\frac{\lambda}{2}\right) - R\,\Omega(R) \\ v_{\rm rel}\left(R+\frac{\lambda}{2}\right) &= \left(R+\frac{\lambda}{2}\right)\Omega\left(R+\frac{\lambda}{2}\right) - R\,\Omega(R), \end{aligned} \tag{15}$$

where $v_{\rm rel}(R-\lambda/2)$ denotes the velocity of a plasma parcel at $R-\lambda/2$ as seen by an observer at R, and $v_{\rm rel}(R+\lambda/2)$ denotes the velocity of a plasma parcel at $R+\lambda/2$ as seen by an observer at R. In a quasi-Keplerian accretion disk, $\Omega \propto R^{-3/2}$, and therefore the first velocity is positive and the second is negative. These expressions for the relative velocities assume that the plasma parcels at R, $R-\lambda/2$, and $R+\lambda/2$ all lie on the same radial line through the central object. If this is not true, then the expressions will contain additional terms, as Mihalas & Binney (1981) show in the context of the relative velocity between the sun and stars in our galaxy. Since we are dealing with material transport over lengths of the order of λ that are very small in

comparison with R, this assumption is quite valid in our accretion disk application. Using equation (15) for the relative velocities, we now obtain

$$\begin{aligned} L_{\rm in} &= 2\pi R\,\Sigma\, w\,\left(R-\frac{\lambda}{2}\right)\left[\left(R-\frac{\lambda}{2}\right)\,\Omega\left(R-\frac{\lambda}{2}\right)-R\,\Omega(R)\right] \\ &\simeq -2\pi R^2\,\Sigma\, w\,\frac{\lambda}{2}\left[R\,\frac{{\rm d}\Omega}{{\rm d}R}+\Omega(R)\right] \\ L_{\rm out} &= 2\pi R\,\Sigma\, w\,\left(R+\frac{\lambda}{2}\right)\left[\left(R+\frac{\lambda}{2}\right)\,\Omega\left(R+\frac{\lambda}{2}\right)-R\,\Omega(R)\right] \\ &\simeq\ 2\pi R^2\,\Sigma\, w\,\frac{\lambda}{2}\left[R\,\frac{{\rm d}\Omega}{{\rm d}R}+\Omega(R)\right], \end{aligned} \tag{16}$$

where the final expressions for $L_{\rm in}$ and $L_{\rm out}$ are correct to first order in λ. We thus obtain for the viscous torque

$$\mathcal{G} = L_{\rm in} - L_{\rm out} = -\,2\pi R^2\,\Sigma\,\beta\,\nu\frac{\rm d}{{\rm d}R}\,(R\,\Omega). \tag{17}$$

This result is identical to equation (12), and therefore it too is incorrect.

4. Derivation based on epicyclic parcel motion

We have demonstrated in section 3 that due to various errors, the previous derivations of the viscous torque based on mean free path theory do not yield results consistent with the classical theory of viscous transport. We shall now focus on a heuristic analysis of the angular momentum transport that combines the mean free path approach with a proper treatment of the epicyclic motion of parcels of gas in adjacent eddies in the accretion disk. The physical picture is presented in Fig. 1. Let us suppose that λ represents the mean distance a parcel travels freely before having its motion disrupted by interaction with the surrounding material in the disk. The disruption in this case involves hydrodynamical interaction, and therefore λ is the damping length for the turbulence as well as the mean free path for the parcel motion. It follows that the turbulence in the disk can be characterized by whirls with a mean radius λ.

Next we focus on the interchange of two gas parcels of unit mass, A and B, which are initially located at radii $R+\lambda/2$ and $R-\lambda/2$, respectively (see Fig. 1). The two parcels each "ride" turbulent eddies with radius λ, and they start out at the outer (parcel A) or inner (parcel B) edge of their respective eddies. Hence each begins its motion with zero radial velocity, at a turning point in its orbit. Parcel A moves in the inward direction, and therefore its angular momentum is sub-Keplerian compared to the average disk at radius $R+\lambda/2$. Similarly, parcel B is super-Keplerian compared to the mean disk at radius $R-\lambda/2$ and therefore it moves in the outward direction. The motion of the parcels is epicyclic as viewed from the reference frame of an observer who remains at the starting radius and travels along with the Keplerian angular velocity. Since λ is the mean damping length for the turbulence, each of the parcels will experience

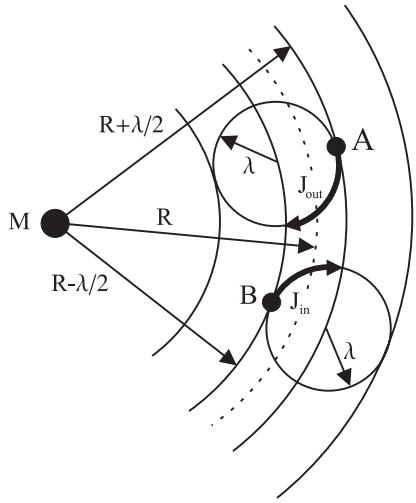

Figure 1. Angular momentum transport in the disk involves the interchange of two parcels, A and B, initally located at radii $R + \lambda/2$ and $R - \lambda/2$, respectively, around central mass M. They each participate in ballistic, epicyclic motion in eddies of radius λ, with A moving inward and B moving outward. See the discussion in the text.

ballistic motion over a radial length scale comparable to λ, after which the ballistic motion (and the parcel itself) will be absorbed by the surrounding gas. It follows that, on average, parcel A will deposit its angular momentum ($J_{\rm out}$) at radius $R - \lambda/2$, and parcel B will deposit its angular momentum ($J_{\rm in}$) at radius $R + \lambda/2$. Hence the two parcels exchange radii during the process. We shall proceed to compute the net angular momentum exchange, $J_{\rm in} - J_{\rm out}$, by considering the motion of these parcels in detail.

Gas parcel A participates in the motion of turbulent eddy A, which has its center located at radius $R - \lambda/2$ and possesses turning points at radii $R + \lambda/2$ and $R - 3\lambda/2$. Likewise, parcel B experiences the motion of eddy B, with its center located at radius $R + \lambda/2$, and with turning points at radii $R + 3\lambda/2$ and $R - \lambda/2$. The specific energy E and the specific angular momentum J of each parcel is conserved during the ballistic phase of its motion, until it travels a mean distance λ and is damped by the surrounding material. For a particle moving ballistically in the Newtonian gravitational field of a central mass M, the quantities E and J are related by the classical energy equation

$$E = \frac{1}{2} v_R^2 + \frac{1}{2} \frac{J^2}{R^2} - \frac{GM}{R}, \tag{18}$$

where v_R is the radial component of the velocity. Turning points in the radial motion occur where v_R vanishes, so that we can write

$$E = \frac{1}{2} \frac{J^2}{R_1^2} - \frac{GM}{R_1} = \frac{1}{2} \frac{J^2}{R_2^2} - \frac{GM}{R_2}, \tag{19}$$

where R_1 and R_2 denote the two turning point radii. This equation can be easily solved for the angular momentum J as a function of R_1 and R_2. The result obtained is

$$J = \left(\frac{2\,GM\,R_1\,R_2}{R_1 + R_2} \right)^{1/2}. \tag{20}$$

We can use equation (20) to conclude that the angular momentum of parcel A is equal to

$$J_{\rm out} = \sqrt{GMR}\,\left(1 + \frac{1}{2}\frac{\lambda}{R}\right)\left(1 - \frac{3}{2}\frac{\lambda}{R}\right)^{1/2}\left(1 - \frac{1}{4}\frac{\lambda^2}{R^2}\right)^{-1/2}. \tag{21}$$

Likewise, the angular momentum of parcel B is given by

$$J_{\rm in} = \sqrt{GMR}\,\left(1 - \frac{1}{2}\frac{\lambda}{R}\right)\left(1 + \frac{3}{2}\frac{\lambda}{R}\right)^{1/2}\left(1 - \frac{1}{4}\frac{\lambda^2}{R^2}\right)^{-1/2}. \tag{22}$$

In the spirit of the mean free path approach, we are interested in computing the value of the net angular momentum transport, $J_{\rm in} - J_{\rm out}$, to first order in the small parameter λ/R. The corresponding results obtained for $J_{\rm in}$ and $J_{\rm out}$ are

$$J_{\rm out} = \sqrt{GMR}\,\left(1 - \frac{1}{4}\frac{\lambda}{R}\right) + {\rm O}\left[\frac{\lambda^2}{R^2}\right], \tag{23}$$

$$J_{\rm in} = \sqrt{GMR}\,\left(1 + \frac{1}{4}\frac{\lambda}{R}\right) + {\rm O}\left[\frac{\lambda^2}{R^2}\right]. \tag{24}$$

The angular velocity $\Omega(R)$ in a quasi-Keplerian accretion disk is very close to the Keplerian value, and therefore we can write

$$\Omega(R) = \sqrt{\frac{GM}{R^3}}. \tag{25}$$

It follows that

$$R^2\,\Omega\left(R + \frac{\lambda}{6}\right) = \sqrt{GMR}\,\left(1 + \frac{1}{6}\frac{\lambda}{R}\right)^{-3/2}, \tag{26}$$

or, to first order in λ/R,

$$R^2\,\Omega\left(R + \frac{\lambda}{6}\right) = \sqrt{GMR}\,\left(1 - \frac{1}{4}\frac{\lambda}{R}\right) + {\rm O}\left[\frac{\lambda^2}{R^2}\right]. \tag{27}$$

This also implies that

$$R^2\,\Omega\left(R - \frac{\lambda}{6}\right) = \sqrt{GMR}\,\left(1 + \frac{1}{4}\frac{\lambda}{R}\right) + {\rm O}\left[\frac{\lambda^2}{R^2}\right]. \tag{28}$$

Comparing equations (23) and (24) with equations (27) and (28), we find that to first order in λ/R, the net angular momentum transfer is given by

$$J_{\rm in} - J_{\rm out} = R^2\,\Omega\left(R - \frac{\lambda}{6}\right) - R^2\,\Omega\left(R + \frac{\lambda}{6}\right) \simeq -\frac{\lambda}{3}\,R^2\,\frac{{\rm d}\Omega}{{\rm d}R}. \qquad (29)$$

By following the same steps leading to equation (8), we now obtain

$$\mathcal{G} = 2\pi R\,\Sigma\,w\,(J_{\rm in} - J_{\rm out}) \simeq -2\pi R^3\,\nu\,\Sigma\,\frac{{\rm d}\Omega}{{\rm d}R}, \qquad (30)$$

where the final expression is correct to first order in λ and we have set $\nu = w\lambda/3$ so that $\beta = 3$. Note that this result agrees very well with the Shakura-Sunyaev form (equation (5)). Hence we have demonstrated using a simple heuristic derivation that the viscous torque is indeed proportional to the gradient of the angular velocity in an accretion disk within the context of a mean free path, parcel-exchange picture.

5. Conclusion

The derivation presented in section 4 clearly employs mean free path theory, since we assumed that the fluid parcels travel an average radial distance λ before being damped by the surrounding gas. We have thus shown that there does exist a simple derivation, based on mean free path theory, that yields an expression for the viscous torque $\mathcal{G}$ (equation (30)) that is directly proportional to the radial derivative of the angular velocity, ${\rm d}\Omega/{\rm d}R$, in agreement with our physical expectation. This expression for $\mathcal{G}$ can be used in equation (4) to proceed further in deriving the structure of the accretion disk, as in Pringle (1981). Our results provide a simple but important unification of the "parcel interchange" viscosity model with the MHD viscosity model, in which the coupling that transports the angular momentum is provided by the magnetic field rather than by fluid turbulence (Frank et al 2002). In the MHD model, the torque is found to be proportional to the gradient of the angular velocity, ${\rm d}\Omega/{\rm d}R$, in agreement with the results we have obtained here by applying the mean free path approach to the case of fluid turbulence.

Note added in proof: After this paper was accepted for publication, we came to know of a paper by Clarke & Pringle (2004) which arrived at very similar conclusions using a different approach.

References

Becker, P. A., Le, T. 2003, *Astrophys. J.*, **588**, 408.

Clarke, C. J., Pringle, J. E. 2004 (to appear in *Monthly Not. Roy. Astron. Soc*, astro-ph/0403407).

Frank, J., King, A., Raine, D. 1985, *Accretion Power in Astrophysics, 1st edition* (Cambridge: Cambridge University Press).

Frank, J., King, A., Raine, D. 1992, *Accretion Power in Astrophysics, 2nd edition* (Cambridge: Cambridge University Press).

Frank, J., King, A., Raine, D. 2002, *Accretion Power in Astrophysics, 3rd edition* (Cambridge: Cambridge University Press).

Hartmann, L. 1998, *Accretion Processes in Star Formation* (Cambridge: Cambridge University Press)
Hayashi, E., Matsuda, T. 2001, *Prog. Theor. Phys.*, **105**, 531 (HM).
Landau, L. D., Lifshitz, E. M. 1987, *Fluid Mechanics, 2nd edition* (New York: Pergamon Press).
Mihalas, D., Binney, J. 1981, *Galactic Astronomy, 2nd edition* (San Francisco: W. H. Freeman & Co.), p. 468.
Pringle, J. 1981, *Ann. Rev. Astron. Astrophys.* **19**, 137.
Shakura, N. I., Sunyaev, R. I. 1973, *Astron. Astrophys.* **24**, 337.
Subramanian, P. 1997, *Ph.D. Thesis*, George Mason University, Fairfax, VA 22030, U.S.A.

J. Astrophys. Astr. (2004) **25,** 93–101

Radial Matrix Elements of Hydrogen Atom and the Correspondence Principle

T. N. Chakrabarty *Applied Physics Department, Fr. Conceicao Rodrigues College of Engineering, Fr. Agnel Ashram, Bandstand, Bandra (W), Mumbai 400 050, India.*
e-mail: tn_chakrabarty@yahoo.co.in

Received 2003 October 1; accepted 2004 February 10

Abstract. Radial dipole matrix elements having astrophysical importance have been computed for highly excited states of hydrogen atom. Computation is based on Heisenberg's form of correspondence principle for Coulomb potential. Particular attention has been paid to the choice of classical analogue (n_c) of principal quantum number (n). The computed radial matrix elements are in good agreement with quantum mechanical results. Further, radial matrix elements for few transitions involving high n neighboring states of hydrogen atom are presented.

Key words. Hydrogen excited states—radial matrix element—correspondence principle.

1. Introduction

In the astrophysical environment, high Rydberg atoms are formed with a wide range of values of the principal quantum number n by radiative recombination process. The availability of such high n Rydberg atoms is basically found in the diffuse interstellar gas, molecular clouds, planetary nebulae, and other sources. The interstellar medium is the most appropriate environment because it is subjected to ultra violet radiation and X-rays from extra galactic objects.

We have noticed sufficient progress and exploring interest on highly excited Rydberg atoms theoretically as well as experimentally from mid 1970s to 1990. Review articles describe (Stebbings 1976; Metcalf 1980; Kleppner *et al* 1981) the high n Rydberg atoms, its availability, production, its spectras, and importance in astrophysics (Dupree & Goldberg 1970; Dalgarno 1982). It is very interesting for example, to see a Rydberg atom where the excited electron has a principal quantum number $n \cong 70$, its orbital radius is 0.27×10^{-6}m which has the same size as a typical animal cell.

The basic methods of formation of highly excited Rydberg atoms are as follows:

(i) Charge transfer between A and B atom

$$A^+ + B \longrightarrow A^{**} + B^+$$

where A^{**} is high n Rydberg atoms.

(ii) Electron impact excitation method

$$e + A \longrightarrow e + A^{**}$$
$$e + A_2 \longrightarrow e + A^{**} + A$$

where e is an electron.

(iii) Photon impact method

$$h\nu + A(nl) \longrightarrow A^{**}(n'l')$$

$h\nu$ is a photon.

A highly excited Rydberg atom can be considered as an ion core and an electron far away revolving lazily around in a slow orbit like a distant planet in the solar system. As the electron orbit diameter grows rapidly, its energy also decreases rapidly. Currently, selective excitation to a particular high n state has become possible by the availability of tunable dye LASER. As a result, theoretical calculations involving transition matrix elements, radiative life times, oscillator strengths, etc. have become important to support experimental results concerning high n, l states of Rydberg atoms, which were not available earlier.

Theoretical calculations concerning high n Rydberg states (i.e., $n \longrightarrow \infty$) for any atom based on quantum mechanics becomes difficult, cumbersome, and very time consuming because it involves long series calculations and computations of the product of two long series where proper choice (Gounand 1979) has to be imposed for the upper limit of the series to terminate it. For example, radial matrix element calculation for high n states, needs proper choice for the cut off value of the upper limit of Laguere Polynomials to get approximate results. Therefore, the best compromise between computation time and long series calculation is the correspondence principle. This principle is more convenient and the best choice to handle high n states in the situation $\Delta E \longrightarrow 0$, $\Delta n \longrightarrow 0$, and $n \longrightarrow \infty$.

2. Theory

In the classical picture, we can imagine that, in a hydrogen atom the electron is revolving around in an elliptical path keeping the nucleus at one of its focii. The eccentricity is ϵ, and a is the semi axis of the ellipse. In the successive excited states of hydrogen atom, correspondence principle can be applied for $n \longrightarrow \infty$, $\triangle E \longrightarrow 0$, $\triangle n \longrightarrow$ very small.

2.1 *Correspondence principle in general*

The classical theory of action and angle variables (Percival 1974) can be written as

$$I = \frac{1}{2\pi} \oint p dq \quad \text{and} \quad W = \frac{\partial}{\partial I} \int p(I) dq,$$

where q and p are the initial values of position and momentum.

$W = \omega t +$ constant, with ω being the classical frequency.

Here, Sommerfield assumed that $I = n\hbar$, where n is an integer, so that the energy of the system is quantized.

Statement of the Correspondence Principle:

In the limit $n \longrightarrow \infty$ and $\triangle n \longrightarrow$ very small, $\triangle E \longrightarrow 0$, the observed quantum frequency

$$\omega_{nn'} = (E_n - E_{n\prime})/\hbar \longrightarrow \triangle n\omega,$$

where $\triangle n = n' - n$, $\omega =$ classical frequency.

2.2 *Heisenberg's form of correspondence principle for radial matrix element*

Statement:

This principle (Percival 1974) states that the quantal matrix elements between the quantal states n and $n\prime$ of the dynamical variable q tends to coincide with the classical Fourier components q_s.

If we write the position coordinate $q(t)$ in terms of Fourier coefficient then

$$q(t) = \sum_s q_s \exp(is\omega t)$$

where q_s is the Fourier coefficient, and hence the quantal matrix element between n and $n\prime$ states can be written as

$$\langle n \mid q(t) \mid n\prime\rangle = q_s. \tag{1}$$

Naccache (1972) expands the position coordinates (x, y, z) in the angle variables w, ψ, φ as follows

$$x(w, \psi, \varphi) = \sum_{s, \triangle l, \triangle m} x_{n,l,m}^{n+s, l+\triangle l, m+\triangle m} \exp i(sw + \triangle l\psi + \triangle m\phi), \tag{2}$$

for x, y components, $\triangle l = \pm 1$, $\triangle m = \pm 1$,
for z components, $\triangle l = \pm 1$, $\triangle m = 0$.
Naccache wrote the three matrix elements as

$$\langle n, l, m \mid x \mid n + s, l + \triangle l, m + \triangle m\rangle = \triangle l/4(1 + m \triangle m/l \triangle l) R_{n,l}^{n+s, l+\triangle l}, \tag{3}$$

$$\langle n, l, m \mid y \mid n + s, l + \triangle l, m + \triangle m\rangle = -i \triangle m \triangle l/4(1+m \triangle m/l \triangle l) R_{n,l}^{n+s, l+\triangle l}, \tag{4}$$

$$\langle n, l, m \mid z \mid n + s, l + \triangle l, m + \triangle m\rangle = -i/2(1 - m^2/l^2) R_{n,l}^{n+s, l+\triangle l}, \tag{5}$$

where

$$R_{n,l}^{n+s, l+\triangle l} = a \triangle l/s \left\{ J_s'(s\epsilon) + \triangle l(1 - \epsilon^2)^{\frac{1}{2}}/\epsilon J_s(s\epsilon) \right\} \tag{6}$$

is the corresponding classical dipole matrix element between n, l and $n+s, l+\triangle l$ states, a is the semi axis of the elliptic orbit, ϵ is the eccentricity of the ellipse, and $J_s(s\epsilon)$ is the Bessel function.

Naccache has written equation (6) in a better form as

$$R_{n,l}^{n+s,l+\triangle l} = (n_c^2/2s) \triangle l \{(1 + l_c \triangle l/n_c) J_{s-1}(s\epsilon) + (1 - l_c \triangle l/n_c) J_{s+1}(s\epsilon)\}. \tag{7}$$

Percival and Richards (unpublished) wrote the square of $(R_{n,l}^{n'l'})$ as follows

$$(R_{n,l}^{n'l'})^2 = (n_c^2/2s)^2 \{(1 + l_c \triangle l/n_c) J_{s+1}(s\epsilon) - (1 - l_c \triangle l/n_c) J_{s-1}(s\epsilon)\}^2, \tag{8}$$

where n_c and l_c are the classical analogue of principle quantum number n and orbital quantum number l, $s = n - n'$, $\triangle l = l' - l$,

$$n_c = n(n-s)/(n - s/2) = 2nn'/(n + n'), \quad \text{and} \quad l_c = \max(l, l'),$$

$\epsilon = (1 - l_c^2/n_c^2)^{\frac{1}{2}}$ = eccentricity of the elliptic orbit in which the electron of the hydrogen atom is revolving, and $J_s(s\epsilon)$ is the Bessel function.

2.3 *Choices on n_c and l_c*

There are infinite number of valid choices on n_c and l_c.

Choosing $l_c = l$ and $n_c = \bar{n}$, results can be very close to quantum mechanical results.

Menzel (1968, 1969) had chosen $n_c = n'(1 + 3s/n')$ and $n_c = n'\{1 + 3s/n' + A(s)/(n')^2\}$ where $A(s)$ is a tabulated function of s.

Naccache's choice (Naccache 1972) is $n_c = n(n-s)/(n-s/2) = 2nn'/(n+n')$ and $l_c = \max(l, l')$.

2.4 *Introduction of the new choice on n_c in the present work*

In the present work, we introduce the new choice on the classical analogue n_c as $n_c = n' \exp(s/2n)$ where n and n' are the initial and the final states and $s = n - n'$. This new choice of n_c, compared to $(n_c)_{\text{naccache}}$, brings the values of $(R_{n,l}^{n'l'})^2$ very close to quantum mechanical results. Here we follow the symbols $(n_c)_{\text{naccache}}$ for $n_c = 2nn'/(n + n')$ and $(n_c)_{\text{presentchoice}}$, $(n_c)_{\text{presentwork}}$ or $(n_c)_{\text{introduced}}$, for $(n_c) = n' \exp(s/2n)$ throughout the whole discussion and particularly in the tables of results.

The basic reason to choose a particular mathematical form of n_c as $(n_c) = n' \exp(s/2n)$ is as follows:

In this work, we concentrate on the radial transition matrix element concerning highly excited neighbouring states of hydrogen atom with small s values. This requirement is implicit in the mathematical form of n_c. As radial matrix elements are dependent on n_c^2, so the value of n_c is very sensitive to get accurate results for the radial matrix elements. Keeping in mind the sensitivity of radial matrix element on n_c, the exponential power $s/2n$ and the multiplication factor n' has been so chosen that for small values of s, and by adjusting with the multiplication factor n', it will lead more accurate results for n_c which ultimately lead to close results with the quantum mechanical

values of radial matrix element. On the contrary, if s increases, $\exp(s/2n)$ becomes very large, which leads to much inaccuracy and large variation from quantum mechanical values of radial matrix element, which has been shown in the results. As radial matrix element depends on n_c^2 and n_c is very sensitive on s, so the mathematical form $n_c = n' \exp(s/2n)$ is justified for high n neighbouring states.

Naccache had calculated radial matrix element with the choice $n_c = n(n-s)/(n - s/2)$ which leads to very close results with the quantum mechanical values of radial matrix element, so it is our advantage to check our values of n_c with Naccache's values. Here, we have found that the exponential form of presentation of n_c closely tallies with the Naccache's form of n_c. Further, crosscheck has been done for the eccentricity, which also is highly satisfactory.

Therefore, we guess that our choice of n_c will be very helpful for calculating radial matrix element for very high n neighbouring states and also for the calculation of oscillator strength.

3. Calculations

The square of the radial dipole matrix elements, i.e., $(R_{n,l}^{n'l'})^2$ has been calculated in the present work. We have taken equation (8) for this calculation. The new introduced choice of n_c has been incorporated in this calculation keeping the choice of l_c by Naccache the same i.e., $l_c = \max(l, l')$. Equation (8) slightly differs from Naccache (1972) because Percival & Richards (unpublished) reported that s of Naccache (1972) is the negative of that used by them because there is an error in a sign of the result in Naccache's paper.

In quantum mechanical calculations of radial dipole matrix elements, the product of two Laguere polynomials appears frequently which is very difficult to solve when $n \longrightarrow \infty, n' \longrightarrow \infty$.

Particularly the choice (Gounand 1979) for the cutoff criterion is imposed to terminate the series quickly for an approximate result. In contrast with the quantum mechanical calculations, the computation of Bessel functions $J_s(s\epsilon)$ is convenient and easier to handle even for very high n states.

Since classical analogue of principle quantum number n_c is represented in the exponential form in our new introduction of choice, we guess that apart from the transition between neighbouring states, if s is large, the difference of values between quantum mechanical and correspondence principle values for $(R_{n,l}^{n'l'})^2$ becomes large. Because when s is large, we take a departure from the condition of applying the correspondence principle for highly excited states. We therefore, concentrate on calculations based on closely lying neighbouring excited states of hydrogen where s is very small.

4. Results and discussion

In general, when $n \longrightarrow \infty, n' \longrightarrow \infty$ and $s = n - n'$ is very small, $\Delta E \longrightarrow 0$, correspondence principle is the meaningful choice for the transition between successive stationary states which can be considered as quasi classical states. In the new choice of $n_c = n' \exp(s/2n)$ introduced here, s is in the exponential power and so s is very sensitive for calculating n_c. Therefore, calculations have been restricted for high n neighbouring states of hydrogen atom.

4.1 *Comparison on the choice of n_c*

The dependence of $(R_{n,l}^{n'l'})^2$ on n_c is $(n_c)^4$.

So, considerable change of n_c i.e., Δn_c will matter much for such a type of calculation. Since the choice $(n_c)_{\text{naccache}}$ reproduces very close agreement to quantum mechanical calculations, we compare $(n_c)_{\text{presentwork}}$ and $(n_c)_{\text{naccache}}$ in Table 1.

Table 1. Comparison of $(n_c)_{\text{naccache}}$ and $(n_c)_{\text{presentchoice}}$.

Transition $(n \to n')$	$(n_c)_{\text{naccache}}$	$(n_c)_{\text{presentchoice}}$	% difference
$8 \to 7$	7.46	7.45	0.13
$20 \to 19$	19.48	19.48	0
$100 \to 99$	99.497	99.496	$\sim 10^{-5}$
$500 \to 499$	499.499	499.499	0

In table 1, we see that as we move from the transition $n = 8 \longrightarrow 7$ to transition between very highly excited neighbouring states i.e., $n = 20 \longrightarrow 19, 100 \longrightarrow 99, 500 \longrightarrow 499$, the % difference between $(n_c)_{\text{naccache}}$ and $(n_c)_{\text{introduced}}$ is in between 0 and 0.13. Therefore, such a choice on n_c will yield very good results for computation of $(R_{n,l}^{n'l'})^2$. Regarding l and l' also we restrict ourselves to the neighbouring l states where Δl is very small.

4.2 *Comparison between neighbouring and far-off states*

If we move apart from neighbouring states transitions to far off states, s value increases. since s is in the exponential power, the introduced choice of n_c, is very sensitive on s. We have seen poor agreement of a result for the calculation of $(R_{n,l}^{n'l'})^2$ with the quantum mechanical results for the transition $n = 13, l = 7 \longrightarrow n' = 20, l' = 8$. So, in Table 2 we compare $(n_c)_{\text{presentchoice}}$ with $(n_c)_{\text{naccache}}$ for upward and downward

Table 2. Comparison of $(n_c)_{\text{naccache}}$ and $(n_c)_{\text{presentchoice}}$ for the upward and downward transition from the level $n = 13$.

Transition from $n = 13$	$(n_c)_{\text{naccache}}$	$(n_c)_{\text{presentchoice}}$	% difference
	Upward transition $\uparrow$		
$13 \to 14$	13.48	13.47	0.07
$13 \to 15$	13.92	13.89	0.21
$13 \to 16$	14.34	14.25	0.62
$13 \to 20$	15.75	15.28	2.98
	Downward transition $\downarrow$		
$13 \to 12$	12.48	12.47	0.08
$13 \to 11$	11.91	11.88	0.03
$13 \to 10$	11.30	11.22	0.70
$13 \to 6$	8.21	7.85	4.38

Table 3. Comparison of the values of $(R^{n'l'}_{n,l})^2$ based on quantum mechanical calculations and correspondence principle with different choice of n_c.

Transition	$(R^{n'l'}_{n,l})^2$ QM values	$(R^{n'l'}_{n,l})^2_{\text{naccache}}$ with choice $(n_c = n - s/2)$	%diff	$(R^{n'l'}_{n,l})^2_{\text{naccache}}$ with choice $n_c = 2nn'/(n+n')$	%diff	$(R^{n'l'}_{n,l})^2_{\text{presentwork}}$ with choice $n_c = n' \exp(s/2n)$	%diff
$2s \rightarrow 3p$	9.393	11.022	17.34	9.270	1.30	8.974	4.46
$3s \rightarrow 5p$	72.553	76.395	5.30	73.181	0.86	71.505	1.44
$6s \rightarrow 7p$	274.19	281.22	2.56	275.25	0.38	272.27	0.7
$4p \rightarrow 5d$	121.86	127.86	4.92	123.18	1.08	120.49	1.12
$4d \rightarrow 5f$	197.83	207.00	4.63	200.46	1.33	196.65	0.596
$13, 7 \rightarrow 20, 8$	39.5	47.18	19.4	37.96	3.89	32	18.98

transition between the neighbouring states from the level $n = 13$. Comparison indicates that when s is small, the percentage difference between present choice of n_c and Naccache's is $< 0.75\%$, but when s is large, % difference for upward transition is around 3% and for downward transition it is around 4%. This clearly indicates that this choice is practically concentrated on the neighbouring states transition for the highly excited Ryderberg states.

4.3 *Comparison of the values of* $(R_{n,l}^{n'l'})^2$

In Table 3 the square of the radial matrix elements of hydrogen i.e., $(R_{n,l}^{n'l'})^2$ based on quantum mechanical calculations is compared with the calculation based on correspondence principle with various choices of n_c and the new choice introduced for n_c in the present work. In the transition presented in Table 3, $\mid s \mid = 1$, $\Delta l = l' - l = 1$ for the five transitions except the last one where $\mid s \mid = 7$ and $\Delta l = +1$. Agreement of the results of the present work with quantum mechanical calculation is fairly good. This result reflects that for highly excited states of hydrogen where the transitions involve neighbouring states, the choice of n_c in the present work will yield better results. In the last transition s is large, therefore % difference of $(n_c)_{\text{naccache}}$ and $(n_c)_{\text{presentwork}}$ is also large which leads to poor agreement, because the dependence of $(R_{n,l}^{n'l'})^2$ on n_c is n_c^4.

4.4 *Results for the high n states with the present choice of* n_c

In Table 4, we present the values of $(R_{n,l}^{n'l'})^2$ of hydrogen atom. The calculation is based on correspondence principle incorporating our introduced choice on n_c. Comparison has been made between $(n_c)_{\text{naccache}}$ and $(n_c)_{\text{presentchoice}}$, which follows the condition of application of correspondent principle. Here, quantum mechanical values for $(R_{n,l}^{n'l'})^2$ for the given transitions could not be presented because of the non availability of theoretical data. Our expectation is that these values of $(R_{n,l}^{n'l'})^2$ will tally perfectly with the quantum mechanical calculations for the given states in Table 4.

Table 4. Computed values of $(R_{n,l}^{n'l'})^2$ of hydrogen atom based on the correspondence principle with the introduced choice of n_c have been presented.

Transition	Values of $(R_{n,l}^{n'l'})^2_{\text{presentwork}}$	Comparison of n_c values		
		$(n_c)_{\text{naccache}}$	$(n_c)_{\text{presentwork}}$	% difference
$10s \rightarrow 11p$	1.631×10^3	10.476	10.463	0.12
$20s \rightarrow 19p$	1.3211×10^4	19.487	19.480	0.03
$29s \rightarrow 30p$	8.7318×10^4	29.491	29.487	0.01
$50s \rightarrow 49p$	6.0×10^5	49.494	49.492	0.004

Acknowledgement

I would like to thank Dr. R. S. Iyer for encouraging me in this work.

References

Dalgarno, A. 1982, Reprinted from R. F. Stebbings and F. B. Dunning (eds) *Rydberg states of atoms and molecules* (C.U. Press) 1.
Dupree, A. K. and Goldberg, L. 1970, *Ann. Rev. Astr. Astrophys*, **8**, 231.
Goldstein, H. 1959, *Classical Mechanics* (Addison Wesley Press).
Gounand, F. 1979, *Le Journal de physique*, **40**, 457.
Kleppner, D., Littman, M.G., Zimmerman, M.L. 1981, *Scientific American*, **244**, No. 5, 130.
Menzel, D. H. 1968, *Nature*, **218**, 756; 1969, *Astro. Phys. J. Supplement Series*, **18**, No. 161, 221.
Metcalf, H. J. 1980, *The Physics Teacher*, March, 199.
Naccache, P. F. 1972, *J. Phys. B: Atom. Molec. Phys.*, **5**, 1308.
Percival, I. C., Richards, D. *The theory of collisions between charged particles and highly excited atoms* (unpublished, available from the authors on request) 1–106
Percival, I. C. 1974, Reprint from *Atoms, Molecules and LASERS*, International Atomic Energy Agency, Vienna, 241.
Stebbings, R. F. 1976, *Science*, **193**, 537.

J. Astrophys. Astr. (2004) **25,** 103–113

TreePM Method for Two-Dimensional Cosmological Simulations

Suryadeep Ray
Harish-Chandra Research Institute, Chhatnag Road, Jhunsi, Allahabad 211019, India.
e-mail: surya@mri.ernet.in

Received 2004 June 23; accepted 2004 December 20

Abstract. We describe the two-dimensional TreePM method in this paper. The 2d TreePM code is an accurate and efficient technique to carry out large two-dimensional N-body simulations in cosmology. This hybrid code combines the 2d Barnes and Hut Tree method and the 2d Particle–Mesh method. We describe the splitting of force between the PM and the Tree parts. We also estimate error in force for a realistic configuration. Finally, we discuss some tests of the code.

Key words. Gravitation—methods: numerical—cosmology: large scale structure of the universe.

1. Introduction

It is believed that large-scale structures in the Universe have formed from the gravitational amplification of initial seed density perturbations. Evolution of density perturbations at scales smaller than the Hubble radius in an expanding background can be studied in the Newtonian limit in the matter-dominated regime. Linear theory can be used to study the growth of small perturbations in density. But in the absence of analytical methods, numerical simulations are the only tool available for studying clustering in the non-linear regime. The last two decades have seen a rapid development of techniques of cosmological simulations as well as computing power and the results of these simulations have provided valuable insight into the study of structure formation.

A number of attempts have been made over the past decade to model the non-linear evolution of constructs like the two-point correlation function using certain non-linear scaling relations (Hamilton *et al*. 1991; Nityananda & Padmanabhan 1994). In these relations, the evolution of the correlation function can be divided into three distinct regimes (Padmanabhan 1996)—the linear regime, the intermediate regime and the non-linear regime. Clearly, a large dynamic range is required in any N-body simulation in order to address the issue in all the three regimes under consideration. It has been pointed out (Bagla, Engineer & Padmanabhan 1998; Munshi & Coles 1998) that by simulating a two-dimensional system a much higher dynamic range can be achieved as compared to a complete three-dimensional simulation with similar computational resources.

The simplest N-Body method that has been used for studying clustering of large scale structure is the Particle–Mesh method. It has two elegant features in that it provides

periodic boundary conditions by default, and the force is softened naturally so as to ensure collisionless evolution of the particle distribution. However, softening of force done at grid scale implies that the force resolution is very poor. In particular, this limits the dynamic range over which we can trust the results of the method (Bouchet & Kandrup 1985; Bagla & Padmanabhan 1997).

A completely different approach to the problem of computing force is used in the Tree method. In this approach we consider groups of particles at a large distance to be a single entity and compute the force due to the group rather than sum over individual particles. There are different ways of defining a group, but by far the most popular method is that due to Barnes and Hut (1986).

Several attempts have been made to combine the high resolution of a Tree code with the natural inclusion of periodic boundary conditions in a PM code (Xu 1995; Bode & Ostriker 2003; Dubinski *et al*. 2004). The TreePM method in three dimensions is a hybrid N-body method which attempts to combine the same features (Bagla 2002). The basic motivation for developing methods of this kind is to improve the acceptable dynamic range of simulations without a proportionate increase in computational requirements. In this paper, we describe the TreePM method for a two-dimensional system.

The plan of the paper is as follows: Section 2 introduces the basic formalism of both Tree and Particle–Mesh codes. Section 3 describes the modelling of the force in two dimensions. Section 4 gives the mathematical model for splitting the force in two dimensions between the Tree force and the Particle–Mesh force components. Section 5 describes the softening scheme used for the 2d force and we analyse errors in force for the 2d TreePM code in section 6. We discuss the integration of the equations of motion that we use in the 2d TreePM code in section 7. We also describe a test for self-similar evolution of power law spectra in the same section. We present some results of a 2d TreePM simulation run in section 8. A discussion of the relative merits of the TreePM code and a PM code is also given. Computational requirements of our implementation of the 2d TreePM code are discussed in section 9.

2. A review of the Tree and the Particle–Mesh methods

2.1 *The Tree method*

We use the same method as the Barnes & Hut (1986) Tree code in our implementation of the 2d TreePM code. In a 2d Tree code the simulation area is taken to be a square. If this were to represent the stem of a tree, then it will be subdivided at each stage into smaller squares (branches) till we reach the particles (leaves). To construct the tree we add particles to the simulation area and subdivide any cell that ends up with two particles (Barnes 1986).

The force on a particle is computed by adding contribution of other particles or of cells. If a cell is too close to the particle, or if it is too big, we consider the subcells of the cell in question instead. The decision is made by computing a quantity θ and comparing it with a threshold θ_c:

$$\theta = \frac{d}{r} \leq \theta_c, \tag{1}$$

where d is the size of the cell and r is the distance from the particle to the centre of mass of the cell. The error in force increases with θ_c.

The number of terms that contribute to the force of a particle is much smaller than the total number of particles for most choices of θ_c and this is where the Tree method gains on a direct-force-summation method.

We will use the Barnes & Hut (1986) Tree code, as already mentioned. A crucial change to the standard tree walk is that we do not follow nodes representing cells that do not have any spatial overlap with the region within the threshold radius ($r_{\rm cut}$, defined later) for computing the short range force.

2.2 *The Particle–Mesh method*

A Particle–Mesh (PM) code is the obvious choice for computing long range interactions. A PM code adds the construct of a regular grid to the distribution of particles. The density field represented by particles is interpolated onto grid points and the Poisson equation is solved in Fourier space. The force is then interpolated back to the positions of particles. Use of a grid makes forces inaccurate at the grid scale and smaller scales. In this scheme, the mesh and the weight function (Cloud-in-Cell (CIC) in our case) used for interpolation between the grid and particle positions are the main sources of anisotropy. However, we use the Particle–Mesh method only for computing the long range force and errors at small scales do not contribute significantly. Also, by *deconvolving* the interpolating function (Bagla & Ray 2002), we reduce errors due to anisotropy effects substantially.

3. The gravitational force in two dimensions

When we go from three to two dimensions, we have, in principle, two different ways of modelling the system (Bagla, Engineer & Padmanabhan 1998):

(1) We can consider two-dimensional perturbations in a three-dimensional expanding Universe. Here we take the force between particles to be $1/r^2$ and assume that all particles (representing perturbations) and their velocities are confined to a single plane at the initial instant.
(2) We can study perturbations that do not depend on one of the three coordinates, *i.e.*, we start with a set of infinitely long straight "needles" all pointing along one axis. The force of interaction then falls as $1/r$. The evolution keeps the "needles" pointed in the same direction, and we study the properties of clustering in an orthogonal plane. Particles in the N-body simulation represent the intersection of these "needles" with this plane.

In both of these approaches, the Universe is three-dimensional and the background is expanding isotropically. Following earlier studies (Bagla *et al.* 1998; Filmore & Goldreich 1984; Munshi & Coles 1998), we choose the second of the two options.

More specifically, in order to obtain the force due to perturbations in a plane, we solve the Poisson equation for the perturbed part of the gravitational potential in two dimensions, whereas the unperturbed background is still the three-dimensional *spherically symmetric* Friedman Universe. Thus the perturbations are described by the *mass per unit length*, where this length is in the direction orthogonal to the two dimensions considered here.

The gravitational force due to a particle (or a needle) situated at the origin in two dimensions then has the form:

$$\mathbf{f}(\mathbf{r}) = -\left[\frac{Gm}{r^2}\right]\mathbf{r}. \tag{2}$$

Here G is the gravitational coupling constant and m is the mass per unit length of the "needle" represented by the particle.

4. The mathematical model for the 2d TreePM code

We split the $1/r$ force into a long range force and a short range force in a manner identical to that for the three-dimensional TreePM force (Bagla 2002). We compute the long range force in Fourier space and the short range force in real space. Following Ewald's method (Ewald 1921), the gravitational potential can be split into two parts in Fourier space:

$$\begin{aligned}\phi_k &= -\frac{2\pi G\rho_k}{k^2} \\ &= -\frac{2\pi G\rho_k}{k^2}\exp\left(-k^2r_s^2\right) - \frac{2\pi G\rho_k}{k^2}\left[1-\exp\left(-k^2r_s^2\right)\right] \\ &= \phi_k^l + \phi_k^s, \end{aligned} \tag{3}$$

$$\phi_k^l = -\frac{2\pi G\rho_k}{k^2}\exp\left(-k^2r_s^2\right), \tag{4}$$

$$\phi_k^s = -\frac{2\pi G\rho_k}{k^2}\left[1-\exp\left(-k^2r_s^2\right)\right], \tag{5}$$

where ϕ^l and ϕ^s are the long range and the short range potentials, respectively. The splitting is done at the scale r_s.

The expression for the 2d short range force in real space is

$$\mathbf{f}^s(\mathbf{r}) = -\exp\left[-\frac{r^2}{4{r_s}^2}\right]\frac{Gm}{r^2}\mathbf{r}. \tag{6}$$

The above equations describe the mathematical model for force in the 2d TreePM code. The long range potential is computed in Fourier space, just as in a PM code, but using equation (4) instead of equation (3). This potential is then used to compute the long range force. The short range force is computed directly in real space using equation (6). This is computed using the Tree approximation. The short range force falls rapidly at scales $r \gg r_s$ and hence we need to take this into account only in a small region around each particle. We call the scale upto which we add the small-scale force as $r_{\rm cut}$.

Evaluation of the short range force can be time-consuming. To save time, we compute an array containing the magnitude of the short range force at the outset. This procedure is identical to that followed in the 3d TreePM code (Bagla 2002). The force between any two objects, particle–cell or particle–particle, is then computed by linearly interpolating between the nearby array elements followed by multiplication by the unit vector $\mathbf{r}$. It is necessary for the array to sample the force at sufficiently closely spaced values of r in order to keep interpolation errors in control.

5. Softening of the force

We need to soften the 2d gravitational force at small scales in order to ensure *collisionless evolution* of the particle distribution in a cosmological simulation. We have considered two schemes for softening of the force at small scales:

1) **Plummer softening**: The force, in this case, will be given by

$$\mathbf{f}(\mathbf{r}) = -\frac{1}{(r^2+\epsilon^2)}\mathbf{r}, \tag{7}$$

where ϵ is the softening length.

2) **Cubic spline softening**: In this case, we solve the Poisson equation in two dimensions with the force due to a point mass replaced by that exerted by an extended mass distribution represented by the following:

$$\rho(r) = mW(r,\epsilon). \tag{8}$$

Here $W(r,\epsilon)$ is the normalised spline kernel used in the SPH formalism (Monaghan 1992) with ϵ the smoothing length.

$W(r,\epsilon)$ has the following form in two dimensions.

$$W(r,\epsilon) = \left(\frac{40}{7\pi\epsilon^2}\right)\begin{cases} 1-6\left(\frac{r}{\epsilon}\right)^2+6\left(\frac{r}{\epsilon}\right)^3 & 0 \geq \frac{r}{\epsilon} \leq 0.5, \\ 2\left(1-\frac{r}{\epsilon}\right)^3 & 0.5 < \frac{r}{\epsilon} \leq 1.0, \\ 0 & \frac{r}{\epsilon} > 1.0. \end{cases} \tag{9}$$

Solving the Poisson equation and using relevant boundary conditions for the potential and its first derivative (*i.e.* the force) to obtain the constants of integration, we get the cubic spline softened potential and then obtain the force $\mathbf{f}$ as a gradient of the potential.

$$\mathbf{f}(\mathbf{r}) = \begin{cases} -\left\{10-\frac{30r^2}{\epsilon^2}+\frac{96r^3}{5\epsilon^3}\right\}\frac{4Gm}{7\epsilon^2}\mathbf{r} & 0 \geq \frac{r}{\epsilon} \leq 0.5; \\ -\left\{\frac{80}{\epsilon^2}-\frac{160r}{\epsilon^3}+\frac{120r^2}{\epsilon^4}-\frac{32r^3}{\epsilon^5}-\frac{1}{r^2}\right\}\frac{Gm}{7}\mathbf{r} & 0.5 < \frac{r}{\epsilon} \leq 1.0; \\ -\frac{Gm}{r^2}\mathbf{r} & \frac{r}{\epsilon} > 1.0. \end{cases} \tag{10}$$

One can easily see that the spline softening has the advantage that the force becomes exactly Newtonian for $r > \epsilon$, while the Plummer force converges relatively slowly to the Newtonian form. Dehnen (2001) has argued that compact softening kernels are superior and we use the spline softened kernel in our implemention of the 2d TreePM code.

6. Error estimation

It is important to estimate the errors in numerical evaluation of force in a realistic situation, even though we do not expect errors to add up coherently. For a comprehensive

study in errors in force introduced by various components of the TreePM code we would like to refer to (Bagla & Ray 2002). Though the above-mentioned work is in the context of the 3d TreePM code, the key features of the analysis actually carry over to the 2d TreePM code as well.

We test errors for two distributions of particles: a homogeneous distribution and a clumpy distribution. For the homogeneous distribution, we use randomly distributed particles in a box. We use 1024^2 particles distributed on a 1024^2 grid. We compute the force using a reference setup ($r_s = 4$, $\theta_c = 0.01$, $r_{\rm cut} = 6r_s$) and the setup we wish to test ($r_s = 1$, $\theta_c = 0.5$, $r_{\rm cut} = 5r_s$). We compute the fractional error in force acting on each particle. This is defined as

$$\epsilon = \frac{|\mathbf{f} - \mathbf{f}_{\rm ref}|}{|\mathbf{f}_{\rm ref}|}. \tag{11}$$

Figure 1 shows the cumulative distribution of fractional errors. The curves show the fraction of particles with errors greater than ϵ. The thick line shows this for the homogeneous distribution. Error ϵ for 99% of particles is less than 4%. Results for the clumpy distribution of particles are shown by the dashed line. For this case, we used the output of a 2d power law ($n = 1$) simulation run in an Einstein deSitter background Universe with the TreePM code. Errors in this case are somewhat smaller as compared

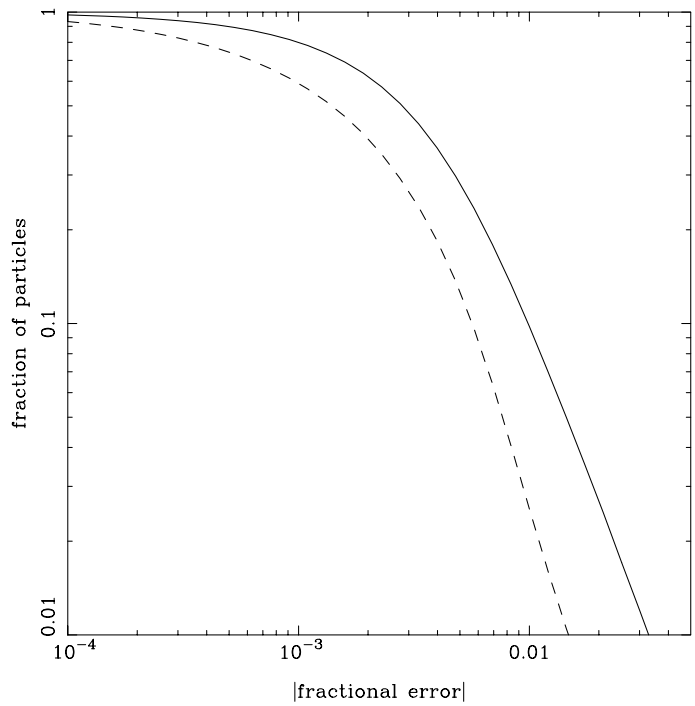

Figure 1. This figure shows the distribution of errors. The variation of the fraction of particles with error greater than a threshold, as a function of the threshold error, is plotted. The thick line marks error for a homogeneous distribution of particles and the dashed line shows the same for a clumpy distribution. These errors were measured with respect to a reference force determined with very conservative values of r_s and θ_c. This panel shows that 99% of the particles have fractional error in force that is less than 4% for the homogeneous distribution and less than 2% for the clumpy distribution.

to the homogeneous distribution for much the same reason as that for a 3d Tree code (Hernquist, Bouchet & Suto 1991) or a 3d TreePM code (Bagla 2002). Error ϵ for 99% of particles is less than 2% for the clumpy distribution.

7. Integrating the equation of motion

Our discussion so far has dealt only with the evaluation of force. This is the main focus of this paper as the key difference between the TreePM and other methods is in the scheme used for evaluation of force. However, for the sake of completeness, we give here details of integration of the equations of motion used in the code. We use an Einstein deSitter background cosmology for all our 2d simulations. The equations of motion are then given by the simple form

$$\ddot{\mathbf{x}} + 2\frac{\dot{a}}{a}\dot{\mathbf{x}} = -\frac{1}{a^2}\vec{\nabla}\phi,$$
$$\nabla^2\phi = 4\pi G a^2 (\rho - \bar{\rho}) . \tag{12}$$

Here $\mathbf{x}$ is the comoving coordinate, a is the scale factor, ϕ is the gravitational potential of perturbations, ρ is the total density and $\bar{\rho}$ is the average density of the Universe. Dot represents differentiation with respect to time. We can recast these equations in the following form:

$$\mathbf{x}'' + \frac{3}{2a}\mathbf{x}' = -\frac{3}{2a}\vec{\nabla}\psi,$$
$$\nabla^2\psi = \delta = \frac{\rho}{\bar{\rho}} - 1. \tag{13}$$

Here prime denotes differentiation with respect to the scale factor, δ is the density contrast and ψ is the appropriately scaled gravitational potential of perturbations.

The equations of motion are identical to that in three dimensions apart from the fact that all the vectors under consideration are two-dimensional vectors. The functional form of the gravitational force given by $\vec{\nabla}\phi$ is, of course, different.

One can see that the equations of motion contain a velocity dependent term and hence we cannot use the usual leap-frog method. We recast the leap-frog method so that velocities and positions are defined at the same instant (Bagla & Ray 2002). We solve the equation for velocity iteratively. Time step is chosen to be a small fraction of the smallest dynamical time in the system at any point in the evolution. The fraction to be chosen is fixed by checking for *scale invariance* in evolution of power law spectra: a simulation is repeated with different choices of timestep until we find the largest timestep for which we can reach the highly non-linear regime and retain scale invariance as well. We then use a timestep that is half of this largest timestep.

Figure 2 shows $\bar{\xi}$ as a function of $r/r_{\rm nl}(t)$ for several epochs obatined from a 2d TreePM simulation of a power law model with index $n = -0.4$. $r_{\rm nl}(t)$ is the scale which is going non-linear at time t and it varies in proportion with $a^{2/(n+2)}$ in the Einstein deSitter model. In the figure, we have only plotted $\bar{\xi}$ at scales more than two times larger than the artificial softening length used in the simulation. We can see that scale invariance holds for the spectrum over a wide range which means that we can probe the non-linear regime in gravitational clustering with a high degree of accuracy using the 2d TreePM code.

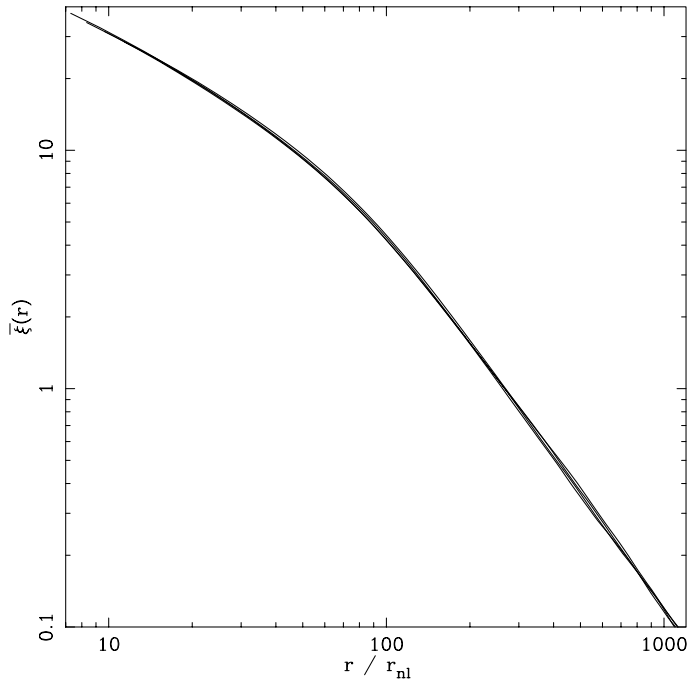

Figure 2. This figure shows $\bar{\xi}$ as a function of $r/r_{\rm nl}(t)$ for several epochs. Here $r_{\rm nl}(t)$ is the scale which is going non-linear at time t and it varies in proportion with $a^{2/(n+2)}$ in the Einstein deSitter model. The index of the power spectrum is $n = -0.4$. We have only plotted $\bar{\xi}$ at scales more than two times larger than the artificial softening length used in the simulation.

8. The 2d TreePM code vs. the 2d Particle–Mesh code

In this section, we present a brief comparison of the 2d TreePM and Particle–Mesh methods with the aim of highlighting the efficacy of our method in 2d cosmological simulations.

We ran a 2d simulation of a power law model with index $n = -0.4$ with 1024^2 particles on a 1024^2 grid in an Einstein deSitter background Universe with a PM code as well as with the TreePM code discussed here. For the TreePM run we used $r_s = 1$, $\theta_c = 0.5$ and softening parameter $\epsilon = 0.2$.

The top panel of Fig. 3 shows identical boxes from two independent simulations with the same initial conditions. The top left panel shows a simulation with the TreePM code and the top right panel shows the same for a PM code. The large scale structures appear to be the same in the two. However, one can see that there are significant differences at small scales when one plots the two-point correlation function for the two cases. $\bar{\xi}(r)$ is plotted as a function of scale r in the bottom left panel of Fig. 3. The thick line shows the correlation function for the TreePM simulation and the dashed line shows the same for the PM simulation. We have only plotted $\bar{\xi}$ at scales more than two times larger than the artificial softening length used in the TreePM simulation. The correlation function in the TreePM simulation matches with that from the PM simulation at large scales, but at scales of the order of unity (in grid units) and below, the TreePM simulation has a higher correlation function. This is to be expected because of the superior force resolution of the TreePM method as opposed to the PM force,

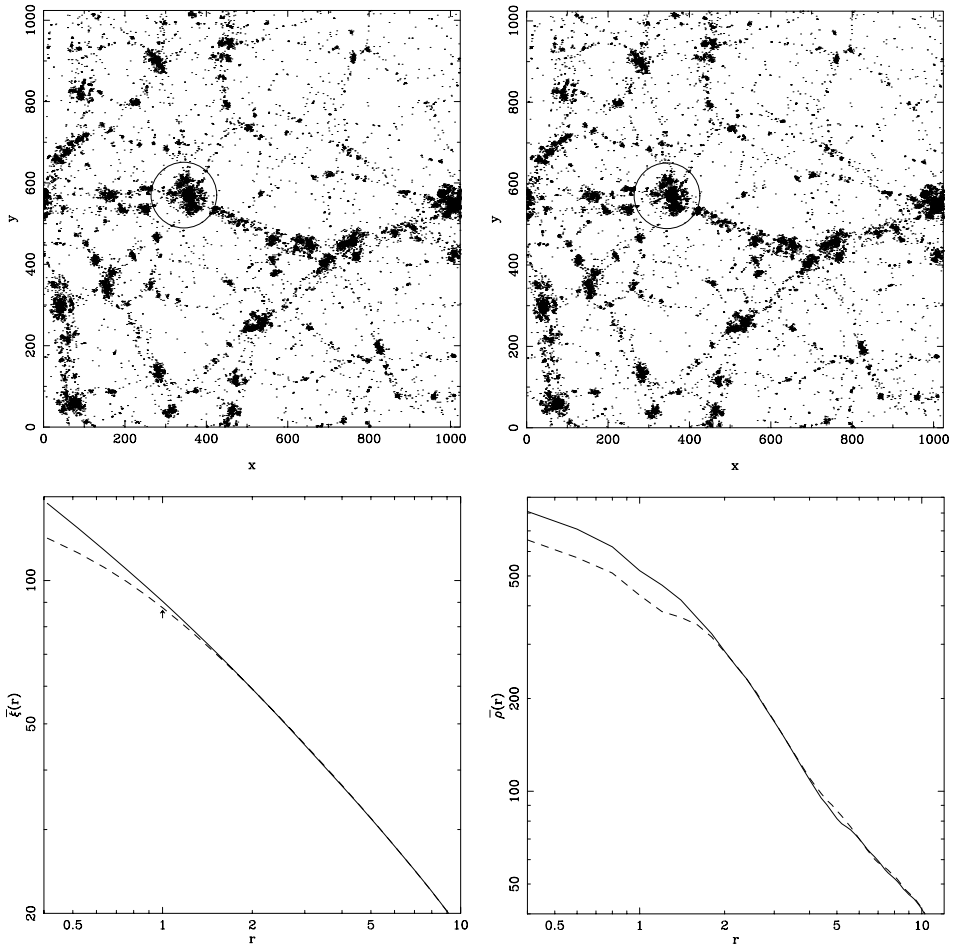

Figure 3. The top panel of this figure shows a box from a simulation of a power law model with index $n = -0.4$ for two cases. The top left panel shows the box from a TreePM simulation. For comparison, we have included the same box from a PM simulation of the same initial conditions in the top right panel. For convenience, we have randomly plotted only one out of every sixteen particles in the original simulations in the figure. The large scale structures appear to be the same in the two. We will look more closely at the circled haloes in both panels in the following discussion. The bottom left panel of this figure shows the averaged correlation function $\bar{\xi}(r)$ as a function of scale in grid units. The thick line shows this quantity for the TreePM simulation and the dashed line shows the same for the PM simulation. We have only plotted $\bar{\xi}$ at scales more than two times larger than the artificial softening length used in the TreePM simulation. The point marked by an arrow in the figure represents the larger softening scale for the PM code. The correlation functions match at large scales but the PM simulation underestimates the clustering at small scales. The bottom right panel is a plot which shows average density $\bar{\rho}$ within a sphere of radius r as a function of r (in grid units) for the two haloes circled in the top panel of this figure. Again, the thick line shows average density for the TreePM simulation and the dashed line shows the same for the PM simulation. Here also we have plotted average density at scales more than two times larger than the artificial softening length used in the TreePM simulation. The density profiles match at large scales as expected, but one can see that the TreePM simulation gives rise to haloes with higher central densities.

where the force is softened naturally at the grid scale. The scale of softening for the PM code is marked by an arrow in the figure.

We also study the density profiles of the two circled haloes in the top panel of Fig. 3. These particular haloes have been chosen as representatives for the analysis because they are reasonably large, dense and spherically symmetric. The bottom right panel of Fig. 3 shows average density $\bar{\rho}$ within a sphere of radius r from the halo centre plotted as a function of r for the two haloes. The full line shows the density profile for the halo from the TreePM simulation and the dashed line the same from the PM simulation. Here we have only plotted average density at scales more than two times larger than the artificial softening length used in the TreePM simulation. We can see that, though not visibly obvious from Fig. 3, the halo from the TreePM simulation is clearly far denser in the central region as compared to the halo from the Particle–Mesh simulation. The density profiles converge at some distance from the halo centres as expected.

9. Computational requirements

In this section, we describe the computational resources required for the present implementation of the 2d TreePM code. Given that we have combined the Tree and the PM codes, the memory requirement is obviously greater than that for either one code. We need four arrays for the PM part *i.e.*, for the potential and the force. The rest is exactly the same as a standard Barnes and Hut 2d Tree code. With efficient memory management, we need less than 75 MB of RAM for a simulation with 1024^2 particles on a 1024^2 grid. The number mentioned is for floating point variables. If we use double precision variables, our requirement will go up by a factor of two.

The time taken (per time step per particle) by the 2d TreePM code ($r_s = 1, \theta_c = 0.5$, $r_{\rm cut} = 4.5 r_s$, $N_{\rm particle} = 1024^2$, $N_{\rm grid} = 1024^2$) is of the order of 240 microseconds. This number was generated using a 2.4 GHz Xeon personal computer where the code was compiled with the Intel F90 compiler.

10. Discussion

In this paper, we have described the two-dimensional TreePM method in detail. Our method offers greater dynamic range and superior resolution as compared to a 2d Particle–Mesh method and can therefore probe the non-linear regime in two-dimensional cosmological simulations more effectively. We believe that a 2d TreePM code will allow us to explore a higher dynamic range in densities (and $\bar{\xi}$) for studying scaling relations in two-dimensions as compared to earlier work done using Particle–Mesh codes (Bagla, Engineer and Padmanabhan 1998). Work is in progress in this direction and will be reported elsewhere.

The 2d TreePM code is also amenable to parallelisation along the lines of the 3d TreePM code (Bagla 2003; Ray & Bagla 2004) and is likely to scale well.

Acknowledgement

The work reported here was done using the Beowulf at the Harish–Chandra Research Institute (http://cluster.mri.ernet.in).

I would sincerely like to thank J. S. Bagla for insightful discussions, suggestions and comments.

References

Bagla, J. S., Padmanabhan, T. 1997, *Pramana – Journal of Physics*, **49**, 161.
Bagla, J. S., Engineer, S., Padmanabhan, T. 1998, *ApJ*, **495**, 25.
Bagla, J. S. 2002, *JAA*, **23**, 185.
Bagla, J. S., Ray, S. 2002, *New Astronomy*, **8**, 665.
Bagla, J. S. 2003, *A parallel TreePM code*, *Numerical Simulations in Astronomy* (eds) K. Tomisaka and T. Hanawa, 2003, p. 32.
Barnes, J., Hut, P. 1986, *Nature*, **324**, 446.
Barnes, J. E. 1990, *J. Comp. Phys.*, **87**, 161.
Bertschinger, E. 1998, *ARA& A*, **36**, 599.
Bode, P., Ostriker, J. 2003, *ApJL*, **145**, 1.
Bouchet, F. R., Kandrup, H. E. 1985, *ApJ*, **299**, 1.
Dehnen, W. 2001, *MNRAS*, **324**, 273.
Dubinski, J., Kim, J., Park, C., Humble, R. 2004, *New Astronomy*, **9**, 111.
Efstathiou, G., Davis, M., Frenk, C. S., White, S. D. M. 1985, *ApJS*, **57**, 241.
Ewald, P. P. 1921, *Ann. Physik*, **64**, 253.
Filmore, J. A., Goldreich, P. 1984, *ApJ*, **281**, 1.
Hamilton, A. J. S., Kumar, P., Edward, L., Matthews, A. 1991, *ApJ*, **374**, L1.
Hernquist, L., Bouchet, F. R., Suto, Y. 1991, *ApJS*, **75**, 231.
Hockney, R. W., Eastwood, J. W. 1988, *Computer Simulation using Particles* (New York: McGraw Hill).
Monaghan, J. J. 1992, *Annu. Rev. Astron. Astrophys.*, **30**, 543.
Munshi, D., Coles, P. 1998, *MNRAS*, **293**, L68.
Nityananda, R., Padmanabhan, T. 1994, *MNRAS*, **271**, 976.
Padmanabhan, T. 1996, *MNRAS*, **278**, L29.
Ray, S., Bagla, J. 2004, astro-ph/0405220.
Springel, V., Yoshida, N., White, S. D. M. 2001, *New Astronomy*, **6**, 79S.
Xu, G. 1995, *ApJS*, **98**, 355.

J. Astrophys. Astr. (2004) **25,** 115–127

The Physics of E × B-Drifting Jets

Wolfgang Kundt[1] & Gopal Krishna[2]
[1]*IfA of Bonn University, Auf dem Huegel 71, D-53121 Bonn.*
e-mail: wkundt@astro.uni-bonn.de
[2]*National Centre for Radio Astrophysics / TIFR, Pune University Campus, Pune- 411 007.*
e-mail: krishna@ ncra.tifr.res.in

Received 2004 March 29; accepted 2005 January 10

Abstract. **E** × **B**-drifting jets have been generally ignored for the past 25 years even though they may well describe all the astrophysical jet sources, both on galactic and stellar scales. Here we present closed-form solutions for their joint field-and-particle distribution, argue that the observed jets are near equipartition, with extremely relativistic, monoenergetic $e^{\pm}$-pairs of bulk Lorentz factor $\gamma \lesssim 10^4$, and are first-order stable. We describe plausible mechanisms for the jets' **(i)** formation, **(ii)** propagation, and **(iii)** termination. Wherever a beam meets with resistance, its frozen-in Poynting flux transforms the delta-shaped energy distribution of the pairs into an almost white power law, $E^2 N_E \sim E^{-\epsilon}$ with $\epsilon \gtrsim 0$, via single-step falls through the huge convected potential.

Key words. Jet sources—monoenergetic beams—**E** × **B**-drift—unified scheme.

1. Background

Pair-plasma jets with ultra-relativistic bulk motion have been proposed twenty-five years ago by one of us (Kundt 1979), then jointly elaborated by us (Kundt & Gopal-Krishna 1980). They were also proposed by Morrison (1981), but have usually not been mentioned (cf. Begelman *et al*. 1984, 1994). Despite intermediate progress reported, e.g., in Kundt & Gopal-Krishna (1986), Blome & Kundt (1988), Baumann (1993), and in Kundt (1996, 2004), they have been treated with a healthy scepticism by the community, cf. Blandford (2001), and Beresnyak *et al*. (2003), with a few notable exceptions, e.g., Reipurth & Heathcote (1993), Scheuer (1996), Prieto *et al*. (2002), Brunetti (2002), and Stawarz (2003). A possible reason for this lack of widespread acceptance may have been a concern about whether or not the beams allowed a stable transport of a broad energy distribution of high-energy charges, in the form of an ordered **E** × **B**-drift. The beams are indeed unlikely to transport a broad distribution.

Instead, their Poynting-flux-flooded formation regions are expected to generate particle distributions at least as sharp in 4-momentum as relativistic Maxwellians, and an onsetting **E** × **B**-drift will further sharpen the narrow distribution towards a delta-type one. Such equipartition pair-plasma flows convect half of their energy as a stationary

Poynting flux which is ready – wherever stalled – to broaden the particle distribution into an almost white power law, starting with Lorentz factors of order 10^2 at their bottom end, and extending up to Lorentz factors of order 10^6, in the form of a long high-energy tail whose radiated power peaks at the top end whereas its energy density peaks near its bottom end. During undisturbed propagation, such beams are loss-free on Mpc scales except for minor inverse-Compton losses on the radiation background. Note that peripheral tapping of a beam can reveal its monoenergetic distribution, as in Sgr A*: the convected fields vanish at the channel wall.

We shall present exact solutions for such monoenergetic beams in section 2, and show that they are stable to first order. In the two subsequent sections, we shall offer reasonings why such beams are expected to form naturally around magnetized rotators, *i.e.*, around rapidly rotating stars as well as in the centers of galactic disks, and why their radiation is expected to take the form of broad power-laws, from the radio to the X-ray and gamma-ray regime, with certain emission dips and excesses which can be understood as due to strong anisotropies in their emission patterns at high frequencies. This uniform model covers the observed jets from

(a) newly forming stars (or YSOs),
(b) forming white dwarfs, inside planetary nebulae (PNe),
(c) young binary neutron stars (within light or heavy accretion disks), and
(d) the nuclear-burning centers of galactic disks (or AGN).

Note that monoenergetic relativistic electron beams have just been produced in the lab: Katsouleas (2004).

A few extreme and/or controversial jet sources are discussed in section 5.

2. Solving the beam equations

As has already been argued – and will be elaborated in the next two sections – the beams of the jet sources are expected to consist of overall electrically neutral and current-free configurations of electrons and positrons at large Lorentz factors $\gamma > 10^2$, convecting toroidal magnetic fields and "radial" electric Hall fields w.r.t. the roughly cylindrical geometry of a beam segment. In reality, such segments of stationary flow have an approximately conical shape, but will be approximated by us, for simplicity of presentation, by cylinder segments. Note that even a conical beam does not have (adiabatic expansion) losses when moving through a (strictly) vacuum channel.

We describe a beam segment by cylindrical coordinates z, s, φ, with z growing parallel to the beam axis, and s, φ being polar coordinates in the cross-sectional planes. In these coordinates, Maxwell's (stationary, axially symmetric) equations $\boldsymbol{\nabla}\cdot\mathbf{E} = 4\pi\rho$, $\boldsymbol{\nabla}\times\mathbf{B} = (4\pi/c)\mathbf{j}$, $\boldsymbol{\nabla}\times\mathbf{E} = 0 = \boldsymbol{\nabla}\cdot\mathbf{B}$ yield respectively:

$$\partial_s(sE_s) = 4\pi s\rho\,, \tag{1}$$

$$\partial_s(sB_\varphi) = 4\pi s\rho\beta_z\,, \qquad \partial_s B_z = -4\pi\rho\beta_\varphi\,, \tag{2}$$

with $\boldsymbol{\beta} := \mathbf{v}/c$, and with all quantities only depending on the radial coordinate s. We restrict our attention to $\mathbf{E}\times\mathbf{B}$-drifting charges, for which the acceleration

$$c(\gamma\boldsymbol{\beta})^{\cdot} = (e/m_e)(\mathbf{E} + \boldsymbol{\beta}\times\mathbf{B}) \tag{3}$$

vanishes, yielding

$$E_s = B_\varphi \beta_z - B_z \beta_\varphi \,. \tag{4}$$

For realistic solutions with net charge and current zero, we have the additional boundary conditions at $s = 0$ and R (:= beam radius):

$$\begin{aligned} (sE_s)(0) &= 0 = (sE_s)(R)\,, \\ (sB_\varphi)(0) &= 0 = (sB_\varphi)(R)\,, \end{aligned} \tag{5}$$

and the general stationary, cylindrically symmetric solution can be Fourier-expanded w.r.t. s/R:

$$sE_s, sB_\varphi \sim \sum_{k\geq 1} C_k \sin(k\pi s/R), \tag{6}$$

of which the first (ground) term already contains most of the physical information.

For large γ ($>10^2$), we have $|\beta_\varphi| \ll \beta_z \approx 1$, and the leading term of the expansion reads:

$$\begin{aligned} E_s &\approx B_\varphi \approx C \sin(\pi s/R)/s\,, \\ \rho &\approx (\pi C/R)\cos(\pi s/R)/s \approx j_z/c\,, \qquad B_z \approx \text{const}\,. \end{aligned} \tag{7}$$

It expresses a uniform flow in z-direction, with a positive (or negative) net charge density inside of $R/2$, and the opposite charge density dominating for $s > R/2$, and correspondingly with a net (positive, negative) current density (inside, outside) of $s = R/2$, both of which peak at both ends, on the axis as well as at the periphery; see Fig. 1.

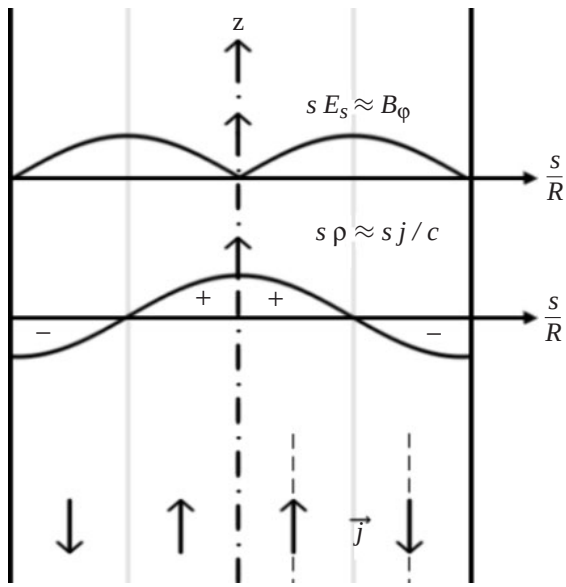

Figure 1. Cross section through (the ground mode of) a beam segment, showing the radial dependences of ρ, j, E_s, and B_φ.

This solution is as simple and transparent as one could have imagined; the involved charge densities ρ are a tiny fraction of those composing the beam: $\rho/en_e = 10^{-9.2}\gamma_3/L_{44}^{1/2}$, *i.e.*, correspond to a minute distortion of charge neutrality. For a jet of power L and cross-sectional area A, (ram) pressure equipartition (among particles and fields) requires

$$\gamma n_e m_e c^2 = (E^2 + B^2)/8\pi \approx B^2/4\pi \approx L/Ac\,, \tag{8}$$

where n_e is the electron number density. (Equipartition is plausible from what we have said, and conforms with the observations, cf. Begelman *et al*. 1984.) Note that the convected electric potential $\Phi = \int E_s ds$ for typical jets can be gigantic, of order $e\Phi \approx e(\pi L/c)^{1/2} = 10^{19.5}\,\mathrm{eV}\; L_{44}^{1/2}$; we shall see below that it can generate a high-energy tail reaching up to electron Lorentz factors of 10^6 and more. Note also that Φ is scale-invariant: A has dropped out, via s^2; Φ depends solely on the source power L, which is still large for stellar jet sources, with $L \approx 10^{35\pm1}$ erg/s.

Realistic jets have $\beta_z < 1$ and $\beta_\varphi \neq 0$. For them, a straight-forward calculation, starting from equation (4) and using the integrated equations (1,2), leads to

$$\rho\beta_\varphi = \partial_s\left[\int ds s^{-2}\partial_s\left(\int ds\rho s\right)^2 - \partial_s\left(\int ds\rho\beta_z s\right)^2\right]^{1/2}$$

$$\approx \partial_s\left[\int ds s^{-2}\partial_s\left(\int ds\rho s\right)^2\right]^{1/2}\Big/\gamma\,, \tag{9}$$

the latter for $\beta_z \approx 1 - 1/2\gamma^2$. It shows that β_φ is small of order $1/\gamma$, *i.e.*, that ordered spiralling of the charges should be unimportant in high-energy jets. This result must not be confused with the existence of helical beams, in interaction with turbulent (heavy) environs.

So far, we have assumed strictly monoenergetic beams, with $\beta_z = \mathrm{const}$, which cannot be expected under realistic conditions. Charges whose β_z deviates from (the local value of) E_s/B_φ will violate equation (4), and start moving radially inward or outward, depending on their sign, whereby both (hard, soft) charges move (inward, outward) for opposite signs. In each case, a glance at equation (3) shows that the radially moving charges of deviant γ must fall through the electric potential Φ such that their 4-momentum is adjusted to the (locally) appropriate value for a stationary drift: more energetic ones lose, less energetic ones gain in energy, independent of the sign of their charge. This key stability is intuitive already on energetic grounds, from the shape of Φ, but follows directly from (3) because any radial drift implies an acceleration in $\pm z$-direction, via the $e(\mathbf{E} + \boldsymbol{\beta}\times\mathbf{B})$-term (whose sign changes with the sign of e, and likewise with the sign of $\boldsymbol{\beta} - \langle\boldsymbol{\beta}\rangle$).

Note that in principle, β_z could have been radius-dependent so that a finite spread in γ-s is transported by the beam. But such a fine-tuning of fields and particles is unlikely to be stable, after what we have just found: The wings of a distribution (in γ) are removed during short distances via radial falls (of proper sign) through the convected **E**-fields – short of order $10^{-10}\ R$ because the **E**-fields are gigantic, as shown below equation (8) – so that individual particle energies are stabilized quickly.

3. Forming the jets

We shall now argue that monoenergetic beams – as have just been considered – are expected for the cosmic jet sources, *i.e.*, are not grossly overidealized.

To begin with, there has to be an abundant source of relativistic $e^{\pm}$: Magnetic reconnections, leading to cavities with dominating Poynting flux (because weak fields would simply be anchored by the charges, hence would not decay) are familiar from the solar surface, and are correspondingly expected near the inner edges of stellar accretion disks, and near the innermost, strongly shearing galactic disks, in scaled-up proportions (Kundt 1996, 2002). Such coronal magnetospheric reconnections in non-rigid rotators are expected to involve comparable powers to thermal emissions – cf. the magnetoid model of Ozernoy & Usov (1977) – because they drain on comparable energy reservoirs (controlled by equipartition). They can easily fill up the local hot bubble seen as the Broad Line Region (BLR) in AGN sources, which discharges to both sides of the disk through Blandford and Rees's (1974) deLaval nozzles, in the form of a supersonic twin-jet (Kundt 1996), see Fig. 2.

Once we deal with a central hot bubble filled with relativistic pair plasma, what will its energy distribution be like? In the laboratory, atomic beams are routinely cooled by shooting at them with a laser beam. In the BLR, the charges are post-accelerated by the simultaneously generated Low-Frequency (LF) waves of the central magnetized

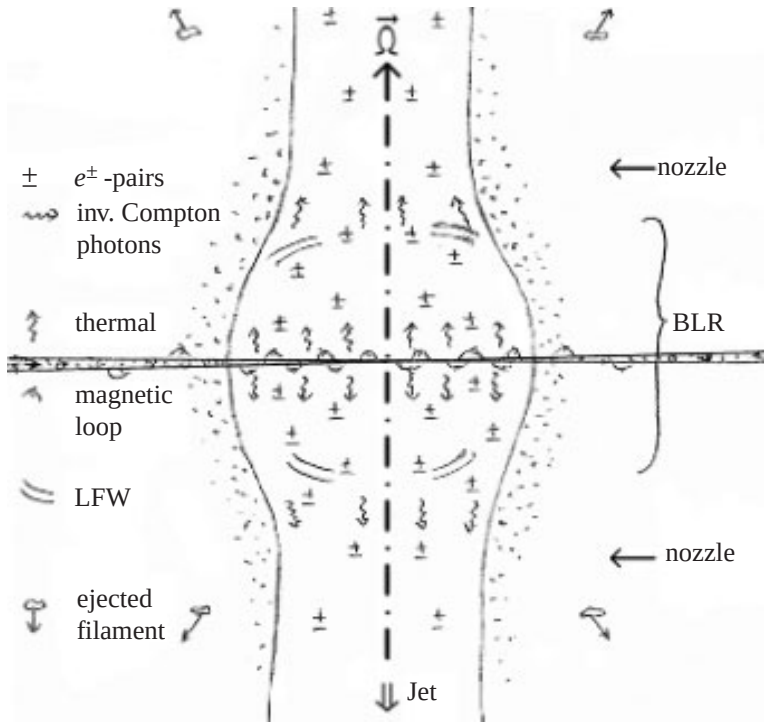

Figure 2. Sketch of a plausible central engine: Coronal magnetic reconnections create $e^{\pm}$-pairs, the warm central (star and/or) disk emits photons, low-frequency waves post-accelerate the escaping $e^{\pm}$, and the latter boost the thermal photons to high-energy γ-rays. An ambient thermal bulge serves as the deLaval nozzle from which a twin jet emerges, along the spin axis of the central rotator; in galactic-center sources, this region is observed as the BLR.

rotator, of angular frequency ω reaching down to some $10^{-4}\mathrm{s}^{-1}$, hence of (large) strength parameter f:

$$f := eB/m_e\, c\omega = 10^{14.2} B_3/\omega_{-4} \tag{10}$$

for a typical coronal field strength B measured in KG; with $B_3 := B/10^3 G$, $\omega_{-4} := \omega/10^{-4}\mathrm{s}^{-1}$. From the windzones of pulsars (like the Crab) we believe to have learned that the LF waves sweep the charges up in energy to Lorentz factors γ of order $f^{2/3} = 10^{9.5}(B_3/\omega_{-4})^{2/3}$, in the absence of damping (Kulsrud *et al*. 1972; Kundt 1986).

Damping occurs in the BLR through the equally present thermal (HF) radiation, a narrow "bump" between IR and X-rays, via inverse-Compton losses which truncate a distribution towards high energies, because they scale as γ^2. For class (d) (of AGN), these inverse-Compton losses are so strong that only some 10% of them are radio-loud and show jets.

As the outgoing charges in the (Thomson-opaque) BLR interact with both the LF and HF photons, their momentum distribution (away from the central engine) is expected to evolve towards a relativistic Maxwellian in radial direction, or even sharper, of Lorentz factor $\gamma > 10^2$ (corresponding to brightness temperatures in excess of 10^{12} K). Such high Lorentz factors are:

(a) expected, after equation (10),
(b) are indicated by the overall energetics,
(c) by an avoidance of the inverse-Compton catastrophe,
(d) by the statistics of superluminal speeds (Kundt 2004), and
(e) by LF intraday variability, cf. Singal & Gopal-Krishna (1985), Wagner & Witzel (1995), but also Jauncey *et al*. (2003) who prefer an interpretation via interstellar scintillations.

When the charges leave the BLR and approach the deLaval nozzle – formed naturally by the obstructing plasma of the ambient circumstellar medium or central galactic bulge respectively, whose inertia (in pressure balance) scales inversely as its temperature T, *i.e.*, is $10^{8.3}/T_4$ times larger – their narrow momentum distribution will be channeled into a monoenergetic one, as inferred above from equation (3), with dominating Poynting flux which carries at least half the energy.

4. Discharging the jets

Once the highly-relativistic $e^{\pm}$-pairs from the BLR enter a vacuum channel, rammed by preceding generations of charges, they form an almost loss-free, monoenergetic $\mathbf{E}\times\mathbf{B}$-drifting beam as calculated explicitly in section 2 whose only losses are inverse-Compton collisions on the radiation background obeying:

$$l_{\mathrm{deg}} := \gamma/\gamma' = 3m_e c^2/4\sigma_T u_{3K}\gamma = \mathrm{Mpc}/\gamma_6(1+z)^4, \tag{11}$$

where l_{deg} is the degradation e-folding length, σ_T the Thomson cross section, u_{3K} the energy density of the 3 K background radiation, and $\gamma_6 := \gamma/10^6$, (Kundt 2004). For a bulk Lorentz factor $\gamma \lesssim 10^4$, thought to be realistic for most jet sources, inverse-Compton losses on Mpc scales are therefore ignorably small at redshifts $z < 2$.

Note that a monoenergetic beam has no collisional losses between its member charges – because they have vanishing relative velocities – nor dynamic-friction losses, for the same reason. Such internal-friction losses would in any case be ignorably small, because of the beam's extremely small electron-number density:

$$n_e = L/A\gamma m_e c^3 = 10^{-8}\,\mathrm{cm}^{-3}(L/A\gamma)_{-3.5}\,. \tag{12}$$

During its propagation through a vacuum channel, a monoenergetic beam has only the inverse-Compton losses described by equation (11).

Conditions change when a beam encounters obstacles, in the form of (heavy) channel-wall material or channel intruders or obstructing material at its downstream end, its 'head'. Such obstructing plasma tends to be highly conductive, hence forbids penetration of electric and magnetic fields. The guiding toroidal magnetic field then gets compressed like the windings of a coil, and so are the convected charge clouds. Both electric charges and currents pile up against such a conducting wall, changing the field geometry in a way conveniently to be described by mirror charges (of opposite sign), and mirror magnetic fields (of same sign), see Fig. 3.

Note that a charge-symmetric beam cannot be arrested or reflected by electric fields alone; the latter can only redistribute the energies among the charges. The reflection of a (neutral) beam at its head is achieved by a changing geometry of both fields,

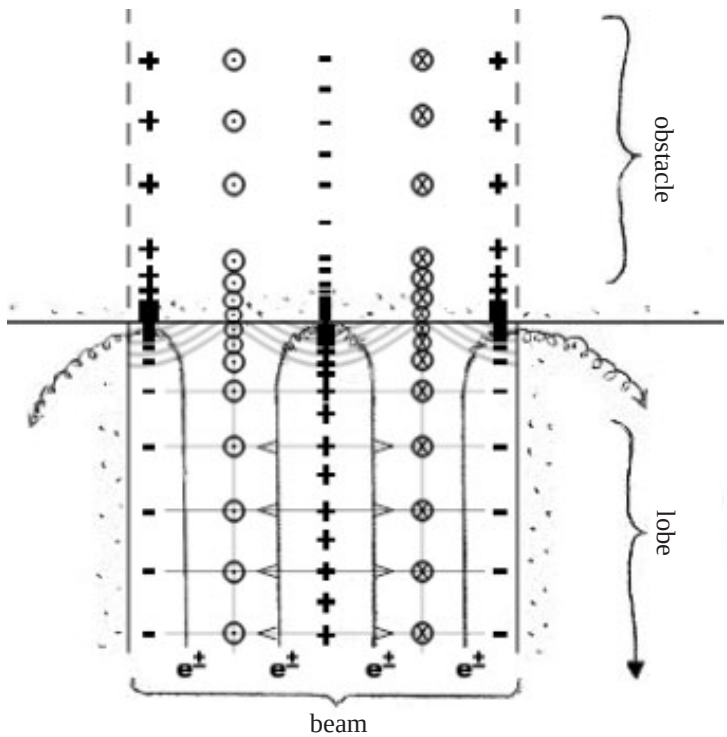

Figure 3. Simplified cross section through a beam head, sketching the distributions of relativistic electrons ($e^{\pm}$), electric and magnetic fields, mirror charges and fields (on the side of the obstructing ambient plasma), and particle orbits. Omitted are the motions of the stalled charges escaping from the impact center, whereby they are post-accelerated by the huge convected potential.

electric and magnetic, such that the formerly quasi-stationary $\mathbf{E} \times \mathbf{B}$-drift in forward direction is diverted, partially towards the beam's axis, and partially sideways towards its periphery (Fig. 3). At the same time, the bulk speed of the charges is reduced, from supersonic to subsonic, whereby straight-line motions change into gyrations. But now the charges are post-accelerated by the huge, convected electric potential, in the form of a space-charge limited flow whose relativistic version was first treated by Michel (1974), in application to pulsar polar-cap discharges.

Michel's derivation of the relativistic generalization of Child's Law restricts itself to stationary, one-dimensional, one-fluid discharges inside a low-density plasma whose asymptotic speed is extremely relativistic, and whose asymptotic charge density realizes force-freeness, also known as Goldreich–Julian (1969) density, or Hones–Bergeson (1965) density. The derivation takes care of the fact that due to distributed screening, individual charges fall only through a tiny fraction of the available potential Φ. This fraction, of order the square root of $e\Phi$ (in units of the electron rest energy), results as a consequence of Maxwell's equations plus conservation of energy, by integration along particle orbits through the (magnetized) polar gap:

$$\gamma_\infty \approx (8\gamma_\Phi)^{1/2}. \tag{13}$$

The electron Lorentz factor γ_∞ is reached exponentially towards the boundary of the polar gap, whose voltage Φ is assumed stabilized by unipolar induction.

In the present case of a stalled beam, the convected potential Φ has its peak near the impact center, somewhat enhanced by compression w.r.t. its convected value, together with a surrounding ring wall of opposite sign. The boosting arena is therefore neither 1-d, 1-fluid, nor stationary. Still, distributed screening will result in the square of the charges' Lorentz factor γ tending (as above) towards some multiple of the maximum available one, γ_Φ, and we expect the energy distribution in the stalled beam to acquire a high-energy power-law tail – after averaging over a spatial ensemble of discharges – reaching up from its convected value ($\gamma_{\rm beam} \lesssim 10^4$) all the way to its peak value, of order $(\gamma_\Phi)^{1/2} \lesssim 10^7$, see equation (8). At the same time, the charges of inappropriate sign (and same instantaneous flow direction) are decelerated to lower energies, extending the spectrum downward in energy below $\gamma_{\rm beam}$. This sudden change of the energy distribution, from delta-like to hard power-law, takes place wherever a beam is stalled by ambient plasma, thanks to its convected Poynting flux.

In this way, an almost loss-free, monoenergetic beam gets radiative whenever obstructed, with a broad power-law spectrum. A broad power law need not form, however, for peripheral tapping, in boundary-layer interactions.

A well-known phenomenological dichotomy among the jet sources relates to the location of their hotspots, and tends to be called by their Fanaroff and Riley class I or II. Eilek *et al*. (2002) have recently revised this classification into type A and type B, whereby class II is a subcase of type A, and speak of "straight" and "tailed" sources in the two cases. All jet sources start out "straight", their heads ramming supersonically into their ambient medium. During growth, the head's ram pressure drops as r^{-2} with distance r from the central engine, and the sound speed of the ambient medium often rises, so that beyond a certain distance – which differs from source to source – the head speed must pass from supersonic to subsonic w.r.t. the medium. From then on, the charges entering the terminating hotspot are no longer reflected (into their lobe) but continue coasting subsonically, in a gyrating mode, and can form a long, radiative "tail" (Gopal-Krishna *et al*. 1988, 1996).

In our understanding, this sonic transition marks the transition from Eilek type A to B. Beyond the decelerating hotspot, particle motions are no longer channelled or lossfree. The stalled jet material "engulfs" the ambient medium during relaxation, and squeezes it into small-filling-factor filaments, of huge relative mass densities ρ_j:

$$\rho_e/\rho_H = 6kT/m_H c^2 = 10^{-5.3} T_7 \tag{14}$$

(in pressure balance, where X-ray temperatures T have been inserted, via T_7). In this process, the pair plasma loses 1/3 of its injected energy, *i.e.*, decelerates significantly, and "entrains" the thermal inclusions at a maximum speed of $c\rho_e/\rho_H = 10^{-6} cT_7$, *i.e.*, leaves them practically in their former state of motion. There is no beam beyond the terminating hotspot, yet there is ordered streaming at less than $(2/3)c$.

5. Realistic jets

Our above treatment of astrophysical jets – being scale-invariant, and involving very similar central engines – is meant to apply to all (hundreds of) known jet sources: from

(a) newly forming stars,
(b) forming white dwarfs,
(c) young neutron stars and BHCs (which latter are held to be neutron stars inside of heavy accretion disks), and
(d) the compact centers of (active) galactic disks; as elaborated in Kundt (1996, 2002, 2004).

In all these cases, the central engine is (thought to be) a rotating magnet involving strongly sheared toroidal magnetic fields, whose intermittent reconnections supply abundant relativistic $e^{\pm}$-pair plasma, whose simultaneously emitted LFWs post-accelerate the pairs, and whose equally present thermal radiation cools the pairs, towards an outgoing relativistic Maxwellian and beyond. A deLaval nozzle forms automatically via the huge inertia of the ambient plasma, and the comoving Poynting flux sharpens the particle distribution to a monoenergetic one, and guides the pairs into the channels rammed by earlier generations. Such extremely relativistic beams are stabilized by their comoving Poynting flux, and by the inertia of the ambient plasma. This (generalized) "unified scheme" for all jet sources deviates in part from most other approaches but compares favourably by being more explicit, more uniform, and more stable, and by not invoking (energy-rising) stochastic accelerations. In the sequel, we will comment on a few well-studied sources standing out by their extreme properties.

The nearest active galactic nucleus is the center of our own galaxy, Sgr A*, the rotation center of the Milky Way disk. Its (unresolved) mass has been determined from the orbits of a few innermost stars as $10^{6.5\pm0.1} M_\odot$, its spectrum ranges from $10^{8.7}$ Hz to beyond 10 TeV, with an integrated luminosity of $10^{3.7} L_\odot$ peaking near GeV energies, and its output shows flares at IR and X-rays with variability timescales of $\lesssim$17 min (Kundt 1990, 2004; Mayer-Hasselwander *et al*. 1998; Melia & Falcke 2001; Genzel *et al*. 2003; Aharonian *et al*. 2004; Roy & Rao 2004). Are we seeing the innermost Galactic disk almost edge-on, whose present-day output reaches us at only $10^{-6.3}$ times its Eddington value? Is its feeding presently throttled by fountain-like evaporation of the innermost disk? In any case, the radio part of the spectrum of Sgr A*, at $\nu \lesssim 10^{13}$ Hz,

of slope $\alpha := \partial \log S_\nu / \partial \log \nu = 0.3$, signals monoenergetic synchrotron emission at Lorentz factor $\gamma \approx 10^4$, as does the Arc region (Anantharamaiah *et al*. 1991), whereas its enclosing emitter – Sgr A East – radiates a hard power-law spectrum at radio frequencies, as expected for stalled populations.

An extreme case among extragalactic jet sources is the giant radio galaxy 3C 445, as concerns lossfree transport through large distances. Prieto *et al*. (2002) emphasized the need for *in situ* electron acceleration inside the hotspots, based on optical (synchrotron) emission nearly 0.3 Mpc away from the nucleus. From our equation (11) it is clear that such a problem does not arise for $\mathbf{E} \times \mathbf{B}$-drifting beams. See also Brunetti (2002), Hardcastle *et al*. (2003), and Stawarz (2004) for similar well-studied sources.

An even more extreme jet source is the quasar 3C 273, almost unique among 10^3 known radio jets by its brightness and one-sidedness (Morrison *et al*. 1984; Kundt & Gopal-Krishna 1986; Jester *et al*. 2001, 2002). Does its head plough almost luminally into its CGM ($\beta_h \gtrsim 0.6$), and nearly towards us, with very little resistance in the (cosmic-ray?) halo of its host galaxy? Does its emitted spectrum soften on approach of its tip because of accumulating radiation losses, or because of increased beaming in forward direction (so that we observe a non-representative spectrum)? A rare source may well require a rare explanation.

Proceeding to stellar jet sources, there is the unique binary neutron star or BHC SS 433, whose interpretation has been controversial ever since its discovery as a jet source, in 1978 (cf. Kundt 1996; Fender 2003). Does it emit "bullets" of local-galactic composition, at largely super-Eddington power, or are its beams composed of pair plasma, like in all the other jet sources? Kundt (2004) interprets its moving optical and X-ray emission lines as emitted by the impacted wind matter of its massive companion star, which forms its channel walls, and which is dragged along by the relativistic flow at a fraction of the speed of light. In the latter interpretation, we deal with a 10^4-year young binary Galactic neutron star inside its SNR W 50, at a distance of 3 Kpc, whose (sub-Eddington) spindown power is still strong enough to prevent accretion from its disk onto its surface, and to blow pairplasma jets whose heads have already crossed the periphery of W 50.

That jets from Galactic binary neutron stars or BHCs may consist of pairplasma has been recently advocated by Kaiser & Hannikainen (2002), via detections of the redshifted 511 KeV pair-annihilation line in eight binary X-ray sources with jets. When compared with that same emission line from the Crab pulsar (Massaro *et al*. 1991), its redshift (of some 7%) is more likely gravitational redshift from a neutron star's surface, where the density of slow pairs should be vastly higher than anywhere downstream along the jet. Another indication of highly relativistic electrons in compact stellar sources is the superluminal X-ray jet in the microquasar XTE J1550-564, whose observed "deceleration" may have to be understood as a varying phase velocity (Corbel *et al*. 2002).

Finally, there are classes (b) (of PNe: Kundt 1996; Balick & Frank 2002), and (a) (of YSOs) which are hard to analyse because enshrouded by dense ionized, atomic, and/or molecular gas and dust. Among the few convincing (nonthermal) YSO candidates are two triple radio sources of (expansion) age $\lesssim 10^3$ yr, one of them S 68 in Serpens (Rodríguez *et al*. 1989), further some 23 often one-sided core radio jets in stellar bipolar flows, including L 1455 (Schwartz *et al*. 1985), and HH 111 (Reipurth & Heathcote 1993; Rodríguez & Reipurth 1994; Reipurth & Bally 2001), and the two-sided synchrotron jet from W3(OH) (Wilner *et al*. 1999). Note that in view of the

opacity effects, a reliable distinction between thermal and synchrotron radiation has not always been possible.

Acknowledgements

WK owes warm thanks to Christoph Hillemanns, Günter Lay, Ole Marggraf, and Christof Wenta for help with the electronic data handling, in connection with this communication, with his homepage, and with saving him from getting drowned by spam mail. Both authors are thankful to Paul Wiita for helpful criticism of an earlier version.

References

Aharonian, F. *et al*. (100 authors) 2004, VHE gamma rays from the direction of Sgr A*, *Astron. & Astrophys.*, **425**, L13–17.

Anantharamaiah, K. R., Pedlar, A., Ekers, R. D., Goss, W. M. 1991, Radio studies of the Galactic Centre II. The arc, threads and related features at 90 cm (330 MHz), *MNRAS*, **249**, 262–281.

Balick, B., Frank, A. 2002, Shapes and Shaping of Planetary Nebulae, *Ann. Rev. Astron. & Astrophys.*, **40**, 439–486.

Baumann, H. 1993, *Astrophysikalische Jet-Phänomene und ihre Deutung als Paarplasma-Strahlen*, Diplomarbeit Bonn.

Begelman, M., Blandford, R. D., Rees, M. J. 1984, Theory of extragalactic radio sources, *Rev. Mod. Phys*., **56**, 255–351.

Begelman, M., Rees, M. J., Sikora 1994, Energetic and Radiative Constraints on Highly Relativistic Jets, *Astrophys. J.*, **286**, L57–L60.

Beresnyak, A. R., Istomin, Ya. N., Pariev, V. I. 2003, Relativistic parsec-scale jets: I. Particle acceleration, *Astron. & Astrophys.*, **403**, 793–804.

Blandford, R. D. 2001, in *Particles and Fields in Radio Galaxies*, ASP Conference Series, **250**, 487–498.

Blandford, R. D., Rees, M. J. 1974, A 'Twin-Exhaust' Model for double Radio Sources, *MNRAS*, **169**, 399–415.

Blome, H.-J., Kundt, W. 1988, Leptonic Jets from Young Stellar Objects?, *Astrophys. & Space Sci.*, **148**, 343–361.

Brunetti, G. 2002, Non-thermal Emission from Extragalactic Radio Sources: a High-Resolution Broad-Band approach, in *The role of VLBI in Astrophysics, Astrometry and Geodesy*, (eds) F. Mantovani & A. Kus, *Nato Science Ser.* **135**, 2004, pp. 29-82. ArXiv: astro-ph/0207671.

Corbel, S., Fender, R. P., Tzioumis, A. K., Tomsick, J. A., Orosz, J. A., Miller, J. M., Wijnands, R., Kaaret, P. 2002, Large-Scale, Decelerating, Relativistic X-ray Jets from the Microquasar XTE J1550-564, *Science*, **298**, 196–199.

Eilek, J., Hardee, P., Markovic, T., Ledlow, M., Owen, F. 2002, On dynamical models for radio galaxies, *New Astron. Rev.*, **46**, 327–334.

Fender, R. 2003, Jets from X-ray binaries, *astro-ph*/0303339, 28 August.

Genzel, R., Schödel, R., Ott, T., Eckart, A., Alexander, T., Lacombe, F., Rouan, D., Aschenbach, B. 2003, Near-infrared flares from accreting gas around the supermassive black hole at the Galactic Centre, *Nature*, **425**, 934–937.

Goldreich, P., Julian, W. H. 1969, Pulsar Electrodynamics, *Astrophys. J.*, **157**, 869–880.

Gopal-Krishna, Wiita, P. J. 1988, Hot gaseous coronae of early-type galaxies and their radio luminosity function, *Nature*, **333**, 49–51.

Gopal-Krishna, Wiita, P. J., Hooda, J. S. 1996, Weak headed quasars, *Astron. Astrophys.*, **316**, L13–16.

Hardcastle, M. J., Worrall, D. M., Kraft, R. P., Forman, W. R., Jones, C., Murray, S. S. 2003, Radio and X-ray observations of the jet in Centaurus A, *Astrophys. J.* **593**, 169–183.

Hones, E. W., Bergeson, J. E. 1965, Electric Field Generated by a Rotating Magnetized Sphere, *J. Geophys. Res.*, **70**, 4951–4958.

Jauncey, D. L., Bignall, H. E., Lovell, J. E. J., Kedziora-Chudczer, L., Tzioumis, A. K., Macquart, J. -P., Rickett, B. J. 2003, Interstellar Scintillation and Radio Intra-Day Variability, in *Radio Astronomy at the Fringe*, (eds) J. A. Zensus, M. H. Cohen & E. Ros, *ASP Conference Series* **300**, 199–210.

Jester, S., Röser, H.-J., Meisenheimer, K., Perley, R., Conway, R. 2001, HST optical spectral index map of the jet of 3C 273, *Astron. & Astrophys.*, **373**, 447–458.

Jester, S., Röser, H.-J., Meisenheimer, K., Perley, R. 2002, X-rays from the jet of 3C 273: Clues from the radio-optical spectra, *Astron. & Astrophys.*, **385**, L27–L30.

Kaiser, C. R., Hannikainen, D. C. 2002, Pair Annihilation and Radio Emission from Galactic Jet Sources: the case of Nova Muscae, *MNRAS*, **330**, 225–231.

Katsouleas, T. 2004, Electrons hang ten on laser wake, *Nature*, **431**, 515–516.

Kulsrud, R. M., Ostriker, J. P., Gunn, J. E. 1972, Acceleration of cosmic rays in supernova remnants, *Phys. Rev. Lett.*, **28**, 636–639.

Kundt, W. 1979, A Model for Galactic Centres, *Astrophys. & Space Sci.*, **62**, 335–345.

Kundt, W. 1986, Particle Acceleration by Pulsars, in: *Cosmic Radiation in Contemporary Astrophysics*, NATO ASI C **162**, Reidel, 67–78.

Kundt, W. 1990, The Galactic Centre, *Astrophys. & Space Sci.*, **172**, 109–134.

Kundt, W. 1996, in *Jets from Stars and Galactic Nuclei*, (ed) W. Kundt, Lecture Notes in Physics **471**, 1–18.

Kundt, W. 2002, Radio Galaxies powered by Burning Disks, *New Astronomy Reviews*, **46**, 257–261.

Kundt, W. 2004, *Astrophysics, a new approach*, Springer, Chapter 11.

Kundt, W., Gopal-Krishna 1980, Extremely-relativistic Electron-Positron Twin-jets from Extraga-lactic Radio Sources, *Nature*, **288**, 149–150.

Kundt, W., Gopal-Krishna 1986, The jet of the quasar 3C 273, *J. Astrophys. Astr.*, **7**, 225–236.

Massaro, E. Matt, G., Salvati, M., Costa, E., Mandrou, P., Niel, M., Olive, J. F., Mineo, T., Sacco, B., Scarsi, L., Gerardi, G., Agrinier, B., Barouch, E., Comte, R., Parlier, B., Masnou, J. L. 1991, *Astrophys. J.*, **376**, L11–L14.

Mayer-Hasselwander, H. A., Bertsch, D. L., Dingus, B. L. Eckart, A., Esposito, J. A., Genzel, R., Hartman, R. C., Hunter, S. D., Kanbach, G., Kniffen, D. A., Lin, Y. C., Michelson, P. F., Mücke, A., von Montigny, C., Mukherjee, R., Nolan, P. L., Pohl, M., Reimer, O., Schneid, E. J., Sreekumar, P., Thompson, D. J. 1998, High-Energy gamma-ray emission from the Galactic Center, *Astron. & Astrophys.*, **335**, 161–172.

Melia, F., Falcke, H. 2001, The Supermassive Black Hole at the Galactic Center, *Ann. Rev. Astron. & Astrophys.*, **39**, 403–455.

Michel, F. C. 1974, Rotating Magnetosphere: Acceleration of Plasma from the Surface, *Astroph. J.*, **192**, 713–718.

Morrison, P. 1981, unpublished evening lecture at Socorro, during the IAU **97** Symposium at Albuquerque on *Extragalactic Radio Sources*.

Morrison, P., Roberts, D., Sadun, A. 1984, Relativistic Jet meets Target: The γ-rays from 3C 273, *Astroph. J.*, **280**, 483–490.

Ozernoy, L. M., Usov, V. V. 1977, Regular Optical Variability of Quasars and Nuclei of Galaxies as a Clue to the Nature of their Activity, *Astron. Astrophys.*, **56**, 163–172.

Prieto, M. A., Brunetti, G., Mack, K.-H. 2002, Particle Accelerations in the Hotspots of Radio Galaxy 3C 445, imaged with the VLT, *Science*, **298**, 193–195.

Reipurth, B., Bally, J. 2001, Herbig-Haro Flows: Probes of Early Stellar Evolution, *Ann. Rev. Astron. & Astrophys.*, **39**, 403–455.

Reipurth, B., Heathcote, S. 1993, Observational Aspects of Herbig-Haro Jets, in: *Astrophysical Jets*, (eds) D. Burgarella, M. Livio & C. P. O'Dea, *Space Tel. Sci. Inst. Symp.*, **6**, 35–71.

Rodríguez, L. F., Reipurth, B. 1994, The exciting source of the HH 111 jet complex: VLA detection of a one-sided radio jet, *Astron. & Astrophys.*, **281**, 882–888.

Rodríguez, L. F., Curiel, S., Moran, J. M., Mirabel, I. F., Roth, M., Garay, G. 1989, Large Proper Motions in the remarkable triple radio source in Serpens, *Astrophys. J.*, **346**, L85–L88.

Roy, S., Rao, A. P. 2004, Sgr A* at low radio frequencies: Giant Metre-wave Radio Telescope Observations, *Mon. Not. R. Astron. Soc.*, **349**, L25–L29.

Scheuer, P. A. G. 1996, Simple Sums on Burning Disks, in *Jets from Stars and Galactic Nuclei, Lecture Notes in Physics*, **471**, Springer, 35–40.

Schwartz, P. R., Frerking, M. A., Smith, H. A. 1985, Pedestal Features in Dark Clouds: a search for radio emission, *Astrophys. J.*, **295**, 89–93.
Singal, A. K., Gopal-Krishna 1985, Ultra-relativistic bulk motion and radio flux variability of Active Galactic Nuclei, *MNRAS*, **215**, 383–393.
Stawarz, L. 2003, Multifrequency Radiation of Electromagnetic Large-Scale Jets, *Chinese Journal of A. & A.* 2005, submitted; astro-ph/0310795 v2.
Wagner, S. J., Witzel, A. 1995, Intraday Variability in Quasars and BL Lac Objects, *Annu. Rev. Astron. Astrophys.*, **33**, 163–197.
Wilner, D. J., Reid, M. J., Menten, K. M. 1999, The synchrotron jet from the H_2O maser source in W3(OH), *Astrophys. J.*, **513**, 775–779.

J. Astrophys. Astr. (2004) **25,** 129–141

On the Origin of the Wide HI Absorption Line towards Sgr A*

K. S. Dwarakanath[1], W. M. Goss[2], J. H. Zhao[3] & C. C. Lang[4]
[1]*Raman Research Institute, Sadashivanagar, Bangalore 560 080, India.*
e-mail: dwaraka@rri.res.in
[2]*National Radio Astronomy Observatory, PO BOX O, Socorro, NM 87801.*
e-mail: mgoss@aoc.nrao.edu
[3]*Harvard-Smithsonian Center for Astrophysics, Cambridge, MA 02138.*
e-mail: jzhao@cfa.harvard.edu
[4]*Department of Physics and Astronomy, University of Iowa, Iowa City, IA 52242.*
e-mail: cornelia-lang@uiowa.edu

Received 2004 May 7; accepted 2004 October 19

Abstract. We have imaged a region of $\sim 5'$ extent surrounding Sgr A* in the HI 21 cm-line absorption using the Very Large Array. A Gaussian decomposition of the optical depth spectra at positions within $\sim 2'$ (~ 5 pc at 8.5 kpc) of Sgr A* detects a wide line underlying the many narrow absorption lines. The wide line has a mean peak optical depth of 0.32 ± 0.12 centered at a mean velocity of $V_{\rm lsr} = -4 \pm 15$ km s^{-1}. The mean full width at half maximum is 119 ± 42 km s^{-1}. Such a wide line is absent in the spectra at positions beyond $\sim 2'$ from Sgr A*. The position-velocity diagrams in optical depth reveal that the wide line originates in various components of the circumnuclear disk (radius $\sim 1.3'$) surrounding Sgr A*. These components contribute to the optical depth of the wide line in different velocity ranges. The position-velocity diagrams do not reveal any diffuse feature which could be attributed to a large number of HI clouds along the line of sight to Sgr A*. Consequently, the wide line has no implications either to a global population of shocked HI clouds in the Galaxy or to the energetics of the interstellar medium as was earlier thought.

Key words. Galaxy: nucleus—radio lines: ISM.

1. Introduction

The Galaxy harbours a compact radio source Sgr A* at its center. The intrinsic size of Sgr A* is constrained by the most recent multi frequency VLBA observations to be 24 ± 2 Schwarzschild radius (~ 2 AU for a 4×10^6 M$_\odot$ black hole) at 43 GHz and scales as $\lambda^{1.6}$ (Bower *et al*. 2004). A filamentary region of ionised gas, Sgr A West of ~ 2.5 pc in extent ($\sim 1'$) surrounds Sgr A* (Lo & Claussen 1983; Roberts & Goss 1993). Both Sgr A* and Sgr A West are surrounded by a ring of molecular material called the circumnuclear disk (CND) the outer edge of which has been traced up to ~ 7 pc (Gusten *et al*. 1987). Surrounding (in projection) both Sgr A* and Sgr A West is the supernova remnant Sgr A East with a radius of ~ 5 pc (Ekers *et al*. 1983,

Maeda *et al*. 2002). The supernova remnant is in close proximity to Sgr A West and is expanding into a molecular cloud complex (Pedlar *et al*. 1989).

The compact source Sgr A* and its surroundings have been a target of HI 21 cm-line measurements for many years. A number of absorption and emission features with a radial velocity range of $-190\,\mathrm{km\,s^{-1}}$ to $+135\,\mathrm{km\,s^{-1}}$ have been detected towards this region which shows little Galactic rotation (Liszt *et al*. 1983). However, many of the components show evidence of non-circular motion. Some of the anomalous absorption features are the $-53\,\mathrm{km\,s^{-1}}$ feature due to the 'Expanding 3-kpc Arm', the $-135\,\mathrm{km\,s^{-1}}$ feature due to the 'Expanding Molecular Ring', and the $+50\,\mathrm{km\,s^{-1}}$ feature due to the molecular cloud into which Sgr A East is expanding.

Early HI 21 cm-line observations towards Sgr A* were carried out using the Parkes Interferometer with a resolution of $3'$ (Radhakrishnan *et al*. 1972). An analysis of the HI 21 cm-line absorption spectrum towards Sgr A* revealed, apart from many familiar features, an unexpected wide, shallow component (Radhakrishnan & Sarma 1980, RS1). This component was centered at $V_{\mathrm{lsr}} = -0.22\,\mathrm{km\,s^{-1}}$ with a peak optical depth of 0.3 and a velocity dispersion of $35\,\mathrm{km\,s^{-1}}$ (full width at half maximum (FWHM) $\sim 80\,\mathrm{km\,s^{-1}}$). This component was attributed to a new population of shocked HI clouds in the Galaxy observed along the line of sight towards Sgr A* (Radhakrishnan & Srinivasan 1980, RS2). Estimates indicated that the kinetic energy in these clouds was ~ 100 times that in the standard HI clouds with consequent implications to the energetics of the interstellar medium.

Subsequent HI absorption measurements towards Sgr A* using the Westerbork Synthesis Radio Telescope (WSRT) did not confirm the existence of this wide line and placed an upper limit to its peak optical depth of 0.1 (Schwarz, Ekers & Goss 1982). Around the same time, Shaver *et al*. (1982), and Anantharamaiah *et al*. (1984) made an analysis of the differences between the terminal velocities of HI absorption spectra and the recombination line velocities in the directions of 38 HII regions of known distances. This analysis provided estimates of the number densities and random velocity dispersions of interstellar HI clouds. Their results supported the earlier postulate of shocked HI clouds in the Galaxy. However, Kulkarni & Fich (1985) found that these results were easily confused by many known systematic effects. After accounting for all these effects they found that the results of Shaver *et al*. (1982) and Anantharamaiah *et al*. (1984) were quite uncertain. Using HI emission data throughout the Galactic Plane, Kulkarni & Fich (1985) suggested that the amount of HI in the high velocity dispersion HI concentrations is an order of magnitude less than proposed by RS2.

More recently, HI absorption measurements towards Sgr A* were carried out using the Australia Telescope Compact Array (ATCA) (Rekhesh Mohan 2003, RM). These observations confirmed the existence of a wide (FWHM $\sim 120\,\mathrm{km\,s^{-1}}$) and shallow ($\tau_{\mathrm{peak}} \sim 0.3$) absorption feature towards Sgr A*. The discrepancy between the earlier two observations can be attributed to the smaller velocity coverage used in the WSRT observations. The spatial distribution of this spectral feature could not be obtained from the recent ATCA observations due to limited visibility coverage and poor sensitivity. A recent HI absorption measurement towards the Galactic Anticenter using the WSRT detected no such wide line to a 3σ optical depth limit of 0.006 indicating that the wide HI absorption line detected towards Sgr A* is not ubiquitous (RM). Thus, the nature of the wide HI absorption line towards Sgr A* remained unclear.

From the earlier HI absorption measurements towards Sgr A*, it is clear that a large velocity coverage $\sim 600\,\mathrm{km\,s^{-1}}$ is required to detect the wide HI absorption line. A

velocity resolution $\sim 1\,\mathrm{km\,s^{-1}}$ is also necessary to identify and remove the narrow (FWHM $\sim$ a few $\mathrm{km\,s^{-1}}$) HI absorption lines which are detected along most lines of sight in the Galaxy and more so towards Sgr A*. In addition, an excellent visibility coverage is necessary to image the complex continuum and HI distribution observed towards Sgr A* and its immediate surroundings. Therefore, we have undertaken a high spectral and spatial resolution HI absorption study of the Sgr A* and its immediate surroundings ($\sim 5'$) with the Very Large Array in order to determine the spatial distribution of the shallow and wide HI absorption component, to characterize its physical properties, and to determine its origin and physical relationship to the center of the Galaxy. In section 2, we present the observations; in section 3, the data analysis; and in section 4, the discussion.

2. Observations and imaging

The observations were carried out using the Very Large Array (VLA) in the 36 km (A), 11 km (B), 3 km (C), and 1 km (D) configurations during January – October 2002. The total integration times in each of these configurations were $\sim$13, 9, 2 and 2 hours respectively. The field center of these observations was α (2000) $= 17^{\mathrm{h}}\,45^{\mathrm{m}}\,40^{\mathrm{s}}.049$, and δ (2000) $= -29^{\circ}\,00'\,27''.98$. The standard observing modes of the VLA spectrometer cannot provide both the required velocity coverage ($\sim 600\,\mathrm{km\,s^{-1}}$) and velocity resolution ($\sim 1\,\mathrm{km\,s^{-1}}$). Therefore, two overlapping bands each with 1.56 MHz bandwidth and 255 spectral channels were arranged to cover the desired velocity range ($\pm 300\,\mathrm{km\,s^{-1}}$) for the Galactic HI 21 cm-line. There were 25 overlapping channels in the flat portions of the bands. After precise bandpass calibration the two bands were combined together to produce a final data base with a velocity coverage of $590\,\mathrm{km\,s^{-1}}$ at a spectral resolution of $1.3\,\mathrm{km\,s^{-1}}$ after Hanning smoothing.

2.1 *Imaging*

The calibration and imaging were carried out using the Astronomical Image Processing System (AIPS). Using the data from the A + B + C + D arrays CLEANed image cubes containing both the continuum and the spectral line data were produced. Continuum images were produced from the respective image cubes by averaging the line-free channels. Spectral line image cubes were produced by constructing a linear fit to the continuum in the line-free channels as a function of the channels and subtracting this linear fit from all channels. Optical depth image cubes were produced by suitably combining the spectral line image cubes and the respective continuum images. A continuum image of the region surrounding Sgr A* is shown in Fig. 1. Representative optical depth spectra at the four positions indicated in this figure are shown in Fig. 2.

Using the data from the C + D arrays, three sets of CLEANed image cubes containing both the continuum and the spectral line data were produced. These three data sets included all visibilities, the visibilities beyond the inner 40 m, and the visibilities beyond the inner 100 m respectively. The upper limit to the included range of visibilities in all the three images was $\sim$3400 m. Continuum images and optical depth image cubes were produced following the procedure described earlier. The contamination due to HI emission was minimal in all the images. However, of the three sets of images, the second set of images had the best spatial resolution and the maximum spatial extent

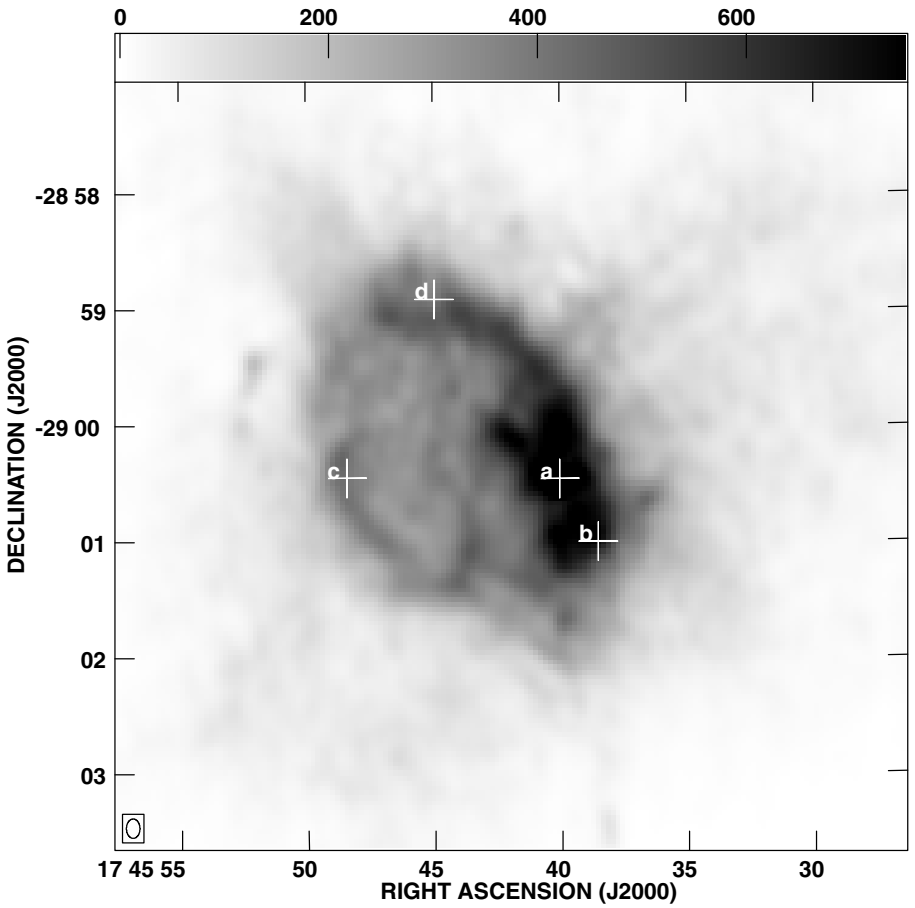

Figure 1. A radio continuum image made from the A+B+C+D array data. The synthesised beam, $10'' \times 7''$ at a position angle of 0°, is shown at the bottom left hand corner. The RMS is 9 mJy/beam. The grey scale flux density range is 0 to 750 mJy/beam. The four crosses marked a, b, c, and d indicate the positions at which the four spectra shown in Fig. 2 were obtained respectively. The cross marked 'a' is the position of Sgr A*.

of the optical depth distribution. Since one of the primary motivations of the current observations was to estimate the spatial distribution of the wide HI absorption line, the second set of images was used in further analysis. A continuum image of the region surrounding Sgr A* from the second data set is shown in Fig. 3. This image has a synthesized beam of $40'' \times 20''$ (position angle $= 0^\circ$) with an RMS of 30 mJy beam^{-1}.

The data from the A+B+C+D arrays provides higher spatial resolution compared to the data from the C+D arrays. However, the radio continuum extent imaged from the high resolution data is rather limited (Fig. 1). The more extended continuum features detected in the C + D arrays data (Fig. 3) are resolved in the high resolution data. The limited extent of the radio continuum precludes the high resolution images being used for tracing the spatial extent of the wide absorption line. However, the high resolution data are used as an independent check of the results from the low resolution data where both are available.

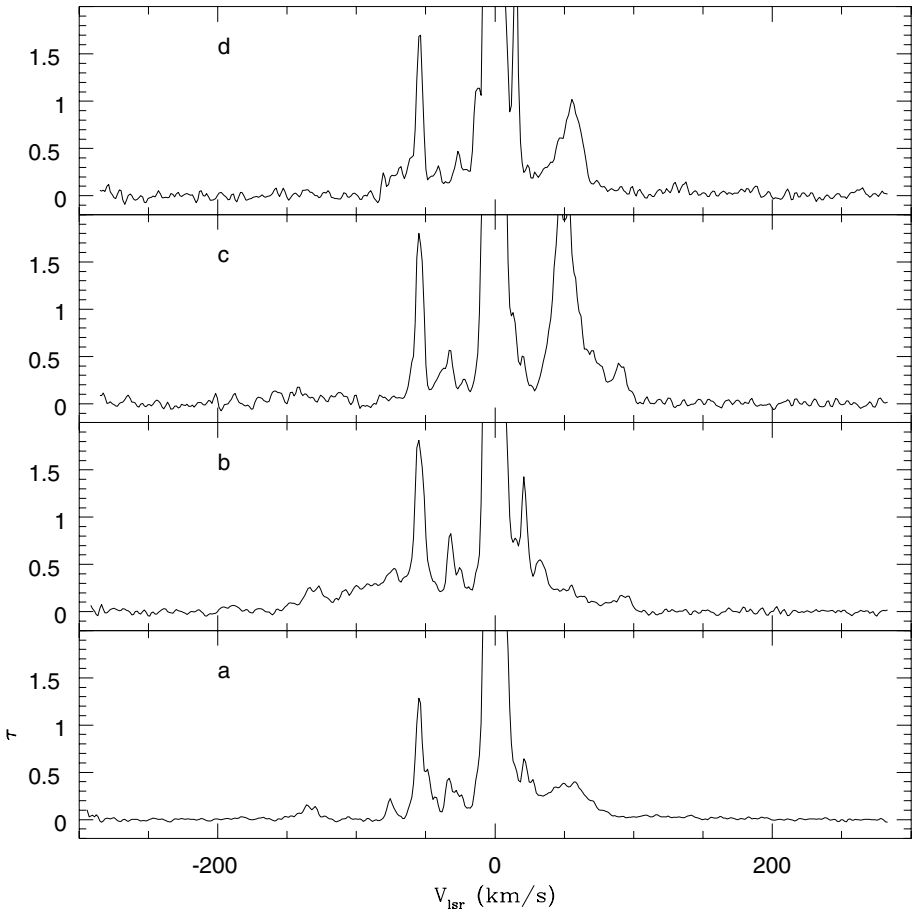

Figure 2. Optical depth spectra from the A + B + C + D array data. The four spectra correspond to the four positions marked in Fig. 1 respectively. Gaussian analysis of the spectra detects a wide line (FWHM ~ 120 km s^{-1}) apart from the many narrow lines that are evident. In many spectra, like for example, the one marked 'b', such a wide line is evident as a broad shoulder underneath the narrow lines.

3. Analysis of the optical depth spectra and images

The motivation for the current observations are (a) to confirm the existence of a wide velocity component in the HI absorption spectra towards Sgr A* and (b) to understand its possible origin. The HI absorption spectra in the Galactic plane are dominated by the presence of deep (optical depth ~ 0.5) and relatively small dispersion ($\sim$ a few km s^{-1}) lines. The presence of a large velocity dispersion ($\sim$30–50 km s^{-1}) HI absorption component can manifest as a broad shoulder underlying the narrow lines in an optical depth spectrum. Often a visual inspection can reveal this shoulder. Representative optical depth spectra from the C + D array data at the positions marked in Fig. 3 are displayed in Figs. 4 and 5. The spectra in Fig. 4 at positions within $\sim 2'$ from Sgr A* reveal such a shoulder which is absent in the spectra at positions outside $\sim 2'$ from Sgr A* (Fig. 5). However, a quantitative analysis of the optical depth spectra is necessary to confirm these visual impressions.

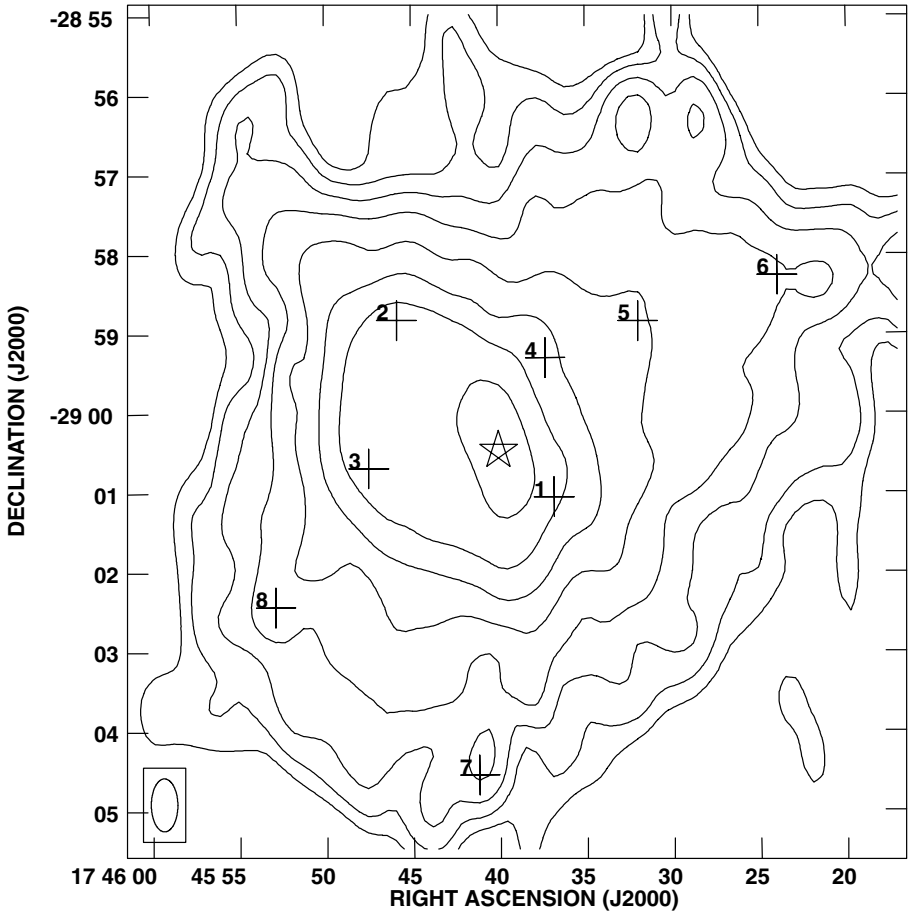

Figure 3. A radio continuum image made from the C + D array data. The synthesised beam, $40'' \times 20''$ at a position angle of 0°, is shown at the bottom left hand corner. The RMS is 30 mJy/beam. Contours start at 50 mJy/beam and increase successively by a factor of 2. The star marks the position of Sgr A*. The crosses mark the positions at which the optical depth spectra shown in Figs. 4 and 5 were extracted.

The HI 21 cm-line absorption or emission studies carried out in the past indicate that most of these profiles are well fit by Gaussians. The Gaussian decomposition of the optical depth spectrum was carried out by a code written for this purpose based on the Levenberg–Marquardt Method (Numerical Recipes in Fortran 1992). This method minimizes the χ^2 by computing both its first and second derivatives with respect to the variables (parameters of the Gaussians to be fitted) and approaching a minimum. The desired number of input Gaussians are fit to the data simultaneously and the best-fit model is derived after a suitable number of iterations during which the parameters of the input Gaussians are varied to obtain the minimum χ^2. Two examples illustrating such an analysis are given in Figs. 6 and 7. The data in Figs. 6 and 7 are the spectra marked '1' and '5' in Figs. 4 and 5 respectively. The best-fit model for the data in Fig. 6 is displayed in the second panel from the top in Fig. 6. The third panel from top is the residual spectrum (data-model), consistent with noise. The bottom panel in

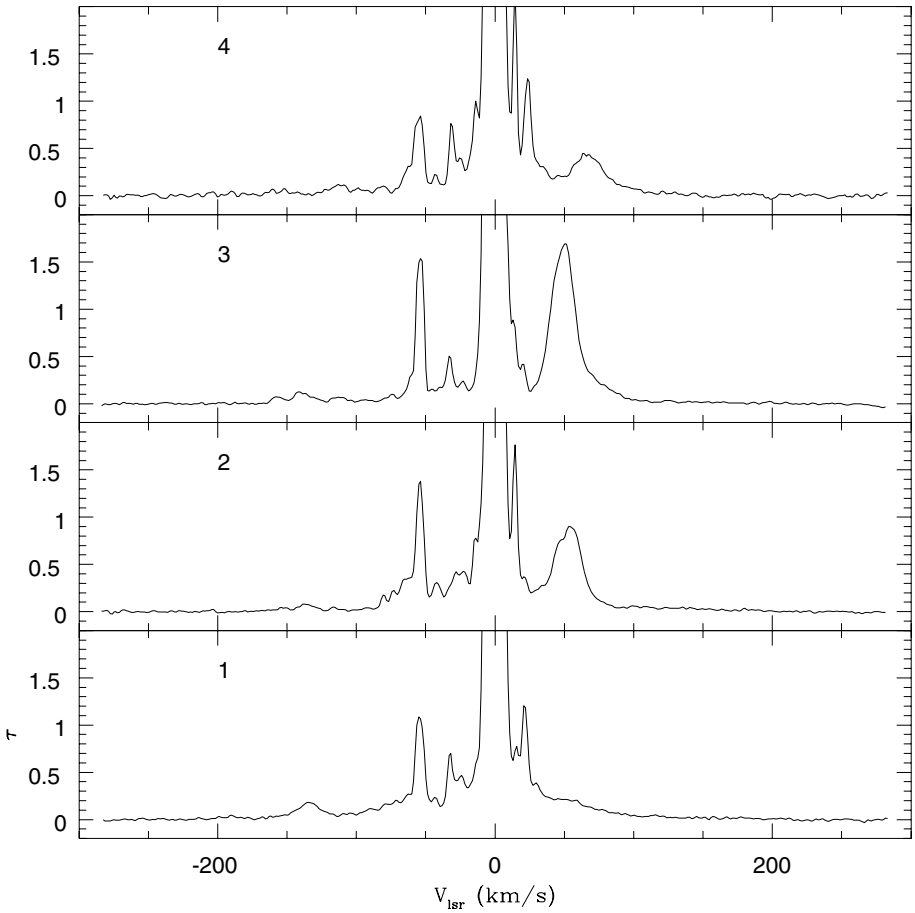

Figure 4. Optical depth spectra from the C+D array data at the positions 1, 2, 3 and 4 respectively marked in Fig. 3. These spectra are representative of the spectra at positions within $\sim 2'$ from Sgr A*. A Gaussian analysis detects a wide line with mean values of $V_{\rm lsr} = -4 \pm 15\,{\rm km\,s^{-1}}$, $\delta V_{1/2} = 119 \pm 42\,{\rm km\,s^{-1}}$, and $\tau_{\rm peak} = 0.32 \pm 0.12$ in the spectra at positions within $\sim 2'$ from Sgr A*.

Fig. 6 displays the residual when the 11 narrow lines in the model are subtracted from the data. A wide line of FWHM $\sim 129\,{\rm km\,s^{-1}}$ is detected in the data. The 11 narrow components have a mean FWHM of $12 \pm 8\,{\rm km\,s^{-1}}$, with the FWHMs in the range 4–24 km s^{-1}. The best-fit Gaussian model for the data in Fig. 7 has 8 components with a mean FWHM of $7 \pm 3\,{\rm km\,s^{-1}}$. No wide line is detected in this spectrum. The quantitative analysis confirms the visual impressions of these spectra.

A Gaussian decomposition of the optical depth spectra from the C + D array data at independent positions across the extent of the source (Fig. 3) was carried out. Such an analysis detected a wide line (FWHM $\sim 120\,{\rm km\,s^{-1}}$) in the spectra at positions within $\sim 2'$ of Sgr A*. No wide line was detected in the spectra at positions beyond $\sim 2'$ of Sgr A*. Wide lines of similar characteristics were also detected in the spectra from the high resolution images (Fig. 2).

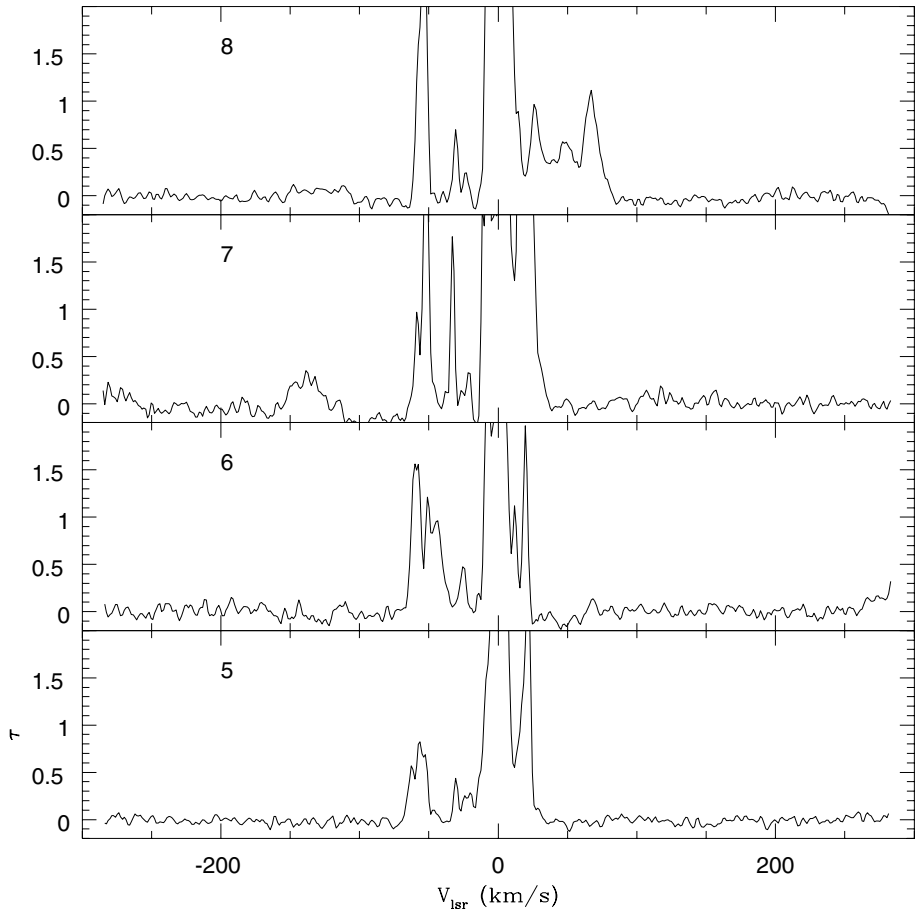

Figure 5. Same as in Fig. 4 but for positions 5, 6, 7 and 8 respectively. These spectra are representative of the spectra at positions beyond $\sim 2'$ from Sgr A*. A wide line of the kind detected in the spectra in Fig. 4 is absent in these spectra.

3.1 *Physical features associated with the wide line*

The position-velocity diagrams are an effective means to identify the physical features associated with spectral lines. As an illustrative example, two declination-velocity images are shown in Figs. 8 and 9, corresponding to the positions marked '1' and '5' respectively (Fig. 3). Both the figures are dominated by optical depth features which are parallel to declination and centered around $V_{\rm lsr} \sim 0,\ -25$ and $-50\,{\rm km\ s^{-1}}$. However, Fig. 8 shows high optical depth features at positive velocities ($\sim 100\,{\rm km\ s^{-1}}$) to the north of Sgr A*, and at negative velocities ($\sim -100\,{\rm km\ s^{-1}}$) to the south of Sgr A*. These two features form two ends of an inverted S-shaped feature (Fig. 8). Detailed modeling has shown that these features result due to the circumnuclear disk (CND) of mean radius 3.2 pc ($\sim 1.3'$) rotating about Sgr A* with a velocity $\sim 100\,{\rm km\ s^{-1}}$ (Liszt *et al*. 1985). Such an inverted S-shaped feature is absent in Fig. 9 due to the finite size of the CND. The optical depth spectrum at the position marked '1' (Figs. 3 and 4) is the spectrum at $\delta = -29^\circ\ 01'\ 03''$ in Fig. 8 and originates from the CND. The

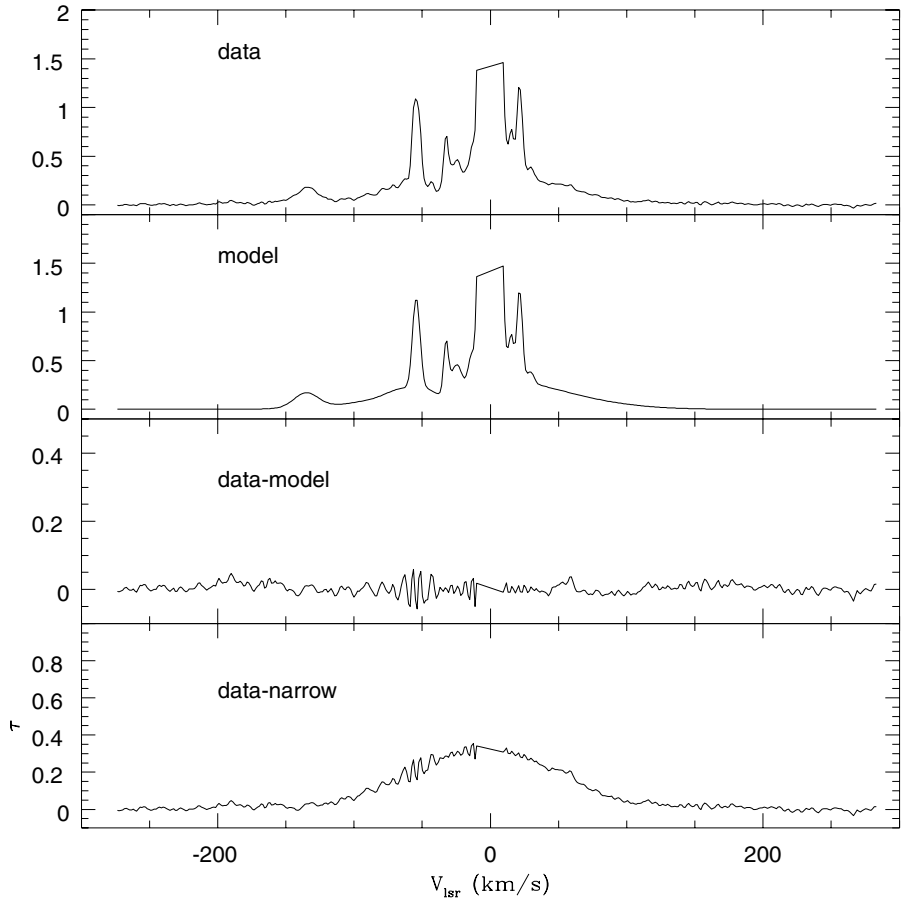

Figure 6. Gaussian decomposition. The data is the optical depth spectrum from the C + D array data (marked '1' in Figs. 3 and 4). The best-fit model consists of 11 narrow Gaussians with a mean FWHM of $12 \pm 8\,\mathrm{km\ s^{-1}}$ and a wide Gaussian of FWHM $129 \pm 1\,\mathrm{km\ s^{-1}}$. The residual (data-model) is consistent with noise. The bottom panel displays the residual when only the narrow lines in the model are subtracted from the data. This wide line is also evident in the data as a broad shoulder.

spectrum at the position marked '5' (Figs. 3 and 5) is the spectrum at $\delta = -28^\circ\ 58'\ 50''$ in Fig. 9.

Although the position-velocity plots demonstrate that the CND is responsible for the wide line, a more direct connection of the wide line to the CND is desirable. A comparison of the spatial distribution of the wide line parameters (central velocity, width, and peak optical depth) with the CND can bring out such a connection. The spatial distributions of the wide line parameters indicate some systematic behaviour in relation to the CND. However, the evidence is rather inconclusive. The basic limitation appears to be that the spatial resolution provided by the C+D arrays is coarse compared to the linear scales over which velocity gradients and turbulence exist in the region surrounding Sgr A* (Gusten *et al*. 1987). The data from the A + B + C + D arrays have adequate spatial resolution for this purpose, but has inadequate surface brightness to trace the spatial distribution of the wide line parameters.

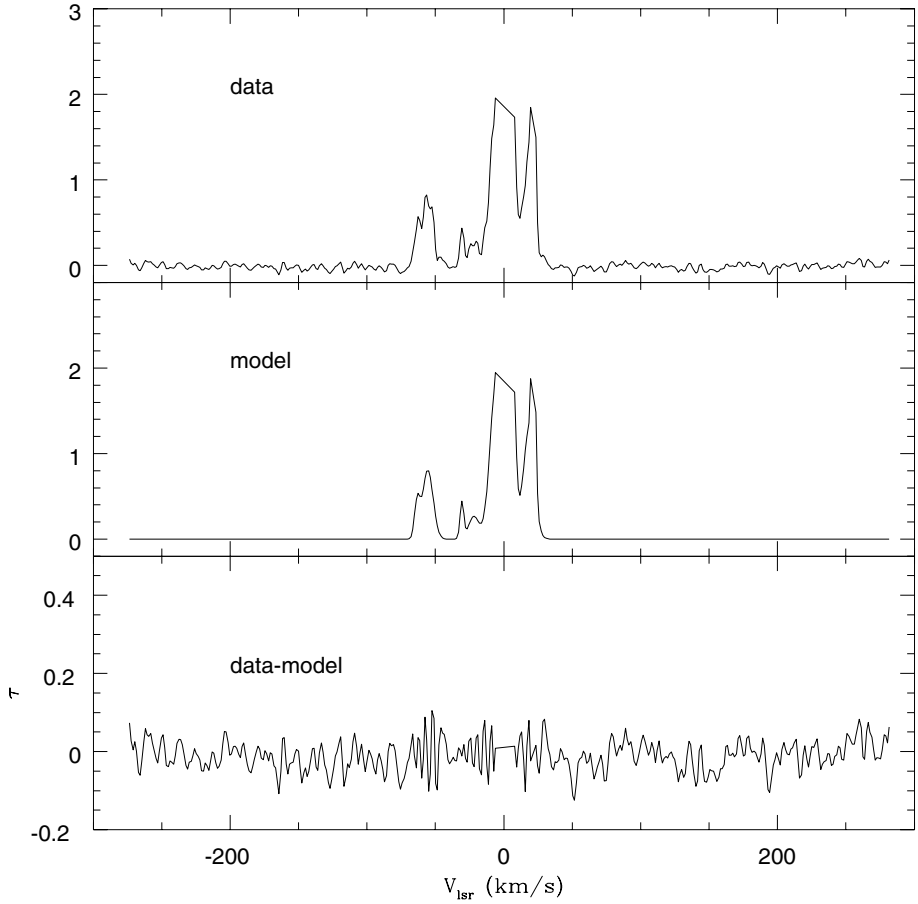

Figure 7. Gaussian decomposition. The data is the optical depth spectrum from the C + D array data (marked '5' in Figs. 3 and 5). The best-fit model consists of 8 narrow Gaussians with a mean FWHM of $7 \pm 3\,\mathrm{km\,s^{-1}}$. The residual (data-model) is consistent with noise. No wide line is detected in this spectrum.

4. Discussion

The current observations have demonstrated the existence of a wide line ($\delta V_{1/2} \sim 120\,\mathrm{km\,s^{-1}}$) in the optical depth spectra towards Sgr A* and its surroundings, confirming the early results of RS1. Since such a wide line is detected in the present observations towards positions within $\sim 2'$ from Sgr A*, it is understandable that the Parkes Interferometer observations towards Sgr A* detected such a wide line even with a poorer resolution of $\sim 3'$. No wide line was detected in the current observations at positions beyond $\sim 2'$ from Sgr A*.

A comparison of the optical depth spectra at positions within $\sim 2'$ from Sgr A* and the corresponding position-velocity diagrams indicate that the origin of the wide line is related to the CND. The wide line at the position marked '1' (Fig. 6) results due to contributions from different parts of the CND in different velocity ranges (Fig. 8). On the other hand, the declination-velocity diagram corresponding to the position marked '5' (Fig. 9) does not show the features corresponding to the CND as the CND

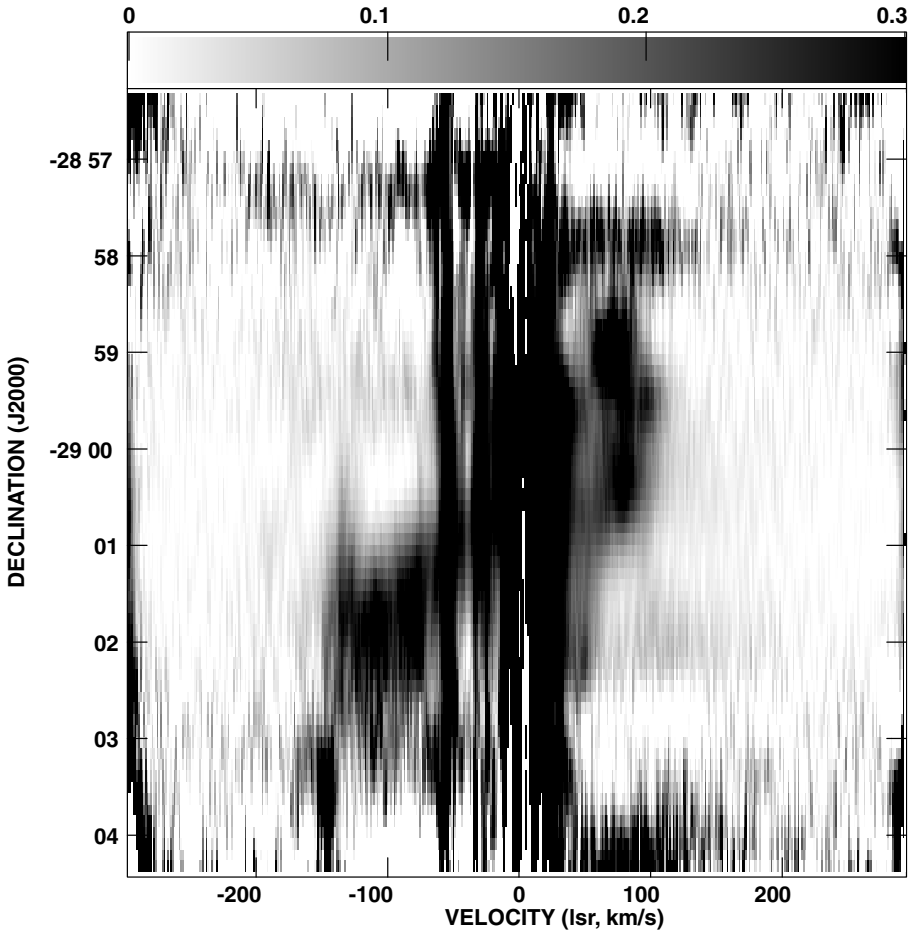

Figure 8. Declination-velocity diagram from the C + D array data at the right ascension of the position marked '1' in Fig. 3. The grey scale is optical depth in the range 0–0.3. The reliable portion of the image is $-29^\circ\ 3' < \delta < -28^\circ\ 57'$. The features to the north of Sgr A* at positive velocities (~ 100 km s^{-1}) and to the south of Sgr A* at negative velocities (~ -100 km s^{-1}) are due to the circumnuclear disk surrounding Sgr A*.

is confined to within $\sim 2'$ of Sgr A*. Consequently, the optical depth spectrum at the position marked '5' (Fig. 7) does not detect a wide line.

The wide line detected in the Parkes Interferometer observations towards Sgr A* was interpreted as a large velocity dispersion line (RS1). The dispersion was attributed to the random motions of a new population of shocked HI clouds in the Galaxy observed along the line of sight towards Sgr A* (RS2). This new population was postulated to be warmer and more abundant (~ 15 clouds/kpc) than the standard cold HI clouds. If such a scenario were correct, a diffuse feature over a range of velocities corresponding to the FWHM of the wide line should have been detected in the declination-velocity diagrams (Figs. 8 and 9). No such feature was detected in these images. The shocked HI cloud picture in this context is thus implausible. Consequently, there are no implications of the wide line to the energetics of the interstellar medium. The current observations

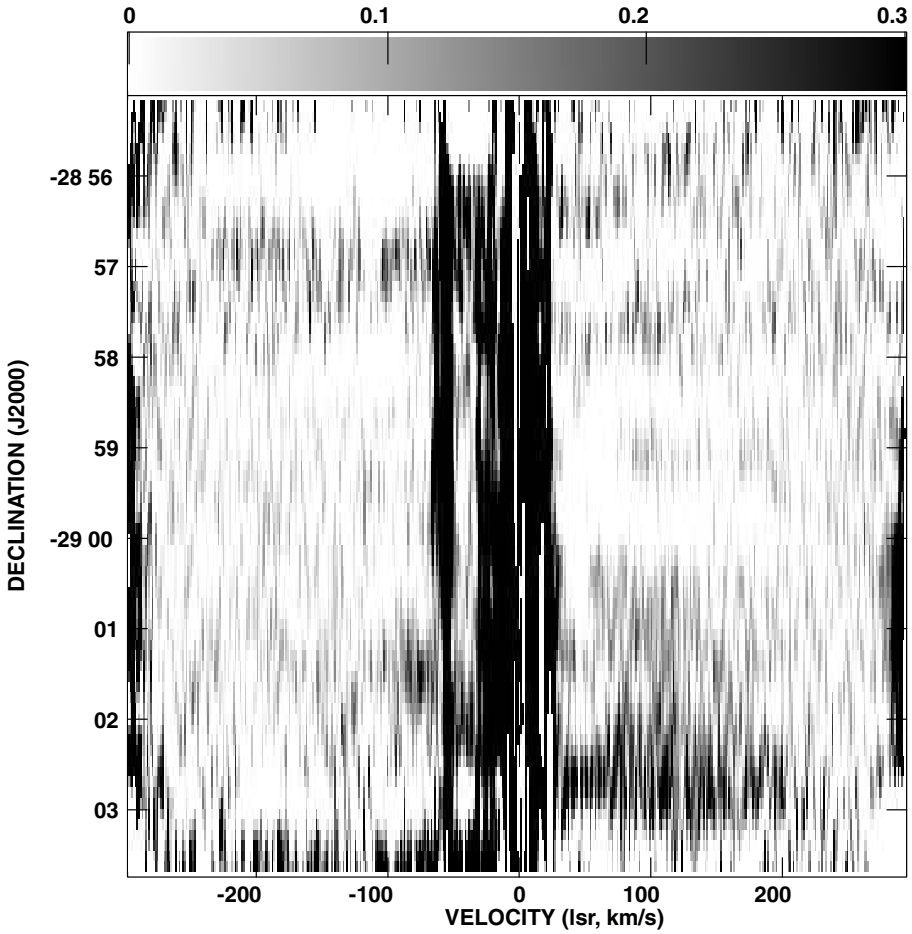

Figure 9. Same as in Fig. 8 but at the right ascension of the position marked '5' in Fig. 3. The CND is not detected in this image since the CND is confined to within $\sim 2'$ from Sgr A*.

have uncovered the origin of the wide HI absorption line towards Sgr A* and have put to rest the related controversies that existed for over two decades.

Acknowledgements

The National Radio Astronomy Observatory (NRAO) is a facility of the National Science Foundation, operated under cooperative agreement by Associated Universities, Inc.

References

Anantharamaiah, K. R., Radhakrishnan, V., Shaver, P. A. 1984, *AA*, **138**, 131.
Bower, G. C., Falcke, H., Herrnstein, R. M., Zhao, J. H., Goss, W. M., Backer, D. C. 2004, *Science*, **304**, 704.
Ekers, R. D., van Gorkom, J. H., Schwarz, U. J., Goss, W. M. 1983, *AA*, **122**, 143.

Gusten, R., Genzel, R., Wright, M. C. H., Jaffe, D. T., Stutzki, J., Harris, A. I. 1987, *ApJ*, **318**, 124.
Kulkarni, S. R., Fich, M. 1985, *ApJ*, **289**, 792.
Liszt, H. S., van der Hulst, J. M., Burton, W. B., Ondrechen, M. P. 1983, *AA*, **126**, 341.
Liszt, H. S., Burton, W. B., van der Hulst, J. M. 1985, *AA*, **142**, 237.
Lo, K. Y., Claussen, M. J. 1983, *Nature*, **306**, 647.
Maeda, Y. *et al*. 2002, *ApJ*, **570**, 671.
Numerical Recipes in FORTRAN 1992, Press, W. H., Teukolsky, S. A., Vetterling, W. T., Flannery, B. P. (Cambridge University).
Pedlar, A., Anantharamaiah, K. R., Ekers, R. D., Goss, W. M., van Gorkom, J. H. *et al*. 1989, *ApJ*, **342**, 769.
Radhakrishnan, V., Goss, W. M., Murray, J. D., Brooks, J. W. 1972, *ApJS*, **24**, 49.
Radhakrishnan, V., Sarma, N. V. G. 1980, *AA*, **85**, 249 (RS1).
Radhakrishnan, V., Srinivasan, G. 1980, *JAA*, **1**, 47 (RS2).
Rekhesh Mohan 2003, PhD Thesis, Jawaharlal Nehru University, New Delhi (RM).
Roberts, D. A., Goss, W. M. 1993, *ApJS*, **86**, 133.
Schwarz, U. J., Ekers, R. D., Goss, W. M. 1982, *AA*, **110**, 100.
Shaver, P. A., Radhakrishnan, V., Anantharamaiah, K. R., Retallack, D. S., Wamsteker, W., Danks, A. C. 1982, *AA*, **106**, 105.

J. Astrophys. Astr. (2004) **25,** 143–183

A High Galactic Latitude HI 21 cm-line Absorption Survey using the GMRT: I. Observations and Spectra

Rekhesh Mohan*[1], K. S. Dwarakanath[2] & G. Srinivasan[3]
Raman Research Institute, Bangalore 560 080, India.
[1]*e-mail: reks@iiap.res.in*
[2]*e-mail: dwaraka@rri.res.in*
[3]*e-mail: srini@rri.res.in*

Received 2004 June 4; accepted 2004 November 3

Abstract. We have used the Giant Meterwave Radio Telescope (GMRT) to measure the Galactic HI 21-cm line absorption towards 102 extragalactic radio continuum sources, located at high ($|b| > 15^\circ$) Galactic latitudes. The Declination coverage of the present survey is $\delta \gtrsim -45^\circ$. With a mean rms optical depth of ~ 0.003, this is the most sensitive Galactic HI 21-cm line absorption survey to date. To supplement the absorption data, we have extracted the HI 21-cm line emission profiles towards these 102 lines of sight from the Leiden Dwingeloo Survey of Galactic neutral hydrogen. We have carried out a Gaussian fitting analysis to identify the discrete absorption and emission components in these profiles. In this paper, we present the spectra and the components. A subsequent paper will discuss the interpretation of these results.

Key words. ISM: clouds, kinematics and dynamics—radio lines: ISM.

1. Introduction

The distribution atomic hydrogen in the Galaxy and its physical properties have been extensively studied. Soon after the discovery of the HI 21-cm line, a number of single dish HI surveys were conducted (see Burton 1988 for a useful compilation of the early HI surveys). The single dish HI absorption spectra are limited by the errors due to the variation of HI emission intensity over the angular scales smaller than the telescope beam. Interferometric surveys are a better alternative for HI absorption studies. An interferometer rejects the low spatial frequencies where HI emission is dominant, resulting in reliable absorption spectra. There have been a number of interferometric HI absorption studies, often supplemented by single dish observations to measure the HI emission.

The early HI 21-cm line absorption and emission studies led to the emergence of a global picture of the interstellar medium (Clark, Radhakrishnan & Wilson 1962; Clark 1965). These and later studies paved the way for the models of the interstellar medium of the Galaxy. Field, Goldsmith & Habbing (1969) modeled the ISM as cool

*Currently at the Indian Institute of Astrophysics, Bangalore 560 034, India.

dense concentrations of gas, often referred to as "interstellar clouds" (the Cold Neutral Medium or CNM) in pressure equilibrium with a warmer intercloud medium (the Warm Neutral Medium or WNM). While this initial model of the ISM has been refined considerably by later studies (Wolfire *et al* 1995), the basic picture of the ISM with cold diffuse clouds and a warmer intercloud medium has survived. The spin temperature of the cold clouds which constitute the CNM was estimated to be ~ 80 K and that of the WNM to be ~ 8000 K. The cold clouds manifest as narrow Gaussian features with typical velocity dispersions of a few km s^{-1} in both HI emission and absorption profiles. The intercloud medium, on the other hand, is identified with broad Gaussian features with typical velocity dispersions $\gtrsim 10$ km s^{-1}. The intercloud medium is usually detected in emission, since the HI absorption in the warm gas is very weak. We summarize the results from some of the important surveys below.

Radhakrishnan *et al*. (1972a, b) used the Parkes Interferometer to study the HI absorption towards 35 extragalactic radio sources, in the Galactic latitude range $6^\circ \leq |b| \leq 74^\circ$ and 53 Galactic radio sources in the lower Galactic latitudes, mostly located at $|b| < 2^\circ$. In addition, the Parkes 64 m telescope was used to obtain the HI emission towards all these directions. The velocity resolution of these observations was 2.1 km s^{-1}. The rms noise in the HI optical depth profiles varied from ~ 0.01 to > 0.1, depending on the flux density of the background source. They concluded that the HI absorption features arise in discrete concentrations of gas with a spin temperature in the range 60–80 K. They also derived the number density of these features to be ~ 2.5 per Kpc (Radhakrishnan & Goss 1972). The number of such concentrations of gas for a given optical depth τ was $\propto e^{-\tau}$. Lack of absorption in the intercloud medium, which was identified as the wide "shoulders" in HI emission profiles, enabled them to put a limit of > 750 K for the spin temperature of this gas.

Dickey & Benson (1982) used the NRAO 300 ft and 140 ft telescopes as an interferometer to detect absorption in the 21-cm line towards 64 radio continuum sources. The HI emission profiles were obtained using the 300 ft telescope alone. These sources were both Galactic and extragalactic and spread over a range of latitudes $0^\circ \lesssim |b| \lesssim 70^\circ$. They have produced HI absorption profiles with an rms optical depth in the range ~ 0.007–0.16, with a velocity resolution ranging from $1.3 - 5.3$ km s^{-1}. Among the main results of this study was the realization that for lower Galactic latitudes ($|b| \lesssim 15^\circ$), HI emission surveys using single dish telescopes would miss a significant amount of gas ($\sim 40\%$) due to HI self absorption, wherein the cold HI gas in the foreground absorbs the HI line emission from the background gas. They also found more HI gas with lower spin temperature ($100 \lesssim T_S \lesssim 150$ K) at lower latitudes ($|b| < 2^\circ$) as compared to the previous HI line surveys. They concluded that such a behaviour is the result of velocity blending.

Mebold *et al*. (1981) carried out an HI absorption survey towards 69 sources in the range $0^\circ \lesssim |b| \lesssim 80^\circ$ using the NRAO 3-element interferometer. They obtained the corresponding HI emission using the Effelsberg 100 m telescope, the 91 m Green Bank telescope or the 64 m Parkes telescope. The velocity resolution of these profiles were in the range 0.42–3.3 km s^{-1}. These profiles, on an average, had an rms in HI optical depth $\gtrsim 0.05$. They found most of the HI absorption features to have a spin temperature in the range 20 to 140 K. For the HI absorption data at $|b| > 15^\circ$, they found indications for a bimodal distribution in the radial velocity distribution of absorbing features. However, since the number of components at higher radial velocities were small, they were unable to study its significance.

Till recently, the Very Large Array (VLA) used to be the only instrument with a collecting area comparable with large single dish telescopes. The survey by Dickey *et al*. (1983) using the VLA is limited to lower Galactic latitudes ($|b| < 10^\circ$). Moreover, the optical depth detection limit for this survey is ~ 0.1 (3σ). From the various HI absorption surveys carried out so far (Radhakrishnan *et al*. 1972a, b; Mebold *et al*. 1981; Dickey & Benson 1982 ; Dickey *et al*. 1983), more than 600 absorption spectra are available, but the optical depth detection limits of more than 75% of these are above 0.1. From the available results, the cloud population observed in HI absorption seem to have a Gaussian random velocity distribution. The dispersion in the random velocities of HI absorption features is $\sim 7\,\mathrm{km\,s^{-1}}$ (Dickey & Lockman 1990, and references therein).

The low optical depth regime of Galactic HI is largely unexplored except for the HI absorption studies using the Arecibo reflector by Dickey *et al*. (1978) and more recently by Heiles & Troland (2003a, b). Dickey *et al*. measured HI absorption and emission towards 27 extragalactic radio continuum sources located at high and intermediate Galactic latitudes ($|b| > 5^\circ$). The rms optical depth in their spectra were typically ~ 0.005. In many of the profiles the systematics in the band dominate the noise in the spectrum. As we noted earlier, these observations are not impervious to HI emission fluctuations introducing errors in the absorption profile (Dickey & Lockman 1990). Radhakrishnan & Goss (1972) found the number of HI absorption features for a given optical depth, τ to be proportional to $e^{-\tau}$. However, the data by Dickey *et al*. (1978) as well as the later survey using the Green Bank Interferometer (Mebold *et al*. 1982) indicated that for $|b| > 15^\circ$ this dependence is steeper than $e^{-\tau}$. This trend was explained as due to increase of low optical depth features with increasing angular and velocity resolution (Mebold *et al*. 1982). Dickey *et al*. (1978) also noted that the velocity distribution of HI absorption features is dependent on the optical depth. For the optically thin clouds ($\tau < 0.1$), the velocity dispersion was $\sim 11\,\mathrm{km\,s^{-1}}$, whereas for the optically thick clouds ($\tau > 0.1$) this value is $\sim 6\,\mathrm{km\,s^{-1}}$. Heiles & Troland (2003a, b) analysed HI absorption and emission profiles toward 79 lines of sight. A good fraction of these directions (66 out of 79) were at Galactic latitudes $|b| > 10^\circ$. They found evidence for an excess of low column density ($N_{\rm HI} < 5 \times 10^{19}\,\mathrm{cm^{-2}}$) CNM components.

2. Motivations for the present survey

The prime motivation for the present survey was to obtain sensitive HI absorption measurements at high Galactic latitudes and to study the random velocity distribution of HI clouds. Although there exist extensive data on Galactic HI absorption, there is a lack of sensitive HI absorption studies. There are indications that the low optical depth features ($\tau < 0.1$) form a distinct class (Dickey *et al*. 1978; Mebold *et al*. 1982; Heiles & Troland 2003b), with larger velocity dispersion. The dependence of HI column density and optical depths of these clouds on their random velocities are not well studied. Our aim was to investigate the nature of low optical depth HI features in the Galaxy and to estimate their velocity distribution. One of the difficulties encountered in studying discrete components in the HI 21 cm-line profiles in the Galactic plane is the plethora of absorption lines. Larger path length through the disk of the Galaxy results in larger number of absorption components. In such cases, the available techniques often result in more than one possible solution for the parameters of individual

features. Moreover, the observed radial velocities are usually the sum of components arising from random motion and the differential rotation of the Galaxy. The distances to the absorbing clouds are seldom known. Hence the systematic component in the observed radial velocity arising from Galaxy's rotation is unknown. Therefore, the lower Galactic latitudes are not suitable for a survey to search for low optical depth components and to study the random velocity distribution of interstellar clouds. We have chosen a lower cutoff of 15° for the Galactic latitude in our observations.

Most of the HI gas at higher latitudes is observed only in HI emission (Dickey & Lockman 1990, and references therein). The HI emission profiles often show components at velocities that cannot arise from Galactic rotation. The existing surveys of HI absorption indicate that there is very little absorption in directions above a latitude of $\sim 45^\circ$, down to optical depths ~ 0.01 (Dickey *et al*. 1978). But, there are indications that HI gas layer of the Galaxy extends to several kpc (Albert 1983; Lockman & Gehman 1991; Kalberla *et al*. 1998). A more sensitive HI absorption search is required to understand the nature of this gas and to characterize it.

We present here the HI absorption measurements with the Giant Metrewave Radio Telescope (GMRT) towards 102 extragalactic radio continuum sources located at intermediate and high latitudes. The present survey, with an rms detection limit of 0.003 in HI optical depth is at least a factor of 5 more sensitive than the existing interferometric surveys and is comparable with the sensitivities achieved in the single dish HI surveys using the Arecibo telescope (Dickey *et al*. 1978; Heiles & Troland 2003a). An overview of the GMRT is given in the next section. The strategy for selecting the sources is outlined in section 4. and the details pertaining to the observations are given in section 5.. A brief description of the data analysis is given in section 6. and section 7. describes a sample HI absorption profile. The list of observed sources is presented in Appendix A, the HI line profiles towards these sources are given in Appendix B, and Appendix C lists the discrete HI features identified from each of these profiles.

3. The Giant Meterwave Radio Telescope

The Giant Meterwave Radio Telescope (GMRT) consists of 30 fully steerable dishes, of 45 meter diameter with a maximum baseline of 25 km (Swarup *et al*. 1991). The aperture efficiency of the dishes is $\sim 40\%$ in the 21 cm band, which implies an effective collecting area of $\sim 19000\,\mathrm{m}^2$. The full width at half maximum of the primary beam is $\sim 25'$ and that of the synthesized beam is $\sim 2''$ (uniform weighting) at 1.4 GHz. The 21 cm receiver is a wide band system covering the frequency range 900–1450 MHz. It is a prime focus uncooled receiver with a characteristic system temperature of ~ 70 K. The 21 cm system has four sub-bands, centered at 1060, 1170, 1280 and 1390 MHz respectively, each with a 3 dB bandwidth of 120 MHz. At the time when these observations were carried out, this telescope was equipped with an FX correlator providing 128 channels per polarization per baseline. A baseband bandwidth ranging from 16 MHz down to 64 kHz variable in steps of 2 can be chosen.

4. Source selection

In selecting the sources, we have used a lower cutoff in flux density of 1 Jy at 20 cm wavelength. This was to ensure that we reach an rms in HI optical depth ~ 0.003

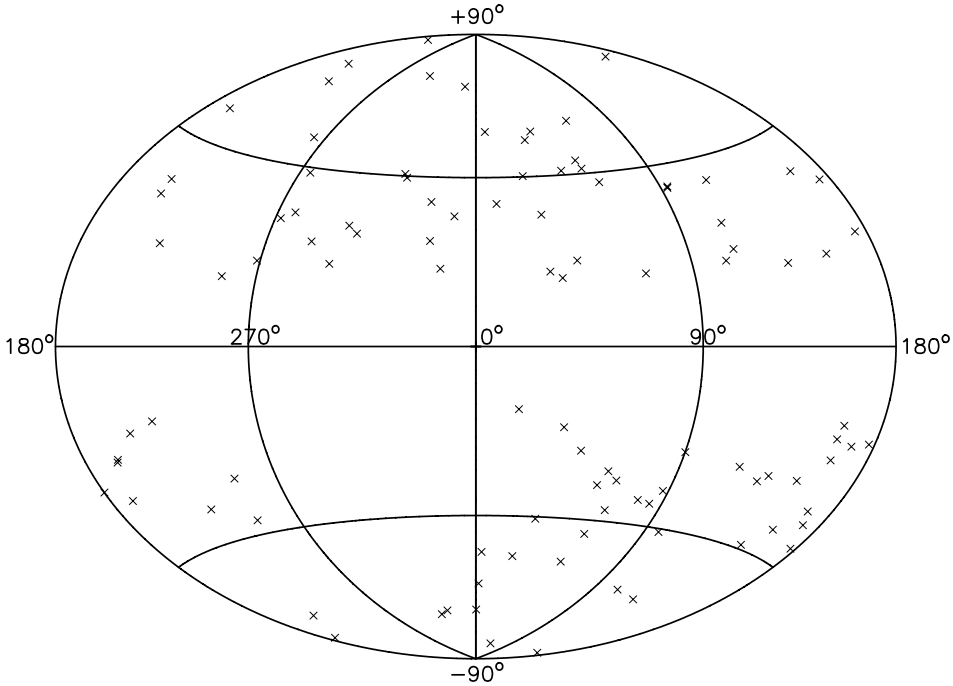

Figure 1. The distribution of program sources in Galactic co-ordinates. The fourth Galactic quadrant ($270^\circ < l < 360^\circ$) is not fully accessible for the GMRT, since this region is mainly in the southern equatorial hemisphere.

within an observing time $\lesssim 1$ h. In order to obtain a sample of these bright sources uniformly distributed all over the sky we used the VLA calibrator manual as the basic finding list. A list of 102 point sources, unresolved in the VLA B array configuration, with their Galactic latitude $|b| \geq 15^\circ$ were selected. Figure 1 shows the distribution of the program sources in the sky. The list of sources is given in Appendix A.

To supplement the absorption spectra, HI emission profiles were extracted from the Leiden–Dwingeloo all sky survey of Galactic neutral hydrogen (LDS, Hartmann & Burton 1995). This survey used the 25 meter Dwingeloo telescope to map the sky in HI emission. The full width at half maximum of the primary beam of the Dwingeloo telescope is $\sim 36'$. The geographic latitude of the Dwingeloo telescope is $\sim +53^\circ$ and that of the GMRT is $\sim +19^\circ$. Therefore some of the lines of sight in the southern hemisphere observed with the GMRT are not accessible to the Dwingeloo telescope.

5. Observations

The HI absorption observations were carried out using the GMRT during March–April 2000, and April–June 2001. On an average, we used ~ 20 antennas in the final analysis, though the actual number varied from 12 to 25. We used a baseband of width 2 MHz, which translates to ≈ 422 km s^{-1} in velocity and a resolution of ~ 3.3 km s^{-1}. The centre of the band was set at 1420.4 MHz. We used one of the VLA primary flux density calibrators (3C48/3C147/3C286) for setting the flux density scale. Since all the

Table 1. The Observational Setup.

Telescope	GMRT
System temperature	~ 70 K
Aperture efficiency	$\sim 40\%$
Baseband bandwidth	2.0 MHz
Number of channels	128
Velocity resolution	3.3 km s^{-1}
On source integration time	$\sim$ 10 to 60 minutes
rms noise (1 hr integration time)	~ 2 mJy beam^{-1} channel^{-1}

program sources were unresolved by the GMRT, they also served as phase calibrators. Bandpass calibration was carried out once every two hours for 10 minutes using 3C286, towards which no HI absorption was detected down to an rms in optical depth of $\tau_{\rm HI} \sim 0.002$. On source integration time ranged from 10 to 60 minutes, depending on its strength. The rms sensitivity in optical depth varied from 0.002 to 0.008 towards different sources, with a mean value ~ 0.003. A summary of the observational setup is given in Table 1.

6. Data analysis

The data were analysed using the Astronomical Image Processing System (AIPS) developed by the National Radio Astronomy Observatory. The observing band was found to be free from any kind of interference. The resulting data set consisted of 102 image cubes. The full width at half maximum of the synthesized beam width was in the range $\sim 6''$ to $\sim 25''$, depending on the number and locations of available antennas. Continuum subtraction was carried out by fitting a second order baseline to the line-free channels in the visibility domain and subtracting the best fit continuum from all the channels. Such a second order fit to the spectral baseline can result in the removal of broad and shallow absorption features. From the nature of the baselines fitted to the present dataset, we infer that any spectral features with FWHM $\gtrsim 50$ km s^{-1} and $\tau_{\rm HI} \lesssim 0.03$ would not be detected. However, the main aim of the present survey is to study the narrow absorption lines arising from the diffuse features in the CNM and the FWHM of such features are usually $\lesssim 10$ km s^{-1}. The second order fit also helps to achieve a better spectral dynamic range over the 2 MHz bandwidth. The resulting spectral dynamic range was ~ 500. However, for a few lines of sight, the bandpass errors were much larger and only a limited part of the observing band was found to be usable. To study the individual HI absorption components multiple Gaussian profiles were fitted to the absorption line spectra using the Groningen Image Processing System (GIPSY).

For an optically thin HI gas, the radiative transfer equation has a solution of the form (Spitzer 1978)

$$T_B = T_S(1 - e^{-\tau}), \tag{1}$$

where T_B is the brightness temperature, T_S is the spin (excitation) temperature and τ is the optical depth of the HI 21-cm line. Hence, knowing the line brightness temperature

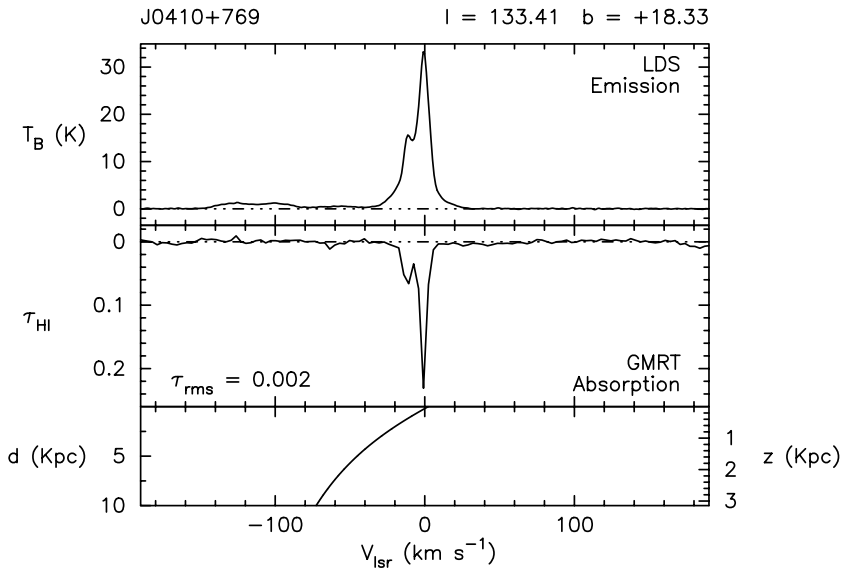

Figure 2. The HI optical depth spectrum from the GMRT towards one of the 102 sources (middle panel) and the corresponding HI brightness temperature profile from the Leiden–Dwingeloo survey (top panel). The lower panel is the Galactic rotation curve for the given line of sight obtained from the Galactic rotation model (Brand & Blitz 1993). The heliocentric distance as a function of radial velocity is labeled on the left of the lower panel and the corresponding height above the mid-plane of the Galaxy is labeled on the right side.

T_B, which is obtained from the HI emission profiles, and the optical depth τ, obtained from HI absorption, one can estimate the spin temperature T_S of HI gas.

Apart from the new HI absorption measurements with the GMRT, we have extracted the HI emission profiles towards these lines of sight (if available) from the Leiden–Dwingeloo sky survey (Hartmann & Burton 1995). We have used Gaussian fitting to the spectra to separate the profiles into discrete components. The HI emission profiles were Hanning smoothed over two channels, with a resulting velocity resolution of $\sim 2\,\mathrm{km\ s^{-1}}$. It is well known that the HI emission features are broader than the corresponding absorption features. This difference in the velocity width usually range from 0–5 km s^{-1} (Radhakrishnan *et al*. 1972b). It is also known that the wider HI emission features (FWHM $> 20\,\mathrm{km\ s^{-1}}$) arise in the warm neutral medium (WNM) (Radhakrishnan *et al*. 1972b). To identify the HI emission and absorption lines that arise from the same cloud, we have adopted the following considerations:

- The central velocities of the HI emission and absorption features are within the channel width, $\sim 3.3\,\mathrm{km\ s^{-1}}$, of the GMRT observations, and
- The difference between the widths of emission and the corresponding absorption line is less than $\sim 5\,\mathrm{km\ s^{-1}}$.

If both the above conditions were satisfied, we assume the features to arise from the same cloud. The second criterion excludes those instances where the velocity of a CNM absorption line match that of a WNM emission component. We have used the fitted values of τ and T_B to calculate the spin temperatures of HI features which are identified in both HI emission and absorption profiles. In those cases, where no HI absorption

feature was detected from our survey corresponding to the HI emission feature in the LDS survey data, we have estimated the lower limit for the spin temperature of the gas.

7. The spectra

Figure 2 is a sample spectrum of HI optical depth and the corresponding HI emission profile. In the figure, the lower panel is the Galactic rotation curve for the given line of sight obtained from the Galactic rotation model by Brand & Blitz (1993). We have used $R_0 = 8.5$ Kpc as the Galacto-centric distance and $\Theta_0 = 220\,\mathrm{km\ s^{-1}}$ as the solar orbital velocity around the Galactic centre. The rest of the spectra are given in Appendix B and the summary of the Gaussian fitting results are given in Appendix C. In all we have obtained 126 spectral components in HI absorption from GMRT and 478 components in HI emission from the LDS survey. The fitted parameters for the discrete components in HI absorption and emission were used to estimate the spin temperature of the respective features. A detailed analysis and interpretation of these spectra are given in an accompanying paper (Mohan *et al*. 2004; this volume).

Acknowledgements

We wish to thank C. R. Subrahmanya for useful discussions related to the GMRT offline software. We thank the referee, Miller Goss, for detailed comments and constructive criticism resulting in an improved version of this paper. We thank the staff of the GMRT who made these observations possible. The GMRT is operated by the National Centre for Radio Astrophysics of the Tata Institute of Fundamental Research. This research has made use of NASA's Astrophysics Data System.

Appendix A: The source list

The list of sources observed with the GMRT. The sixth column gives the rms optical depth in the HI absorption spectra and the last column lists the observed flux densities of the respective sources.

Source	α(J2000) (h	m	s)	δ(J2000) (○	′	″)	l (○)	b (○)	τ_{rms}	S (Jy)
J0010 − 418	00	10	52.52	−41	53	10.8	329.68	−73.07	0.002	4.55
J0022 + 002	00	22	25.43	+00	14	56.1	107.46	−61.75	0.003	3.11
J0024 − 420	00	24	42.99	−42	02	04.0	321.35	−74.12	0.003	2.17
J0025 − 260	00	25	49.17	−26	02	12.7	42.27	−84.17	0.003	7.12
J0029 + 349	00	29	14.24	+34	56	32.2	117.79	−27.71	0.002	2.03
J0059 + 001	00	59	05.51	+00	06	51.6	127.11	−62.70	0.004	2.64
J0116 − 208	01	16	51.40	−20	52	06.8	167.11	−81.47	0.003	3.91
J0119 + 321	01	19	35.00	+32	10	50.1	129.83	−30.31	0.003	3.12
J0137 + 331	01	37	41.30	+33	09	35.1	133.96	−28.72	0.003	15.9
J0204 + 152	02	04	50.41	+15	14	11.0	147.93	−44.04	0.003	3.96
J0204 − 170	02	04	57.67	−17	01	19.8	185.99	−70.23	0.003	1.19
J0237 + 288	02	37	52.41	+28	48	09.0	149.47	−28.53	0.003	2.10
J0238 + 166	02	38	38.93	+16	36	59.3	156.77	−39.11	0.004	1.05
J0240 − 231	02	40	08.17	−23	09	15.7	209.79	−65.13	0.003	5.50

Source	α(J2000) (h	m	s)	δ(J2000) (○	′	″)	l (○)	b (○)	τ_{rms}	S (Jy)
J0318 + 164	03	18	57.80	+16	28	32.7	166.64	−33.60	0.002	8.65
J0321 + 123	03	21	53.10	+12	21	14.0	170.59	−36.24	0.002	2.07
J0323 + 055	03	23	20.26	+05	34	11.9	176.98	−40.84	0.003	3.04
J0329 + 279	03	29	57.67	+27	56	15.5	160.70	−23.07	0.003	1.40
J0336 + 323	03	36	30.11	+32	18	29.3	159.00	−18.77	0.004	2.71
J0348 + 338	03	48	46.90	+33	53	15.0	160.04	−15.91	0.003	2.32
J0403 + 260	04	03	05.59	+26	00	01.5	168.03	−19.65	0.004	1.08
J0409 + 122	04	09	22.01	+12	17	39.8	180.12	−27.90	0.003	1.46
J0410 + 769	04	10	45.61	+76	56	45.3	133.41	+18.33	0.002	5.70
J0424 + 020	04	24	08.56	+02	04	24.9	192.04	−31.10	0.004	1.33
J0431 + 206	04	31	03.76	+20	37	34.3	176.81	−18.56	0.003	3.40
J0440 − 435	04	40	17.18	−43	33	08.6	248.41	−41.57	0.003	3.28
J0453 − 281	04	53	14.65	−28	07	37.3	229.09	−37.02	0.004	2.18
J0459 + 024	04	59	52.05	+02	29	31.2	197.01	−23.34	0.003	1.93
J0503 + 020	05	3	21.20	+02	03	04.7	197.91	−22.82	0.004	2.26
J0538 − 440	05	38	50.36	−44	05	08.9	250.08	−31.09	0.002	2.75
J0541 − 056	05	41	38.08	−05	41	49.4	210.05	−18.11	0.004	1.42
J0609 − 157	06	09	40.95	−15	42	40.7	222.61	−16.18	0.007	2.78
J0614 + 607	06	14	23.87	+60	46	21.8	153.60	+19.15	0.005	1.17
J0713 + 438	07	13	38.16	+43	49	17.2	173.79	+22.20	0.004	2.33
J0814 + 459	08	14	30.31	+45	56	39.5	173.90	+33.17	0.005	1.13
J0825 + 031	08	25	50.34	+03	09	24.5	221.22	+22.39	0.002	1.12
J0834 + 555	08	34	54.90	+55	34	21.1	162.23	+36.56	0.002	9.15
J0842 + 185	08	42	05.09	+18	35	41.0	207.28	+32.48	0.004	1.17
J0854 + 201	08	54	48.87	+20	06	30.6	206.81	+35.82	0.002	1.65
J0921 − 263	09	21	29.35	−26	18	43.4	255.07	+16.48	0.003	1.41
J0958 + 324	09	58	20.95	+32	24	02.2	194.17	+52.32	0.005	1.47
J1018 − 317	10	18	09.28	−31	44	14.1	268.61	+20.73	0.002	3.44
J1057 − 245	10	57	55.42	−24	33	48.9	272.47	+31.51	0.004	1.10
J1111 + 199	11	11	20.07	+19	55	36.0	225.01	+66.00	0.003	1.52
J1119 − 030	11	19	25.30	−03	02	51.3	263.01	+52.54	0.002	1.44
J1120 − 251	11	20	09.12	−25	08	07.6	278.09	+33.30	0.003	1.31
J1125 + 261	11	25	53.71	+26	10	20.0	210.92	+70.89	0.003	0.96
J1130 − 148	11	30	07.05	−14	49	27.4	275.28	+43.64	0.002	5.96
J1146 + 399	11	46	58.30	+39	58	34.3	164.95	+71.47	0.009	0.47
J1154 − 350	11	54	21.79	−35	05	29.0	289.93	+26.34	0.002	5.48
J1221 + 282	12	21	31.69	+28	13	58.5	201.74	+83.29	0.004	1.03
J1235 − 418	12	35	41.93	−41	53	18.0	299.80	+20.89	0.003	1.57
J1254 + 116	12	54	38.26	+11	41	05.9	305.87	+74.54	0.005	0.93
J1257 − 319	12	57	59.06	−31	55	16.9	304.55	+30.93	0.003	1.21
J1316 − 336	13	16	07.99	−33	38	59.2	308.80	+28.94	0.006	1.11
J1344 + 141	13	44	23.74	+14	09	14.9	349.16	+72.09	0.003	1.34
J1351 − 148	13	51	52.65	−14	49	14.9	324.03	+45.56	0.003	1.16

Source	α(J2000) (h	m	s)	δ(J2000) (○	′	″)	l (○)	b (○)	τ_{rms}	S (Jy)
J1357 − 154	13	57	11.24	−15	27	28.8	325.42	+44.52	0.015	1.11
J1435 + 760	14	35	47.10	+76	05	25.8	115.07	+39.40	0.003	1.19
J1445 + 099	14	45	16.47	+09	58	36.1	5.79	+58.17	0.002	2.62
J1448 − 163	14	48	15.05	−16	20	24.5	339.45	+38.11	0.003	1.63
J1506 + 375	15	06	09.53	+37	30	51.1	61.65	+59.90	0.003	1.15
J1513 + 236	15	13	40.19	+23	38	35.2	34.77	+57.79	0.002	1.73
J1517 − 243	15	17	41.81	−24	22	19.5	340.68	+27.58	0.004	2.53
J1520 + 202	15	20	05.49	+20	16	05.6	29.64	+55.42	0.003	3.17
J1526 − 138	15	26	59.44	−13	51	00.1	350.48	+34.29	0.002	2.63
J1553 + 129	15	53	32.70	+12	56	51.7	23.79	+45.22	0.003	1.49
J1554 − 270	15	54	02.49	−27	04	40.2	345.68	+20.27	0.003	1.52
J1557 − 000	15	57	51.43	+00	01	50.4	9.58	+37.68	0.004	0.95
J1602 + 334	16	02	07.26	+33	26	53.1	53.73	+48.71	0.002	3.33
J1609 + 266	16	09	13.32	+26	41	29.0	44.17	+46.20	0.003	4.57
J1613 + 342	16	13	41.06	+34	12	47.9	55.15	+46.38	0.001	5.35
J1634 + 627	16	34	33.80	+62	45	35.9	93.61	+39.38	0.002	4.67
J1635 + 381	16	35	15.49	+38	08	04.5	61.09	+42.34	0.002	3.45
J1638 + 625	16	38	28.21	+62	34	44.3	93.22	+39.01	0.003	4.65
J1640 + 123	16	40	47.93	+12	20	02.1	29.43	+34.51	0.003	1.87
J1737 + 063	17	37	13.73	+06	21	03.5	30.15	+19.38	0.005	0.87
J1745 + 173	17	45	35.21	+17	20	01.4	41.74	+22.12	0.004	1.19
J1751 + 096	17	51	32.82	+09	39	00.7	34.92	+17.65	0.002	1.76
J1800 + 784	18	00	45.68	+78	28	04.1	110.04	+29.07	0.002	2.71
J1845 + 401	18	45	11.12	+40	07	51.5	69.36	+18.21	0.003	1.41
J1923 − 210	19	23	32.19	−21	04	33.3	17.18	−16.25	0.003	2.82
J2005 + 778	20	05	31.00	+77	52	43.2	110.46	+22.73	0.003	1.38
J2009 + 724	20	09	52.30	+72	29	19.4	105.36	+20.18	0.003	1.00
J2011 − 067	20	11	14.22	−06	44	03.6	36.01	−20.80	0.002	3.39
J2047 − 026	20	47	10.35	−02	36	22.2	44.56	−26.80	0.002	2.94
J2130 + 050	21	30	32.88	+05	02	17.5	58.65	−31.81	0.002	5.05
J2136 + 006	21	36	38.59	+00	41	54.2	55.47	−35.58	0.002	5.22
J2137 − 207	21	37	50.00	−20	42	31.8	30.35	−45.56	0.002	3.87
J2148 + 069	21	48	05.46	+06	57	38.6	63.66	−34.07	0.002	3.74
J2212 + 018	22	12	37.98	+01	52	51.2	63.68	−42.02	0.001	3.95
J2214 − 385	22	14	38.57	−38	35	45.0	3.47	−55.44	0.002	1.76
J2219 − 279	22	19	40.94	−27	56	26.9	22.57	−56.48	0.003	2.55
J2225 − 049	22	25	47.26	−04	57	01.4	58.96	−48.84	0.003	5.32
J2232 + 117	22	32	36.41	+11	43	50.9	77.44	−38.58	0.003	7.43
J2236 + 284	22	36	22.47	+28	28	57.4	90.12	−25.65	0.004	1.38
J2246 − 121	22	46	18.23	−12	06	51.3	53.87	−57.07	0.003	2.26
J2250 + 143	22	50	25.54	+14	19	50.6	83.89	−39.20	0.002	2.16
J2251 + 188	22	51	34.74	+18	48	40.1	87.35	−35.65	0.002	3.24
J2302 − 373	23	02	23.89	−37	18	06.8	2.16	−64.91	0.002	3.09
J2340 + 135	23	40	33.22	+13	33	00.9	97.80	−45.83	0.002	2.82
J2341 − 351	23	41	45.89	−35	06	22.1	0.45	−73.12	0.004	2.06

Appendix B: The spectra

In this Appendix, we present the HI optical depth profiles obtained from the high latitude Galactic HI absorption survey using the GMRT along with the HI emission profiles in the respective lines of sight from the Leiden–Dwingeloo survey of Galactic neutral hydrogen (if available). The figures are arranged in order of increasing right ascension. The spectra are labeled by the radio continuum source name in J2000.0 co-ordinates (top left) and its Galactic co-ordinates (top right).

For each of the figures, the HI emission profile from the Leiden–Dwingeloo survey is shown in the top panel and the HI optical depth profile from the GMRT is shown in the middle panel. The lower panel is the Galactic rotation curve for the given line of sight. The heliocentric distance as a function of radial velocity ($V_{\rm lsr}$) is labeled on the left of this panel and the corresponding height above the mid-plane of the Galaxy is labeled on its right side. For a few lines of sight, only the reliable part of the observing band is shown.

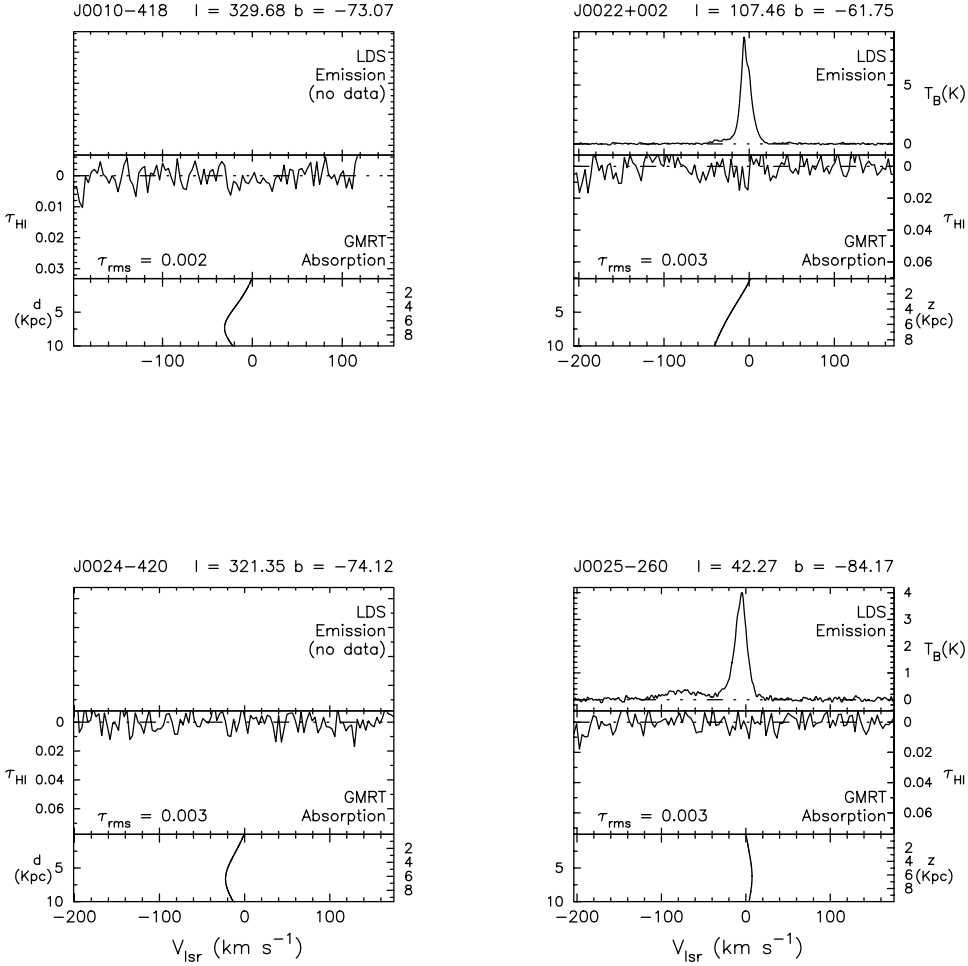

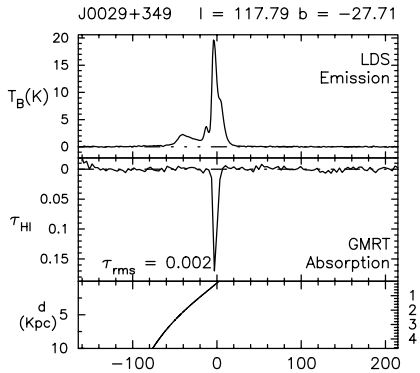
J0029+349 l = 117.79 b = −27.71
LDS
Emission
T_B(K)
GMRT
Absorption
τ_{rms} = 0.002
τ_{HI}
d
(Kpc)

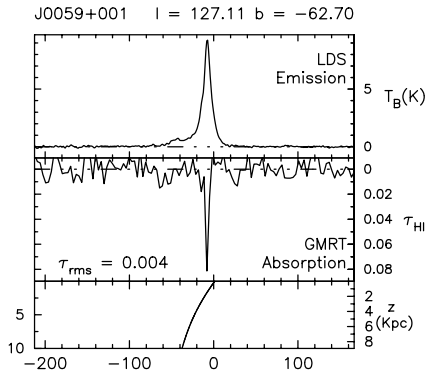
J0059+001 l = 127.11 b = −62.70
LDS
Emission
T_B(K)
GMRT
Absorption
τ_{rms} = 0.004
τ_{HI}
z
(Kpc)

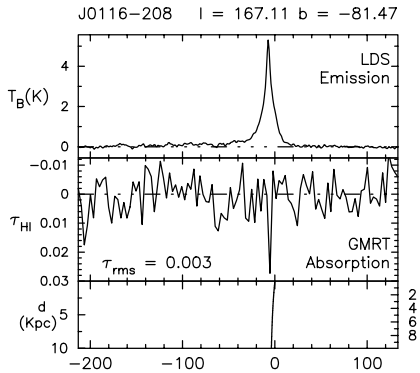
J0116−208 l = 167.11 b = −81.47
LDS
Emission
T_B(K)
GMRT
Absorption
τ_{rms} = 0.003
τ_{HI}
d
(Kpc)

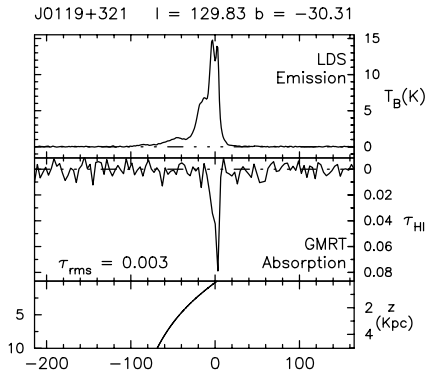
J0119+321 l = 129.83 b = −30.31
LDS
Emission
T_B(K)
GMRT
Absorption
τ_{rms} = 0.003
τ_{HI}
z
(Kpc)

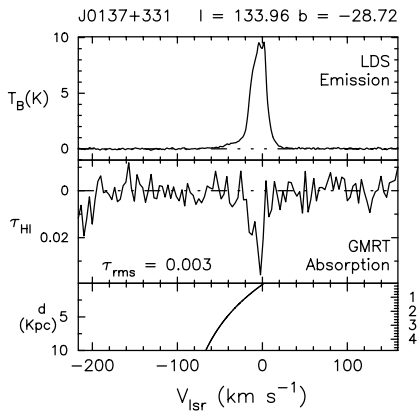
J0137+331 l = 133.96 b = −28.72
LDS
Emission
T_B(K)
GMRT
Absorption
τ_{rms} = 0.003
τ_{HI}
d
(Kpc)
V_{lsr} (km s^{-1})

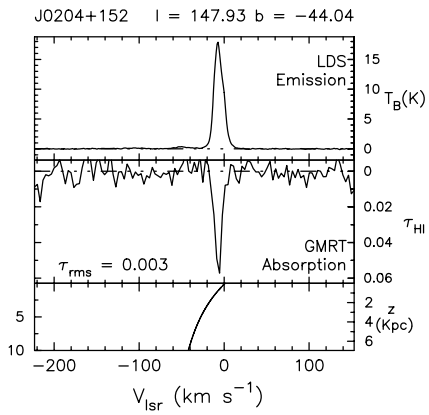
J0204+152 l = 147.93 b = −44.04
LDS
Emission
T_B(K)
GMRT
Absorption
τ_{rms} = 0.003
τ_{HI}
z
(Kpc)
V_{lsr} (km s^{-1})

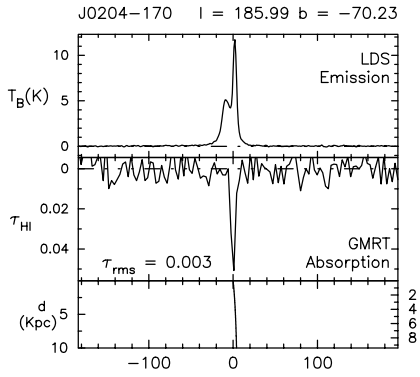
J0204−170 l = 185.99 b = −70.23
LDS
Emission
T_B(K)
GMRT
Absorption
τ_{rms} = 0.003
τ_{HI}
d
(Kpc)
z
(Kpc)

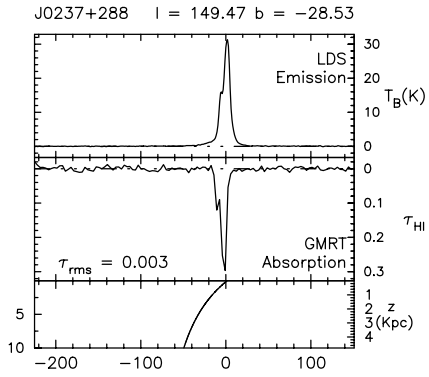
J0237+288 l = 149.47 b = −28.53
LDS
Emission
T_B(K)
GMRT
Absorption
τ_{rms} = 0.003
τ_{HI}
z
(Kpc)

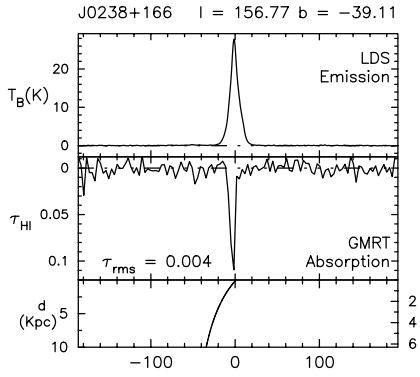
J0238+166 l = 156.77 b = −39.11
LDS
Emission
T_B(K)
GMRT
Absorption
τ_{rms} = 0.004
τ_{HI}
d
(Kpc)

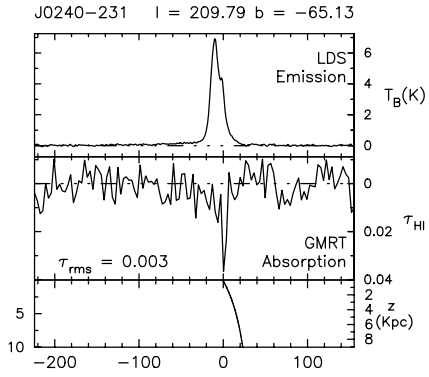
J0240−231 l = 209.79 b = −65.13
LDS
Emission
T_B(K)
GMRT
Absorption
τ_{rms} = 0.003
τ_{HI}
z
(Kpc)

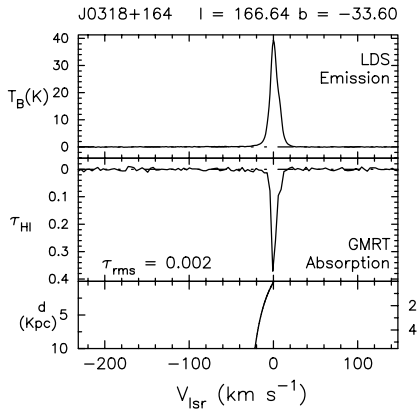
J0318+164 l = 166.64 b = −33.60
LDS
Emission
T_B(K)
GMRT
Absorption
τ_{rms} = 0.002
τ_{HI}
d
(Kpc)
V_{lsr} (km s^{-1})

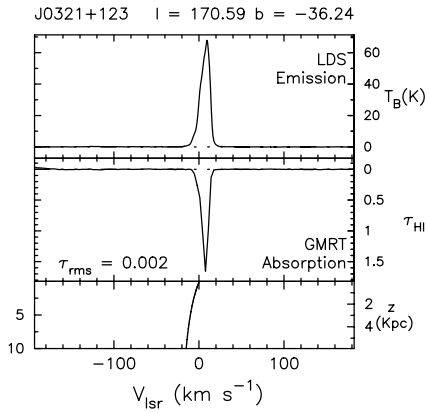
J0321+123 l = 170.59 b = −36.24
LDS
Emission
T_B(K)
GMRT
Absorption
τ_{rms} = 0.002
τ_{HI}
z
(Kpc)
V_{lsr} (km s^{-1})

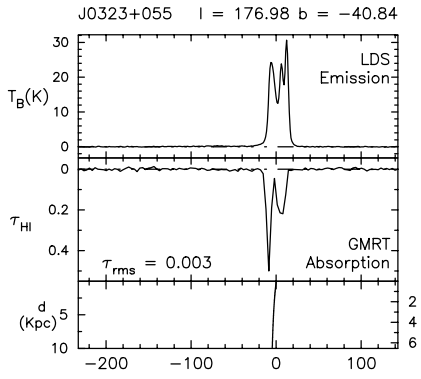
J0323+055 l = 176.98 b = −40.84
LDS
Emission
T_B(K)
GMRT
Absorption
τ_{rms} = 0.003
τ_{HI}
d
(Kpc)

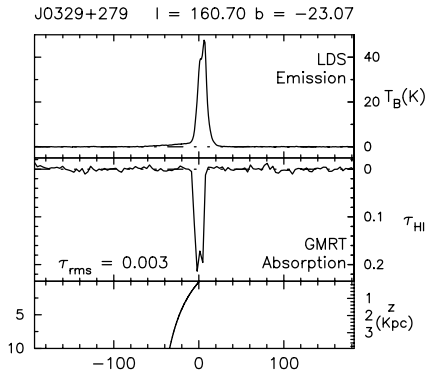
J0329+279 l = 160.70 b = −23.07
LDS
Emission
T_B(K)
GMRT
Absorption
τ_{rms} = 0.003
τ_{HI}
z
(Kpc)

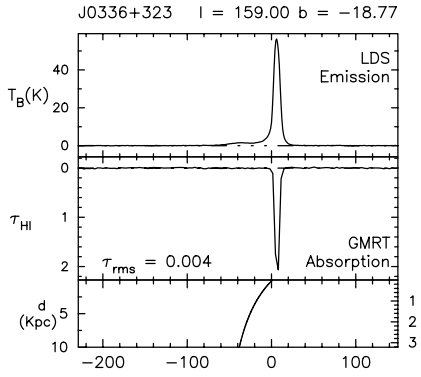
J0336+323 l = 159.00 b = −18.77
LDS
Emission
T_B(K)
GMRT
Absorption
τ_{rms} = 0.004
τ_{HI}
d
(Kpc)

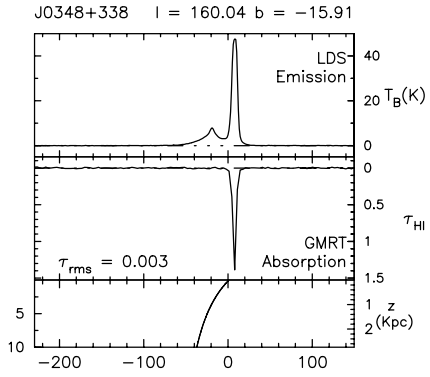
J0348+338 l = 160.04 b = −15.91
LDS
Emission
T_B(K)
GMRT
Absorption
τ_{rms} = 0.003
τ_{HI}
z
(Kpc)

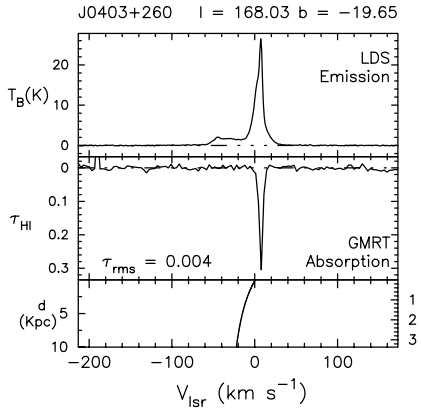
J0403+260 l = 168.03 b = −19.65
LDS
Emission
T_B(K)
GMRT
Absorption
τ_{rms} = 0.004
τ_{HI}
d
(Kpc)
V_{lsr} (km s^{-1})

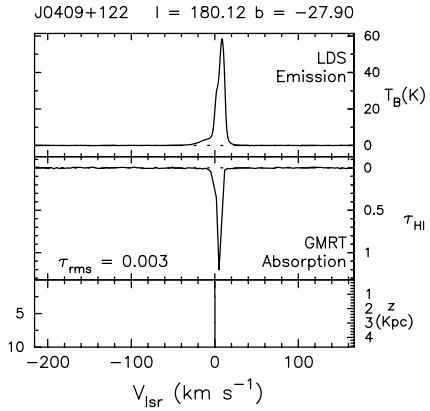
J0409+122 l = 180.12 b = −27.90
LDS
Emission
T_B(K)
GMRT
Absorption
τ_{rms} = 0.003
τ_{HI}
z
(Kpc)
V_{lsr} (km s^{-1})

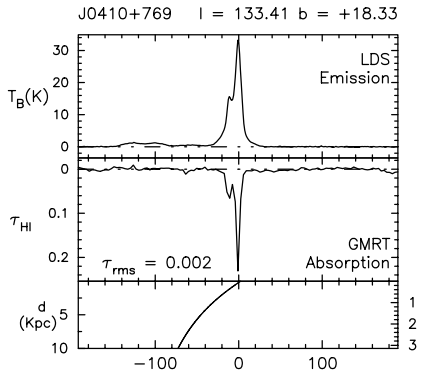
J0410+769 l = 133.41 b = +18.33
LDS
Emission
T_B(K)
GMRT
Absorption
τ_{rms} = 0.002
τ_{HI}
d
(Kpc)
z
(Kpc)

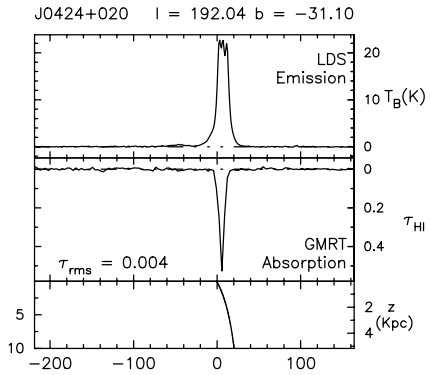
J0424+020 l = 192.04 b = −31.10
LDS
Emission
T_B(K)
GMRT
Absorption
τ_{rms} = 0.004
τ_{HI}
z
(Kpc)

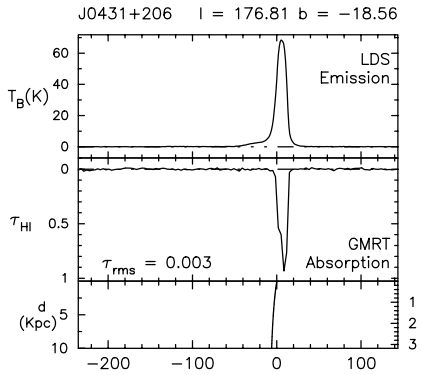
J0431+206 l = 176.81 b = −18.56
LDS
Emission
T_B(K)
GMRT
Absorption
τ_{rms} = 0.003
τ_{HI}
d
(Kpc)
z
(Kpc)

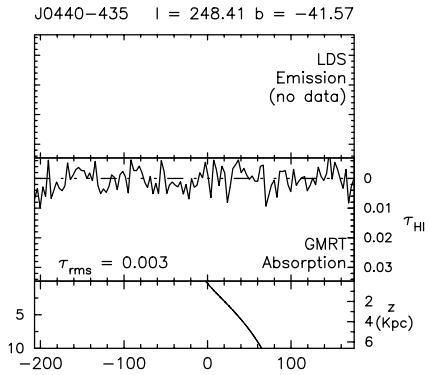
J0440−435 l = 248.41 b = −41.57
LDS
Emission
(no data)
GMRT
Absorption
τ_{rms} = 0.003
τ_{HI}
z
(Kpc)

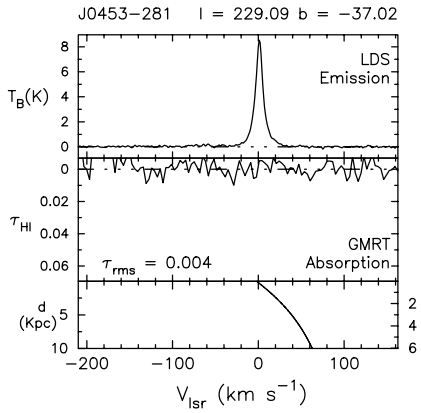
J0453−281 l = 229.09 b = −37.02
LDS
Emission
T_B(K)
GMRT
Absorption
τ_{rms} = 0.004
τ_{HI}
d
(Kpc)
V_{lsr} (km s^{-1})

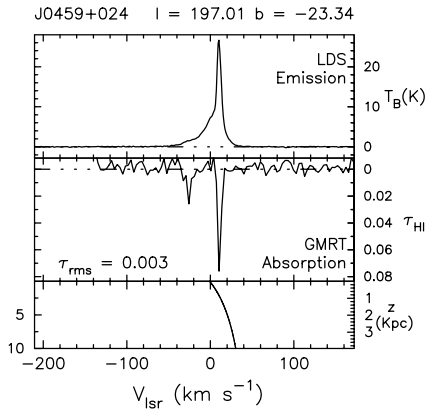
J0459+024 l = 197.01 b = −23.34
LDS
Emission
T_B(K)
GMRT
Absorption
τ_{rms} = 0.003
τ_{HI}
z
(Kpc)
V_{lsr} (km s^{-1})

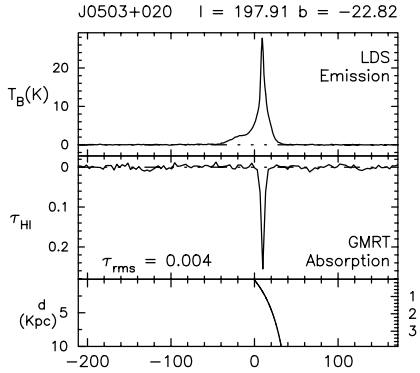
J0503+020 l = 197.91 b = −22.82
LDS
Emission
T_B(K)
τ_{HI}
GMRT
Absorption
τ_{rms} = 0.004
d
(Kpc)

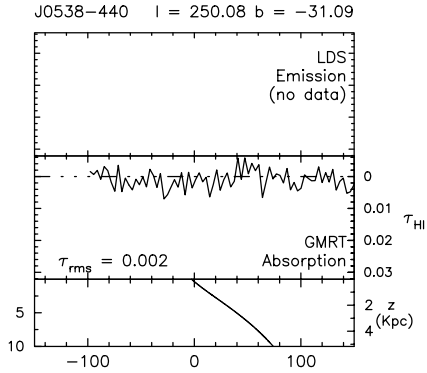
J0538−440 l = 250.08 b = −31.09
LDS
Emission
(no data)
τ_{HI}
GMRT
Absorption
τ_{rms} = 0.002
z
(Kpc)

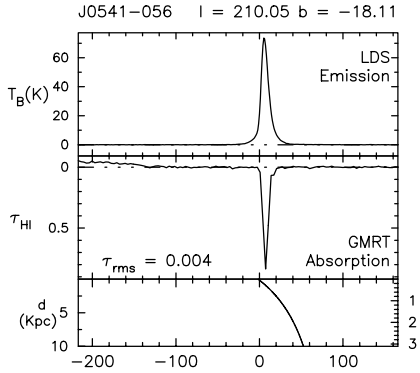
J0541−056 l = 210.05 b = −18.11
LDS
Emission
T_B(K)
τ_{HI}
GMRT
Absorption
τ_{rms} = 0.004
d
(Kpc)

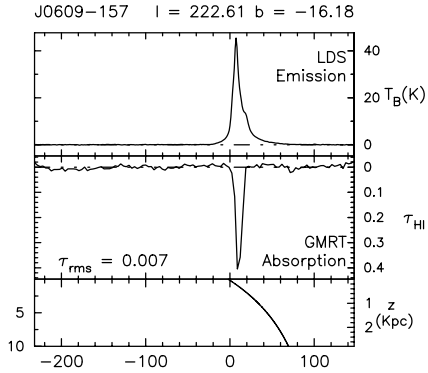
J0609−157 l = 222.61 b = −16.18
LDS
Emission
T_B(K)
τ_{HI}
GMRT
Absorption
τ_{rms} = 0.007
z
(Kpc)

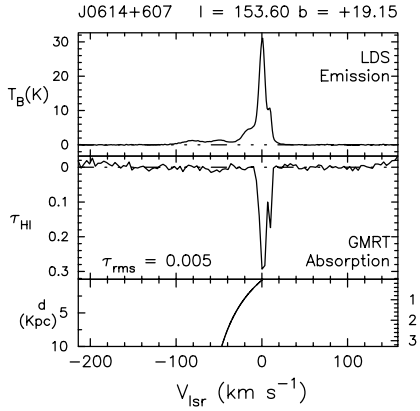
J0614+607 l = 153.60 b = +19.15
LDS
Emission
T_B(K)
τ_{HI}
GMRT
Absorption
τ_{rms} = 0.005
d
(Kpc)
V_{lsr} (km s^{-1})

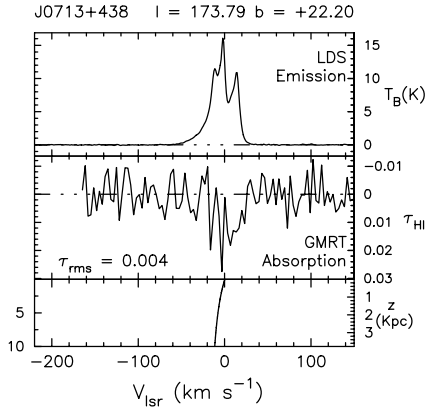
J0713+438 l = 173.79 b = +22.20
LDS
Emission
T_B(K)
τ_{HI}
GMRT
Absorption
τ_{rms} = 0.004
z
(Kpc)
V_{lsr} (km s^{-1})

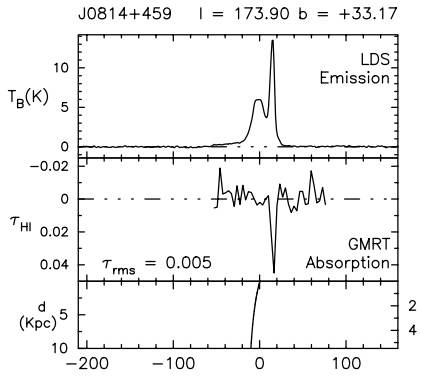
J0814+459 l = 173.90 b = +33.17
LDS
Emission
T_B(K)
GMRT
Absorption
τ_{rms} = 0.005
τ_{HI}
d
(Kpc)

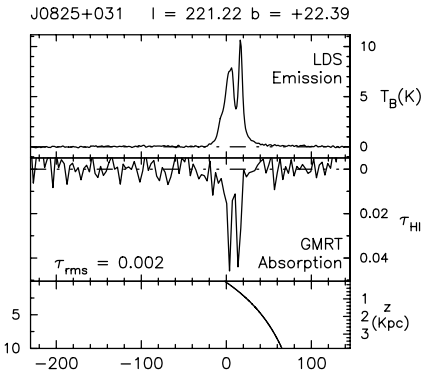
J0825+031 l = 221.22 b = +22.39
LDS
Emission
T_B(K)
GMRT
Absorption
τ_{rms} = 0.002
τ_{HI}
z
(Kpc)

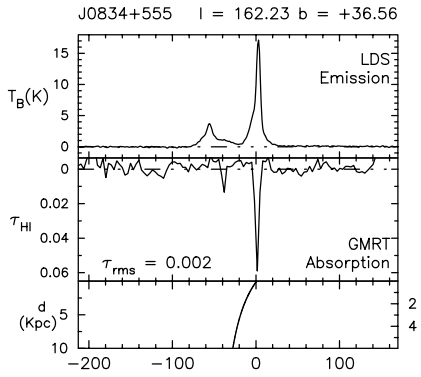
J0834+555 l = 162.23 b = +36.56
LDS
Emission
T_B(K)
GMRT
Absorption
τ_{rms} = 0.002
τ_{HI}
d
(Kpc)

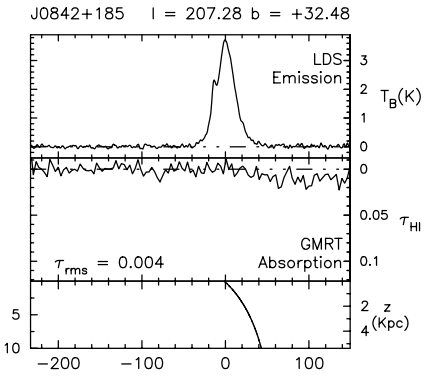
J0842+185 l = 207.28 b = +32.48
LDS
Emission
T_B(K)
GMRT
Absorption
τ_{rms} = 0.004
τ_{HI}
z
(Kpc)

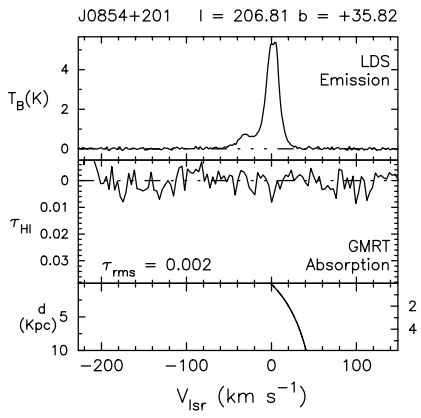
J0854+201 l = 206.81 b = +35.82
LDS
Emission
T_B(K)
GMRT
Absorption
τ_{rms} = 0.002
τ_{HI}
d
(Kpc)
V_{lsr} (km s^{-1})

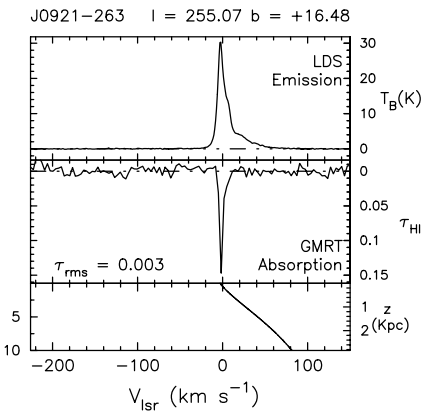
J0921−263 l = 255.07 b = +16.48
LDS
Emission
T_B(K)
GMRT
Absorption
τ_{rms} = 0.003
τ_{HI}
z
(Kpc)
V_{lsr} (km s^{-1})

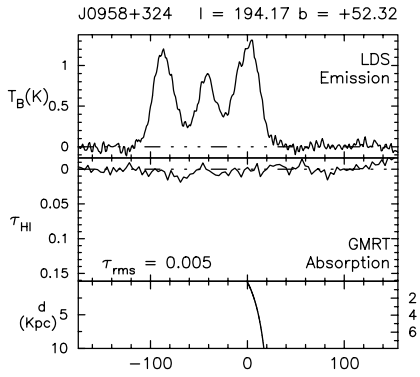
J0958+324 l = 194.17 b = +52.32
LDS
Emission
T_B(K)
GMRT
Absorption
τ_{rms} = 0.005
τ_{HI}
d
(Kpc)

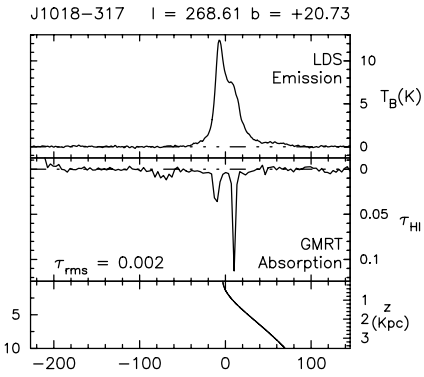
J1018−317 l = 268.61 b = +20.73
LDS
Emission
T_B(K)
GMRT
Absorption
τ_{rms} = 0.002
τ_{HI}
z
(Kpc)

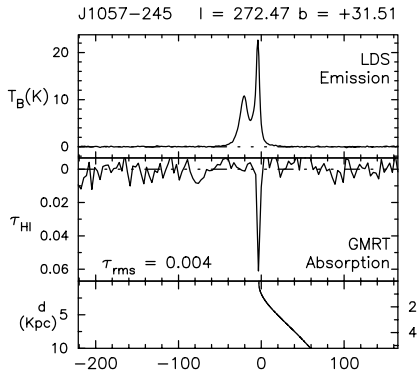
J1057−245 l = 272.47 b = +31.51
LDS
Emission
T_B(K)
GMRT
Absorption
τ_{rms} = 0.004
τ_{HI}
d
(Kpc)

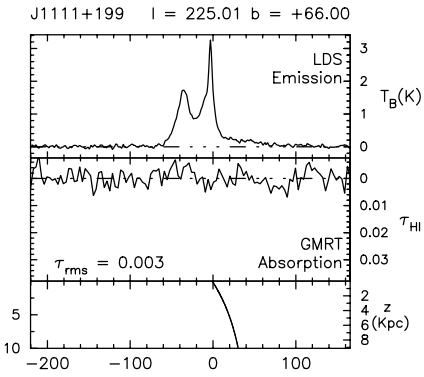
J1111+199 l = 225.01 b = +66.00
LDS
Emission
T_B(K)
GMRT
Absorption
τ_{rms} = 0.003
τ_{HI}
z
(Kpc)

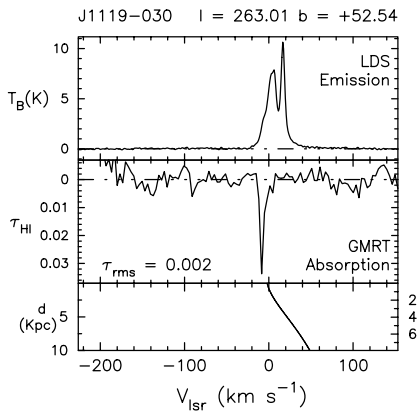
J1119−030 l = 263.01 b = +52.54
LDS
Emission
T_B(K)
GMRT
Absorption
τ_{rms} = 0.002
τ_{HI}
d
(Kpc)
V_{lsr} (km s^{-1})

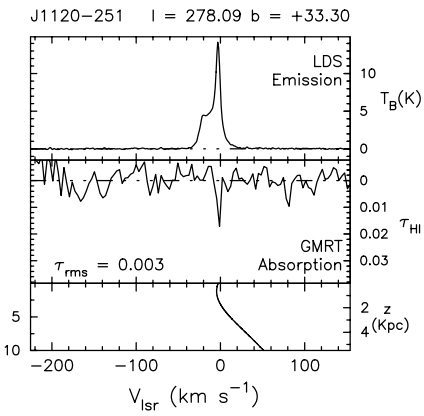
J1120−251 l = 278.09 b = +33.30
LDS
Emission
T_B(K)
GMRT
Absorption
τ_{rms} = 0.003
τ_{HI}
z
(Kpc)
V_{lsr} (km s^{-1})

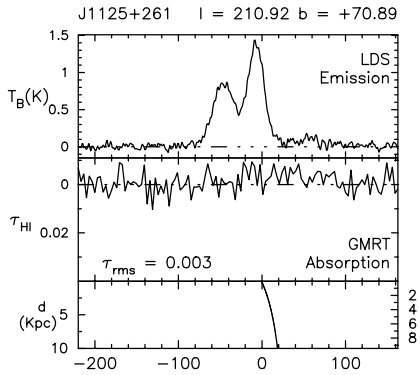
J1125+261 l = 210.92 b = +70.89
LDS
Emission
T_B(K)
τ_{HI}
GMRT
Absorption
τ_{rms} = 0.003
d
(Kpc)

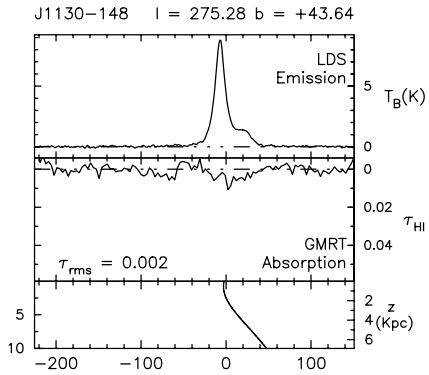
J1130−148 l = 275.28 b = +43.64
LDS
Emission
T_B(K)
τ_{HI}
GMRT
Absorption
τ_{rms} = 0.002
z
(Kpc)

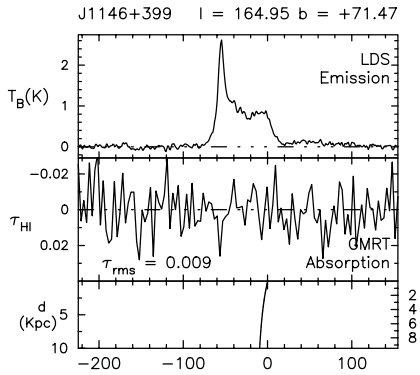
J1146+399 l = 164.95 b = +71.47
LDS
Emission
T_B(K)
τ_{HI}
GMRT
Absorption
τ_{rms} = 0.009
d
(Kpc)

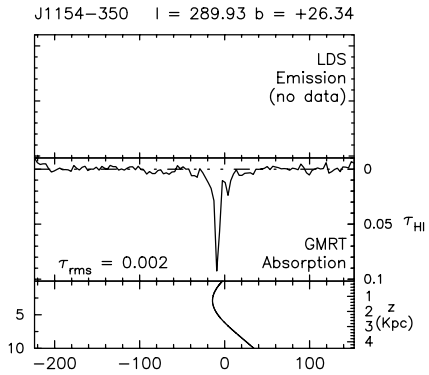
J1154−350 l = 289.93 b = +26.34
LDS
Emission
(no data)
τ_{HI}
GMRT
Absorption
τ_{rms} = 0.002
z
(Kpc)

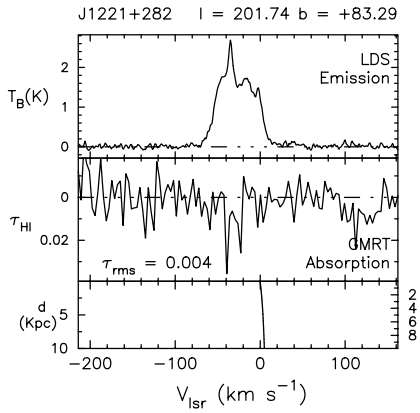
J1221+282 l = 201.74 b = +83.29
LDS
Emission
T_B(K)
τ_{HI}
GMRT
Absorption
τ_{rms} = 0.004
d
(Kpc)
V_{lsr} (km s^{-1})

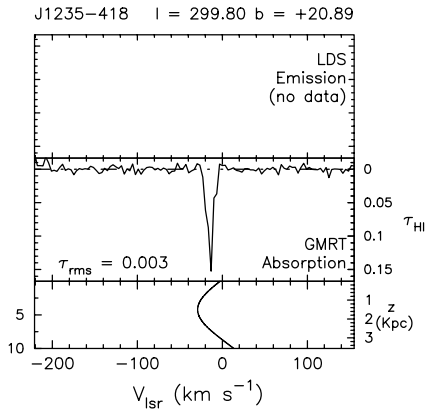
J1235−418 l = 299.80 b = +20.89
LDS
Emission
(no data)
τ_{HI}
GMRT
Absorption
τ_{rms} = 0.003
z
(Kpc)
V_{lsr} (km s^{-1})

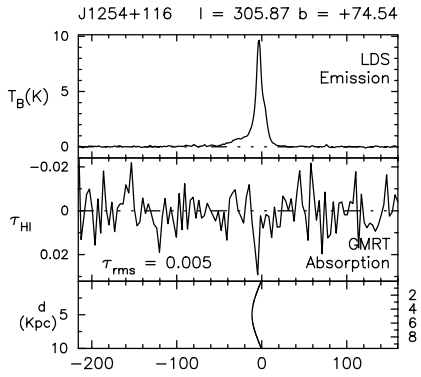
J1254+116 l = 305.87 b = +74.54
LDS
Emission
T_B(K)
τ_{HI}
GMRT
Absorption
τ_{rms} = 0.005
d
(Kpc)

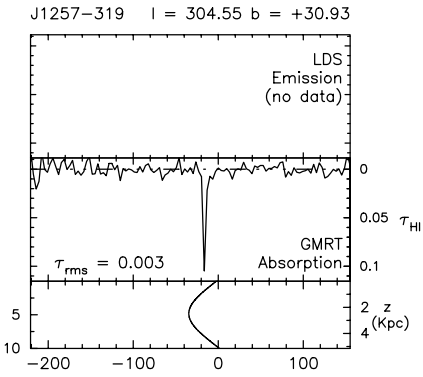
J1257−319 l = 304.55 b = +30.93
LDS
Emission
(no data)
τ_{HI}
GMRT
Absorption
τ_{rms} = 0.003
z
(Kpc)

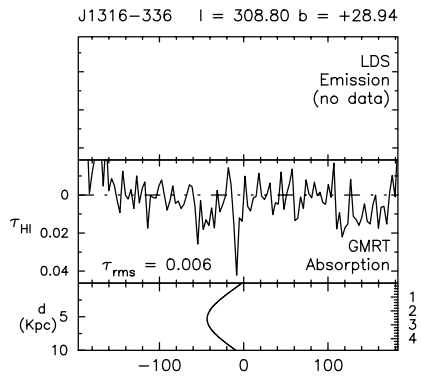
J1316−336 l = 308.80 b = +28.94
LDS
Emission
(no data)
τ_{HI}
GMRT
Absorption
τ_{rms} = 0.006
d
(Kpc)

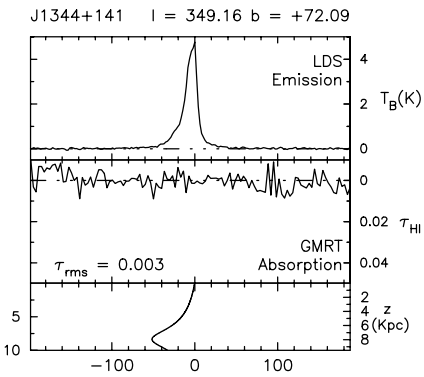
J1344+141 l = 349.16 b = +72.09
LDS
Emission
T_B(K)
τ_{HI}
GMRT
Absorption
τ_{rms} = 0.003
z
(Kpc)

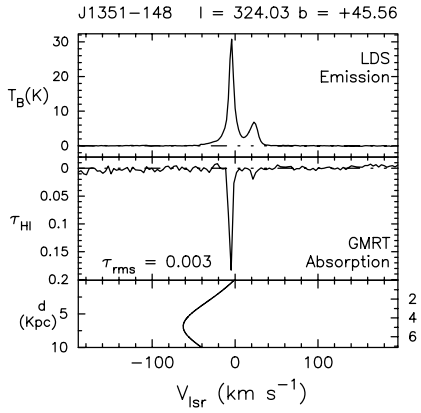
J1351−148 l = 324.03 b = +45.56
LDS
Emission
T_B(K)
τ_{HI}
GMRT
Absorption
τ_{rms} = 0.003
d
(Kpc)
V_{lsr} (km s^{-1})

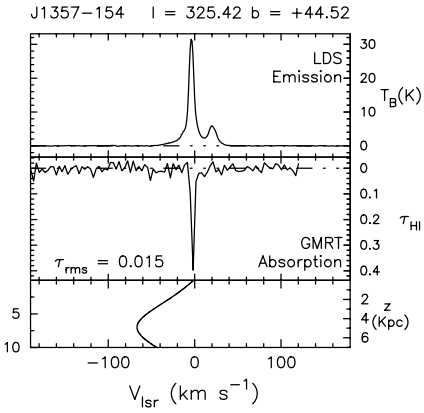
J1357−154 l = 325.42 b = +44.52
LDS
Emission
T_B(K)
τ_{HI}
GMRT
Absorption
τ_{rms} = 0.015
z
(Kpc)
V_{lsr} (km s^{-1})

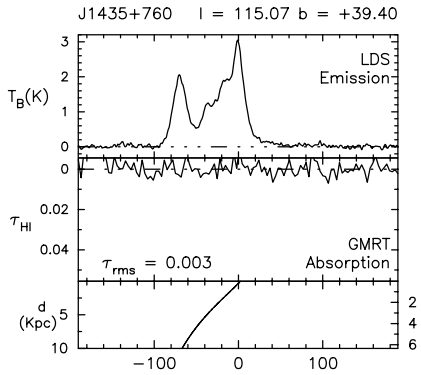
J1435+760 l = 115.07 b = +39.40
LDS
Emission
T_B(K)
τ_{HI}
GMRT
Absorption
τ_{rms} = 0.003
d
(Kpc)

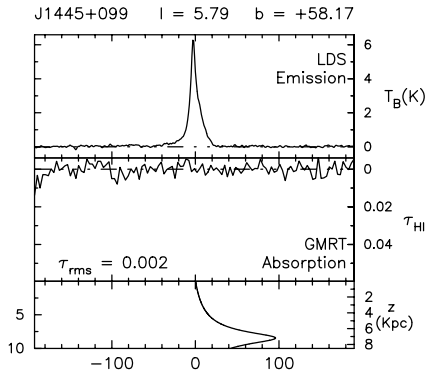
J1445+099 l = 5.79 b = +58.17
LDS
Emission
T_B(K)
τ_{HI}
GMRT
Absorption
τ_{rms} = 0.002
z
(Kpc)

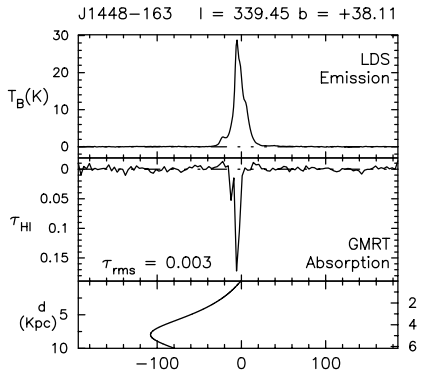
J1448−163 l = 339.45 b = +38.11
LDS
Emission
T_B(K)
τ_{HI}
GMRT
Absorption
τ_{rms} = 0.003
d
(Kpc)

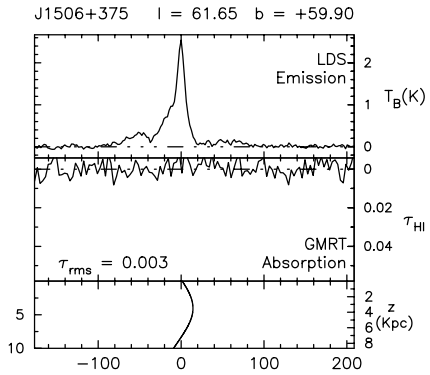
J1506+375 l = 61.65 b = +59.90
LDS
Emission
T_B(K)
τ_{HI}
GMRT
Absorption
τ_{rms} = 0.003
z
(Kpc)

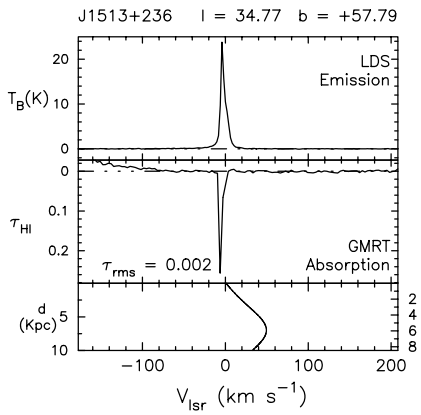
J1513+236 l = 34.77 b = +57.79
LDS
Emission
T_B(K)
τ_{HI}
GMRT
Absorption
τ_{rms} = 0.002
d
(Kpc)
V_{lsr} (km s^{-1})

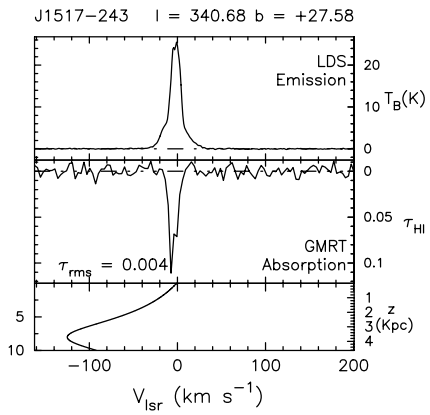
J1517−243 l = 340.68 b = +27.58
LDS
Emission
T_B(K)
τ_{HI}
GMRT
Absorption
τ_{rms} = 0.004
z
(Kpc)
V_{lsr} (km s^{-1})

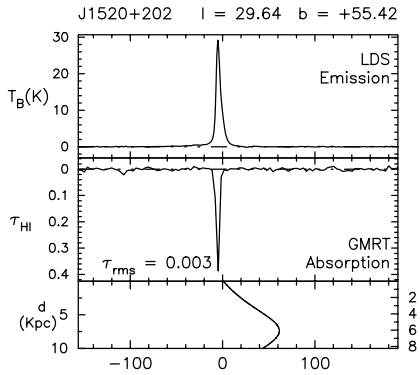
J1520+202 l = 29.64 b = +55.42
LDS
Emission
T_B(K)
GMRT
Absorption
τ_{rms} = 0.003
τ_{HI}
d
(Kpc)

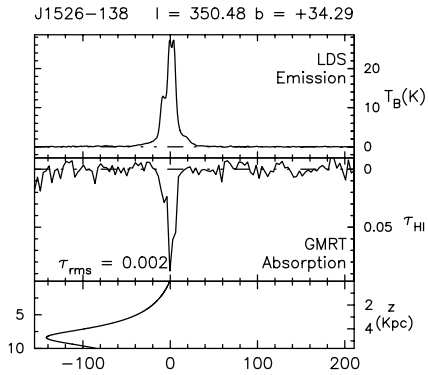
J1526−138 l = 350.48 b = +34.29
LDS
Emission
T_B(K)
GMRT
Absorption
τ_{rms} = 0.002
τ_{HI}
z
(Kpc)

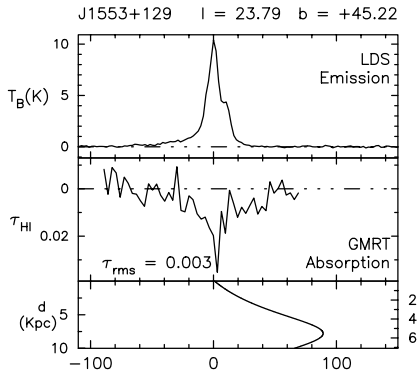
J1553+129 l = 23.79 b = +45.22
LDS
Emission
T_B(K)
GMRT
Absorption
τ_{rms} = 0.003
τ_{HI}
d
(Kpc)

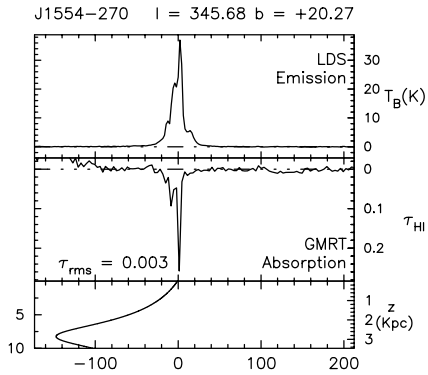
J1554−270 l = 345.68 b = +20.27
LDS
Emission
T_B(K)
GMRT
Absorption
τ_{rms} = 0.003
τ_{HI}
z
(Kpc)

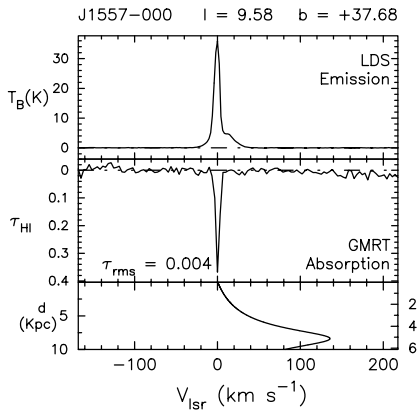
J1557−000 l = 9.58 b = +37.68
LDS
Emission
T_B(K)
GMRT
Absorption
τ_{rms} = 0.004
τ_{HI}
d
(Kpc)
V_{lsr} (km s^{-1})

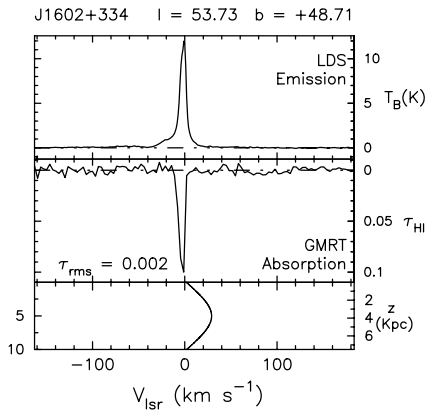
J1602+334 l = 53.73 b = +48.71
LDS
Emission
T_B(K)
GMRT
Absorption
τ_{rms} = 0.002
τ_{HI}
z
(Kpc)
V_{lsr} (km s^{-1})

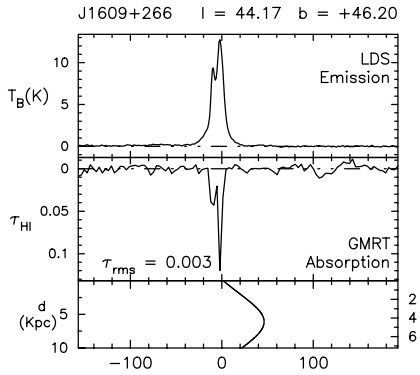
J1609+266 l = 44.17 b = +46.20
LDS
Emission
T_B(K)
GMRT
Absorption
τ_{rms} = 0.003
τ_{HI}
d
(Kpc)

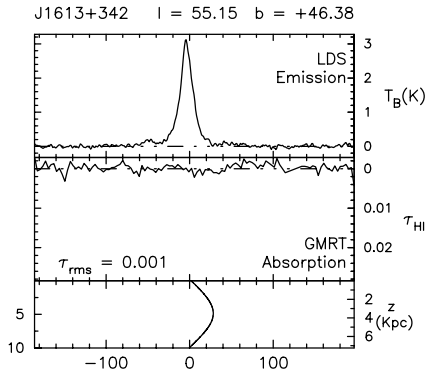
J1613+342 l = 55.15 b = +46.38
LDS
Emission
T_B(K)
GMRT
Absorption
τ_{rms} = 0.001
τ_{HI}
z
(Kpc)

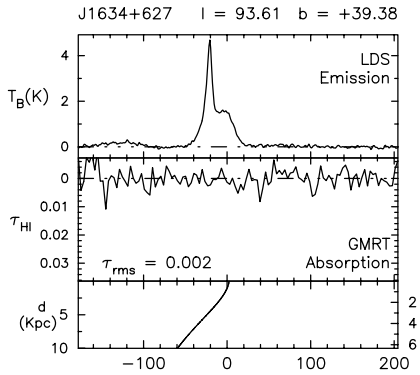
J1634+627 l = 93.61 b = +39.38
LDS
Emission
T_B(K)
GMRT
Absorption
τ_{rms} = 0.002
τ_{HI}
d
(Kpc)

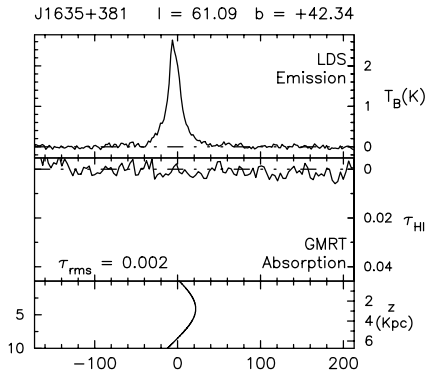
J1635+381 l = 61.09 b = +42.34
LDS
Emission
T_B(K)
GMRT
Absorption
τ_{rms} = 0.002
τ_{HI}
z
(Kpc)

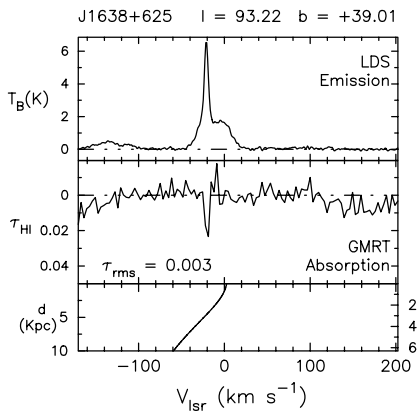
J1638+625 l = 93.22 b = +39.01
LDS
Emission
T_B(K)
GMRT
Absorption
τ_{rms} = 0.003
τ_{HI}
d
(Kpc)
V_{lsr} (km s^{-1})

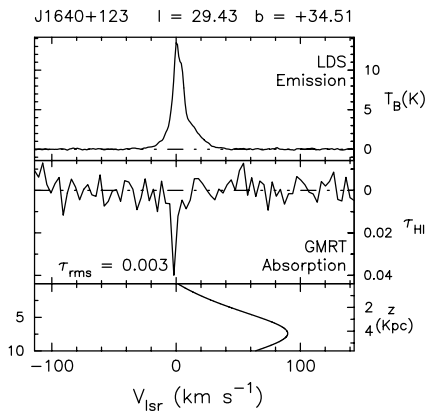
J1640+123 l = 29.43 b = +34.51
LDS
Emission
T_B(K)
GMRT
Absorption
τ_{rms} = 0.003
τ_{HI}
z
(Kpc)
V_{lsr} (km s^{-1})

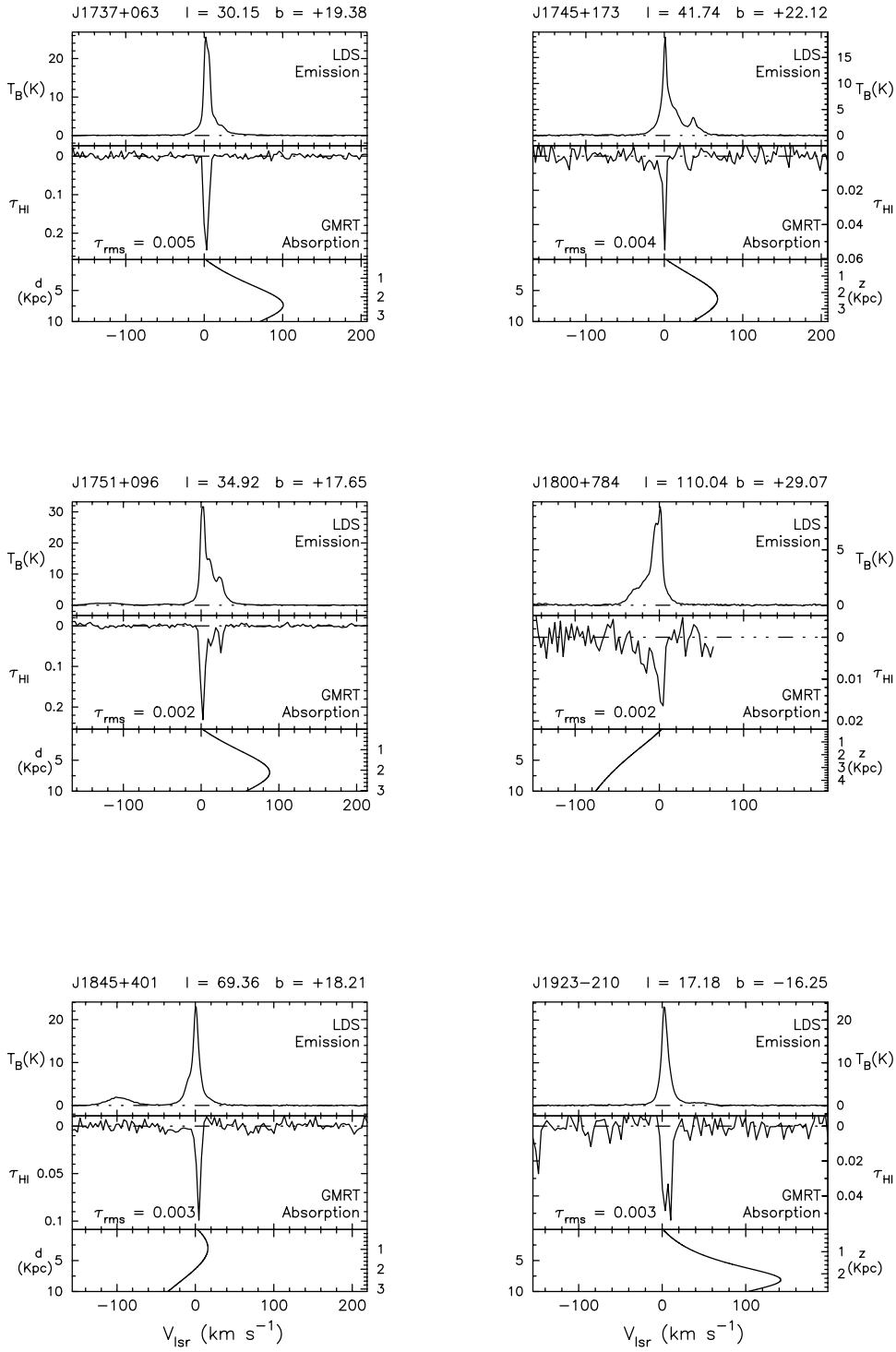
J1737+063 l = 30.15 b = +19.38
J1745+173 l = 41.74 b = +22.12
J1751+096 l = 34.92 b = +17.65
J1800+784 l = 110.04 b = +29.07
J1845+401 l = 69.36 b = +18.21
J1923−210 l = 17.18 b = −16.25
LDS Emission
GMRT Absorption
T_B(K)
τ_{HI}
τ_{rms} = 0.005
τ_{rms} = 0.004
τ_{rms} = 0.002
τ_{rms} = 0.003
d (Kpc)
z (Kpc)
V_{lsr} (km s^{-1})

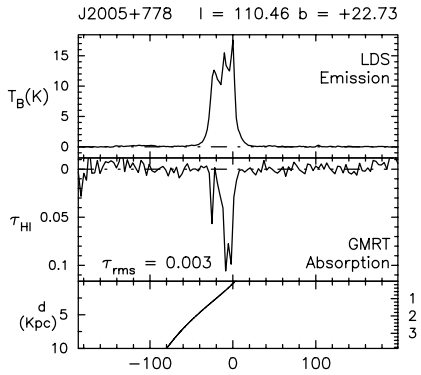
J2005+778 l = 110.46 b = +22.73
LDS
Emission
T_B(K)
GMRT
Absorption
τ_{rms} = 0.003
τ_{HI}
d
(Kpc)

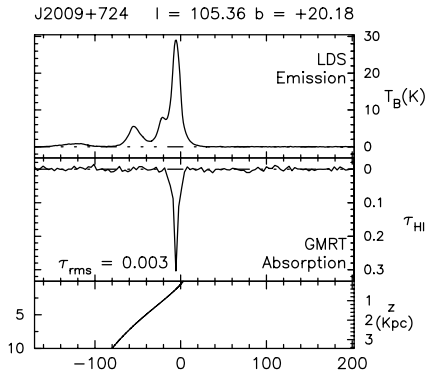
J2009+724 l = 105.36 b = +20.18
LDS
Emission
T_B(K)
GMRT
Absorption
τ_{rms} = 0.003
τ_{HI}
z
(Kpc)

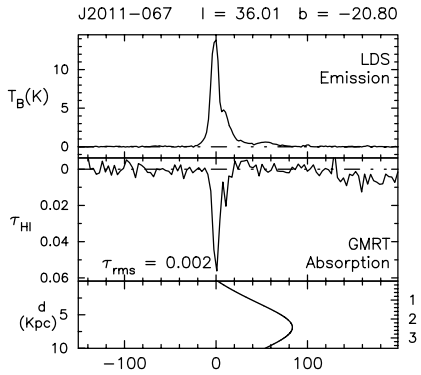
J2011−067 l = 36.01 b = −20.80
LDS
Emission
T_B(K)
GMRT
Absorption
τ_{rms} = 0.002
τ_{HI}
d
(Kpc)

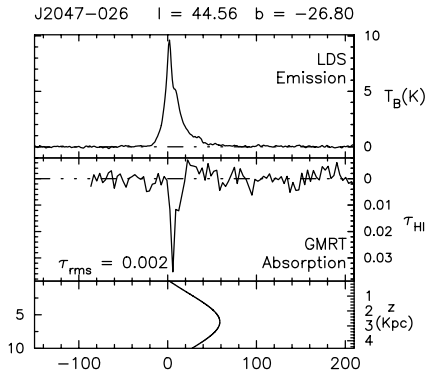
J2047−026 l = 44.56 b = −26.80
LDS
Emission
T_B(K)
GMRT
Absorption
τ_{rms} = 0.002
τ_{HI}
z
(Kpc)

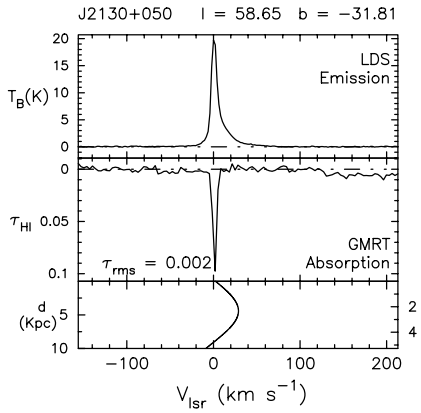
J2130+050 l = 58.65 b = −31.81
LDS
Emission
T_B(K)
GMRT
Absorption
τ_{rms} = 0.002
τ_{HI}
d
(Kpc)
V_{lsr} (km s^{-1})

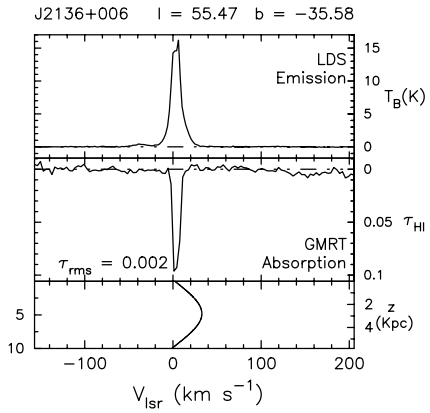
J2136+006 l = 55.47 b = −35.58
LDS
Emission
T_B(K)
GMRT
Absorption
τ_{rms} = 0.002
τ_{HI}
z
(Kpc)
V_{lsr} (km s^{-1})

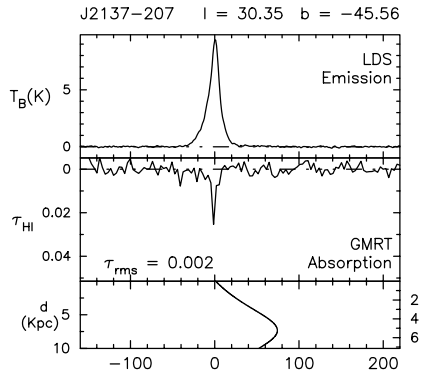
J2137−207 l = 30.35 b = −45.56
LDS
Emission
T_B(K)
τ_{HI}
GMRT
Absorption
τ_{rms} = 0.002
d
(Kpc)

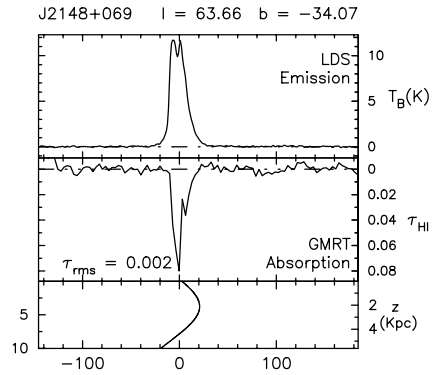
J2148+069 l = 63.66 b = −34.07
LDS
Emission
T_B(K)
τ_{HI}
GMRT
Absorption
τ_{rms} = 0.002
z
(Kpc)

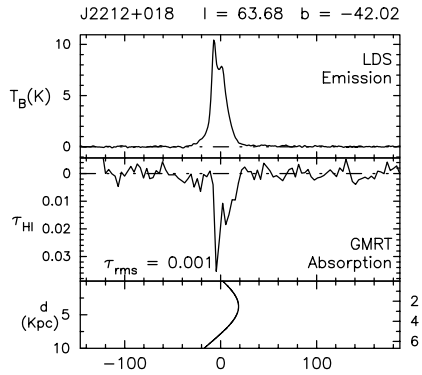
J2212+018 l = 63.68 b = −42.02
LDS
Emission
T_B(K)
τ_{HI}
GMRT
Absorption
τ_{rms} = 0.001
d
(Kpc)

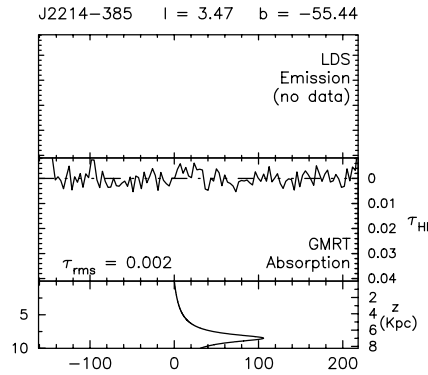
J2214−385 l = 3.47 b = −55.44
LDS
Emission
(no data)
τ_{HI}
GMRT
Absorption
τ_{rms} = 0.002
z
(Kpc)

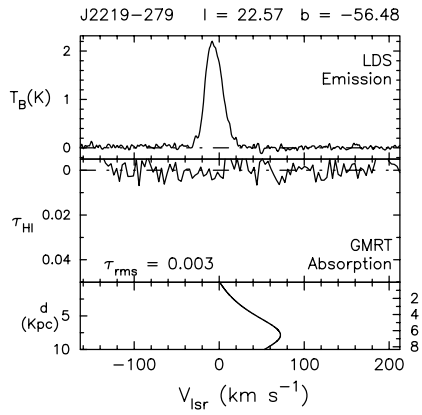
J2219−279 l = 22.57 b = −56.48
LDS
Emission
T_B(K)
τ_{HI}
GMRT
Absorption
τ_{rms} = 0.003
d
(Kpc)
V_{lsr} (km s^{-1})

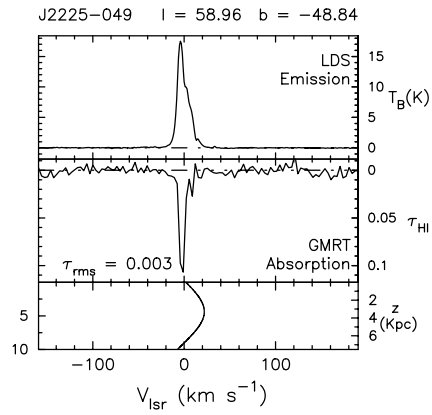
J2225−049 l = 58.96 b = −48.84
LDS
Emission
T_B(K)
τ_{HI}
GMRT
Absorption
τ_{rms} = 0.003
z
(Kpc)
V_{lsr} (km s^{-1})

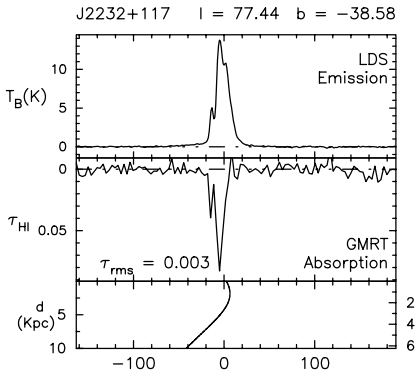
J2232+117 l = 77.44 b = −38.58
LDS
Emission
T_B(K)
τ_{HI}
GMRT
Absorption
τ_{rms} = 0.003
d
(Kpc)

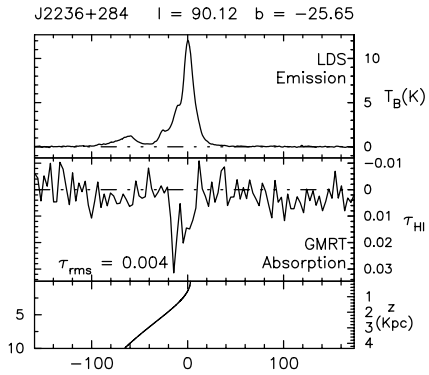
J2236+284 l = 90.12 b = −25.65
LDS
Emission
T_B(K)
τ_{HI}
GMRT
Absorption
τ_{rms} = 0.004
z
(Kpc)

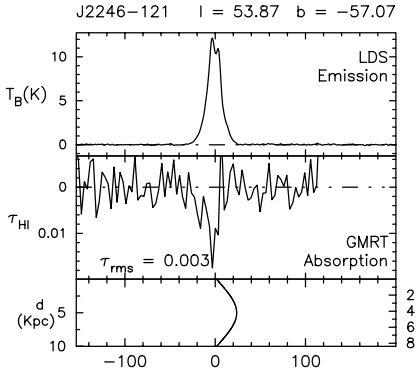
J2246−121 l = 53.87 b = −57.07
LDS
Emission
T_B(K)
τ_{HI}
GMRT
Absorption
τ_{rms} = 0.003
d
(Kpc)

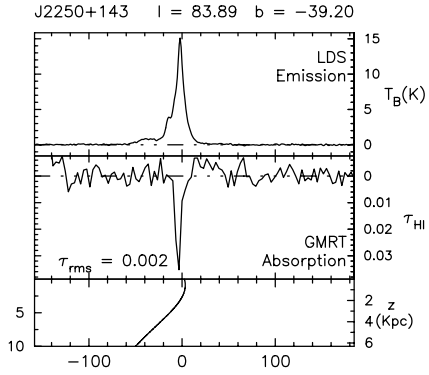
J2250+143 l = 83.89 b = −39.20
LDS
Emission
T_B(K)
τ_{HI}
GMRT
Absorption
τ_{rms} = 0.002
z
(Kpc)

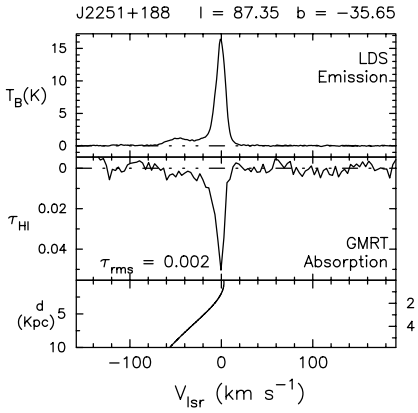
J2251+188 l = 87.35 b = −35.65
LDS
Emission
T_B(K)
τ_{HI}
GMRT
Absorption
τ_{rms} = 0.002
d
(Kpc)
V_{lsr} (km s^{-1})

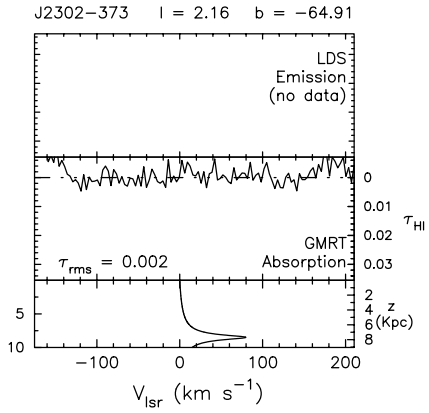
J2302−373 l = 2.16 b = −64.91
LDS
Emission
(no data)
τ_{HI}
GMRT
Absorption
τ_{rms} = 0.002
z
(Kpc)
V_{lsr} (km s^{-1})

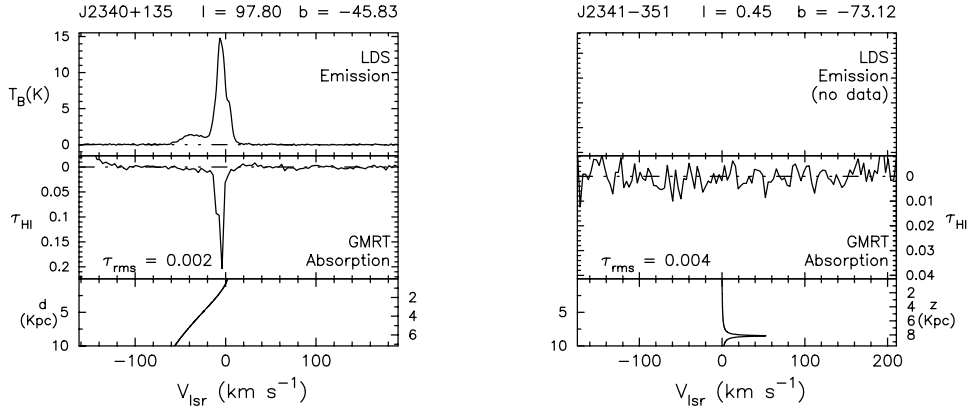

Appendix C

In this Appendix, we list the discrete HI features identified from the high latitude Galactic HI absorption survey using the GMRT and from the HI emission data along the respective lines of sight from the Leiden–Dwingeloo survey of Galactic neutral hydrogen. We have used the HI emission and absorption data to estimate the spin temperature of the absorbing gas.

In the following table, the first column lists the name of the background source, towards which the absorption was measured using the GMRT. Columns 2, 3 and 4 list the peak optical depth, the mean LSR velocity and the FWHM respectively of discrete components identified using Gaussian fitting. The value of FWHM is deconvolved for a channel width of 3.26 km s^{-1}. The unresolved lines are marked with a "–". Columns 5, 6 and 7 list the same for the HI emission profile along the same line of sight, obtained from the Leiden–Dwingeloo survey of Galactic neutral hydrogen (Hartmann & Burton, 1995). The formal 1σ errors estimated in the last digit of the fitted parameters are given within brackets. Column 8 lists the spin temperature, calculated using the absorption and emission data. Column 2 also lists the 3σ optical depth limit obtained from the HI absorption profiles along the respective directions.

	HI Absorption (GMRT)			**HI Emission** (LDS)			
Source	$\tau_{\rm HI}$	$V_{\rm lsr}$ (km s^{-1})	FWHM (km s^{-1})	T_B (K)	$V_{\rm lsr}$ (km s^{-1})	FWHM (km s^{-1})	T_S (K)
J0010 − 418	< 0.006				No data		
J0022 + 002	< 0.009			2.5(2)	−1.1(2)	6.2(4)	> 278
				3.8(2)	−2.2(2)	17.4(4)	> 422
				3.4(9)	−5.89(6)	3.8(3)	> 340
				2.3(6)	−8(1)	7(1)	> 256
				0.40(3)	−17(1)	47(2)	> 44
J0024 − 420	< 0.009				No data		
J0025 − 260	< 0.009			2.8(1)	−5.21(8)	13.3(3)	> 311
				1.1(1)	−8.7(5)	28(1)	> 122
				0.31(1)	−74(1)	55(3)	> 34

Source	**HI Absorption** (GMRT)			**HI Emission** (LDS)			
	$\tau_{\rm HI}$	$V_{\rm lsr}$ (km s^{-1})	FWHM (km s^{-1})	T_B (K)	$V_{\rm lsr}$ (km s^{-1})	FWHM (km s^{-1})	T_S (K)
J0029 + 349	< 0.006			8.27(7)	+2.7(1)	10.9(2)	> 1378
	0.193(5)	−2.02(6)	3.3(2)	16.1(2)	−3.68(1)	5.11(5)	29
				2.58(7)	−12.68(5)	4.5(1)	> 430
				1.23(3)	−20.2(8)	55(1)	> 205
				1.35(4)	−39.8(2)	14.1(6)	> 225
J0059 + 001	0.09(1)	−7.6(4)	–	3.59(9)	−7.50(3)	5.1(1)	42
	< 0.012			5.14(8)	−7.60(4)	14.9(2)	> 428
				0.78(2)	−21.4(8)	51(1)	> 65
				0.24(3)	−46.2(5)	9(1)	> 20
J0116 − 208	< 0.009			2.48(5)	−6.57(8)	15.1(3)	> 276
	0.030	−5.79	–	2.32(5)	−7.15(3)	3.7(1)	78
				0.44(4)	−14(1)	38(2)	> 49
				0.118(9)	−69(7)	127(11)	> 13
J0119 + 321	0.08(4)	+2.8(8)	–	8.0(2)	+2.81(1)	3.62(5)	104
	< 0.009			5.9(5)	−0.4(4)	12.5(3)	> 656
	0.034(7)	−3(3)	7(5)	7.9(5)	−3.41(4)	6.0(1)	236
				5.7(1)	−14.6(2)	15.3(4)	> 633
				0.93(7)	−29.9(7)	66(2)	> 103
				0.40(4)	−46.6(6)	17(2)	> 44
				0.17(2)	−86.6(7)	11(2)	> 19
J0137 + 331	< 0.009			2.99(9)	+2.46(3)	3.9(1)	> 322
	0.037(5)	−2.6(5)	6(1)	0.6(2)	−3.3(2)	4.6(9)	17
				8.2(2)	−3.7(1)	17.5(2)	> 910
	0.020(4)	−13(1)	7(3)	1.7(2)	−13.1(2)	6.9(5)	86
				0.82(4)	−15.0(7)	49(1)	> 91
J0204 + 152	< 0.009			4.8(1)	−0.37(6)	6.0(1)	> 533
				4.0(3)	−5.0(1)	18.4(3)	> 444
	0.057(4)	−6.8(3)	9(7)	14.0(3)	−7.61(5)	8.4(2)	253
				1.7(2)	−12.21(6)	4.0(3)	> 189
				0.31(1)	−48.7(4)	23(1)	> 34
				0.104(9)	−111(2)	45(4)	> 12
J0204 − 170	0.054(6)	0.0(3)	5(1)	8.90(4)	+2.05(1)	4.43(3)	169
	< 0.009			3.81(5)	−4.47(8)	18.4(1)	> 423
				1.91(5)	−9.73(6)	6.5(2)	> 212
				0.136(9)	−20(2)	117(6)	> 15
J0237 + 288	< 0.009			7(1)	+4.5(9)	8.7(8)	> 778
				14(2)	+3.25(7)	3.8(1)	> 280
	0.347(7)	−2.12(5)	4.7(2)	21(2)	−0.01(9)	4.9(2)	72

Source	**HI Absorption** (GMRT)			**HI Emission** (LDS)			
	τ_{HI}	V_{lsr} (km s^{-1})	FWHM (km s^{-1})	T_B (K)	V_{lsr} (km s^{-1})	FWHM (km s^{-1})	T_S (K)
				2.56(7)	−3.9(2)	27.8(4)	> 284
	0.127(7)	−10.0(2)	3.5(3)	12.6(2)	−5.78(5)	5.28(7)	106
				0.16(1)	−10(3)	140(9)	> 18
J0238 + 166	< 0.012			17.1(1)	−0.38(2)	15.46(6)	> 1425
	0.122(8)	−2.8(1)	4.7(4)	10.6(1)	−1.49(1)	5.52(5)	92
				0.14(1)	−22(5)	115(10)	> 12
J0240 − 231	0.04(1)	+1.4(5)	4(1)	1.83(6)	−1.13(4)	5.01(1)	47
	< 0.009			2.1(1)	−5.2(2)	21.4(4)	> 233
				4.9(1)	−10.51(3)	9.5(1)	> 544
				0.152(7)	−33(2)	124(5)	> 17
J0318 + 164	0.095(8)	+7.5(2)	4.0(7)	2.7(1)	+7.86(6)	3.7(2)	30
	< 0.006			23.9(3)	+1.49(2)	13.06(8)	> 3983
	0.404(5)	+0.23(4)	4.6(1)	14.9(3)	−0.17(2)	5.63(6)	45
				1.5(1)	−1.1(4)	31(1)	> 250
				0.11(1)	−57(8)	85(17)	> 18
J0321 + 123	1.5(1)	+8.1(1)	6.2(1)	47(2)	+10.74(4)	6.71(7)	60
	0.39(5)	+2(1)	9(1)	44.4(6)	+4.5(1)	10.5(2)	137
	< 0.006			1.6(3)	+2.2(7)	30(3)	> 267
				3.6(2)	−6.5(1)	4.4(3)	> 600
				0.17(3)	−111(7)	80(16)	> 28
J0323 + 055	0.21(2)	+9.2(2)	–	23.8(4)	+12.51(1)	4.22(4)	126
	< 0.009			10(2)	+6.4(6)	14.4(8)	> 1111
	0.229(9)	+3.3(2)	5.5(4)	12.7(5)	+6.29(3)	4.33(8)	62
				17.9(7)	−4.65(8)	7.8(1)	> 1989
				2(1)	−5(9)	21(7)	> 222
	0.500(5)	−8.64(3)	4.62(6)	6.6(4)	−7.35(3)	3.9(1)	17
				0.176(8)	−57(4)	117(7)	> 20
J0329 + 279	0.25(2)	+3.3(2)	–	22.1(3)	+6.96(1)	4.12(4)	100
	< 0.009			25.7(5)	+4.57(3)	12.91(9)	> 2855
	0.23(2)	−2.8(3)	3.7(8)	15.7(4)	+1.18(3)	6.04(8)	76
				1.24(2)	−14.9(6)	56(1)	> 138
J0336 + 323	2.62(1)	+6.698(8)	3.7(3)	33.7(4)	+8.36(4)	5.57(4)	36
	< 0.012			9.8(2)	+5.30(6)	15.3(2)	> 817
				33.2(5)	+4.42(3)	4.96(3)	> 36
				2.6(2)	−20.4(6)	48.2(8)	> 217
J0348 + 338	< 0.009			15.3(5)	+10.30(2)	3.29(5)	> 1700
	1.33(2)	+7.69(2)	–	38.76(7)	+7.52(6)	6.22(7)	53
	0.07(2)	+7.1(5)	13(2)	3.5(2)	+7.5(1)	15.1(6)	52

Source	**HI Absorption** (GMRT)			**HI Emission** (LDS)			
	$\tau_{\rm HI}$	$V_{\rm lsr}$ (km s^{-1})	FWHM (km s^{-1})	T_B (K)	$V_{\rm lsr}$ (km s^{-1})	FWHM (km s^{-1})	T_S (K)
				7.1(9)	+5.57(3)	2.7(1)	> 789
				1.2(3)	+1.5(2)	2.6(3)	> 133
				2.73(6)	−18.81(3)	5.5(1)	> 303
				3.0(1)	−19.1(6)	44.0(5)	> 333
				2.2(1)	−19.8(2)	17.0(7)	> 244
J0403 + 260	0.305(5)	+7.61(6)	3.78(1)	13.8(1)	+7.61(7)	3.47(3)	52
	< 0.012			6.1(2)	+4.85(7)	21.6(3)	> 508
				9.8(2)	+3.94(6)	9.3(1)	> 817
				0.31(5)	−20(2)	99(7)	> 26
				1.42(5)	−29.9(5)	25(2)	> 118
				1.19(9)	−45.9(2)	11.3(6)	> 99
J0409 + 122	< 0.009			11.0(2)	+11.41(6)	3.4(1)	> 1222
				28(1)	+8.9(1)	4.9(2)	> 3111
	1.25(1)	+5.9(1)	3.5(2)	30.9(8)	+6.40(3)	9.68(4)	43
	0.22(2)	0.0(6)	5.6(7)	8.7(3)	+1.43(4)	3.97(7)	44
				0.14(2)	−21(4)	75(6)	> 16
J0410 + 769	< 0.006			0.5(2)	+18(1)	13.2(4)	> 56
				3.9(3)	+3.62(7)	3.3(1)	> 650
	0.230(3)	−0.88(5)	3.78(8)	17.4(8)	−0.40(2)	5.4(1)	85
				9.8(8)	−2.3(3)	11.6(7)	> 1633
				8.2(4)	−7.0(6)	24.9(5)	> 1366
	0.069(3)	−11.5(2)	6.9(5)	6.6(2)	−11.85(4)	4.9(1)	99
				0.52(2)	−57.4(6)	34(2)	> 58
				1.14(2)	−99.4(4)	23.5(9)	> 127
				1.20(2)	−127.5(4)	24.7(8)	> 133
J0424 + 020	< 0.012			8.9(5)	+11.92(5)	3.8(1)	> 741
	0.523(5)	+5.63(3)	5.4(7)	12.4(8)	+7.96(9)	12.5(3)	30
				5.8(7)	+6.93(3)	3.1(2)	> 483
				4.4(2)	+3.7(2)	24.4(3)	> 367
	0.5(3)	+2.2(9)	–	10.9(4)	+2.36(4)	4.36(7)	28
				0.37(1)	−46.3(6)	30(2)	> 31
J0431 + 406	< 0.009			8.4(7)	+11.92(2)	2.84(9)	> 933
	1.19(3)	+10.01(2)	–	27.1(6)	+9.47(5)	5.32(9)	39
				29(1)	+4.27(4)	14.5(2)	> 3222
	0.70(1)	+3.61(4)	4.4(1)	34(1)	+4.09(4)	8.2(1)	68
				3.7(1)	−6.3(8)	41(1)	> 411
				0.5(1)	−31.9(5)	16(2)	> 56
				0.14(1)	−98(4)	74(9)	> 16

Source	**HI Absorption** (GMRT)			**HI Emission** (LDS)			
	τ_{HI}	V_{lsr} (km s^{-1})	FWHM (km s^{-1})	T_B (K)	V_{lsr} (km s^{-1})	FWHM (km s^{-1})	T_S (K)
J0440 − 435	< 0.009				No data		
J0453 − 281	< 0.012			3.3(1)	+1.19(7)	19.0(3)	> 275
				5.1(1)	+1.14(3)	7.1(1)	> 425
				0.11(1)	−25(5)	136(11)	> 9
J0459 + 024	0.080(5)	+11.1(2)	–	19.2(1)	+10.44(1)	5.40(4)	250
	< 0.009			7.1(4)	+6.7(1)	22.7(6)	> 789
				1.9(2)	−12(3)	40(3)	> 211
	0.026(4)	−25.6(5)	–	0.21(8)	−28(1)	6(3)	8
J0503 + 020	< 0.009			6.1(2)	+10.53(7)	6.0(1)	> 508
				10.0(1)	+10.25(5)	18.0(1)	> 833
	0.26(9)	+9.92(6)	–	12.0(2)	+9.03(1)	2.98(4)	52
				2.40(3)	−12.8(4)	31.6(8)	> 200
				0.08(2)	−31(8)	131(18)	> 7
J0538 − 440	< 0.006				No data		
J0541 − 056	< 0.012			37.8(1)	+4.19(4)	5.97(3)	> 3150
	0.842(5)	+7.44(2)	6.06(5)	16(2)	+7.5(1)	6.1(2)	28
				12.6(2)	+8.23(3)	23.3(2)	> 1050
				23(2)	+8.9(2)	9.6(2)	> 1917
				0.48(4)	+9.9(8)	74(3)	> 40
	0.069(7)	+17.8(9)	–				
J0609 − 157	< 0.021			6.7(2)	+3.10(2)	2.97(6)	> 319
				18.6(3)	+7.057(9)	3.71(4)	> 885
	0.432(9)	+10.51(8)	7.1(2)	20.3(4)	+8.37(5)	10.2(1)	58
				6.6(2)	+12.2(1)	26.6(6)	> 314
				4.8(1)	+18.89(5)	5.9(1)	> 229
				1.7(1)	+25.5(9)	52.5(8)	> 81
J0614 + 607	0.09(2)	+10.1(8)	–	7.96(5)	+9.40(1)	4.69(4)	88
	< 0.015			1.4(1)	+1.34(6)	2.5(2)	> 93
	0.29(1)	+02.2(2)	10.7(6)	25.9(1)	+0.410(8)	7.72(2)	103
				5.17(4)	−7.1(1)	29.3(2)	> 345
				0.68(5)	−18.6(2)	7.9(6)	> 45
				1.30(2)	−49.1(2)	20.8(6)	> 87
				1.21(2)	−79.9(3)	30.0(7)	> 81
J0713 + 438	< 0.012			3.1(2)	+14.57(3)	4.1(1)	> 258
				6.3(1)	+12.9(2)	11.0(3)	> 525
	0.015(3)	+5(3)	27(6)	6.5(3)	−1.57(2)	4.03(9)	433
				3.6(4)	−4.7(2)	9.3(3)	> 300
				7.5(2)	−6.6(4)	29.0(4)	> 625

Source	**HI Absorption** (GMRT)			**HI Emission** (LDS)			
	τ_{HI}	V_{lsr} (km s^{-1})	FWHM (km s^{-1})	T_B (K)	V_{lsr} (km s^{-1})	FWHM (km s^{-1})	T_S (K)
				3.9(1)	−12.27(4)	5.5(1)	> 325
				0.66(5)	−36(1)	22(1)	> 55
J0814 + 459	0.035(2)	+16.8(9)	–	9.5(5)	+15.4(1)	3.8(1)	276
	< 0.015			3.4(2)	+12.8(3)	12.6(7)	> 226
				4.0(6)	+12.6(2)	3.5(2)	> 267
				1.1(2)	+2.9(1)	5.0(5)	> 73
				5.38(7)	−2.9(2)	13.5(3)	> 359
				0.64(3)	−12(1)	55(2)	> 43
J0825 + 031	< 0.006			0.24(2)	+27(3)	84(5)	> 40
				1.6(2)	+19(1)	15(1)	> 267
	0.034(7)	+14.8(6)	4(1)	8.6(2)	+16.70(2)	4.93(8)	257
	0.043(7)	+4.9(7)	–	6.4(6)	+5.3(1)	9.7(5)	152
				3.1(3)	−3(1)	13(1)	> 207
J0834 + 555	< 0.006			0.111(8)	+61(10)	123(20)	> 19
				0.7(2)	+13(3)	15(3)	> 117
	0.059(3)	+1.4(2)	3.4(3)	12.7(1)	+3.005(9)	4.89(4)	222
				5.4(2)	−1.0(4)	14.8(5)	> 900
	0.016(4)	−39(1)	–	0.97(6)	−40(2)	30(4)	61
				1.74(7)	−55.44(8)	5.9(2)	> 290
				1.6(2)	−58.7(5)	17.9(9)	> 267
J0842 + 185	< 0.012			0.21(2)	+29(2)	21(4)	> 18
				3.54(2)	+0.3(1)	25.5(3)	> 295
				0.84(5)	−14.5(1)	4.4(3)	> 70
J0854 + 201	< 0.006			0.7(2)	+11(2)	11(2)	> 117
				1.2(1)	+6.15(8)	4.8(3)	> 200
				4.7(1)	+0.4(3)	14.1(3)	> 783
				0.70(2)	−12.6(8)	49(1)	> 117
				0.30(2)	−32.9(3)	10.0(9)	> 50
J0921 − 263	0.15(1)	−1.7(8)	–	19.1(4)	−1.77(8)	10.1(2)	137
	< 0.009			9.4(5)	−3.00(2)	4.3(1)	> 1044
	0.022(6)	+5(4)	5(9)	6.1(2)	+6.78(9)	6.4(1)	280
				3.4(2)	+11.0(5)	31(1)	> 378
				1.3(1)	+23(2)	55(1)	> 144
J0958 + 324	< 0.015			1.27(1)	+0.2(1)	28.0(4)	> 85
				0.83(1)	−41.9(2)	25.6(6)	> 55
				1.16(1)	−86.4(1)	24.9(3)	> 77
J1018 − 317	< 0.006			0.66(6)	+24(3)	80(3)	> 73
	0.109(6)	+13.5(1)	–	5.0(3)	+6.3(2)	20.6(6)	48

Source	**HI Absorption** (GMRT)			**HI Emission** (LDS)			
	τ_{HI}	V_{lsr} (km s^{-1})	FWHM (km s^{-1})	T_B (K)	V_{lsr} (km s^{-1})	FWHM (km s^{-1})	T_S (K)
				2.3(3)	−1(1)	36(2)	> 256
	0.035(3)	−7.0(3)	5.7(8)	8.4(1)	−7.36(4)	9.5(1)	240
J1057 − 245	0.063(7)	−3.0(4)	–	14.2(2)	−4.118(8)	3.82(3)	233
	< 0.012			7.7(2)	−5.65(9)	10.2(2)	> 642
				1.3(1)	−14.6(4)	41(2)	> 108
				3.7(3)	−20.84(7)	6.9(3)	> 308
				5.9(3)	−21.2(1)	14.4(4)	> 492
J1111 + 199	< 0.009			0.23(1)	+12(3)	96(4)	> 26
				0.70(2)	−2.1(4)	6.4(8)	> 78
				1.2(2)	−3.21(8)	3.3(2)	> 133
				1.35(6)	−7.2(6)	19(1)	> 150
				0.4(1)	−23(1)	10(3)	> 44
				1.2(8)	−34.2(4)	12(3)	> 133
				0.7(5)	−41(8)	19(6)	> 78
J1119 − 030	0.034(3)	−8.2(3)	3.7(4)	3.1(3)	−3(1)	14(1)	93
	< 0.006			6.4(6)	+5.3(1)	9.7(5)	> 1067
				8.6(2)	+16.70(2)	4.93(8)	> 1433
				1.6(2)	+19(1)	15(1)	> 267
				0.24(2)	+27(3)	84(5)	> 40
J1120 − 251	< 0.009			0.11(1)	+16(5)	105(10)	> 12
	0.020(4)	−2(1)	–	5(1)	−2.74(3)	4.2(2)	253
				4.9(9)	−2.77(4)	6.9(4)	> 544
				4.95(4)	−9.3(1)	23.4(2)	> 550
				1.85(6)	−21.47(7)	7.3(2)	> 206
J1125 + 261	< 0.009			0.088(6)	+51(3)	74(8)	> 10
				1.36(1)	−7.2(1)	22.5(3)	> 151
				0.857(9)	−45.6(2)	30.9(5)	> 95
J1130 − 148	< 0.006			0.21(2)	−9(2)	103(6)	> 35
	0.007(1)	+7(3)	37(6)	3.9(1)	−7.13(4)	8.9(2)	557
				4.7(1)	−6.72(8)	20.3(4)	> 783
				1.22(2)	+20.1(2)	19.8(5)	> 203
J1146 + 399	< 0.027			0.110(7)	+55(3)	75(8)	> 4
				0.82(2)	−7.2(3)	25.4(8)	> 30
				1.11(1)	−43.0(4)	33.7(7)	> 41
				1.77(3)	−55.11(5)	7.7(1)	> 66
J1154 − 350	0.022(3)	+3.7(4)	8(1)				
	0.092(4)	−8.3(1)	4.2(4)		No data		
	0.016(3)	−16(2)	13(5)				

Source	**HI Absorption** (GMRT)			**HI Emission** (LDS)			
	$\tau_{\rm HI}$	$V_{\rm lsr}$ (km s^{-1})	FWHM (km s^{-1})	T_B (K)	$V_{\rm lsr}$ (km s^{-1})	FWHM (km s^{-1})	T_S (K)
J1221 + 282	< 0.012			0.77(3)	−1.4(2)	9.0(5)	> 64
	0.01(0)	−20(0)	–	0.47(4)	−18.9(4)	11(1)	47
				1.52(3)	−26.3(7)	43.2(7)	> 127
	0.02(0)	−38(0)	–	1.06(4)	−34.8(1)	6.1(3)	53
				0.89(4)	−46.9(3)	16.0(9)	> 74
J1235 − 418	0.132(7)	−14.2(2)	8.1(5)		No data		
J1254 + 116	< 0.015			3.1(3)	+2.4(4)	8.7(3)	> 207
	0.03(1)	−5.9(8)	4(2)	6.3(6)	−3.49(3)	5.1(1)	213
				2.3(5)	−6(1)	10(1)	> 153
				0.92(2)	−14.7(5)	41.3(8)	> 61
				0.082(9)	−80(3)	48(8)	> 5
J1257 − 319	0.108(6)	−16.0(2)	–		No data		
J1316 − 336	0.042(9)	−8.5(7)	4(1)		No data		
J1344 + 141	< 0.009			1.40(5)	+00.40(5)	3.9(1)	> 156
				3.20(6)	−03.9(1)	12.7(2)	> 356
				0.14(3)	−08(2)	93(9)	> 11
				1.1(1)	−10.7(4)	30(1)	> 122
J1351 − 148	0.19(3)	−05.5(1)	3.4(1)	17.2(5)	−04.52(2)	4.4(1)	90
	< 0.009			10.9(5)	−04.4(1)	11.0(3)	> 1211
				3.1(1)	−02.8(5)	41(1)	> 344
	0.020(4)	+22.0(6)	4(1)	5.7(1)	+22.9(1)	10.5(2)	285
J1357 − 154	0.40(2)	−2.1(2)	–	25.1(1)	−3.779(7)	5.75(3)	76
	< 0.045			6.6(5)	−2.6(2)	18.5(7)	> 147
				5(2)	+20.2(3)	10.0(9)	> 111
				1.2(3)	−18(5)	30(5)	> 27
				0.9(1)	+26(12)	15(9)	> 20
J1435 + 760	< 0.009			0.08(1)	+9(10)	146(15)	> 9
				1.51(3)	+0.42(8)	11.0(2)	> 168
				1.82(2)	−12.3(3)	39.0(6)	> 202
				0.60(4)	−38.5(5)	11(1)	> 67
				0.26(3)	−51(1)	12(3)	> 29
				1.94(2)	−69.8(1)	18.6(3)	> 216
				0.08(1)	−137(2)	16(4)	> 9
J1445 + 099	< 0.006			2.68(5)	+0.36(9)	17.3(3)	> 447
				3.44(4)	−2.81(2)	5.14(7)	> 573
				0.35(4)	−8(1)	46(3)	> 58
J1448 − 163	< 0.009			0.29(3)	+10(2)	77(4)	> 32
				3.1(2)	+6.03(4)	4.7(2)	> 344

Source	**HI Absorption** (GMRT)			**HI Emission** (LDS)			
	τ_{HI}	V_{lsr} (km s^{-1})	FWHM (km s^{-1})	T_B (K)	V_{lsr} (km s^{-1})	FWHM (km s^{-1})	T_S (K)
				11.3(5)	−1.63(5)	19.8(3)	> 1256
	0.203(8)	−4.60(7)	–	12.1(4)	−3.37(4)	7.9(2)	66
	0.05(3)	−12(2)	–	8.9(1)	−6.00(1)	3.08(4)	182
				1.91(4)	−22.6(1)	6.7(2)	> 212
J1506 + 375	< 0.009			0.28(2)	−53(1)	33(3)	> 33
				0.98(3)	−07.1(5)	31(1)	> 111
				1.64(4)	+00.2(1)	8.9(3)	> 177
				0.13(1)	+57(2)	44(6)	> 11
J1513 + 236	0.15(3)	00.0(1)	–	9.5(1)	−00.9(1)	9.2(1)	63
	< 0.006			1.1(1)	−03.4(4)	23(1)	> 183
	0.26(5)	−05.73(5)	–	15.8(1)	−04.06(1)	3.23(2)	61
				0.22(2)	−19(4)	84(8)	> 33
J1517 − 243	< 0.012			13.2(6)	+2.3(2)	5.2(2)	> 667
				6.2(1)	−1.1(2)	29.0(2)	> 517
	0.071(5)	−1.1(3)	5.7(6)	14(1)	−1.3(1)	4.0(3)	204
	0.105(6)	−7.5(6)	3.8(3)	16(1)	−4.92(8)	3.9(3)	161
				5.8(9)	−8.3(3)	4.0(4)	> 483
				2.1(1)	−14.7(2)	10.0(1)	> 175
J1520 + 202	< 0.009			8.7(6)	−2.7(1)	6.9(2)	> 967
				3.7(4)	−2.78(9)	13.8(5)	> 411
	0.409(7)	−5.28(5)	–	19.4(5)	−5.331(8)	3.83(4)	58
				0.49(2)	−17(1)	52(1)	> 54
J1526 − 138	< 0.006			1.32(4)	+18.6(1)	8.5(4)	> 220
	0.073(9)	+4.4(3)	4.3(9)	15.6(3)	+4.07(1)	4.51(4)	222
				11.7(5)	0.0(1)	15.4(3)	> 1950
	0.092(8)	−1.1(7)	–	13.3(5)	−0.76(2)	4.02(8)	151
				1.90(9)	−3.3(4)	44.5(9)	> 317
				0.8(2)	−5.9(2)	2.3(5)	> 133
	0.029(5)	−7(3)	9(5)	6.4(2)	−9.15(5)	4.8(1)	224
				0.16(1)	−82(2)	45(5)	> 27
J1553 + 129	0.010(1)	+6(4)	26(5)	3.1(1)	+11.0(2)	7.3(4)	312
	0.021(5)	+2.4(7)	5(3)	3.1(3)	+1.0(1)	4.6(4)	148
	< 0.009			6.8(3)	−0.7(2)	7.3(4)	> 756
				0.94(5)	−9(1)	51(2)	> 104
J1554 − 270	< 0.009			3.7(4)	+15.1(7)	9(1)	> 411
	0.259(6)	+1.2(2)	–	28.5(9)	+2.68(4)	4.4(1)	125
				10.8(9)	−4.1(7)	21(1)	> 1200
				11.1(9)	−4.2(1)	6.3(5)	> 1233

Source	**HI Absorption** (GMRT)			**HI Emission** (LDS)			
	$\tau_{\rm HI}$	$V_{\rm lsr}$ (km s^{-1})	FWHM (km s^{-1})	T_B (K)	$V_{\rm lsr}$ (km s^{-1})	FWHM (km s^{-1})	T_S (K)
				0.8(3)	−5(5)	73(17)	> 89
	0.04(2)	−16(8)	8(5)				
J1557 − 000	0.371(8)	+0.34(7)	5.4(1)	28.0(3)	−1.19(4)	6.88(6)	90
	< 0.012			5.1(3)	+0.2(6)	22.6(5)	> 425
				10.5(2)	+1.37(3)	2.6(2)	> 875
				1.3(4)	+13.8(3)	9(1)	> 108
				1.8(3)	+19(2)	19(2)	> 150
J1602 + 334	< 0.006			7.5(2)	−0.03(3)	3.65(4)	> 1250
				3.11(6)	−2.77(7)	16.0(2)	> 518
	0.111(4)	−3.0(1)	5.6(3)	6.14(9)	−3.49(6)	4.51(8)	58
				0.143(7)	−19(2)	149(5)	> 24
				0.66(2)	−21.1(2)	12.7(5)	> 110
J1609 + 266	< 0.009			0.11(2)	+43(1)	13(3)	> 12
	0.123(5)	−1.7(2)	–	9.39(8)	−1.90(1)	7.79(5)	81
				3.36(8)	−5.42(8)	23.8(3)	> 373
	0.056(9)	−10(2)	4(1)	5.86(6)	−9.99(2)	4.26(4)	108
				0.152(6)	−63(5)	133(10)	> 17
J1613 + 342	< 0.003			2.14(6)	−3.48(8)	19.9(4)	> 713
				0.80(6)	−4.5(1)	7.4(5)	> 267
				0.18(2)	−7(2)	83(5)	> 60
				0.10(2)	−49.9(8)	9(2)	> 33
J1634 + 627	< 0.002			1.51(2)	−1.6(4)	22.2(7)	> 252
				2.73(5)	−20.91(4)	6.1(1)	> 455
				1.72(7)	−23.2(4)	19.4(5)	> 287
				0.19(1)	−128(1)	44(3)	> 32
J1635 + 381	< 0.006			0.09(2)	+2(5)	105(15)	> 15
				0.92(8)	−0.3(6)	7.7(9)	> 153
				1.03(5)	−4.7(3)	29(1)	> 172
				1.3(1)	−6.7(3)	6.4(5)	> 217
J1638 + 625	< 0.009			1.64(3)	−1.6(4)	22.6(7)	> 182
	0.028(4)	−20.1(4)	4(1)	4.50(6)	−21.05(2)	5.05(7)	161
				1.97(7)	−23.1(3)	19.0(5)	> 219
				0.40(1)	−133.0(7)	46(2)	> 44
J1640 + 123	0.040(5)	−1.5(4)	–	3.7(5)	+0.13(4)	3.1(2)	94
	< 0.009			6.6(6)	+0.9(2)	8.1(2)	> 733
				3.1(4)	+4.7(1)	3.7(3)	> 344
				3.76(5)	+5.49(9)	26.5(2)	> 418
J1737 + 063	0.258(7)	+2.63(9)	6.0(2)	19.8(1)	+1.62(3)	4.65(4)	87

Source	**HI Absorption** (GMRT)			**HI Emission** (LDS)			
	τ_{HI}	V_{lsr} (km s^{-1})	FWHM (km s^{-1})	T_B (K)	V_{lsr} (km s^{-1})	FWHM (km s^{-1})	T_S (K)
	< 0.015			14.6(1)	+6.02(3)	4.41(5)	> 973
				4.69(6)	+6.8(1)	26.1(3)	> 313
				0.59(5)	+20(2)	64(3)	> 39
J1745 + 173	0.060(8)	0.0(4)	–	11.2(1)	+0.80(1)	4.27(4)	192
	< 0.012			5.7(1)	+3.3(1)	20.2(4)	> 475
				2.2(1)	+14.7(9)	48(1)	> 183
				2.0(2)	+36.9(2)	6.0(4)	> 167
				0.6(1)	+44(2)	12(3)	> 50
J1751 + 096	0.066(3)	+25.6(2)	3.3(2)	3.9(1)	+25.1(1)	7.1(3)	61
	< 0.006			0.32(8)	+25(7)	91(13)	> 53
				7.5(2)	+13.1(2)	29.9(5)	> 1250
	0.051(3)	+12.7(2)	6.2(6)	7.0(2)	+10.54(6)	7.4(3)	141
	0.235(3)	+2.02(5)	5.5(1)	27.6(1)	+1.91(2)	6.43(4)	132
				0.28(5)	−47(2)	22(6)	> 47
				0.56(9)	−112(4)	28(6)	> 93
				0.5(1)	−137(5)	26(6)	> 83
J1800 + 784	0.016(2)	+1.4(7)	9(2)	5.3(1)	+1.58(3)	4.23(6)	334
	< 0.006			4.41(6)	−4.04(7)	7.7(2)	> 735
				3.04(6)	−6.3(3)	27.5(6)	> 507
				0.98(5)	−30.3(5)	18.9(7)	> 163
J1845 + 401	0.099(5)	+4.3(1)	4.6(3)	11.0(3)	+1.3(1)	10.4(1)	117
	< 0.009			2.93(7)	+1.3(1)	36.1(4)	> 326
				9.5(3)	+0.36(2)	4.84(8)	> 320
				3.2(1)	−9.0(2)	9.2(4)	> 356
				1.81(1)	−97.4(1)	36.3(3)	> 201
J1923 − 210	0.053(7)	+2.5(6)	5(2)	10.2(2)	+2.24(5)	4.66(9)	192
	< 0.009			11.7(2)	+3.78(3)	12.7(2)	> 1300
	0.055(8)	+9.7(6)	3.4(7)	1.9(2)	+5.7(1)	3.2(3)	35
				1.8(1)	+7.4(4)	35(1)	> 200
				0.58(2)	+47.4(6)	22(1)	> 64
J2005 + 778	0.07(2)	−3(1)	–	9.3(1)	0.07(2)	3.90(5)	138
	0.05(3)	−7(2)	16(3)	5.1(6)	−5.0(3)	11.5(7)	105
	0.08(3)	−8(3)	–	4.0(2)	−10.71(5)	3.3(1)	52
	< 0.009			8.8(7)	−11.8(1)	26.9(5)	> 978
				0.11(2)	−17(9)	141(31)	> 12
				1.8(4)	−17.6(2)	5.0(7)	> 200
	0.05(1)	−25(4)	–	7.2(3)	−23.59(8)	7.4(2)	148
				0.18(2)	−113(2)	34(5)	> 20

Source	**HI Absorption** (GMRT)			**HI Emission** (LDS)			
	$\tau_{\rm HI}$	$V_{\rm lsr}$ (km s^{-1})	FWHM (km s^{-1})	T_B (K)	$V_{\rm lsr}$ (km s^{-1})	FWHM (km s^{-1})	T_S (K)
J2009 + 724	0.20(2)	−5.2(1)	–	22.8(1)	−5.11(1)	9.54(5)	126
	< 0.009			7.0(1)	−10.1(2)	29.2(3)	> 778
				3.4(1)	−22.23(8)	8.3(3)	> 378
				3.9(2)	−52.9(2)	21.5(5)	> 433
				1.7(2)	−55.1(1)	8.7(6)	> 189
				0.83(2)	−123.6(4)	35(1)	> 92
J2011 − 067	< 0.006			0.57(2)	+53.6(7)	27(2)	> 95
				0.40(4)	+30.6(6)	11(1)	> 44
	0.020(3)	+11.1(6)	–	0.8(1)	+9.9(2)	4.9(8)	40
				4.4(2)	+4.4(1)	23.9(4)	> 733
	0.058(1)	+0.1(2)	7.2(4)	5.9(3)	+1.25(4)	3.7(1)	105
				9.7(1)	−2.93(7)	6.5(1)	> 1617
J2047 − 026	< 0.006			1.1(4)	−2(1)	5(1)	> 183
	0.035(3)	+6(1)	4(2)	4.7(5)	+2.0(2)	4.4(2)	134
				4.2(3)	+3.9(0.2)	19(1)	> 700
	0.012(4)	+13(3)	5(7)	0.8(1)	+9.4(3)	4.9(9)	67
				1.1(0.3)	+18(5)	33(5)	> 183
				0.30(4)	+35.5(3)	4.7(8)	> 50
				0.10(1)	+48(8)	50(5)	> 17
J2130 + 050	0.10(1)	+01.40(7)	3.8(1)	16.3(2)	+00.60(3)	6.7(1)	163
	< 0.006			4.1(2)	+06.1(4)	18.1(8)	> 683
				1.3(2)	+14(2)	50(3)	> 216
J2136 + 006	0.14(2)	0(2)	–	8.6(1)	+00.8(4)	6.0(1)	61
	0.10(5)	+05.5(1)	4.7(4)	8.5(1)	+06.20(3)	4.0(1)	85
	< 0.006			6.9(1)	+04.80(6)	19.6(2)	> 1150
				0.40(2)	−36.0(8)	23(2)	> 67
J2137 − 207	0.025(2)	−1.2(3)	3.8(5)	3.7(2)	+1.03(4)	7.1(1)	150
	< 0.006			3.6(1)	−0.6(1)	15.7(6)	> 600
				2.4(2)	−3.7(2)	29.3(6)	> 400
J2148 + 069	< 0.006			7.8(1)	−7.62(4)	5.92(9)	> 1300
	0.079(3)	−2.1(2)	8.0(4)	6.7(3)	+0.63(9)	11.2(3)	88
				4.3(3)	+2.3(2)	23.6(5)	> 717
	0.040(4)	+7.7(2)	–				
J2212 + 018	< 0.003			0.08(1)	+35(8)	109(12)	> 27
	0.016(1)	+7.0(9)	14(2)	4.5(1)	+0.32(8)	11.2(3)	284
				3.4(1)	−1.7(1)	24.2(4)	> 1133
	0.037(4)	−3.6(2)	–	6.05(8)	−7.23(2)	4.64(6)	167
J2214 − 385	< 0.006			No data			

Source	**HI Absorption** (GMRT)			**HI Emission** (LDS)			
	τ_{HI}	V_{lsr} (km s^{-1})	FWHM (km s^{-1})	T_B (K)	V_{lsr} (km s^{-1})	FWHM (km s^{-1})	T_S (K)
J2219 − 279	< 0.009			0.7(4)	−13.2(4)	11(2)	> 78
				1.4(5)	−4(2)	18(4)	> 156
				0.6(4)	−3.9(7)	32(4)	> 67
J2225 − 049	< 0.009			0.15(2)	−10(3)	60(6)	> 17
				9.2(2)	−5.24(9)	5.09(1)	> 1022
				2.8(4)	−2.50(5)	2.8(2)	> 200
	0.124(4)	−2.4(1)	5.4(3)	10.15(7)	+0.15(7)	15.2(1)	87
	0.029(4)	+8(2)	–	1.25(8)	+8.77(6)	3.4(2)	44
				0.68(4)	+16.8(1)	4.8(4)	> 76
J2232 + 117	< 0.009			9.87(8)	+0.6(1)	14.1(2)	> 1097
				0.77(5)	−3.4(0.6)	50(2)	> 86
	0.079(3)	−4.6(2)	8.3(5)	7.4(2)	−5.81(2)	5.3(1)	94
	0.040(4)	−15.3(3)	–	3.83(7)	−13.88(3)	3.92(8)	96
J2236 + 284	< 0.012			4(1)	+5(2)	14(2)	> 333
	0.018(4)	−1(1)	12(4)	8(2)	−0.16(4)	8.7(4)	448
				0.6(1)	0(3)	51(4)	> 50
	0.031(5)	−14.2(6)	5(1)	3.6(2)	−11.0(2)	10.1(3)	118
				1.5(1)	−24.3(2)	12.3(7)	> 125
				0.64(5)	−61.0(3)	13.5(9)	> 53
				0.61(4)	−68(2)	40(2)	> 51
J2246 − 121	< 0.009			4.36(6)	+3.84(3)	4.67(6)	> 484
				7.33(9)	−1.31(3)	21.6(1)	> 814
	0.016(3)	−2.9(9)	8(2)	4.93(8)	−3.46(3)	7.05(9)	308
J2250 + 143	0.037(3)	−4.2(3)	5.0(6)	5.7(1)	−2.02(2)	4.06(7)	157
	< 0.006			8.6(1)	−2.52(3)	13.9(1)	> 1433
				0.91(3)	−13.2(9)	53(2)	> 152
				2.01(5)	−15.34(6)	5.2(2)	> 335
				0.38(4)	−40.7(5)	13(2)	> 63
J2251 + 188	0.041(4)	−0.3(3)	7.3(9)	14.74(8)	−0.27(2)	10.51(6)	367
	< 0.006			1.88(8)	−7.5(4)	30.0(9)	> 313
	0.015(3)	−9(3)	22(3)	1.47(8)	−8.6(1)	5.4(3)	99
J2302 − 373	< 0.006				No data		
J2340 + 135	< 0.006			2.12(9)	+4.84(7)	4.4(2)	> 353
				2.3(2)	−2.20(6)	3.0(2)	> 383
	0.216(5)	−4.60(7)	3.5(1)	9.1(2)	−4.58(7)	15.5(1)	47
	0.098(5)	−11(3)	–	5.8(1)	−6.27(5)	5.6(1)	62
				1.41(2)	−36.2(2)	27.9(5)	> 235
J2341 − 351	< 0.012				No data		

References

Albert, C. E. 1983, *Astrophys. J.*, **272**, 509.
Brand, J., Blitz, L. 1993, *Astron. Astrophys.*, **275**, 67.
Burton, W. B. 1988, in *Galactic and Extragalactic Radio Astronomy*, (eds) G. L. Verschuur & K. I. Kellermann (New York: Springer-Verlag), p. 295.
Clark, B. G., Radhakrishnan, V., Wilson, R. W. 1962, *Astrophys. J.*, **135**, 151.
Clark, B. G. 1965, *Astrophys. J.*, **142**, 1398.
Dickey, J. M., Salpeter, E. E., Terzian, Y. 1978, *Astrophys. J. Suppl.*, **36**, 77.
Dickey, J. M., Benson, J. M. 1982, *Astron. J.*, **87**, 278.
Dickey, J. M., Kulkarni, S. R., Heiles, C. E., van Gorkom, J. H. 1983, *Astrophys. J. Suppl.*, **53**, 591.
Dickey, J. M., Lockman, F. J. 1990, *Ann. Rev. Astron. Astrophys.*, **28**, 215.
Field, G. B., Goldsmith, D. W., Habing, H. J. 1969, *Astrophys. J. Lett.*, **155**, L149.
Hartmann, D., Burton, W. B. 1995, *An Atlas of Galactic Neutral Hydrogen*, Cambridge Univ. Press.
Heiles, C., Troland, T. H. 2003a, *Astrophys. J. Suppl.*, **145**, 329.
Heiles, C., Troland, T. H. 2003b, *Astrophys. J.*, **586**, 1067.
Kalberla, P. M. W., Westphalen, G., Mebold, U., Hartmann, D., Burton, W.B. 1998, *Astron. Astrophys. Lett.*, **332**, L61.
Lockman, F. J., Gehman, C. S. 1991, *Astrophys. J.*, **382**, 182.
Mebold, U., Winnberg, A., Kalberla, P. M. W., Goss, W. M. 1981, *Astron. Astrophys. Suppl.*, **46**, 389.
Mebold, U., Winnberg, A., Kalberla, P. M. W., Goss, W. M. 1982, *Astron. Astrophys.*, **115**, 223.
Mohan, R., Dwarakanath, K. S., Srinivasan, G. 2004 (Paper II), *J. Astrophys. Astron.*, (this volume).
Radhakrishnan, V., Murray, J. D., Lockhart, P., Whittle, R. P.J. 1972a, *Astrophys. J. Suppl.*, **24**, 15.
Radhakrishnan, V., Goss, W. M., Murray, J. D., Brooks, J. W. 1972b, *Astrophys. J. Suppl.*, **24**, 49.
Radhakrishnan, V., Goss, W. M. 1972, *Astrophys. J. Suppl.*, **24**, 161.
Spitzer, L. Jr. 1978, *Physical Processes in the interstellar Medium*, New York: Wiley Interscience.
Swarup, G., Ananthakrishnan, S., Kapahi, V. K., Rao, A. P., Subrahmanya, C. R., Kulkarni, V. K. 1991, *Current Science*, **60**, 95.
Wolfire, M. G., Hollenbach, D., McKee, C. F., Tielens, A. G. G. M., Bakes, E. L. O. 1995, *Astrophys. J.*, **443**, 152.

J. Astrophys. Astr. (2004) **25,** 185–201

A High Galactic Latitude HI 21 cm-line Absorption Survey using the GMRT: II. Results and Interpretation

Rekhesh Mohan*[1], K. S. Dwarakanath[2] & G. Srinivasan[3]
Raman Research Institute, Bangalore 560 080, India.
[1]*e-mail: reks@iiap.res.in*
[2]*e-mail: dwaraka@rri.res.in*
[3]*e-mail: srini@rri.res.in*

Received 2004 June 4; accepted 2004 November 3

Abstract. We have carried out a sensitive high-latitude ($|b| > 15^\circ$) HI 21 cm-line absorption survey towards 102 sources using the GMRT. With a 3σ detection limit in optical depth of ~ 0.01, this is the most sensitive HI absorption survey. We detected 126 absorption features most of which also have corresponding HI emission features in the Leiden Dwingeloo Survey of Galactic neutral Hydrogen. The histogram of random velocities of the absorption features is well-fit by two Gaussians centered at $V_{\rm lsr} \sim 0$ km s^{-1} with velocity dispersions of 7.6 ± 0.3 km s^{-1} and 21 ± 4 km s^{-1} respectively. About 20% of the HI absorption features form the larger velocity dispersion component. The HI absorption features forming the narrow Gaussian have a mean optical depth of 0.20 ± 0.19, a mean HI column density of $(1.46 \pm 1.03) \times 10^{20}$ cm^{-2}, and a mean spin temperature of 121 ± 69 K. These HI concentrations can be identified with the standard HI clouds in the cold neutral medium of the Galaxy. The HI absorption features forming the wider Gaussian have a mean optical depth of 0.04 ± 0.02, a mean HI column density of $(4.3 \pm 3.4) \times 10^{19}$ cm^{-2}, and a mean spin temperature of 125 ± 82 K. The HI column densities of these fast clouds decrease with their increasing random velocities. These fast clouds can be identified with a population of clouds detected so far only in optical absorption and in HI emission lines with a similar velocity dispersion. This population of fast clouds is likely to be in the lower Galactic Halo.

Key words. ISM: clouds, kinematics and dynamics—radio lines: ISM.

1. Introduction

A number of HI 21 cm-line absorption surveys have been carried out in the last 50 years or so. While interferometric surveys are a better alternative for such studies, since it rejects the more extended HI emission, the lack of collecting area of the interferometers has limited the sensitivity of the HI absorption surveys. Until recently, the Very Large

*Currently at the Indian Institute of Astrophysics, Bangalore 560 034, India.

Array (VLA) used to be the only instrument with a collecting area comparable to large single dish telescopes. From the various HI absorption surveys carried out so far, more than 600 absorption spectra are available, but the optical depth detection limits of more than 75% of these are above 0.1 (see for e.g., Mohan *et al.* 2004 – hereafter paper I – for a summary of previous surveys).

The motivation for the present survey, the observing strategy, the sources observed, their HI 21 cm-line spectra and the parameters of the discrete HI line components are presented in paper I. Here, we discuss their interpretation. As was mentioned in paper I, the low optical depth regime of Galactic HI is largely unexplored, except for the HI absorption study by Dickey *et al*. (1978) and by Heiles & Troland (2003a, b). Dickey *et al*. (1978) measured HI absorption/emission towards 27 extragalactic radio sources located at high and intermediate Galactic latitudes ($|b| > 5^\circ$) using the Arecibo telescope. The rms optical depth in their spectra was ~ 0.005. These profiles can be considered the best in terms of signal-to-noise ratio, though in many of the profiles the systematics in the band dominate the noise. Despite these limitations, Dickey *et al*. (1978) noted that the velocity distribution of HI absorption features is dependent on their optical depths. For the optically thin clouds ($\tau < 0.1$), the velocity dispersion was ~ 11 km s^{-1}, whereas for the optically thick clouds ($\tau > 0.1$) this value was ~ 6 km s^{-1}. Similar trend was also noticed in the Effelsberg–Green Bank survey (Mebold *et al*. 1982). More recently, Heiles & Troland (2003b) also found indications for an independent population of lower optical depth HI absorption features.

One of the first efforts to study the nature of the ISM was the observation of interstellar absorption in the optical line of singly ionized calcium (CaII) towards early type stars by Adams (1949). He noted that the observed extent in the radial velocities exceeded 50 km s^{-1} in the local standard of rest frame (LSR). Blaauw (1952) analysed the random velocity distribution of interstellar absorption lines in Adams' data. One of the main conclusions of this analysis was that the random velocity distribution of interstellar absorption features cannot be explained by a single Gaussian distribution. Support for this conclusion came from the study of Routly–Spitzer (1952), who found the ratios of column densities of neutral sodium (NaI) to singly ionized calcium (CaI) to decrease systematically with increasing random velocities of the absorption features. This effect, called the "Routly–Spitzer effect" was later confirmed from a much larger sample of stars by Siluk & Silk (1974). Field, Goldsmith & Habbing (1969) modeled the ISM as cool dense concentrations of gas, often referred to as "interstellar clouds" (the Cold Neutral Medium or CNM), in pressure equilibrium with a warmer intercloud medium (the Warm Neutral Medium or WNM). While this initial model of the ISM has been refined considerably by later studies, the basic picture of the ISM with cold diffuse clouds and the warmer intercloud medium has remained. However, there has been a discrepancy in the velocity distribution of interstellar clouds (the CNM) obtained from the optical absorption line studies and from the HI 21-cm line observations. The optical as well as UV absorption line studies indicated the presence of features with larger spread in random velocities, which was absent in the 21-cm line observations (Mohan *et al*. 2001 and the references therein). This is clear from Fig. 1.

According to one hypothesis, the high velocity ($|v| \gtrsim 15$ km s^{-1}) optical absorption lines arise in interstellar clouds, shocked and accelerated by supernova remnants in their late phases of evolution (Siluk & Silk 1974; Radhakrishnan & Srinivasan 1980). Such a mechanism would naturally result in the higher random velocity clouds being warmer

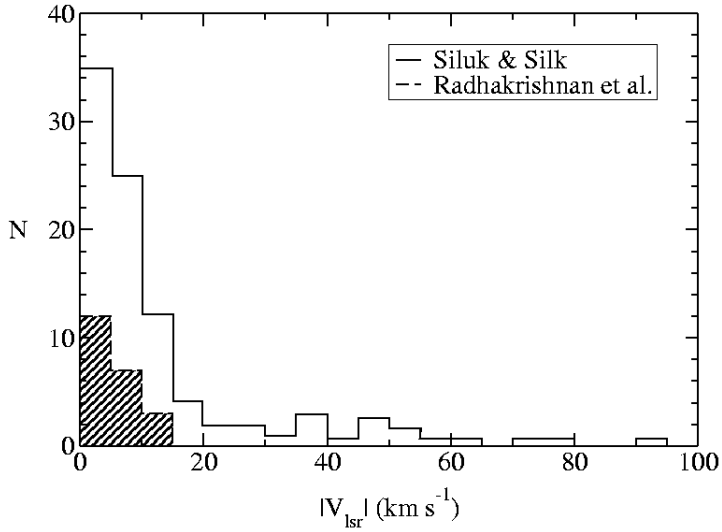

Figure 1. Histogram of radial (random) velocities from the optical absorption line studies by Siluk & Silk (1974), along with that from the HI absorption line survey by Radhakrishnan *et al.* 1972 (dashed line; shaded). The higher velocity tail is missing in the radio observations.

and having lower column densities due to shock heating and evaporation, as compared to the low random velocity clouds. Lower column density explains the non-detections of such clouds in HI emission, since the intensity of the HI 21 cm-line emission is directly proportional to the HI column density. Higher temperature, along with lower column density ($N_{\rm HI}$) results in lower optical depth, since $\tau_{\rm HI} \propto N_{\rm HI}/T$, where T is the excitation temperature of the spectral line (Siluk & Silk 1974; Radhakrishnan & Srinivasan 1980; Rajagopal *et al*. 1998). If this scenario is correct, then a sensitive HI absorption survey should detect those features with lower optical depth and higher random velocities which are presumably the counterparts of the higher velocity optical absorption lines. We have used the present dataset to address this scenario.

In the next section, we discuss a method to estimate the contributions from the Galactic differential rotation to the observed radial velocities of the HI absorption features. To supplement the absorption spectra, the corresponding HI 21 cm emission profiles from the Leiden–Dwingeloo HI emission survey (LDS, Hartman & Burton 1995) were analyzed. Appendices B and C of paper I list the HI line profiles (absorption and emission), and their fitted line parameters respectively. In section 3., we compare the present dataset with the previous HI absorption surveys. In section 4., we discuss the statistics of HI absorption line parameters obtained from the GMRT. The velocity dispersion of the interstellar clouds estimated from the present survey and the low optical depth features are highlighted. In section 5., we compare our results with various other existing studies to discuss the location of the newly detected high random velocity and low optical depth features.

2. The differential Galactic rotation

As was discussed in paper I, we carried out a survey at higher Galactic latitudes to avoid the blending of components in the absorption spectra and to minimize the

contribution of the systematic velocities in the observed radial velocities due to the Galaxy's differential rotation. For a given Galactic longitude (l) and latitude (b), the observed radial component of differential Galactic rotation for objects in the solar neighbourhood is (Burton 1988)

$$v_r = Ar \sin 2l \cos b, \tag{1}$$

where $A = 14\,\mathrm{km\ s^{-1}\ Kpc^{-1}}$ is the Oort's constant and r is the heliocentric distance to the object.

In Fig. 2, we have plotted the radial velocities with respect to the local standard of rest (LSR) of the various HI absorption features as a function of the Galactic longitude. If the contribution to radial velocities from the Galactic differential rotation is dominant, there should be a pronounced signature of a "sine wave" in such a plot, provided the absorption features are at the same heliocentric distance r (equation 1). There is a suggestion that absorption features with $|V_{\mathrm{lsr}}| \lesssim 15\,\mathrm{km\ s^{-1}}$ may have significant contribution from differential rotation.

Including an additional term for the random motion of the cloud, equation (1) becomes,

$$v_r = v_{\mathrm{random}} + Ar \sin 2l \cos b. \tag{2}$$

It would appear that this function can be fitted to the observed distribution (Fig. 2) to estimate the systematic component. However, the distances to the absorbing features are unknown. Consider an ensemble of interstellar clouds, each with its own random motion and distance. The random motions can be approximated by a Gaussian with a zero mean. If we assume the number density of clouds to be only a function of height, $|z|$, from the Galactic plane and the Sun to be in the plane, the distances for a distribution of clouds in the Galaxy can be assumed to be an exponential deviate with a scale height (Dickey & Lockman 1990). Adding these two terms, the above equation can be re-written as

$$v_r = a_1 v_{\mathrm{gauss}} + a_2 \left(\frac{z_{\mathrm{exp}}}{|\sin b|} \right) \sin 2l \cos b, \tag{3}$$

where z_{exp} is an exponential deviate with unit scale height and v_{gauss} is a Gaussian deviate. The term $z_{\mathrm{exp}}/|\sin\ b|$ is to take into account the variation of path length through the disk as a function of the Galactic latitude. We have carried out a Monte-Carlo simulation to generate such a distribution and compare with the observed distribution (Fig. 2). The simulation used the Monte Carlo routines discussed by Press *et al.* (1992).

We used the *F-test* (Press *et al.* 1992) to check if the simulated and the observed data can be derived from the same distribution. We found no well defined peak for the probability distribution. The 3σ level indicates that similar confidence levels can be achieved even with a_1 or $a_2 = 0.0$. Therefore, the *F-test* results imply that a systematic pattern in the distribution is negligible (for a detailed discussion see Mohan 2003). Hence, we have not applied any correction to the observed velocity for differential Galactic rotation. The observed radial velocities are considered to be random motions. A similar conclusion was also reached by Heiles & Troland (2003b) for the recent Arecibo survey of HI absorption/emission measurements for Galactic latitudes $|b| > 10^{\circ}$.

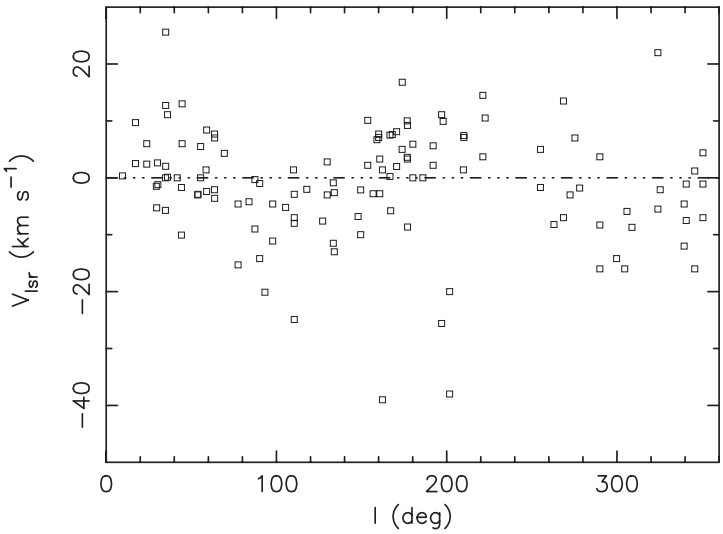

Figure 2. The radial velocities (in the LSR frame) of the HI absorption features detected in the present survey as a function of Galactic longitude.

3. Comparison of the GMRT data with the previous HI and optical surveys

In this section we compare the histogram of random velocity distribution obtained from the present survey with those from the previous HI absorption line surveys and optical absorption line surveys of interstellar NaI and CaII. For the case of radio surveys, we have used those lines of sight from the previous surveys with $|b| > 15^{\circ}$. While comparing our data with the results obtained from optical surveys, we have not put this restriction since the stars observed are located in the solar neighbourhood and the contribution from the differential Galactic rotation (if any) would be negligible. We have, however, carefully analysed the optical surveys to exclude those lines of sight where the velocities of the absorption lines were due to systematic motions.

3.1 *Comparison of the GMRT data with the previous HI surveys*

Figure 3 shows the frequency distribution of radial velocities of HI absorption features from the present survey along with that of 22 HI absorption features from the Parkes Interferometer survey by Radhakrishnan *et al*. (1972), 37 discrete HI absorption features from the Arecibo measurements by Dickey, Salpeter & Terzian (1978) and 51 absorption features from the Effelsberg–Green Bank HI absorption survey by Mebold *et al*. (1981, 1982). No feature at radial velocities larger than 15 km s^{-1} was detected in the Parkes survey (Fig. 3a). The Arecibo HI absorption survey by Dickey *et al*. (1978) had an rms sensitivity comparable to the present survey. Although the number of absorption features from their survey is smaller, the spread in the radial velocities are found to be similar to the present survey. The Effelsberg-Green Bank survey by Mebold *et al*. (1982) lists 69 lines of sight. We have used only the Interferometric measurements from Mebold *et al*. (1982). Figure (3c) shows a comparison of radial velocity histogram from the present survey to that by Mebold *et al*. (1982). It is

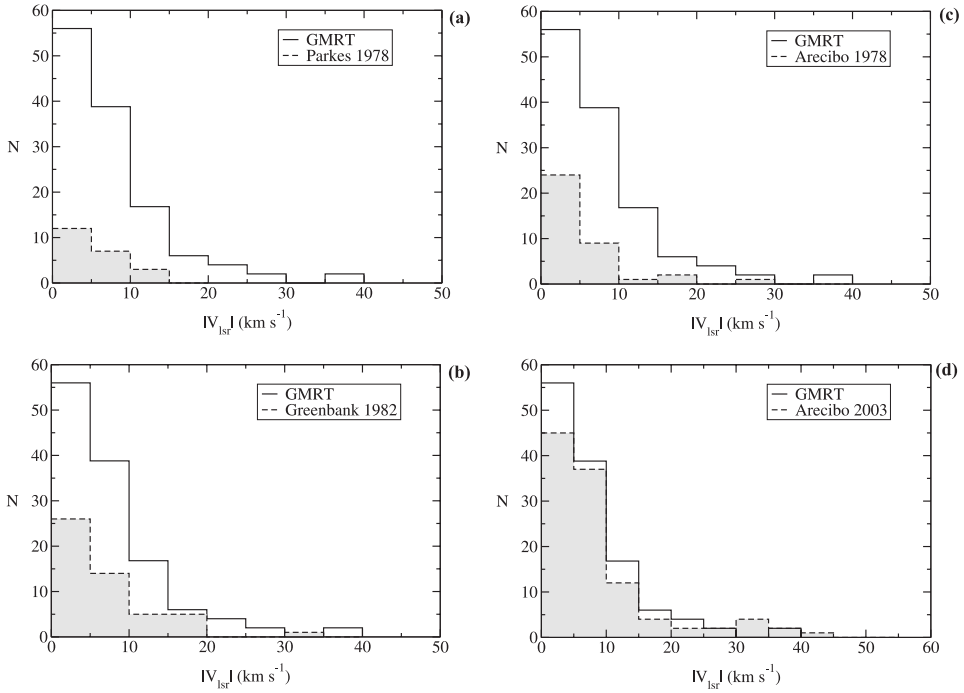

Figure 3. The frequency distribution of mean LSR velocities of the HI absorption features identified from the GMRT survey is compared with that from Radhakrishnan *et al*. (1972) **(a)**, Dickey, Salpeter & Terzian (1978) **(b)**, Mebold *et al*. (1982) **(c)** and from Heiles & Troland (2003a) **(d)** respectively.

evident from the figure that except for the single absorption feature at $\sim 35\,\mathrm{km\ s^{-1}}$, all the features in the survey by Mebold *et al*. (1982) are at velocities below $\sim 20\,\mathrm{km\ s^{-1}}$.

It is clear from Fig. 3(a–c) that the present dataset has not only detected more absorbing clouds, but also more higher velocity clouds. The peak optical depths of these features at higher velocities are found to be lower as compared to the rest of the clouds (see Fig. 7). The random velocity distribution of the features detected in the present survey agrees well with that from the recent Arecibo survey by Heiles & Troland (2003a) (Fig. 3d).

There are six common sources between the present survey and the Arecibo observations. While the rms sensitivity in HI optical depth of the Arecibo survey is slightly worse ($\tau_{\mathrm{HI}} \sim 0.006$) compared to the present survey, its velocity resolution ($0.16\,\mathrm{km\ s^{-1}}$) is better compared to the current HI absorption measurements ($3.3\,\mathrm{km\ s^{-1}}$). Therefore, the number of HI absorption components detected in their observations are higher than that in the present survey. For the six common sources, the fitted values for the peak optical depths from the present survey and the Arecibo survey agree to within $\sim 30\%$. The fitted values for line centers and widths of the corresponding features differ by less than $\sim 2\,\mathrm{km\ s^{-1}}$ between the two surveys.

3.2 *Comparison of the GMRT HI absorption data with the optical surveys*

The CaII and NaI absorption studies of Adams (1949), Blaauw (1952), Münch (1957), Münch & Zirin (1961) and others revealed two set of absorption features, one at lower

and the other at higher random velocities. More recently, high resolution spectra of NaI lines (e.g., Welty *et al*. 1994) and CaII lines (Welty *et al*. 1996) were obtained towards a number of stars.

Figure 4(a) shows the frequency distribution of the velocities of the HI absorption features from the present survey with that from Blaauw's (1952) study. The secondary peak at high velocity in Blaauw's histogram is an artifact of the binning used by Blaauw (1952). He counted all the features with radial velocities $V_{\rm lsr} \geq 21$ km s^{-1} in a single bin. Excluding this secondary peak, there is reasonable agreement between the two histograms.

In Fig. 4(b), we compare the velocity distribution of HI absorption components from the present survey with that from Siluk & Silk (1974). Some of the absorption at higher velocities in their data may not represent random velocities of diffuse HI clouds; they could be due to large systematic motions (spiral arms, IVCs, HVCs, etc.) superimposed on random motions (Mohan 2003). Excluding those features, we have re-constructed the histogram of optical absorption line velocities from the data of Siluk & Silk (Fig. 4b). The modified histogram from Siluk & Silk (1974) is in good agreement with the current HI absorption velocity histogram.

Figure 4c compares the frequency distributions of radial velocities from the present survey with that of a recent high resolution survey of CaII lines (Welty *et al*. 1996). Out of the 44 stars towards which they measured CaII absorption, eight stars were located at a distance of 450 pc, in the constellation Orion, and one star, HD72127, in Vela. The CaII absorption features towards these nine stars were not included in the comparison since the velocities of the absorption features were dominated by systematic motions.

It is clear from Fig. 4 that the extent of velocities of CaII absorption line features are comparable to that of the HI absorption lines in the present survey. The problem of larger spread in the velocities of interstellar optical absorption lines as compared to the HI 21-cm line features have been an open problem for decades. Our analysis makes it clear that many of the often quoted interstellar optical absorption features at higher velocities may not represent true random motions. Leaving aside such features, the higher velocity HI absorption features detected in the present survey can account for the "missing high random velocity" interstellar clouds in the earlier HI 21-cm line studies.

4. Statistics of the HI absorption line parameters

The details of the observing strategy, the HI absorption spectra from GMRT and the discrete line components identified by fitting Gaussians to the spectra are presented in paper I. Here we discuss their interpretation.

4.1 *The frequency distribution of HI absorption line parameters*

The frequency distribution of the mean LSR velocities of the HI absorption line components is shown in Fig. 5(a). This histogram was discussed in section 3.. It was noticed in earlier studies that the average optical depth of HI absorption features is higher at lower Galactic latitudes (see for e.g., Mebold *et al*. 1982). This apparent excess of large optical depth features in the Galactic plane has been attributed to superposition of absorbing clouds along the line of sight. However, there are only seven features in

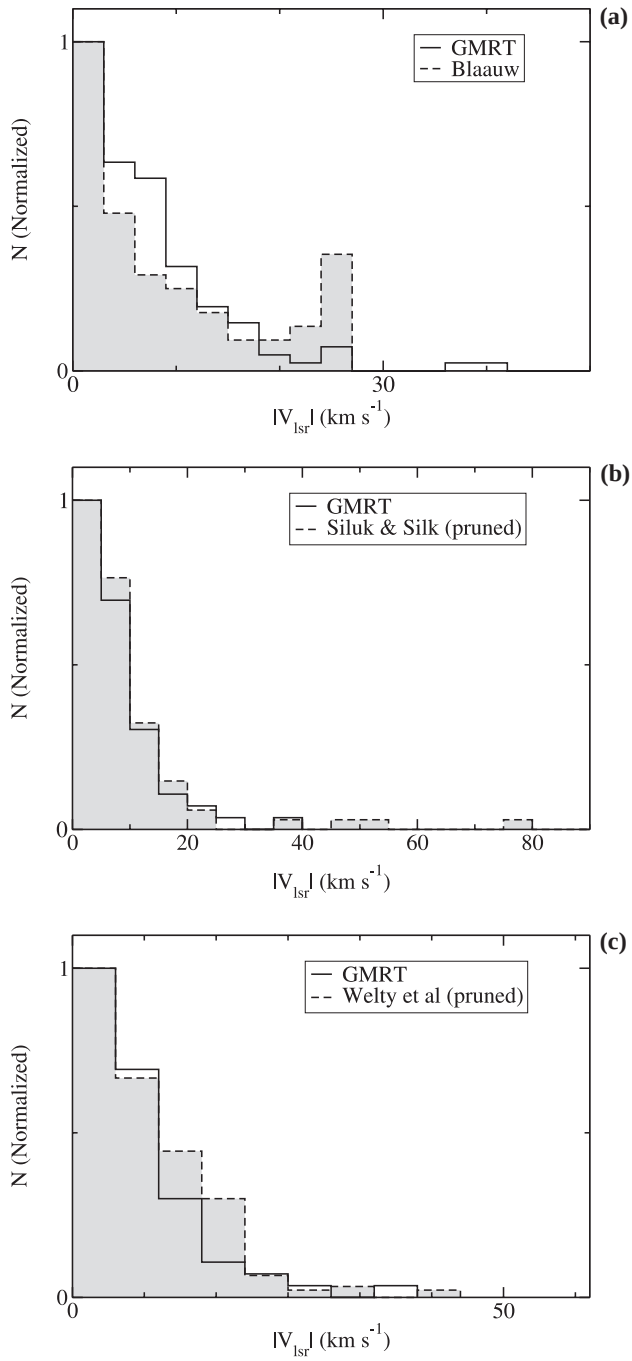

Figure 4. The frequency distribution of the radial velocities of HI absorption features identified from the present survey along with those from optical surveys. **(a)**: Blaauw 1952 (dashed line). The secondary peak at high velocity in Blaauw's histogram is an artifact of the binning used by Blaauw. **(b)**: Optical absorption line data from Siluk & Silk 1974 (pruned), and **(c)**: The CaII absorption survey by Welty, Morton & Hobbs 1996 (pruned).

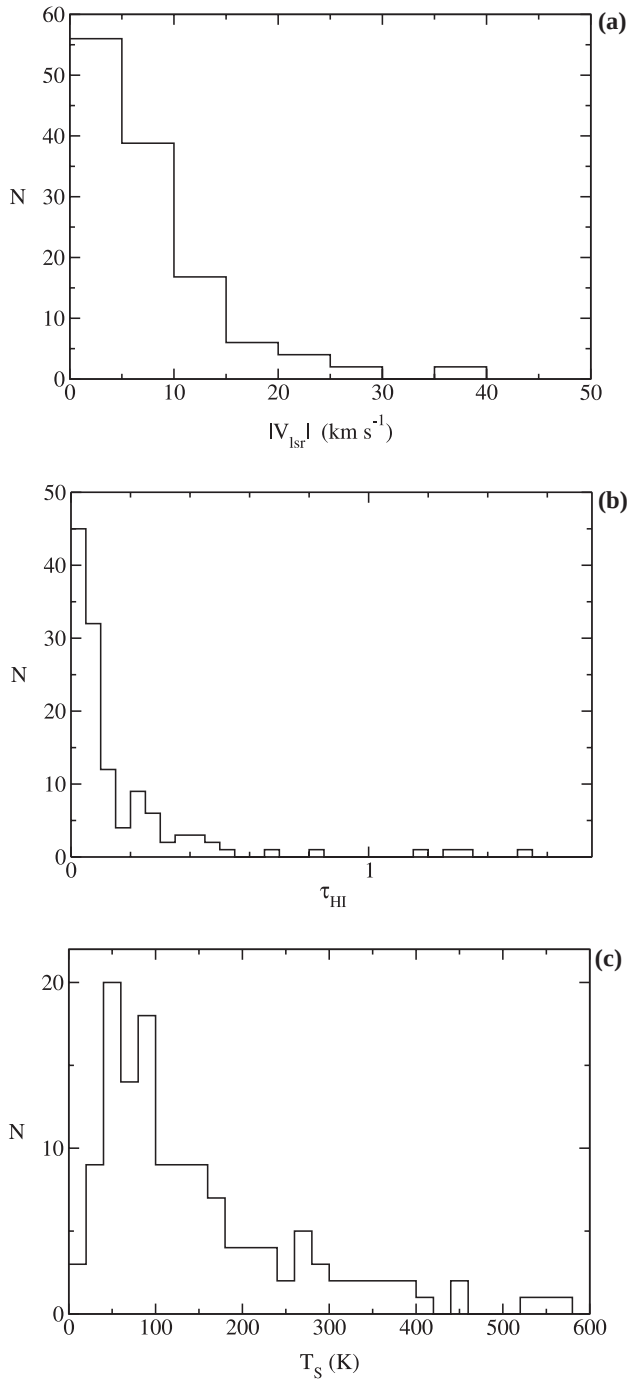

Figure 5. The frequency distribution of the absorption line parameters from the present survey. **(a)**: The histogram of random velocities of the HI absorption components, in 5 km s^{-1} bins. **(b)**: The frequency distribution of peak optical depths of HI absorption features, in bins of 0.05 and **(c)**: The frequency distribution of estimated spin temperatures of the HI absorption features in 20 K bins.

our survey with their peak optical depths above 0.5 (Fig. 5b). This is an evidence that in the present dataset the superposition of more than one HI absorption feature along the line of sight is minimal. This is expected since we are sampling relatively small path lengths through the gas layer at higher Galactic latitudes.

As we discussed in paper I, we have used the HI emission data from the Leiden–Dwingeloo survey along with the present GMRT HI absorption data to estimate the spin temperatures of the HI absorption features. The mean value of the spin temperature from the present survey was found to be ~ 120 K, with considerable scatter. For the lower optical depth features ($\tau \lesssim 0.1$), we find spin temperature, $T_s = 150 \pm 78$ K. For the higher optical depth features ($\tau \gtrsim 0.1$), we find $T_s = 74 \pm 30$ K. The mean spin temperature of the lower optical depth features, though having a large scatter, is two times higher than that of the higher optical depth features. Figure 5(c) shows the histogram of the spin temperatures of the HI absorption features. The distribution of spin temperature peaks below 100 K, which agrees in particular with Heiles & Troland (2003b), who found the spin temperature distribution to peak near 40 K. Both the Arecibo observations and the present survey indicate the presence of a higher temperature "tail" in the spin temperature histogram.

4.2 *The τ–T_s relation*

Several studies in the past had reckoned an inverse correlation between $\log(1 - e^{-\tau})$ and $\log(T_s)$ (Lazareff 1975; Dickey *et al.* 1979; Crovisier 1981). It was noted that a relationship of the form

$$\log T_s = \log T_{s0} + A \log(1 - e^{-\tau}) \tag{4}$$

exists between the observed optical depth and the estimated spin temperature. However, Mebold *et al.* (1982) found no significant correlation between the spin temperature and optical depth. Figure 6 is a plot of $(1 - e^{-\tau})$ v/s (T_s) from the present dataset. We

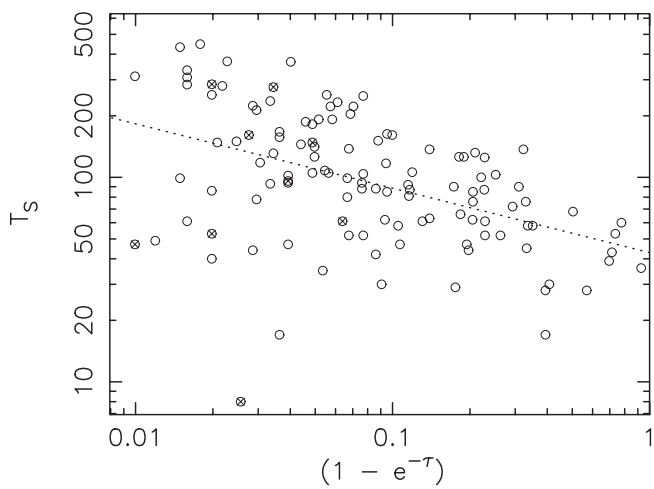

Figure 6. $\log(1 - e^{-\tau}) - \log(T_s)$ plot for the HI absorption features detected in the present survey. HI emission data are from the Leiden–Dwingeloo survey. The dotted line is the best fit for the observed data points. The circles with crosses inside them correspond to the high random velocity HI absorption features (Table 1).

do find an inverse correlation, though the scatter is larger at lower optical depths. A least square fit to the present dataset provides $T_{s0} = 43$ K and $A = -0.31$ (equation 4). The values obtained from the previous studies were $\sim$60 K and -0.35 respectively (Kulkarni & Heiles 1988). A similar least-squares fit to the recent Arecibo data yields $A = -0.29$ and $T_{s0} = 33$ K. However, Heiles & Troland (2003b) have carried out a detailed analysis of the correlation between the various parameters like the spin temperature, the HI column density, the optical depth and the kinetic temperature of the absorption features detected in the Arecibo survey. They emphasize that the mutual correlation that exists between the four parameters renders meaningless the results of least-square fit carried out on only selected pairs of variables. They conclude that there is no physically significant relation between optical depth, spin temperature and HI column density.

4.3 *The τ_{HI}–V_{lsr} relation*

The peak optical depth as a function of $|V_{lsr}|$ is shown in Fig. 7. The peak τ_{HI} drops sharply near $|V_{lsr}| \sim 10\,\mathrm{km\,s^{-1}}$. No spectral features at velocities above $10\,\mathrm{km\,s^{-1}}$ have peak optical depth above $\sim$0.1. On the other hand, low optical depth features are detected over a larger velocity range. In section 4.1 we found that lower optical depth features have higher mean spin temperature, almost a factor of two higher than the higher optical depth features. Fig. 7 conveys extra information that these higher spin temperature features are also spread over a larger range in random velocity.

4.4 *The distribution of the HI optical depth as a function of b*

HI optical depth of the absorption features are plotted against their Galactic latitude in Fig. 8. The optically thick components ($\tau > 1.0$), though very few, are all confined to $|b| \lesssim 30^\circ$. The low optical depth features ($\tau \lesssim 0.1$), on the other hand, are almost uniformly distributed with respect to the Galactic latitude. This is an indication that the scale height of the low optical depth features are different from that of the higher optical depth features.

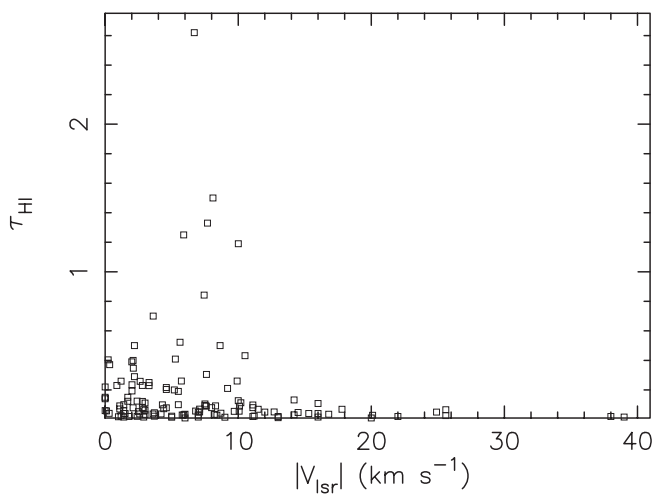

Figure 7. τ_{HI}–$|V_{LSR}|$ plot. The higher optical depth features are confined to $|V_{LSR}| \lesssim 15\,\mathrm{km\,s^{-1}}$.

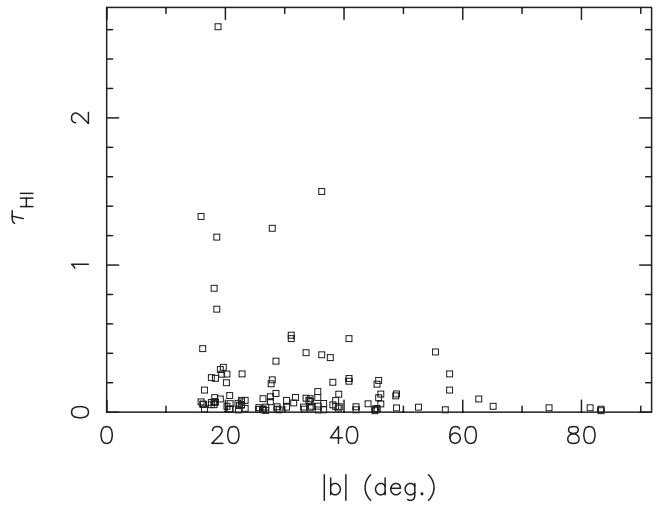

Figure 8. The distribution of optical depth of the HI absorption line features as a function of Galactic latitude. The number of higher optical depth features drop gradually with increasing latitude, but the number of low optical depth features ($\tau \lesssim 0.1$) remain more or less the same.

4.5 *The velocity dispersion of interstellar clouds*

The velocity distribution of cold atomic gas in the Galaxy is known to be a Gaussian with a dispersion of $\sim 7\,\mathrm{km\,s^{-1}}$ (Dickey & Lockman 1990). As we concluded in section 2., the observed radial velocities of the HI absorption components detected in the present survey are essentially random velocities. We have carried out a Gaussian fit to the observed frequency distribution of the radial velocities of the HI absorption features detected in the present study (Fig. 9). A non-linear least square method was used to fit Gaussians to this histogram. A two Gaussian model was found to be a good fit for the distribution, with a reduced chi-square value of 1.4. The low velocity features were found to form a Gaussian distribution with a velocity dispersion of $\sigma_1 = 7.6 \pm 0.3\,\mathrm{km\,s^{-1}}$, which agrees well with the earlier results. For e.g., Belfort & Crovisier (1984) had performed a statistical analysis of the radial velocities of HI clouds observed by surveys using the Arecibo (Dickey *et al*. 1978), and Effelsberg & Green Bank (Mebold *et al*. 1982). Their value for the velocity dispersion of HI clouds was $\sim 6.9\,\mathrm{km\,s^{-1}}$. The higher velocity features in the present survey seem to form a distribution with a velocity dispersion of $\sigma_2 = 21 \pm 4\,\mathrm{km\,s^{-1}}$ (Fig. 9). The presence of two Gaussian features in the velocity distribution of interstellar clouds is indicative of two distinct populations of interstellar clouds. From the area under the respective curves, this data indicates that $\sim 20\%$ of the clouds belong to the second population, with larger velocity dispersion.

A study of the velocities of interstellar optical absorption lines (NaI & CaII) were carried out by Sembach & Danks (1994). They observed that only a two component model can be fitted to the velocity distribution of CaII line components. The values which they obtained were: $\sigma_1 \sim 8\,\mathrm{km\,s^{-1}}$ and $\sigma_2 \sim 21\,\mathrm{km\,s^{-1}}$, which agree well with the velocity dispersions of the two components obtained from the present data of HI absorption lines.

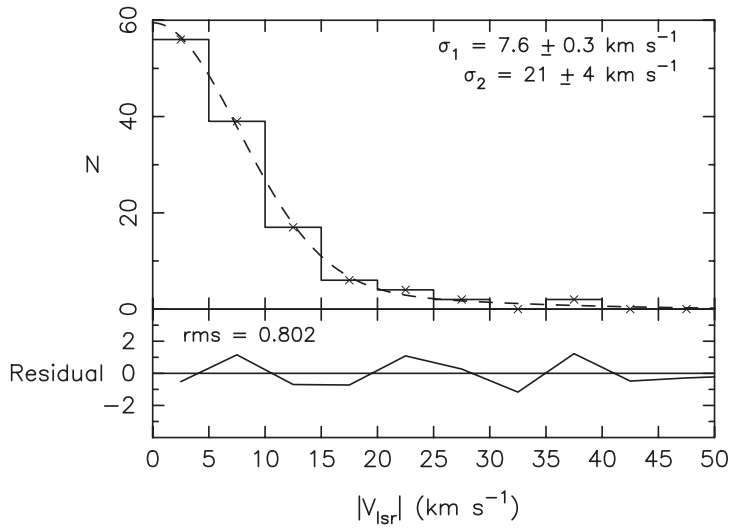

Figure 9. The frequency distribution of LSR (random) velocities of HI absorption components from the present survey. The dashed line is the sum of two Gaussian components with $\sigma_1 = 7.6 \pm 0.3\,\mathrm{km\,s^{-1}}$ and $\sigma_2 = 21 \pm 4\,\mathrm{km\,s^{-1}}$. Both the Gaussians are centered at $v_{\mathrm{LSR}} = 0\,\mathrm{km\,s^{-1}}$. The lower panel shows the residual after subtracting the fitted model from the observed distribution.

4.6 *The high velocity HI absorption features*

We have detected 13 HI absorption features at higher random velocities ($|v| > 15\,\mathrm{km\,s^{-1}}$), out of the 126 total HI absorption features (table 1). The optical depths of these higher velocity features are below 0.1. The mean value of peak optical depth of all these features is 0.04 ± 0.02. In most cases, we could identify the corresponding HI emission feature in the HI emission profile from the Leiden–Dwingeloo survey. If the velocity difference between the absorption and the emission line was less than or comparable to the channel width of the GMRT observations ($\sim 3.3\,\mathrm{km\,s^{-1}}$), and if the difference between line widths was within $\sim 5\,\mathrm{km\,s^{-1}}$, the spectral lines were assumed to originate in the same physical feature. The mean brightness temperature of these features was ~ 4 K and a mean HI column density of $(4.3 \pm 3.4) \times 10^{19}\,\mathrm{cm^{-2}}$. The mean value of the spin temperatures of these clouds is 125 ± 82 K.

We analysed the HI emission profiles from the Leiden–Dwingeloo survey towards 91 directions along which we measured HI absorption using the GMRT. HI column density of individual features along these directions were calculated using the emission data. However, 11 out of the 102 directions studied using the GMRT were beyond the declination limit of the Leiden–Dwingeloo survey. Towards these sources we assumed a spin temperature of 120 K and the observed widths of the HI absorption lines to estimate the column density.

The estimated HI column density as a function of the LSR velocity is shown in Fig. 10. The measured HI column density ranges from $\sim 2.4 \times 10^{18}$ to $\sim 9 \times 10^{20}\,\mathrm{cm^{-2}}$. It is clear from Fig. 10 that the column densities of the features are decreasing systematically with increasing velocity. This is in agreement with the results from UV absorption line studies (Martin & York 1982; Hobbs 1984).

Table 1. The higher random velocity ($|v| \gtrsim 15\,\mathrm{km\ s^{-1}}$) HI absorption features detected in the present survey. Columns 2, 3 and 4 list the peak optical depth, the mean LSR velocity and the FWHM respectively of discrete components identified using the Gaussian fitting. The value of FWHM is deconvolved for a channel width of $3.26\,\mathrm{km\ s^{-1}}$. The unresolved lines are marked with a "–". Columns 5, 6 and 7 list the same for the HI emission profile along the same line of sight, obtained from the Leiden–Dwingeloo survey of Galactic neutral hydrogen (Hartman & Burton 1995) The formal 1σ errors estimated in the last digit of the fitted parameters are given within brackets. The implied HI column densities are listed in column 8 and the estimated spin temperatures are given in column 9.

	HI Absorption (GMRT)			HI Emission (LDS)				
Source	$\tau_{\rm HI}$	$V_{\rm lsr}$ (km/s)	Δv (km/s)	$T_{\rm B}$ (K)	$V_{\rm lsr}$ (km/s)	Δv (km/s)	$N_{\rm HI}\times 10^{19}$ cm^{-2}	$T_{\rm S}$ (K)
J0459 + 024	0.026(4)	−25.6(5)	4.6(8)	0.21(8)	−28(1)	6(3)	0.24	8
J0541 − 056	0.069(7)	+17.8(9)	3.2(5)	–	–	–	–	
J0814 + 459	0.035(2)	+16.8(9)	4(2)	9.5(5)	+15.4(1)	3.8(1)	7.0	276
J1154 − 350	0.016(3)	−16(2)	13(5)	–	–	–	–	
J1221 + 282	∼ 0.01	−20	–	0.47(4)	−18.9(4)	11(1)	1.0	47
	∼ 0.02	−38	–	1.06(4)	−34.8(1)	6.1(3)	1.2	53
J1257 − 319	0.108(6)	−16.0(2)	3.8(3)	–	–	–	–	
J1351 − 148	0.020(4)	+22.0(6)	5(1)	5.7(1)	+22.9(1)	10.5(2)	12.0	285
J1554 − 270	0.04(2)	−16(8)	8(5)	–	–	–	–	
J1638 + 625	0.028(4)	−20.1(4)	5(1)	4.50(6)	−21.05(2)	5.05(7)	4.4	161
J1751 + 096	0.066(3)	+25.6(2)	4.6(2)	3.9(1)	+25.1(1)	7.1(3)	5.3	61
J2005 + 778	0.05(1)	−25(4)	2(2)	7.2(3)	−23.59(8)	7.4(2)	10.0	148
J2232 + 117	0.040(4)	−15.3(3)	2.9(7)	3.83(7)	−13.88(3)	3.92(8)	2.3	96

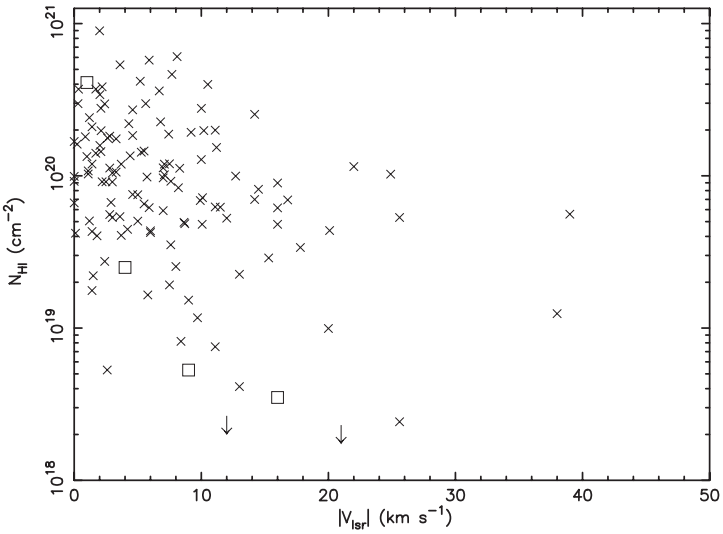

Figure 10. The column densities of the HI absorption features detected in the present survey. The brightness temperature and line width of the HI emission feature corresponding to each absorption feature was obtained from the Leiden–Dwingeloo survey. For those directions where HI emission data are not available, we have assumed a spin temperature of 120 K and the velocity width of the HI absorption line to calculate the column density. The squares are the HI column density estimates from the UV absorption line data from Martin and York (1982) and the arrows are the upper limits.

5. Discussion

The present high-latitude, high-sensitivity HI absorption survey from the GMRT has confirmed many of the known results. These results are summarised in the histograms (Fig. 5) of random velocity, peak optical depth, and spin temperature of the absorption components. In addition, variation of peak optical depth w.r.t. spin temperature, random velocity and Galactic latitude are displayed in Figs. 6, 7 and 8 respectively. However, a completely new result is the detection of the low optical depth absorption features forming the high velocity tail in the histogram shown in Fig. 5(a). Most of these low optical depth features are below the detection limit of the earlier HI absorption surveys. The velocity histogram (Fig. 5a) is well-fit by two Gaussians indicating two populations of HI absorbing clouds identified by velocity dispersions ~ 7 and $\sim 21\,\mathrm{km\,s^{-1}}$ respectively (Fig. 9). While the slow clouds were first detected in the optical absorption lines and subsequently in the HI absorption and emission surveys, the fast clouds were only detected in optical absorption lines. The non-detection of the fast clouds remained a puzzle for a long time. The present observations have clarified the nature of the fast clouds to some extent.

There have been attempts in the past to explain the high velocity tail seen in the histogram of random velocities of the optical absorption lines (Siluk & Silk 1974, Radhakrishnan & Srinivasan 1980, Rajagopal *et al*. 1998). According to these authors, the high velocity optical absorption lines arise in interstellar clouds, shocked and accelerated by supernova remnants in their late phases of evolution. The fast clouds are therefore warmer and also of lower HI column density as compared to the slow clouds, due to shock heating and evaporation. The present observations indicate that

these fast clouds have three times larger velocity dispersion and ten times lower column densities compared to the slow clouds as might be expected if they were from a shocked population of clouds. The decrease in the HI column densities of the fast clouds as a function of their random velocities (Fig. 10) is also consistent with this scenario. The shocked HI clouds are also expected to be warmer than the slow clouds. The mean spin temperature of the fast clouds detected in the GMRT survey is similar to that of the standard slow clouds (Fig. 6). However, this might be a selection effect since for a given optical depth detection limit and an HI column density, clouds with lower spin temperature will be preferentially detected.

The fast clouds with three times higher dispersion are expected to have a scale height about ten times larger compared to the slow HI clouds. Given an effective thickness of 250 pc for the slow clouds, the fast clouds can have an effective thickness of ~ 2.5 kpc. Therefore, fast clouds can be part of the halo of the Galaxy. Alternative evidence supports the existence of atomic gas in the Galactic halo. Albert (1983) selected lines of sight wherein a halo star and a nearby star are aligned one behind the other. Absorption lines of TiII, CaII and NaI were measured towards these stars. Though with a limited sample size of nine directions, the results of this study clearly indicate that the higher velocity absorption lines are seen only towards the distant star. She concludes that the high velocity tail seen in the optical line studies arise from the gas in the Galactic halo. Later, similar studies (Danly 1989; Danly *et al*. 1992; Albert *et al*. 1994; Kennedy *et al*. 1996, 1998a, 1998b) confirmed this result. The halo gas shows a larger spread in velocity, as compared to the gas in the Galactic disk. Furthermore, recent HI emission studies using the Green Bank telescope have led to the discovery of a population of discrete HI clouds in the Galactic halo with a velocity dispersion similar to that of the fast clouds reported here (Lockman 2002). The mean HI column density of these clouds was estimated to be a few times 10^{19} cm^{-2}. He concludes that a cloud population with line of sight velocity dispersions of $\sigma_v \sim 15$–20 km s^{-1} is capable of explaining the observed velocity spread of these features. Lockman (2002) finds that many clouds in the halo have narrow line widths implying temperatures below 1000 K. In addition, indications for a core-halo structure for these clouds was also found. The fast clouds detected in the present survey are likely to be part of the same halo gas detected in HI emission from Green Bank. The fast clouds, once detected only in optical absorption lines, have now been detected in both HI absorption and emission leading to a clearer picture of the interstellar medium.

Acknowledgements

We wish to thank Shiv Sethi for useful discussions relating to the numerical techniques. We thank the referee, Miller Goss, for detailed comments and constructive criticism resulting in this improved version of the paper. We also thank the staff of the GMRT who made these observations possible. The GMRT is operated by the National Centre for Radio Astrophysics of the Tata Institute of Fundamental Research. This research has made use of NASA's Astrophysics Data System.

References

Albert, C. E. 1983, *Astrophys. J.*, **272**, 509.
Albert, C. E., Welsh, B. Y., Danly, L. 1994, *Astrophys. J.*, **437**, 204.
Adams, W. A. 1949, *Astrophys. J.*, **109**, 354.

Belfort, P., Crovisier, J. 1984, *Astron. Astrophys.*, **136**, 368.
Blaauw, A. 1952, *Bull. Astr. Inst. Netherland*, **11**, 459.
Burton, W. B. 1988, in *Galactic and Extragalactic Radio Astronomy*, (eds) G. L. Verschuur & K. I. Kellermann (New York: Springer-Verlag), 295.
Crovisier, J. 1981, *Astron. Astrophys.*, **94**, 162.
Danly, L. 1989, *Astrophys. J.*, **342**, 785.
Danly, L., Lockman, F. J., Meade, M. R., Savage, B. D. 1992, *Astrophys. J. Suppl.*, **81**, 125.
Dickey, J. M., Lockman, F. J. 1990, *Ann. Rev. Astron. Astrophys.*, **28**, 215.
Dickey, J. M., Salpeter, E. E., Terzian, Y. 1978, *Astrophys. J. Suppl.*, **36**, 77.
Dickey, J. M., Salpeter, E. E., Terzian, Y. 1979, *Astrophys. J.*, **228**, 465.
Field, G. B., Goldsmith, D. W., Habing, H. J. 1969, *Astrophys. J. Lett.*, **155**, L149.
Hartmann, D., Burton, W. B. 1995, *An Atlas of Galactic Neutral Hydrogen* (Cambridge Univ. Press).
Heiles, C., Troland, T. H. 2003a, *Astrophys. J. Suppl.*, **145**, 329.
Heiles, C., Troland, T. H. 2003b, *Astrophys. J.*, **586**, 1067.
Hobbs, L. M. 1984, *Astrophys. J. Suppl.*, **56**, 315.
Kennedy, D. C., Bates, B., Kemp, S. N. 1996, *Astron. Astrophys.*, **309**, 109.
Kennedy, D. C., Bates, B., Keenan, F. P., Kemp, S. N., Ryans, R. S. I., Davies, R. D., Sembach, K. R. 1998a, *Mon. Not. R. Astron. Soc.*, **297**, 849.
Kennedy, D. C., Bates, B., Kemp, S. N. 1998b, *Astron. Astrophys.*, **336**, 315.
Kulkarni, S. R., Heiles, C. 1988, in *Galactic and Extragalactic Radio Astronomy*, (eds) G. L. Verschuur & K. I. Kellermann (New York: Springer-Verlag), 95.
Lazareff, B. 1975, *Astron. Astrophys.*, **42**, 25.
Lockman, F. J. 2002, *Astrophys. J. Lett.*, **580**, L47.
Martin, E. R., York, D. G. 1982, *Astrophys. J.*, **257**, 135.
Mebold, U., Winnberg, A., Kalberla, P. M. W., Goss, W. M. 1981, *Astron. Astrophys. Suppl.*, **46**, 389.
Mebold, U., Winnberg, A., Kalberla, P. M. W., Goss, W. M. 1982, *Astron. Astrophys.*, **115**, 223.
Mohan, R., Dwarakanath, K. S., Srinivasan, G., Chengalur, J. N. 2001, *J. Astrophys. Astron.*, **22**, 35.
Mohan, R., Ph.D. Thesis, 2003, Jawaharlal Nehru University, New Delhi.
Mohan, R., Dwarakanath, K. S., Srinivasan, G. 2004 (Paper I), *J. Astrophys. Astron.*, (this volume).
Münch, G. 1957, *Astrophys. J.*, **125**, 42.
Münch, G., Zirrin, H. 1961, *Astrophys. J.*, **133**, 11.
Press, W. H., Teukolsky, S. A., Vetterling, W. T., Flannery, B. P. 1992, *Numerical Recipes, The Art of Scientific Computing*, (Cambridge: Cambridge Univ. Press).
Radhakrishnan, V., Goss, W. M., Murray, J. D., Brooks, J. W. 1972, *Astrophys. J. Suppl.*, **24**, 49.
Radhakrishnan, V., Srinivasan, G. 1980, *J. Astrophys. Astr.*, **1**, 47.
Rajagopal J., Srinivasan, G., Dwarakanath, K. S. 1998, *J. Astrophys. Astr.*, **19**, 117.
Routly, P. M., Spitzer, L. Jr. 1952, *Astrophys. J.*, **115**, 227.
Sembach, K. R., Danks, A. C. 1994, *Astron. Astrophys.*, **289**, 539.
Siluk, R. S., Silk, J. 1974, *Astrophys. J.*, **192**, 51.
Welty, D. E., Hobbs, L. M., Kulkarni, V. P. 1994, *Astrophys. J.*, **436**, 152.
Welty, D. E., Morton D. C., Hobbs, L. M. 1996, *Astrophys. J. Suppl.*, **106**, 533.

J. Astrophys. Astr. (2004) **25,** 203–211

An Apparent Descriptive Method for Judging the Synchronization of Rotation of Binary Stars

Li Lin-sen
Department of Physics, Northeast Normal University, Changchun 130 024, China.

Received 2003 August 22; accepted 2004 November 6

Abstract. The problem of the synchronous rotation of binary stars is judged by using a synchronous parameter Q introduced in an apparent descriptive method. The synchronous parameter Q is defined as the ratio of the rotational period to the orbital period. The author suggests several apparent phenomenal descriptive methods for judging the synchronization of rotation of binary stars. The first method is applicable when the orbital inclination is well-known. The synchronous parameter is defined by using the orbital inclination i and the observable rotational velocity $(V_{1,2}\sin i)_M$. The method is mainly suitable for eclipsing binary stars. Several others are suggested for the cases when the orbital inclination i is unknown. The synchronous parameters are defined by using $a_{1,2}\sin i$, $m_{1,2}\sin^3 i$, the mass function $f(m)$ and semi-amplitudes of the velocity curve, $K_{1,2}$ given in catalogue of parameters of spectroscopic binary systems and $(V_{1,2}\sin i)_M$. These methods are suitable for spectroscopic binary stars including those that show eclipses and visual binary stars concurrently. The synchronous parameters for fifty-five components in thirty binary systems are calculated by using several methods. The numerical results are listed in Tables 1 and 2. The statistical results are listed in Table 3. In addition, several apparent descriptive methods are discussed.

Key words. Binary stars—synchronization of rotation—judgement of apparent phenomenal descriptive methods.

1. Introduction

In binary system the rotational period of components and its orbital period usually show a synchronous phenomenon. This is the secular evolutional result arising from tidal friction in binary systems. Investigation of this synchronous phenomenon is very meaningful for exploring the evolutional process of binary systems. Therefore, recently some authors have studied this subject by using various methods. Some authors explore the mechanism of synchronous rotational phenomenon of binary stars from theory, such as Zahnn (1966, 1975, 1977), Tassoul (1987, 1988). Some authors explore this subject from observation, such as Tan Hui-song *et al.* (1985, 1989, 1995) and Pan Kai-ke (1996, 1997). Some authors explore this subject from an apparent phenomenal descriptive method, such as this author's work (Li 1997, 1998). The author had earlier defined the ratio of rotational velocity of primary stars with orbital velocity

of components as the synchronous parameter (Li 1997). He also defined the ratio of theoretical calculated value of the period of advance of apsidal line to its observational value as the synchronous parameter (Li 1998). But the first method studies the synchronous phenomenon in the evolutional process. The later method needs a great number of the observational data of apsidal line motion of binary stars. So far, however, we have a few observational data of the velocity or period of advance of apsidal line of binary stars. So this method brings certain difficulty for judgement. Hence the author further explores how one can use a great deal of the observational data such as $a_{1,2} \sin i$, $m_{1,2} \sin^3 i$, $K_{1,2}$ and $f(m)$ in tables of binary stars to judge synchronization of rotation of binary stars by using apparent phenomenal descriptive methods. These methods are not only suitable to spectroscopic binary stars, but also eclipsing and visual binary stars. This paper will divide the case of inclination i of binary star into well known and unknown and suggest five apparent phenomenal descriptive methods to study this problem.

2. Definition of the synchronous parameters

The character of apparent phenomenal descriptive methods needs the definition of synchronous parameter for judging the synchronization of binary stars to start with. This paper defines a synchronous parameter Q as the ratio of the rotational period $P_{\rm rot}$, of binaries (primary or secondary) to the orbital period of component

$$Q = P_{\rm rot}/P. \tag{1}$$

It reflects the multiple relation between the rotational period of primary or secondary stars with the orbital period of component apparently.

While $Q = 1$, $P_{\rm rot} = P$, is called as complete synchronism, $Q \to 1$, $P_{\rm rot} \to P$, is called as approachable synchronism, and when Q differs from 1, it is called as non-synchronism.

In general, the orbital period $P >$ the rotational period, $P_{\rm rot}$, so, $Q < 1$ usually. But as the binary system evolves the orbital period shortens and the rotational period lengthens, so, $P_{\rm rot} \to P$ or $Q \to 1$. From the evolutional point of view, $P_{\rm rot}$ cannot exceed P, so we cannot have Q greater than 1. However the observational data may give $Q > 1$, *i.e.*, $P_{\rm rot} > P$, due to errors in the estimated parameters of the binary system.

In discussing the problem of synchronization of binary stars, one author defined $\omega \leq 1.5\Omega$ (ω: primary rotational velocity, Ω: orbital velocity of component) as the range of the synchronous judgement (Plavec 1970; Levato 1976; Giuricin *et al.* 1984, Li 1998), but another author defined $\omega \leq 1.3\Omega$ as the synchronous judgement according to the estimation of the range of error (Pan Kai-ke *et al.* 1996, 1997). Therefore this paper adopted this judgement. However, this is the case when $P > P_{\rm rot}$ or $Q < 1$. For the case: $P < P_{\rm rot}$ or $Q > 1$, we take $\Omega \leq 1.3\omega$. Further $Q = 1$ represents complete synchronization. Then we have the following five cases:

Case A:	$0.95 \leq Q \leq 1.05$	– Almost complete synchronization.
Case B:	$0.80 \leq Q < 0.95$	– Approaching synchronization.
	$1.05 < Q \leq 1.20$	– Approaching synchronization.
Case C:	$0.70 \leq Q \leq 0.80$	– Critical synchronization.
	$1.20 < Q \leq 1.30$	– Critical synchronization.

Case D: $Q < 0.70$ – Non-synchronization.

Case E: $Q > 1.3$ – Slow rotators (slow rotation).

Case E is not a product of evolution.

3. Apparent phenomenal descriptive methods for judging the synchronization of rotation of binary stars

(1) When inclination is well-known, we adopt the following method, if binary star is an eclipsing binary.

Let $(V_{1,2}\sin i)_M$ be the observed rotational velocities of two components observed from spectral lines. i is the inclination. $P_{\rm rot}$ is the rotational period, $R_{1,2}$ are the radii of two components, then apparent rotational velocities of two components are written as

$$(V_{1,2}\sin i)_M = \left(\frac{2\pi R_{1,2}}{P_{\rm rot}}\right)\sin i. \tag{2}$$

Substituting $P_{\rm rot}$ into expression (1), we obtain

$$Q = \frac{2\pi R_{1,2}\sin i}{P\left[V_{1,2}\sin i\right]_M}. \tag{3}$$

We denote $(V_{1,2}\sin i)_M$ in the units of km/s, radii $R_{1,2}$ by R_θ (solar radius), the orbital period by d (day), the expression (3) becomes

$$Q_{e,e'} = 50.6139\frac{R_{1,2}\sin i}{P\left[V_{1,2}\sin i\right]_M} \tag{4}$$

$Q_{e,e'}$ denotes Q_e and Q'_e, *i.e.*, synchronous parameters of primary and secondary stars.

The formula (4) is suitable to the visual or eclipsing binary stars.

(2) When the inclination is unknown, we adopt the following three methods, if the table of spectroscopic binary gives $a_{1,2}\sin i$, $m_{1,2}\sin^3 i$ or K_1 and K_2 for double-lined binaries.

The first method: The method uses $a_{1,2}\sin i$.

The expression (3) or (4) is written as

$$Q_{1,1'} = \frac{2\pi R_{1,2}(a_{1,2}\sin i)}{P\left[V_{1,2}\sin i\right]_M a_{1,2}}, \tag{5}$$

$Q_{1,1'}$ denotes Q_1 or Q'_1, *i.e.*, synchronous parameters of two components.

According to the motion of center of mass and Kepler's third law, we have,

$$a_{1,2} = \left(\frac{G}{4\pi^2}\right)^{1/3}\frac{M_{2,1}}{(M_1+M_2)^{2/3}}P^{2/3}. \tag{6}$$

Substituting (6) into (5), let $q_1 = M_2/M_1 = m_2/m_1, q_2 = M_1/M_2 = m_1/m_2$, $q_{1,2}$ denotes q_1 or q_2 and $m_{1,2}$ denotes m_1 or m_2, $M_1 = m_1 M_\odot$, $M_2 = m_2 M_\odot$, we obtain,

$$Q_{1,1'} = 1.7290 \times 10^{-5} \frac{R_{1,2}(1+q_{1,2})^{2/3}(a_{1,2}\sin i)}{P^{5/3} q_{1,2} m_{1,2}^{1/3} (V_{1,2}\sin i)_M}. \tag{7}$$

The second method: The method uses $m_{1,2}\sin^3 i$.

Formula (3) or (4) is written as

$$Q = \frac{2\pi R_{1,2}(M\sin^3 i)^{1/3}}{P(V_{1,2}\sin i)_M M^{1/3}}.$$

The units are the same as in the previous method, then the above expression can be written as:

$$Q_{2,2'} = 50.6139 \frac{R_{1,2}(m_{1,2}\sin^3 i)^{1/3}}{P m_{1,2}^{1/3}(V_{1,2}\sin i)_M}. \tag{8}$$

The third method: The method uses K_1 and K_2.

Some catalogues of the orbital elements of spectroscopic binary systems gives the following formula (Batten *et al*. 1989, Kopal 1959)

$$m_{1,2}\sin^3 i = 1.0385 \times 10^{-7}(1-e^2)^{3/2}(K_1+K_2)^2 K_{1,2} P.$$

Substituting the formula for $m_{1,2}\sin^3 i$ into (8) and putting $K = K_1 + K_2$, we obtain

$$Q_{3,3'} = 0.2377 \frac{R_{1,2}(1+q_{1,2})^{2/3}(1-e^2)^{1/2} K_{1,2}}{P^{2/3} q_{1,2} m_{1,2}^{1/3}(V_{1,2}\sin i)_M}, \tag{9}$$

where $K_{1,2}$ denotes the semi-amplitudes of the velocity curves of primary and secondary components, e is the orbital eccentricity.

The above three methods are mainly suitable for the double-lined spectroscopic binary stars.

The fourth method: The method uses mass function $f(m)$ for single-lined spectroscopic binaries. We use the following method, only if the spectrum of primary component appears, the mass function $f(m)$ is written as

$$f(m) = \frac{m_2^3 \sin^3 i}{(m_1+m_2)^2} = 1.0385 \times 10^{-7}(1-e^2)^{3/2} K_1^3 P.$$

The above formula can be written as

$$m_2 \sin^3 i = f(m)(m_1+m_2)^2/m_2^2.$$

Substituting it into (8), and putting $q_1 = m_2/m_1$, we get

$$Q_4 = 50.6139 \frac{R_1(1+q_1)^{2/3}\,[f(m)]^{1/3}}{P q_1 m_1^{1/3}\,[(V_1 \sin i)]_M}, \tag{10}$$

where Q_4 is the synchronous parameter for single-lined spectroscopic primary stars. Therefore this method is suitable for single-lined spectroscopic binary stars or eclipsing binary stars concurrently.

$a_{1,2} \sin i$, $m_{1,2} \sin^3 i$, $K_{1,2}$ and $f(m)$ in formulas (7)–(10) are taken from the catalogue of spectroscopic binary systems (Batten *et al*. 1989).

4. Calculation for the synchronous parameters of fifty-five components in thirty binary systems

We calculate the synchronous parameters for eclipsing binary stars and double- and single-lined spectroscopic binary stars by using previous methods. In computation, $(V_{1,2} \sin i)_M$ are quoted from the date given by (Tan 1985, 1989, 1995). The synchronous parameters of eclipsing binary stars are calculated by using the formula (4) (the inclination is well-known). The periods, stellar radius and mass are quoted from the catalogue of parameters of eclipsing binary stars (Brancewicz *et al*. 1980). The calculated results are listed in Table 1. The synchronous parameters of double-lined and single-lined spectroscopic binary stars are calculated by using formulas (7)–(10) (the inclination is unknown). The orbital periods P, $a_{1,2} \sin i$, $m_{1,2} \sin^3 i$, $K_{1,2}$ and $f(m)$ are quoted from the catalogue of the orbital elements of spectroscopic binary systems (Batten *et al*. 1989). Because the stellar mass and radius are not given in the catalogue, the calculated binary systems are all spectroscopic binary stars which are also eclipsing binary stars concurrently, so the stellar mass and radius are quoted from the catalogue of parameters of eclipsing binary stars. The calculated results are listed in Table 2, which also indicates the categories A, B, C, D, E, as defined earlier.

5. Statistical results for synchronization of rotation of fifty-five components

Table 3 which shows the statistical results for synchronization of rotation of fifty-five components can be obtained from Tables 1 and 2.

It can be seen from the statistical table 3 that 14% components have achieved almost complete synchronism (A), 33% are approaching synchronism (B), 18% are at critical synchronism (C) and 31% are non-synchronous (D). The remaining two components are slow rotators (E) which need theoretical explanation. Further among the binaries containing category A stars GT Cep and AH Cep can be considered to have complete synchronism for both components.

6. Discussions and summary

- The characteristic of this paper is that it introduces a synchronous parameter Q. It not only judges directly synchronization of two components, but also analyses

Table 1. The calculated results for synchronous parameters of twenty components in ten eclipsing binary systems by using the apparent descriptive method of formula (4).

Name		Sp type	P(d)	i(deg)	$R_{1,2}(R_\odot)$	$(V_{1,2}\sin i)_M$ (km/s)	$Q_{e,e'}$	$P_R \gtrless P$	Synch
GT Cep	1	B2V	4.9087	78	4.64	42	1.11	$P_R > P$	B
	2	A0			6.04	58	1.05	$P_R > P$	A
My Cyg	1	Am	4.0051	89	2.32	26	1.13	$P_R > P$	B
	2	Am			2.06	47	0.55	$P_R < P$	D
V451 Oph	1	B9V	2.1966	87	2.48	48	1.19	$P_R > P$	B
	2	A0			1.98	45	1.01	$P_R > P$	A
U Oph	1	B4.5	1.6773	86.6	3.27	110	0.89	$P_R < P$	B
	2	B5.5			3.02	100	0.91	$P_R < P$	B
V505 Sgr	1	A2v	1.8287	75	2.30	100	0.95	$P_R < P$	A
	2	F81V			2.35	50	1.94	$P_R > P$	E
CV Vel	1	B2V	6.8925	88.2	4.27	50	0.63	$P_R < P$	D
	2	B2V			4.16	85	0.36	$P_R > P$	D
CD Tau	1	F7V	3.4351	88	1.49	34	0.64	$P_R < P$	D
	2	F7V			1.50	34	0.65	$P_R > P$	D
V1143 Cyg	1	F5V	7.6407	87	1.34	9	0.98	$P_R < P$	A
	2	F5V			1.04	20	0.34	$P_R < P$	D
ZZ Boo	1	F2V	4.9917	88	1.76	12	1.48	$P_R > P$	E
	2	F2V			1.70	25	0.69	$P_R < P$	D
AS Cam	1	B8V	3.4309	89	2.06	40	0.7	$P_R < P$	C
	2	A0V			2.47	30	1.21	$P_R > P$	C

the evolutionary progress of binary systems. Because the synchronous parameter Q indicates the evolutionary status of the binary system in that the variation of the value Q tends to unity due to tidal friction. In the end the binary system arrives at the synchronous phenomenon of the orbital and rotational periods.

- There are different suitable methods for several apparent descriptive methods suggested in this paper. The method of formula (4) suits only eclipsing binary stars including visual binary stars for which inclination i is well-known. It is not suitable for spectroscopic binary stars as their inclinations are unknown. Although some spectroscopic binary stars are eclipsing binary stars concurrently also, this method can be used, but some spectroscopic binary stars are not eclipsing binary stars. Therefore, this method cannot be used. However, for the spectroscopic binary star for which inclination i is unknown, we can make use of $a_{1,2}\sin i$, $m_{1,2}\sin i^3 i$, $k_{1,2}$ and $f(m)$ in the table of spectroscopic binary stars by using the formulas (7)–(10). But the mass is unknown for spectroscopic binary stars. However the mass may be well-known, if the spectroscopic binary stars are eclipsing binary stars concurrently or visual binary stars. Because this paper selects two types of spectroscopic binary stars as eclipsing binary stars concurrently, so, its masses are quoted from the data in the table of eclipsing binary stars.

Table 2. The calculated results for synchronous parameters of thirty-five components in twenty single-lined and double-lined spectroscopic binary systems by using four apparent descriptive methods.

The first method calculated by using $a_{1,2}\sin i$											
Name		Sp type	P(d)	$R_{1,2}$ ($R_\odot$)	$m_{1,2}$ ($m_\odot$)	$q_{1,2}$	$(V_{1,2}\sin i)_M$ (km/s)	$a_{1,2}\ \sin^3 i$ (km)	$Q_{1,1}$	$P_R \lesseqgtr P$	Synch
AG Per	1	B5pV	2.0287	3.02	5.08	0.89	105	4.53	0.69	$P_R < P$	D
	2	F6		2.78	4.52	1.1	120	4.97	0.55	$P_R < P$	D
V448 Cyg	1	O9.5	6.5179	10.00	22.25	0.73	95	$1.92\times10^{+1}$	1.08	$P_R > P$	B
	2	BII		17.34	16.24	1.37	92	$1.50\times10^{+1}$	1.10	$P_R > P$	B
GK Cep	1	A2V	0.9362	2.67	2.67	0.93	106	2.21	1.29	$P_R > P$	C
	2	A4		2.45	2.48	1.08	100	2.41	1.27	$P_R > P$	C
EI Cep	1	FI	8.4397	2.99	1.80	0.95	15	9.42	1.25	$P_R > P$	C
	2	FI		2.31	1.71	1.05	10	8.92	1.31	$P_R > P$	D
AH Cep	1	O8	1.7748	6.44	16.52	0.87	175	6.08	1.08	$P_R > P$	B
	2	O9		5.98	14.37	1.15	160	6.91	1.02	$P_R > P$	A
The second method calculated by using $m_{1,2}\sin^3 i$											
Name		Sp type	P(d)	$R_{1,2}$ ($R_\odot$)	$m_{1,2}$ ($m_\odot$)	$q_{1,2}$	$(V_{1,2}\sin i)_M$ (km/s)	$m_{1,2}\ \sin^3 i$ ($m_\odot$)	$Q_{2,2}$	$P_R \lesseqgtr P$	Synch
EK Cep	1	A1V	4.4278	1.59	2.11	0.55	45	2.0	0.63	$P_R < P$	D
	2	G5		1.19	1.16	1.82	14	1.1	1.02	$P_R > P$	B
NY CeP	1	B01V	15.2767	10.56	16.51	0.67	80	$2.7\times10^{+1}$	0.52	$P_R < P$	D
	2	B01 V		8.66	11.06	1.49	71	$1.3\times10^{+1}$	0.43	$P_R < P$	D
RX Her	1	B9.5 V	1.7786	2.37	2.86	0.86	73	2.7	0.93	$P_R < P$	B
	2	A0.5 V		2.05	2.50	1.07	60	2.3	0.94	$P_R < P$	B
Z Vul	1	B4 V	2.4454	4.54	5.42	0.43	98	5.4	0.95	$P_R < P$	A
	2	A3III		4.57	2.33	2.32	115	2.2	0.79	$P_R < P$	C
λ Tau	1	B3V	3.9529	5.64	6.04	0.24	85	6.4	0.87	$P_R < P$	B
	2	A4IV		4.33	1.45	4.16	60	1.7	0.97	$P_R < P$	A

Table 2. (*Continued*)

Name		Sp type	P(d)	$R_{1,2}$ ($R_\odot$)	$m_{1,2}$ ($m_\odot$)	$q_{1,2}$	e	$(V_{1,2}\sin i)_M$ (km/s)	$m_{1,2}\ \sin^3 i$ ($m_\odot$)	$Q_{3,3}$	$P_R \lessgtr P$	Synch
				The third method calculated by using $k_{1,2}$								
EG Ser	1	A0	9.9473	2.17	3.05	0.78	0	48	75.8	0.22	$P_R < P$	D
	2	A2		1.93	2.37	1.29	0	68	83.8	0.12	$P_R < P$	D
V624 Her	1	A_{3m}	3.8950	2.93	2.23	0.86	0	36	96.6	1.02	$P_R > P$	A
	2	A_{4m}		2.32	1.90	1.17	0	36	117.2	0.84	$P_R < P$	B
Sig Aq	1	B_3V	1.9503	4.12	6.48	0.86	0	108	16.42	0.90	$P_R < P$	B
	2	B_3V		3.44	5.58	1.16	0	125	208	0.71	$P_R > P$	C
WW Air	1	A7V	2.5250	1.93	1.81	0.96	0	35	115.6	1.09	$P_R > P$	B
	2	A7V		1.92	1.74	1.04	0	35	127.7	1.15	$P_R > P$	B
RZ Cha	1	F5IV	2.8321	2.94	1.90	0.84	0	39	108.2	1.34	$P_R > P$	D
	2	F5IV		3.19	1.59	1.19	0	39	107.6	1.27	$P_R > P$	C
				The fourth method calculated by using $f(m)$								
Name		Sp type	P(d)	R_1 ($R_\odot$)	m_1 ($m_\odot$)	q_1		$(V_1\sin i)_M$ (km/s)	$m_1\ \sin^3 i$ ($m_\odot$)	Q_4	$P_R \lessgtr P$	Synch
UW Vir_1		A_4	1.8107	1.52	1.77	0.24		76	1.9×10^{-2}	0.59	$P_R < P$	D
TW Dra_1		A_5V	2.8067	2.06	2.24	0.43		123	5.9×10^{-2}	0.59	$P_R < P$	D
QS Aql_1		B5V	2.4968	2.65	6.82	0.17		75	2.7×10^{-2}	0.74	$P_R < P$	C
DV Aql_1		LateA	1.5755	2.16	2.20	0.59		92	1.4×10^{-1}	0.70	$P_R < P$	C
UX Her_1		A3	1.5489	1.80	1.92	0.30		61	2.1×10^{-2}	0.85	$P_R < P$	B

Table 3. The statistical results for synchronization of rotation of fifty-five components in binary systems.

Type	No. of systems	No. of components	$Q < 1$ $P_R < P$	$Q > 1$ $P_R > P$	A	B	C	D	E
EB	10	20	11	9	4	6	2	6	2
DSB	15	30	16	14	4	11	6	9	0
SSB	5	5	5	0	0	1	2	2	0
Sum (total)	30	55	32	23	8	18	10	17	2

EB: Eclipsing binary stars.
DSB: Double-line spectroscopic binary stars.
SSB: Single-line spectroscopic binary stars.

References

Batten, A. H. *et al.* 1989, *Publ. Dom. Astrophys,* **17**, 1–127.
Brancewicz, H. K., Dworak, T. Z. 1980, *Acta Astronomica*, **30**(4), 501.
Giuricin, G. *et al.* 1984, *A & A*, **131**, 152; **135**, 393.
Kopal, Z. 1959, *Close binary system* (London: Chapman and Hall) p. 470.
Levato, H. 1976, *Ap J*, **203**, 680.
Li, Lin-sen, *Acta Astrophys. Sinica*, 1998, **18**, 77; 1977, **17**, 407.
Pan Kai-ke 1996, *Acta Astrophys. Sinica*, **16**, 291; 370.
Pan Kai–ke 1997, *A & A*, **321**, 202.
Pan Kai–ke *et al.* 1997, *Acta Astrophys. Sinica*, **17**, 386.
Pan Kai-ke *et al.* 1997, Publ Yunnan Obs, No. 2, 87.
Plavec, M. 1970, in *Slettebok Rotation*, (ed.) A. Slettebok (Dordrecht: Reidel) p. 133.
Tan Hui-song *Acta Astron. Sinica*, 1989, **30**, 135; 1985, **26**, 226.
Tan Hui-song *et al.* 1995, *Acta Astrophys. Sinica*, **15**, 57.
Tassoul, J. L. 1988, *Ap J*, **324**, L71; 1987, **322**, 856.
Zahn, J. P. 1966 *Ann. Ap*., **29**, 489.
Zahn, J. P. 1978 *A & A*, **67**, 162; 1977, **57**, 383; 1975, **41**, 329.

J. Astrophys. Astr. (2004) **25,** 213–220

Relation between a Function of the Right Ascension and the Angular Distance to the Vertex for Hyades Stars

M. A. Sharaf[1], M. I. Nouh[2] & A. S. Saad[2]
[1]*Department of Astronomy, Faculty of Science, King Abdul Aziz University, Jeddah, Saudi Arabia.*
[2]*Department of Astronomy, National Research Institute of Astronomy and Geophysics, Helwan, Egypt.*

Received 2003 July 14; accepted 2004 December 17

Abstract. In this paper, relation was developed for Hyades stars between a function of the right ascensions and the angular distances from the vertex. The precision criteria of this relation are very satisfactory and a correlation coefficient value of $\simeq 1$ was found which proves that the attributes are completely related linearly. The importance of this relation was illustrated through its usages as:

- a criterion for membership of the cluster,
- a generating function for evaluating some parameters of the cluster,
- a generating function for the initial values of the vertex equatorial coordinates which could then be improved iteratively using the procedure of differential corrections.

Key words. Moving clusters—Hyades cluster—open clusters—Hyades astrometric and kinematic.

1. Introduction

The open star cluster known as the Hyades occupies a unique place in the history and literature of astronomy. It is one of the few star clusters to have been recognized by the ancients, and shares with the Pleiades and the Coma clusters the distinction of being sufficiently close to us for the brighter members to be individually visible to the naked eye. Hyades cluster, with some 300 possible members, a total mass of some 300–400$M_{\odot}$, and an age of around 600–800Myr, has an extension in the sky of about 20°. Hyades cluster provides a well known example of a moving cluster, that is, a group of stars whose parallel motions in space yield, on the celestial sphere, directions of proper motion that appear to converge to a point called the vertex of the motion (or of the cluster). The determination of the equatorial coordinates of the vertex, that is, its right ascension and declination (A, D) is one of the most important problems in the kinematical and physical studies of moving clusters (Wayman 1965; Hanson 1975; Eggen 1984; Gunn *et al.* 1988; Sharaf *el al.* 2000). In particular, the color-magnitude diagram of the Hyades cluster has been of prime importance in establishing the Zero Age Main Sequence (ZAMS) as well as in calibrating luminosity criteria which permit

the determination of the absolute magnitudes of the stars from observable features in their spectra (Perryman *et al.* 1998; de Bruije *et al.* 2001). The kinematic distance of the Hyades derived from a combination of proper motions and spectroscopic radial velocities, has been one of the fundamental starting points for the calibration of the photometric distance scale (Hanson 1975; Gunn *et al.* 1988; Schwan 1991). In fact, the availability of the final results of the Hipparcos astrometry mission, provide a radical improvement in astrometric data on all stars in the Hipparcos observing programme, including approximately 240 candidate Hyades members. The first detailed study of the distance, structure, membership, dynamics and age of the Hyades cluster, using Hipparcos data was by Perrymant *et al.* (1998). Recently (Sharaf 2003) a relation was established between the apparent magnitude and the parallax for Hyades stars using the best rational approximation technique. The precision criteria of such a relation were very satisfactory and some utilizations of the relation were also given.

In the present paper, a relation was developed between a function of the right ascensions and the angular distances from the vertex. As a test for the existence of such a relation for Hyades cluster, we used 133 stars of Schwan's table (Schwan 1991). Although these data are not the most accurate as compared with those of Hipparcos, the precision criteria of the relation are very satisfactory and a correlation coefficient value of $\simeq 1$ was found which proves that the attributes are completely related linearly. The importance of this relation was illustrated through its usages as: a criterion for membership of the cluster, generating function for evaluating some parameters of the cluster, and the initial values of the vertex equatorial coordinates which could then be improved iteratively using the procedure of differential corrections (Sharaf *et al.* 2000).

2. Basic formulations

The material of this section is a summary of the corresponding section of Sharaf *et al.* (2000), and is given through the following subsections:

2.1 *Determination of the vertex of a moving cluster*

If we know the right ascensions α_i, declinations δ_i and the components $(\mu_\alpha^{(i)}, \mu_\delta^{(i)})$ of the total proper motion $\mu^{(i)}; i = 1, \ldots, N$, where N is the number of the cluster members, then the equatorial coordinates (A, D) of a moving cluster could be determined from

$$A = \tan^{-1}(\eta/\xi), \tag{1}$$

$$D = \tan^{-1}[(\eta^2 + \xi^2)^{-1/2}], \tag{2}$$

where

$$\xi = (T_5T_2 - T_3T_4)/\Delta, \tag{3}$$

$$\eta = (T_3T_2 - T_5T_1)/\Delta, \tag{4}$$

$$T_1 = \sum_{i=1}^{N} a_i^2, \qquad T_2 = \sum_{i=1}^{N} a_i b_i, \qquad T_3 = \sum_{i=1}^{N} a_i c_i,$$

$$T_4 = \sum_{i=1}^{N} b_i^2, \qquad T_5 = \sum_{i=1}^{N} c_i b_i, \tag{5}$$

$$a_i = \mu_\alpha^{(i)} \sin\delta_i \cos\alpha_i \cos\delta_i - \mu_\delta^{(i)} \sin\alpha_i,$$

$$b_i = \mu_\alpha^{(i)} \sin\delta_i \sin\alpha_i \cos\delta_i + \mu_\delta^{(i)} \cos\alpha_i,$$

$$c_i = \mu_\alpha^{(i)} \cos^2\delta_i. \tag{6}$$

2.2 *Differential corrections to the vertex coordinates*

The differential corrections ΔA and ΔD to the vertex coordinates A and D are given as:

$$\Delta A = (G_5 G_2 - G_3 G_4)/E, \tag{7}$$

$$\Delta D = (G_3 G_2 - G_5 G_1)/E, \tag{8}$$

where

$$E = G_2^2 - G_4 G_1, \tag{9}$$

$$G_1 = \sum_{i=1}^{N} \Psi_i^2, \qquad G_2 = \sum_{i=1}^{N} \Psi_i \Phi_i, \qquad G_3 = \sum_{i=1}^{N} \Psi_i \Delta\theta_i,$$

$$G_4 = \sum_{i=1}^{N} \Phi_i^2, \qquad G_5 = \sum_{i=1}^{N} \Phi_i \Delta\theta_i, \tag{10}$$

$$\Psi_i = \sin^2\theta_{\text{cal}}^{(i)} [\cos\delta_i \tan D \cos(A - \alpha_i) - \sin\delta_i] / \sin^2(A - \alpha_i), \tag{11}$$

$$\Phi_i = -\sin^2\theta_{\text{cal}}^{(i)} [\cos\delta_i \sec^2 D] / \sin(A - \alpha_i), \tag{12}$$

$$\Delta\theta_i = \theta_{\text{obs}}^{(i)} - \theta_{\text{cal}}^{(i)}, \tag{13}$$

$$\theta_{\text{obs}}^{(i)} = \tan^{-1}(\mu_\alpha^{(i)} \cos\delta_i / \mu_\delta^{(i)}), \tag{14}$$

$$\theta_{\text{cal}}^{(i)} = \cos^{-1}[(\sin D - \sin\delta_i \cos\lambda_i) / \cos\delta_i \sin\lambda_i], \tag{15}$$

θ is the position angle of the total proper motion and λ_j is the angular distance of the jth star to the vertex and is given by

$$\lambda_j = \cos^{-1}(\sin\delta_j \sin D + \cos\delta_j \cos D \cos(A - \alpha_j)). \tag{16}$$

Now having obtained the corrections ΔA and ΔD, one can determine the corrected values of the coordinates of the vertex, A^* and D^* from

$$A^* = A + \Delta A, \tag{17}$$

$$D^* = D + \Delta D. \tag{18}$$

This process of corrections could be repeated in an iterative manner until the desired accuracy is thus achieved, for instance, $|\Delta A| \leq \in_1$ and $|\Delta D| \leq \in_2$, where $\in_1$ and $\in_2$ are two given tolerances.

2.3 *Velocity components V_α, V_δ and ρ*

Let V_α, V_δ and ρ be the components of the velocity $\mathbf{V}$ (as a basic assumption, all members of a moving cluster have the same $|\mathbf{V}|$) along coordinate system whose center is a star and consisting of three mutually perpendicular unit vectors $(\hat{\alpha}, \hat{\delta}, \hat{\mathbf{r}})$ defined as follows:

- The unit vector $\hat{\alpha}$ tangent to the circle of constant declination and pointing in the direction of increasing right ascension.
- The unit vector $\hat{\delta}$ tangent to the circle of constant right ascension and pointing towards the north celestial pole.
- The unit vector $\hat{\mathbf{r}}$ lying on the radius vector, which joins the sun to the star, so ρ is the radial velocity of the star. These components are given as,

$$V_\alpha = 4.738\mu_\alpha \cos\delta/p, \tag{19}$$

$$V_\delta = 4.738\mu_\delta/p, \tag{20}$$

$$V_t^2 = V_\alpha^2 + V_\delta^2, \tag{21}$$

where p is the parallax. Also we have

$$V_t = V \sin\lambda, \tag{22}$$

$$\rho = V \cos\lambda, \tag{23}$$

V is the velocity of the cluster.

3. Numerical applications

3.1 *Data*

For the present applications we used 133($= N$) stars of Schwan's table (Schwan 1991). Using these data and the algorithm of section 2.1 we get for A and D (both in degrees) together with their probable errors the values

$$A = 96.533 \pm 0.563, \tag{24}$$

$$D = 6.5735 \pm 0.226. \tag{25}$$

3.2 *Relation between H and λ*

Using the data of Schwan's table and the formulations of section 2 together with the numerical values of equations (24) and (25) we get very simple and a very significant

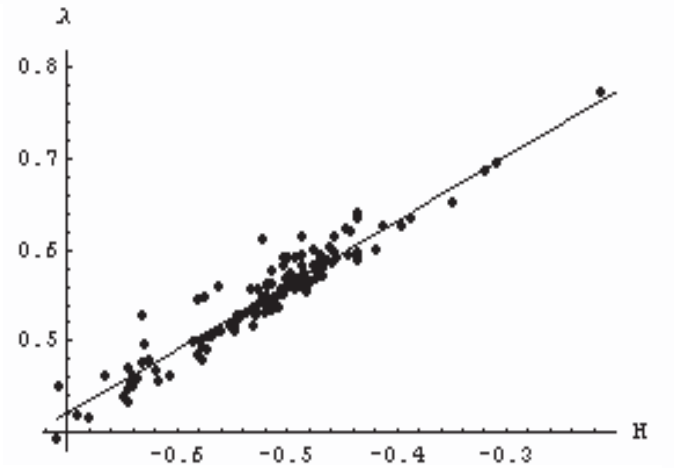

Figure 1. Graphical representation between the raw and the fitted data.

relation between the right ascension α and the angular distance to the vertex λ, this relation is given as;

$$\lambda = c_1 + c_2\, H, \tag{26}$$

$$H = \cos\alpha - \sin\alpha, \tag{27}$$

where the coefficients and their probable errors are

- $c_1 = 0.912854 \pm 0.00522729$.
- $c_2 = 0.703744 \pm 0.010081$.
- The probable error of the fit is $e = 0.0117353$.
- The average squared distance between the exact solution and the least squares solution (Kopal and Sharaf 1980) is $Q = 0.00028344$.
- The linear correlation coefficient between (H, λ) is $r = 0.971705$.
- The graphical representation between the raw and the fitted data is given in Fig. 1:

4. Utilizations of the relation

Assuming equation (26) as a given relation for Hyades cluster, it could be utilized in generating some important knowledge about the cluster. They are the following:

4.1 *Right ascension criterion*

Equation (26) may provide an additional membership criterion of Hyades cluster as follows. Assume that the right ascension α_0 of a star, suspected of being a member of the cluster was known. Now from this value of α_0, the spherical distance λ_0 of the star from the vertex could be obtained from equation (26). With the spherical distance λ_c calculated by means of equation (16) and, if $\mid \lambda_0 - \lambda_c \mid$ is reasonably small, we can conclude that possibly the star is a member of the cluster. This is what we may call *right ascension criterion.*

4.2 *Generating function*

Equation (26) may also be used as a generating function for evaluating some important parameters of the cluster. Assuming that the tangential velocities $V_t^{(i)}$ are known together with $\alpha_i, \delta_i, \mu_\alpha^{(i)}$ and $\mu_\delta^{(i)}$ for L (say) stars; $i = 1, 2, \ldots, L$, then from equation (26) we get the corresponding spherical distances λ_i. Having obtained λ's, some parameters could then be evaluated, as in the following.

- *The velocity of the cluster*

  Equation (22) can be considered as an equation of condition for determining the velocity V of the cluster and we derive

$$V = \sum_{i=1}^{L} V_t^{(i)} \sin \lambda_i \Big/ \sum_{i=1}^{L} \sin^2 \lambda_i . \tag{28}$$

- *The radial velocities of the cluster stars*

  From equations (22) and (23) the radial velocities $\rho_i, i = 1, 2, \ldots, L$ follow from

$$\rho_i = V_t^{(i)} \cot \lambda_i . \tag{29}$$

- *The parallaxes of the cluster stars*

  The total proper motions $\mu_i; i = 1, 2, \ldots, L$ are computed from

$$\mu_i = \sqrt{(\mu_\alpha^{(i)} \cos \delta_i)^2 + (\mu_\delta^{(i)})^2},$$

  then the parallaxes $p_i; i = 1, 2, \ldots, L$ are computed from

$$p_i = 4.738 \mu_i / V_t^{(i)}. \tag{30}$$

- *The absolute magnitudes of the cluster stars*

  If the apparent magnitudes $m_i, i = 1, 2, \ldots, L$ of the cluster stars are also known, then their absolute magnitudes can be found from

$$M_i = m_i + 5 + 5 \log p_i , \tag{31}$$

  where p_i are given from equation (30).

- *The center of the cluster*

  The center of the cluster (x_c, y_c, z_c) can be derived by the simple method of finding the equatorial coordinates of the center of mass for a number of discrete objects, so

$$x_c = \left[\sum_{i=1}^{L} \cos\delta_i \cos\alpha_i / p_i\right] \Big/ L, \tag{32}$$

$$y_i = \left[\sum_{i=1}^{L} \cos\delta_i \sin\alpha_i / p_i\right] \Big/ L, \tag{33}$$

$$z_i = \left[\sum_{i=1}^{L} \sin\delta_i / p_i\right] \Big/ L, \tag{34}$$

where p_i are given from equation (30).

- *The distance of the cluster*

  The distance of the cluster is given by

$$d = L \Big/ \left[\sum_{i=1}^{L} p_i\right], \tag{35}$$

  where p_i are given from equation (30).

4.3 *Initial values of the vertex coordinates*

Select a few N_0 (say) stars which are adopted as Hyades members. In what follows we shall illustrate the usage of equation (26) in generating initial values of the vertex equatorial coordinates A_0 and D_0. These values could then be improved iteratively using the procedure of differential corrections as mentioned in section 2.

1. Compute $\theta_{\text{obs}}^{(i)}$; $i = 1, 2, \ldots, N_0$ from equation (14).
2. Compute λ_i; $i = 1, 2, \ldots, N_0$ from equation (26).
3. Compute $D_0^{(i)}$ and $A_0^{(i)}$; $i = 1, 2, \ldots, N_0$ from

$$D_0^{(i)} = \sin^{-1}(\cos\theta_{\text{obs}}^{(i)} \cos\delta_i \sin\lambda_i + \sin\delta_i \cos\lambda_i),$$

$$A_0^{(i)} = \alpha_i + \cos^{-1}[\{\cos\lambda_i - \sin\delta_i \sin D_0^{(i)}\}/\cos\delta_i \cos D_0^{(i)}].$$

4. Compute A_0 and D_0 from

$$A_0 = \sum_{i=1}^{N_0} A_0^{(i)} / N_0,$$

$$D_0 = \sum_{i=1}^{N_0} D_0^{(i)} / N_0.$$

As a simple example let us consider the first five stars of Schwan's table, then from the above computational sequence we get

$$A_0 = 96^\circ.3741,$$

$$D_0 = 6^\circ.75983,$$

which are very reasonable initial values for the differential corrections procedure.

In concluding the present paper, a relation was developed for Hyades stars between a function of the right ascensions and the angular distances from the vertex. Precision criteria of this relation which are the uncertainties of its coefficients, probable error of the fit, and the Q value are all very satisfactory, also a correlation coefficient of value $\simeq 1$ was found, which proves that the attributes are completely related linearly. The importance of this relation was illustrated through its usages as:

- A criterion for membership of the cluster which we may call *right ascension criterion*.
- A generating function for evaluating some parameters of the cluster for example, the velocity and the center of the cluster, also the parallaxes, radial velocities and the absolute magnitudes of the cluster stars.
- Finally, the relation could be utilized to generate initial values of the vertex equatorial coordinates which could then be improved iteratively using the procedure of differential correction.

References

de Bruije, J. H. J., Hoogerwerf, R. de Zeeuw, P. T. 2001, *A & A*, **367**, 111.
Eggen, O. J. 1984, *ApJ*, **89**, 1350.
Gunn, J. E, Griffin, R. F., Griffin, R. E. M., Zimmerman, B. A. 1988, *AJ*, **96**, 198.
Hanson, R. B. 1975, *AJ*, **80**, 379.
Kopal, Z., Sharaf, M. A. 1980, *Astrophysics and Space Science*, **70**, 77.
Perryman, M. A. C., Brown, A. G. A., Lebreton, Y. 1998, *A & A*, **331**, 81.
Radic, R. R., Lockwood, G. W., Skiff, A. B., Thompson, D. T. 1995, *ApJ*, **452**, 332.
Schwan, H. 1991, *A & A*, **243**, 386.
Sharaf, M. A., Bassuny, A. A., Korany, B. A. 2000, *Astrophysical Letter and Communications*, **40**, 39.
Sharaf, M. A. 2003, *New Astronomy*, **8**, 645.
Wayman, P. A., Symms, L. S. T., Blacwell, K. C. 1965, *Joint Publication of the Royal Greenwich Observatory*, **98**.